SOLID STATE NUCLEAR MAGNETIC RESONANCE METHODOLOGY FOR BIOMOLECULAR STRUCTURE DETERMINATION

by

Chad Michael Rienstra

B.A. Chemistry
Macalester College (1993)

Submitted to the Department of Chemistry
in Partial Fulfillment of the Requirements for the
Degree of

DOCTOR OF PHILOSOPHY
in Chemistry
at the

June 1999

Signature of Author _____
Department of Chemistry
May 14, 1999

Certified by _____
Professor Robert G. Griffin
Thesis Supervisor

Accepted by _____
Professor Dietmar Seyferth
Chairman, Department Committee on Graduate Students

This Doctoral thesis has been examined by a Committee of the Department of Chemistry as follows:

Professor Andrei Tokmakoff_____
Chairman

Professor Robert G. Griffin _____ _____
Thesis Supervisor

Professor Keith A. Nelson _____

Solid State Nuclear Magnetic Resonance Methodology for Biomolecular Structure Determination

by
Chad Michael Rienstra

Submitted to the Department of Chemistry
on May 14, 1999 in partial fulfillment of the
requirements of the Degree of Doctor of Philosophy

Abstract

Several developments in solid state nuclear magnetic resonance (SSNMR) spectroscopy methods are presented. All studies are performed with magic angle spinning (MAS) and high-power proton decoupling, for optimal sensitivity and resolution.

Chemical shift are assigned by multi-dimensional correlation spectroscopy in isotopically enriched molecules. Resolution in 2D spectra of uniformly-^{13}C-labeled molecules is sufficient to assign small peptides (Gly-Phe-Ala-Asp-OH and formyl-MLF-OH, with 19 and 21 ^{13}C signals, respectively) and the macrolide antibiotic erythromycin A (37 ^{13}C signals). New pulse sequences improve polarization transfer bandwidth and/or efficiency in 2D and 3D spectra, thereby increasing crosspeak intensity relative to earlier methods. These improvements are derived from the broadband application of C7-style pulse sequences for γ-encoded homonuclear polarization transfer, and band-selective adiabatic cross polarization for heteronuclear transfer.

Signals assigned through multi-dimensional correlation spectra can provide direct structural information in an additional spectral dimension. Secondary structure is determined by measuring relative orientations of dipole vectors. New 3D experiments for the determination of multiple NH-CH and CH-CH dipole vector projection angles are demonstrated. Each pulse sequence employs two dimensions of chemical shifts, for site resolution, with a third dimension of synchronous ^{1}H-X and ^{1}H-Y dipolar evolution, to provide projection angle constraints. The sequences exploit γ-encoded elements (such as CMR7, SPC-5, and T-MREV) for optimal dynamic range and sensitivity.

Internuclear distances are determined for constraint of tertiary structure. Weak homonuclear dipolar couplings between isolated spin pairs are measured with high precision and accuracy using the CMR7 sequence. Thorough analysis of relaxation, RF errors and isotopic dilution effects permits the determination of ^{13}C-^{13}C distances with precision $\pm$0.01 Å in favorable cases.

Thesis Supervisor:	Prof. Robert G. Griffin
Title:	Professor of Chemistry Director of the Francis Bitter Magnet Laboratory

Dedication

This thesis is dedicated to my Grandparents, Richard and Henrietta Rienstra, who passed away during my third and fourth years of graduate school.

Contents

List of Figures

List of Tables

Abbreviations

1D	One-dimensional
2D	Two-dimensional
3D	Three-dimensional
AHT	Average Hamiltonian Theory
APHHCP	Adiabatic Passage Hartmann-Hahn Cross-Polarization
CMR7	Composite MLEV-Refocusing and C7
CP	Cross Polarization
CPMAS	Cross Polarization and Magic Angle Spinning
CS(A)	Chemical Shift (Anisotropy)
CT	Constant Time
CW	Continuous Wave
DCP	Double Cross Polarization
DIPSHIFT	Dipolar Chemical Shift Correlation Spectroscopy
DQ	Double-Quantum
FID	Free Induction Decay
FSLG	Frequency-Switched Lee-Goldburg
FWHM	Full Width at Half Maximum
HH	Hartmann-Hahn
HORROR	Homonuclear Rotary Resonance Recoupling
LG	Lee-Goldburg (Homonuclear Decoupling)
MAS	Magic Angle Spinning
MLEV	Malcolm Levitt (Composite Rotation Supercycle)
MREV	Mehring, Rhim, Elleman and Vaughn
MW	Maricq and Waugh
NMR	Nuclear Magnetic Resonance
PAS	Principal Axis System
POST-C7	Permutationally Offset-Stabilized C7
ppm	parts per million
R^2	Rotational Resonance
R^2T	Rotational Resonance Tickling
R^2TR	Rotational Resonance in the Tilted Frame
R^3	Rotary Resonance Recoupling
REDOR	Rotational Echo Double Resonance
RF	Radio-frequency
RFDR	Radio-Frequency Driven Dipolar Recoupling
SEDRA	Simple Excitation for the Dephasing of Rotational Echoes
SLF	Separated Local Field
SPC-5	Supercycled POST-C5
SSNMR	Solid State Nuclear Magnetic Resonance
TEDOR	Transferred Echo Double Resonance
TPPM	Two Pulse Phase Modulation
T-MREV	Transverse MREV
ZQ	Zero-Quantum

Acknowledgments

The past five and a half years have been truly memorable and productive, due to the unique environment at MIT and within the Griffin Group. This is true for many reasons: first, Bob has consistently set high standards for the lab; second, the inherent energy and intensity of MIT have pushed me forward when I least expected it; third, the abundant financial resources available at the Francis Bitter Magnet Laboratory, including funding from the National Institutes of Health and the Howard Hughes Medical Institute, have permitted research to proceed efficiently. But without question, the defining aspect of life here has been the range of talents and personalities to which I have been exposed.

Soon after arriving in January 1994, Phil Costa, Doug Maus, and Joanna Long put together a full course introduction to pulse programming, computer networking, and spectrometer hardware. At the time I considered the level of detail to be more than sufficient for my anticipated research needs; little did I realize that I would spend a large fraction of the next few years building equipment. In my early days of independent work, Janet Griffiths provided perspective with her many years' experience. Boqin Sun was always willing to offer explanations in his unique spoken language, and his simulation language—NMRLAB—on many occasions saved me days of programming. Andrew Bennett taught most of my early lessons in average Hamiltonian and decoupling theory, and was always willing to suggest where to focus my intellectual energy.

During my second year, when I began to design and build transmission line probes, I became very familiar with the outstanding technical staff at the Magnet Lab. Without question the most distinctive among them is Dave Ruben; though eternally confined to the 1970's, and terminally addicted to tobacco and caffeine, he carries with his pipe and coffee mug the most extensive catalog of spectrometer hardware expertise known. Peter Allen's irreverence and creative problem solving skills were simultaneously entertaining and helpful; he was always willing to

talk, sometimes for hours at a time. Ajay Thakkar's consistent productivity, sense of humor, and ability to manage the extremes of group psychology were appreciated. Ron Durocher's machining skills were timely and professional. Aldona Shumway was gracious enough to tolerate my frequent frustrations with "EREQ", MIT's notoriously ineffective, redundant, inconsistent, clumsy, user-unfriendly and lethargic purchasing system, which finally is being replaced, a few years too late for some of us. To those new students who now use SAPweb, be glad you were not around to experience the EREQ years. Elka Shortsleeve taught me more than a thing or two about Word master documents, and was indispensable during times of grant-writing stress. Jennifer Blanchard and Wanda Molina managed to hold together the rest of third floor, and never complained when I turned in receipts for reimbursements years after purchases.

The early assistance of Robert McKay was essential for the introduction of transmission line probes to our lab. In the process of designing and building probes, I also benefited enormously from many discussions with John Stringer, Allen Palmer, and David Doty. As one probe turned into the next, I enjoyed many late nights of soldering and tuning with Alex Gamburg and Boris Itin. John Gross, while working on the 500 MHz room temperature probe, derived perverse pleasure out of blasting the propane torch on those 3" copper pipes; Quentin Tarrantino would have been proud. Jingui Hu, who designed and built the 317 MHz low temperature probe, never ceased to amaze me with the creativity and effectiveness of his mechanical designs. David Rovnyak showed phenomenal persistence with all of the headaches of our first 750 MHz probe.

In the second half of my graduate career, I was constantly challenged and educated by the steady stream of post-docs and visiting scientists coming to the lab. Any time it seemed the intellectual environment was about to became ordinary, another wave of fresh ideas and perspectives arrived. Mei Hong introduced us to the idea of torsion angle measurements by separated local field spectroscopy under MAS. Len Mueller was often a broken record on the subject of Monte Carlo simulations for data fitting and error estimation, but I hope some of his insight rubbed off. Mary Hatcher displayed tremendous courage and resolve, contributing to the lab and learning everything she could, despite difficulties with samples and personalities; in

particular the time we spent preparing samples and the experimentally refining CMR7 supercycles was productive and enjoyable.

Among the recent visitors to the Magnet Lab, Morten Hohwy stands out. Within days of his arrival, we had acquired a large chunk of data for our first publication, and after that the flurry of ideas accelerated. He taught me that with Schrödinger, Magnus, and a few CPU cycles, all things can be simulated; though this tends to bring out my compulsive data-fitting side, it is reassuring to know that with Morten around, sooner or later the model will fit. In the last year, Chris Jaroniec and Bernd Reif have also been productive collaborators, and have reminded me of all the details that fifth year students seem to forget. In recent months of writing and planning additional experiments, Nathan Astrof has been a constant source of encouragement, there to lend a positive word or two in moments of frustration; his unceasingly positive attitude is an inspiration to us all.

Personally, I would like to thank my parents, Richard and Carol Rienstra, for financial and emotional support during my years of poverty; all the housemates at 20 Prospect Hill Avenue (among the many, Caroline and Alan) and Paul, for helping me through the black hole of self-esteem known as second and third year at MIT; the chemical engineers—Chase, Tim, Jeff, Dew, Josh, Randy, the Gregs, Terry, and the others—for Tuesday and Thursday morning basketball games, and colossal intramural contests with the Sloan School; the evening workout crew at World Gym Somerville—especially my training partner Rey, Andy, Larry, John, Lucio, Michael, the Steves (big and bigger), and Tony—who have collaborated in my continuing studies of the stress-induced conversion of protein to muscle.

And last but certainly not least, I would like to recognize the love of my life, Jennifer Gartside, who fell for my ridiculous pickup line, who has provided stability and balance when I needed it most, and who has made the last year the happiest and most productive of my life. I look forward to enjoying many more with her.

Section I: Background

Chapter 1. Introduction to Solid State NMR

Preface

Solid state NMR (SSNMR) continues to develop as a third viable method—in addition to *X*-ray crystallography and solution NMR—for determining structure and dynamics in biological molecules.[1,2] One strong motivation to develop SSNMR is that it may supply atomic resolution structural and dynamic information in cases that other methods cannot effectively address. Most often cited with potential to benefit from SSNMR studies are large molecular systems possessing microscopic but not macroscopic order, such as: peptide aggregates, membrane proteins, microcrystalline globular proteins, and glasses. In addition, the ability to perform SSNMR experiments at low temperatures permits the study of meta-stable photointermediates and trapped enzyme-substrate complexes.

Traditionally, samples for SSNMR have been prepared with sparsely labeled nuclei, specifically for measurement of a small set of observables.[3] For example, most often in proteins, a single site or pair of sites has been labeled with ^{15}N and/or ^{13}C, and the chemical shifts and couplings measured to determine a single distance or angular constraint. Though this approach has proved to be quite successful in addressing specific questions of biological relevance, the wonderful potential of NMR is that dozens, if not hundreds or thousands, of sites can be resolved in a single experiment. By using unique sets of chemical shifts as a bookkeeping devices, structural constraints may be measured for all spins in a single experiment. and correlated directly with sites in the molecule. If site resolution is possible, this strategy is far more efficient than site-specific labeling, and is naturally compatible with the uniform, biosynthetic labeling strategies. This paradigm has been quite successful in solution NMR, and structure determination of small to medium-sized (<20 kDa) globular proteins is now routine, with over 1,500 solved.[4,5] However, to follow this model in solids requires some advances: (1) hardware must be made robust enough to routinely perform experiments at high RF power levels and with

signal reception efficiency in order to achieve optimal resolution and sensitivity; (2) the numerous ^{13}C and ^{15}N chemical shifts must be resolved and assigned to unique positions in the molecular structure; and (3) molecular torsion angles and distances must be measured with high accuracy despite the potential complications of the multi-spin Hamiltonian.

The goal of this thesis is to address these issues, and to present a collection of SSNMR experimental techniques suitable for total structure determination of uniformly labeled small molecules. Of course this goal is quite general, common to a many SSNMR researchers, and requires an extensive background of theoretical and experimental data. Therefore throughout the text, liberal references will be made to recent literature, and in particular the contributions of many recent members of the Griffin Group. SSNMR has developed at a dizzying pace in the last decade, and many of the recent innovations (in pulse sequence methodology especially) have come from within MIT. Specifically, developments by Andrew Bennett[6] (RFDR,[7,8] FDR,[9,10] TPPM decoupling[11]), Phil Costa[12] (rotational resonance developments including R2T,[13] R2W, analysis of multi-spin dipolar dynamics, torsion angle techniques[14]), Boqin Sun (MELODRAMA,[15] RFDR-CP,[16] 3D ^{15}N-^{13}C-^{13}C correlation spectroscopy[17]), John Gross[18] (TCn methods, torsion angles), Mei Hong (torsion angles[19,20]), and Morten Hohwy (C7-style sequences,[21,22] TMREV,[23] and applications thereof[24]) have provided a strong foundation of fundamental work on which the thesis builds. For this reason, every effort will be made to give credit where due. In several cases, I have co-authored work with the aforementioned group members. Only portions of this work for which I have been primarily responsible will be presented here.

By way of introduction, we will briefly discuss the underlying physics of NMR, and analysis of the SSNMR spin Hamiltonian. Chapter 1 serves as an overview of the basics and a compilation of references to the literature, but by no stretch of the imagination attempts to be a complete treatment of NMR theory. Such discussions are readily available in numerous recent textbooks and theses. In particular, the reader is urged to consult the introductory chapters of the excellent book by Schmidt-Rohr and Spiess,[25] the treatment of average Hamiltonian theory by

Gerstein and Dybowski,[26] the lucid discussion of coherent spin dynamics by Munowitz,[27] and the overview of multi-dimensional techniques of Cavanagh and co-workers.[28] Needless to say, the encyclopedic opus of Ernst also deserves mention as an abundant source of theoretical information.[29] Advanced discussions of Floquet and average Hamiltonian theory have been presented recently by Augustine[30] and Hohwy.[31] In addition, several recent reviews from the Griffin Group address recoupling and decoupling methods.[32-34]

Although there are numerous reviews of spin physics theory in the recent literature, only a handful of publications address the issues involved in modern NMR hardware—especially probe—design. Reviews by Doty consider detailed theoretical modeling of sophisticated multi-resonant probe circuits, and indeed also address many practical issues as well.[35-38] Though highly detailed and useful treatments of some aspects of probe designs, these works have a strong bias based on the author's experience, and few alternative views have been presented in sufficient detail for end-user application. In particular, the requirement both for high efficiency and power-handling in probe circuits is an issue not adequately addressed by Doty. For this reason, we perceive a greater need for a thorough introduction to probe design than another review of spin dynamics, and in particular the necessary tools for analysis and design of transmission line probe circuits in the style of McKay.[39-42] Therefore, in Chapter 2, we will present a detailed treatment of introductory analog RF electronics of direct relevance to NMR probe circuits, along with the analysis of several common multiple resonance circuits.

The assignment of chemical shift by multi-dimensional methods is a solved problem in solution NMR, but has required additional developments for solids. Many of the methods used for assignment in solids are derivative in their basic organization of the pulse sequences in solution. However, achieving adequate polarization transfer efficiency and bandwidth in solids presents many unique challenges. Because the dipolar (rather than scalar) Hamiltonian is used for most transfer schemes, polarization transfer efficiency over the powder average depends on the functional form of the effective dipolar coupling over all crystallites. Averaging over two Euler angles (β and γ) results in a theoretical efficiency of only ~52% polarization transfer in a

two-spin system. However, new schemes based on the HORROR and C7 sequences of Nielsen and Levitt,[43,44] permit the removal of dependence on the angle γ. These sequences are thus referred to as "γ-encoded", because information from all crystallites is retained, independent of γ angle. This results in a theoretical efficiency of 73%. Experimentally, it is possible to achieve values in very good agreement with the theory, as demonstrated in Chapter 3. Application of this method to 2D ^{13}C-^{13}C experiments has resulted in superior polarization transfer efficiency, and facilitated the assignment of a U-^{13}C-labeled sample of erythromycin A, with 37 ^{13}C signals. In Chapter 4, some spectra with the RFDR recoupling method are presented. Although theoretically less efficient, RFDR is very robust with respect to RF pulse imperfections and therefore is still commonly used for peptide and protein spectroscopy. Studies of transfer efficiency and polarization loss as a function of decoupling field here are useful for optimization in 2D experiments. In Chapter 5, improved methods for 2D and 3D correlation spectroscopy in peptides and proteins are presented, based on γ-encoded homonuclear pulse sequences and adiabatic heteronuclear sequences. Though experimentally more challenging than RFDR, the gain in sensitivity and resolution observed is sufficient motivation to ensure that such experiments can be done more routinely in the future. The uniformly labeled tripeptide, formyl-Met-Leu-Phe-OH (MLF), is used as a test case.

With all signals assigned in the MLF sample, determination of secondary structure can be attempted by applying separated local field (SLF) techniques. These schemes are based upon addition of multiple local fields over the powder average. The evolution of the quantum state under multiple local fields depends upon the relative orientation of the vectors in question, which can therefore be determined by comparison of experimental polarization decay trajectories with those calculated from the multi-spin Hamiltonian. Fundamental to this treatment is the ability to frequency label coherences from pairs of ^{13}C-^{13}C or ^{15}N-^{13}C spins, and then apply pure ^{1}H-^{13}C and/or ^{1}H-^{15}N local field Hamiltonians to the coherences in each dimension. This strategy is described in greater detail in Chapter 6, and several constraints on backbone torsion angles in the MLF tripeptide are determined. Although the complete structural analysis is not yet complete, it

appears that the torsion angle data will be sufficient to completely determine the backbone and sidechain structure in MLF.

Such relative orientation constraints are sufficient to determine secondary structure in small peptides. However, determination of tertiary structure requires some information about internuclear distances between sites that are not close in primary structure. In Chapter 7, we demonstrate use of the CMR7 sequence for determining distances between spin pairs with high precision (<0.1 Å), independent of chemical shift differences; therefore these measurements are complementary to those obtained by rotational resonance. The dynamic range of CMR7, and the ability to measure a distribution of couplings, is enhanced by the use of the γ-encoded DQ homonuclear Hamiltonian; supercycling techniques borrowed from solution decoupling theory provide experimentally robust performance.

Theory

Attempting to coverage all of time-dependent quantum mechanics and NMR would be futile in this short section. The reader is encouraged to consult one of the numerous classic references on the subject for a thorough introduction. The fundamental physics of magnetic resonance are well chronicled by Abragam[45], Haeberlen,[46,47] Mehring,[48] Slichter,[49], and Ernst.[29] More recent developments with emphasis on particular subject areas are the focus of books by Schmidt-Rohr (polymer structure and dynamics)[25] and Cavanagh (multi-dimensional experiments for biological samples).[28] The various review articles and theses highlighted in the previous section also serve as suitable introductions to some modern research topics.

Spin Hamiltonian Fundamentals

The SSNMR Hamiltonian can be partitioned into an internal part and an RF part:

$$H = H_{\text{int}} + H_{RF}. \tag{1}$$

The internal Hamiltonian contains five types of interactions, the Zeeman, chemical shift, dipolar, scalar, and quadrupolar interactions :

$$H_{\text{int}} = H_Z + H_{CS} + H_D + H_J + H_Q. \tag{2}$$

A brief review of each follows.

Zeeman Interaction

The Zeeman term corresponds to the energy level splitting due to external magnetic fields. Nuclei with non-zero angular momentum split into 2 I + 1 energy levels, with a spacing:

$$H_Z = -\vec{M}_I \cdot \vec{B}_0 = -\gamma \hbar \vec{I} \cdot \vec{B}_0, \tag{3}$$

where γ is the gyromagnetic ratio, $\hbar$ is Planck's constant, $\boldsymbol{I}$ is the nuclear spin operator and $\boldsymbol{B_0}$ is the magnetic field vector (generally assumed to be projected along the z-axis of the laboratory frame of reference). Therefore the Zeeman term usually simplifies to a scalar,

$$H_Z = -\gamma \hbar I_z B_0, \tag{4}$$

depending on the nucleus and magnetic field. Modern superconducting solenoid magnets normally generate B_0 fields somewhere between 2.35 and 18.8 T (Tesla); therefore the ^{1}H Larmor frequency $\omega = \Delta E / \hbar$, corresponding to this energy level difference, typically ranges from ~100 to 800 MHz.

Table 1-1. Spin Properties for Common Spin-1/2 Nuclei

Isotope	Natural Abundance (%)	Gyromagnetic Ratio (MHz / T)	NMR Frequency (MHz at ~2.35 T)
^{1}H	99.985	42.577	100.000
^{13}C	1.108	10.708	25.151
^{15}N	0.37	-4.316	-10.138
^{19}F	100	40.077	94.128
^{31}P	100	17.254	40.524

Even for ^{1}H at very high magnetic fields, this energy is several orders of magnitude smaller than kT at room temperature. This accounts for the "high temperature" approximation of the Boltzmann population, which results in net magnetization:

$$M = \frac{N\gamma^2\hbar^2 I(I+1)}{3kT} B_0 = \chi_0 B_0. \tag{5}$$

Here M is the total magnetization, and k is Boltzmann's constant. The value χ_0 is often referred to as the nuclear receptivity. Typical population differences in the high temperature limit at ~1 ppm.

Despite this extremely small energy level difference by the standards of many forms of spectroscopy, the Zeeman interaction dominates other terms (with the exception of the quadupolar) by a few orders of magnitude, and therefore we usually presume the energy eigenvalues and treat all other terms as perturbations, by using the interaction representation of the Zeeman energy rotating frame.

Chemical Shielding

The local magnetic field induced by electron wavefunctions near the nucleus depends strongly on chemical environment, and hence is referred to as the chemical shift.[48] These shifts are, like the Zeeman term, directly proportional to the external magnetic field, and therefore the values (in relative units) serve as universal reporters of chemical environment. [25,50] The shielding is in general a tensorial property:

$$H_{CS} = \gamma_I \vec{I} \cdot \hat{\sigma} \cdot \vec{B}_0 \qquad (6)$$

The principal values of the chemical shielding tensor (σ_{11}, σ_{22}, σ_{33}) reflect the dependence of the shielding upon orientation relative to the magnetic field (i.e., the chemical shift anisotropy).

The chemical shift scale is generally denoted in ppm of the Larmor frequency, with the upfield or least shielded values displayed on the right side of spectra. Thus the "shifts" are downfield from a reference value, such as TMS:

$$\delta = \frac{\sigma_{ref} - \sigma_{sample}}{1 - \sigma_{ref}} \cong \sigma_{ref} - \sigma_{sample} \qquad (7)$$

The indirect relationship of molecular structure to chemical shifts can be determined from *ab initio* calculations, and has become is a major area of computational chemistry and NMR research unto itself.[51,52] In this thesis, the use of chemical shifts primarily to provide site resolution, and the structural implications of the chemical shift itself is not discussed in detail.

Dipolar Couplings

Dipolar couplings reflect the interaction of two nuclear magnetic moments through space, according to

$$H_D = \vec{I} \cdot \hat{D} \cdot \vec{S} \ , \qquad (8)$$

which is expressed according to the Correspondence Principle as

$$H_D = \frac{\hbar^2 \gamma_I \gamma_S}{r^3} \frac{\mu_0}{4\pi} \left(\vec{I} \cdot \vec{S} - 3 \frac{\left(\vec{I} \cdot \vec{r}_{IS}\right)\left(\vec{S} \cdot \vec{r}_{IS}\right)}{r_{IS}^2} \right) \tag{9}$$

This expression is usually decomposed as follows:

$$H_D = \frac{\hbar^2 \gamma_I \gamma_S}{r^3} \frac{\mu_0}{4\pi} (A + B + C + D + E + F) \tag{10}$$

where the coupling constant b_{IS} is

$$b_{IS} = -\frac{\hbar^2 \gamma_I \gamma_S}{r^3} \frac{\mu_0}{4\pi} \tag{11}$$

and the "dipolar alphabet" (Abragam, p. 104)[45]

$$A = \left(3\cos^2\theta - 1\right) I_z S_z, \tag{12a}$$

$$B = -\frac{1}{4}\left(3\cos^2\theta - 1\right)\left(I_+ S_- + I_- S_+\right), \tag{12b}$$

$$C = \frac{3}{2}\sin\theta\cos\theta e^{-i\varphi}\left(I_+ S_z + I_z S_+\right), \tag{12c}$$

$$D = \frac{3}{2}\sin\theta\cos\theta e^{i\varphi}\left(I_- S_z + I_z S_-\right), \tag{12d}$$

$$E = \frac{3}{4}\sin^2\theta e^{-2i\phi} I_+ S_+, \text{ and} \tag{12e}$$

$$F = \frac{3}{4}\sin^2\theta e^{2i\phi} I_- S_-. \tag{12f}$$

The terms A and B commute with the Zeeman interaction and are referred to as the secular terms. Truncation of the dipolar Hamiltonian amounts to removing all terms that correspond to non-energy conserving processes. Measurement of dipolar couplings provides direct structural information in the form of internuclear distances.

Scalar Coupling

The indirect or *J* coupling between nuclei results from electronic interactions. It has the same spin and distance dependence, to first order, as the dipolar coupling, and is expressed as:

$$H_J = \vec{I} \cdot \hat{J} \cdot \vec{S} \cong J \vec{I} \cdot \vec{S}, \tag{13}$$

the approximation valid when the *J* anisotropy is small, which is true in most instances for non-metals. In most instances the chemical shifts are much larger than the scalar coupling, and therefore the form of the latter can be reduced to its longitudinal component:

$$H_J = J I_z S_z \tag{14}$$

Quadrupolar Couplings

The final internal term is the quadrupolar coupling, which occurs for I>1/2 nuclei:

$$H_Q = \frac{eQ}{2I(2I-1)} \vec{I} \cdot \hat{V} \cdot \vec{I} \tag{15}$$

where *e* is the elementary charge, *Q* is the quadrupole moment, and *V* is the electric field gradient tensor. In this thesis, quadupolar couplings are not encountered and therefore will not be considered further. This assumption is justified in the context of U-^{15}N,^{13}C-labeled biomolecules, without ^{2}H- or ^{17}O-enrichment.

RF Perturbations

The final term in the spin-1/2 Hamiltonian is due to the transverse oscillatory magnetic field induced by high voltage RF frequency pulses in the solenoid coil.

$$H_{RF} = \omega_1(t)\left[I_x \cos\varphi(t) + I_y \sin\varphi(t)\right] \tag{16}$$

The nutation frequency is defined by the customary relationship,

$$\omega_1 = \gamma B_1, \tag{17}$$

where B_1 is the radiofrequency magnetic field, with amplitude usually in the range 10-50 G, resulting in ^1H nutation frequencies of ~40 to 200 kHz. With modern spectrometers, pulse sequence schemes can be arbitrarily complex, with *relative* phase defined to within 0.1° and timings within <0.02 μs. It is the design and implementation of complex pulse sequences that will comprise the bulk of this thesis.

Magnitude of Interactions in the Spin Hamiltonian

Typical magnitudes of interactions in the spin Hamiltonian are summarized in Table 1-1. The Zeeman terms, in this case at a static magnetic field strength of 11.7 Tesla, define the rotating frame of reference for each type of spin. All other interactions are usually less than 25 kHz. In comparison, solid state NMR probes can achieve pulsed transverse magnetic fields (B_1) that result in nutation frequencies (γB_1) ranging from 25 to 250 kHz. Therefore it may often be possible to work in a limit where the RF perturbations dominate the non-Zeeman terms in the Hamiltonian. This follows intuitively from perturbation theory, and will be described in greater detail below, using the formalism of average Hamiltonian theory (AHT). Although this requires probe hardware can consistently generate B_1 fields near the top of the range indicated here, this is feasible under favorable conditions. Among all forms of spectroscopy, NMR is unique in the extent to which the quantum evolution can be controlled by applying extremely sophisticated RF pulse sequences.

Table 1-2. Interactions in the Spin-1/2 Solid State NMR Hamiltonian.[a]

Interaction	Spin 1	Spin 2	Typical Magnitude
Zeeman	^{1}H		500 MHz
	^{13}C		125 MHz
	^{15}N		50 MHz
CS & CSA	^{1}H		10 kHz (20 ppm)
	^{13}C		25 kHz (200 ppm)
	^{15}N		15 kHz (300 ppm)
Dipolar couplings	^{1}H	^{1}H	20-25 kHz
	^{13}C	^{1}H	20-25 kHz
	^{15}N	^{1}H	10-12 kHz
	^{13}C	^{13}C	2.2 kHz
	^{15}N	^{13}C	1.1 kHz
Scalar couplings	^{1}H	^{13}C, ^{15}N	50-200 Hz
	^{13}C	^{13}C	35-75 Hz
	^{13}C	^{15}N	5-15 Hz

[a]Magnitudes are approximately the *maximum* observed in organic solids; couplings reflect values for directly bonded spin pairs.

A relevant observation at this point concerns the uncertainty with which observables may be determined in SSNMR. In true "solids", where molecular motion is restricted to small amplitude lattice vibration, spin-lattice relaxation occurs on the time scale of many seconds or minutes, and spin-spin relaxation can in principle be similar (provided that spin decoupling is performed with high efficiency, as discussed in Chapter 4). The implication with respect to Heisenberg uncertainty is that energy level splittings can be measured with sub-Hz precision.

Therefore SSNMR (and NMR in general) has two unique spectroscopic characteristics. First, the spin Hamiltonian can be manipulated with exquisite specificity and complexity, in order to extract desired observables according to experimental design. Second, observables can be measured with uncertainties of less than 1 Hz in many cases, a precision rarely possible with any other form of spectroscopy.

Symmetry: Spatial & spin tensor rank

Sometimes many NMR interactions are similar in magnitude and therefore not independently observable. More often, large interactions—such as the ^{1}H-^{13}C dipolar couplings—dominate the appearance of the spectrum. In order to observe weaker interactions, or to choose among those comparable in magnitude, it will be necessary to remove some terms from the Hamiltonian with "decoupling" sequences. Doing so requires uniquely identifying each term according to symmetry. Dipolar couplings between ^{1}H and ^{13}C, for example, can easily be differentiated from spin terms that involve only ^{13}C, and a pulse sequence applied to ^{1}H for purposes of heteronuclear decoupling. However, it is not immediately clear how one might separate the ^{13}C-^{13}C dipolar coupling from the ^{13}C CSA.

The differentiation of such terms from one another relies on the fact that the each term in the spin Hamiltonian possess both spatial and spin dependence. The dipolar alphabet above foreshadowed this fact, in that terms A through F each have spatial terms (in θ and ϕ) that are second-order spherical harmonics, to go along with each spin term. Thus, mechanical rotation can be used in conjunction with manipulations of the spin terms, to impose a collective time-evolution that will depend on both terms. This statement will be formalized in the following section, but for now it suffices to categorize the rank of the angular momentum tensors for the aforementioned terms in the Hamiltonian.

Table 1-3. Symmetry of Terms in the Spin Hamiltonian.

Interaction	λ	μ	l	m
Zeeman & CS	1	0, ±1	2	0
CSA	1	0, ±1	2	±1, ±2
Homonuclear Dipole*	2	0, ±1,±2	2	±1, ±2
Heteronuclear Dipole*			2	±1, ±2
--I spin	1	0, ±1		
--S spin	1	0, ±1		

*m=0 component vanishes with MAS

The variable l refers to the rank with respect to spatial modulation, m the spatial rotational component ($m = \{-l, -l+1, ...l\}$), λ the rank with respect to spin modulations, and μ the spin rotational component ($\mu = \{-\lambda, -\lambda+1 \ ... \lambda\}$). The modulations of both spin and spatial terms are most conveniently described in terms of irreducible spherical tensor operators (ISTO).[53,54] Correspondence between the (implicitly Cartesian) spin terms , used thus far, with the ISTO basis is achieved by the relations:

$$T_{10} = I_z, \tag{18a}$$

$$T_{1\pm1} = \mp\frac{1}{\sqrt{2}} I_{\pm} \tag{18b}$$

$$T_{20} = \frac{1}{\sqrt{6}}\left(3I_z S_z - \boldsymbol{I}\cdot\boldsymbol{S}\right), \tag{18c}$$

$$T_{2\pm1} = \mp\frac{1}{\sqrt{2}}\left(I_{\pm}S_z + I_z S_{\pm}\right) \tag{18d}$$

$$T_{2\pm2} = \frac{1}{2} I^{\pm} S^{\pm}. \tag{18e}$$

In all instances within this thesis, modulation of the spatial terms will proceed according to the assumption of MAS, where there are four spatially independent terms for the CSA and dipole interactions, corresponding to m=±1,±2.[55] Furthermore, we will primarily be concerned quantitatively with the dipolar couplings, and therefore show this case as an example. The transformations from the molecular frame to the laboratory frame (not shown in detail) result in:

$$\omega_D(t) = \sum_{m=-2}^{2} \omega_D^{(m)} e^{im\omega_r t} \tag{19a}$$

$$\omega_{D_{jk}}^{(0)} = 0, \tag{19b}$$

$$\omega_D^{(\pm1)} = -\frac{b_{IS}}{2\sqrt{2}} \sin(2\beta_{PR}) e^{\pm i\gamma_{PR}}, \tag{19c}$$

$$\omega_D^{(\pm2)} = \frac{b_{IS}}{4} \sin^2(\beta_{PR}) e^{\pm 2i\gamma_{PR}}, \tag{19d}$$

where b_{IS} is from Eq. 11, and β_{PR} and γ_{PR} are the Euler angles that describe the rotation from the principal axis system (molecular frame) to the rotor frame.

Time Evolution of the Density Matrix

The density operator $\rho(t)$ describes the state of the spin system at all times. The statistical ensemble must satisfy the time-dependent Liouville equation:[54]

$$\frac{d}{dt}\rho(t) = -i[H(t), \rho(t)], \tag{20}$$

which can be solved in the general case:

$$\rho(t) = U(t,0)\rho(0)U^{-1}(t,0) \tag{21}$$

with the propagator defined as

$$U(t,0) = T\exp\left[-i\int_0^t H(t')dt'\right] \tag{22}$$

T here is the Dyson time-ordering operator.

From these expressions two simple results emerge. First, if the density matrix and Hamiltonian commute, no evolution occurs. Second, if the Hamiltonian is self-commuting, evolution can be described exactly by solving Eq. 22. For modern NMR problems, these two cases are of limited interest, and in general more precise solutions for time-dependent Hamiltonians must be determined, either by numerically evaluating Eq. 21 with short time steps, or by approximating Eq. 22 for fixed time-intervals by a perturbative expansion of the Hamiltonian. We address the later, more conceptually insightful alternative first.

Pulse Sequence Design: Average Hamiltonian Theory

A formalized framework for the design and analysis of multiple pulse sequences is provided by average Hamiltonian theory (AHT).[56] In essence, AHT attempts to solve Eq. 22 according to the Magnus expansion:

$$H = H^{(1)} + H^{(2)} + H^{(3)} + ..., \tag{23}$$

through third order (numbered to be consistent with perturbation theory), defined as

$$H^{(0)} = \frac{1}{\tau_c}\int_0^{\tau_c} H(t)dt, \tag{24a}$$

$$H^{(1)} = \frac{-i}{2\tau_c}\int_0^{\tau_c} dt_1 \int_0^{t_1} \left[H(t_1), H(t_2)\right]dt_2, \tag{24b}$$

$$H^{(3)} = \frac{-1}{6\tau_c}\int_0^{\tau_c} dt_1 \int_0^{t_1} dt_2 \int_0^{t_2} dt_3 \left(\left[H(t_1),\left[H(t_2),H(t_3)\right]\right] + \left[H(t_3),\left[H(t_2),H(t_1)\right]\right]\right), \tag{24c}$$

These expressions provide a Hermitian operator regardless of the order used; therefore the propagator in Eq. 22 is always unitary, and can be applied repeatedly to describe long-time evolution. Higher order terms in the AHT expansion account for "residual" interactions; that is, terms that disrupt the tidy first order AHT approximation. These can generally be viewed as quantum mechanical garbage which must be discarded before spoiling the entire density matrix. Errors arising from RF pulse imperfections, such as finite pulse widths, inhomogeneity of the B_1 field, risetime and transient effects (e.g., phase transients, risetime and falltime asymmetries, etc.) can in practice lead to error terms that are comparable to the first order term. However, with appropriate modeling of the RF excitation, or correction at low order for effects such as phase transients, the errors can be systematically removed.

Recently, Hohwy and Nielsen have derived an alternative formulation of the Magnus expansion that permits convenient calculation of higher order terms.[31,57] In practice, terms up to 3rd order are significant for design of pulse sequences involving only low-γ nuclei, where the

interactions are dominated by the RF field defining the cycle time τ, whereas 5th order may be necessary for ^{1}H-based pulse sequences because the couplings are an order of magnitude larger.

Interaction Frame

The usual presumption in the context of multiple pulse sequences is that the applied RF field is significantly larger than the internal interactions such as dipolar couplings and chemical shifts, i.e.,

$$|\omega_1| >> |H_{\text{int}}| \tag{25}$$

That is, the pulse sequence exactly defines the modulation of spin terms, according to:

$$U_{RF} = T\exp\left[-i\int_0^t H_{RF}(t')dt'\right] \tag{26}$$

If we denote the interaction frame with a tilde, the following expression,

$$\tilde{H}_{\text{int}} = U_{RF}^{-1}(t,0)H_{\text{int}}U_{RF}, \tag{27}$$

which can be used along with

$$U(t,0) = U_{RF}(t,0)\left[T\exp\left[-i\int_0^t \tilde{H}_{\text{int}}(t')dt'\right]\right] \tag{28}$$

to describe the evolution. The expression takes on a particularly convenient form when the cyclic condition

$$U_{RF}(\tau_c,0) = \pm 1 \tag{29}$$

is satisfied.

The precise evolution of the system can be described by numerical diagonalization of the Hamiltonian matrix at short times (compared to all modulations, both spin and spatial) and application of Eq. 21 and 22. This method is computationally demanding but reliable, and serves as a standard against which approximate analytical methods such as AHT can be compared. In recent years, a number of improvements to computational methods have appeared in the literature.[8,58-60] Here we do not discuss these in detail, but merely mention that improved powder averaging schemes in combination with clever recycling of the propagator where possible can save a large fraction of the computation effort. With these approaches, numerical simulations in two-spin systems are sufficiently fast that interactive, exploratory simulations of spin dynamics are feasible, and this is often useful in the course of pulse sequence design, in conjunction with the AHT and quaternion rotation models.[61-63]

Whenever possible, it is highly desirable to derive analytical expressions (usually from AHT expansion) that express the dominant time-dependence of the system. Such expressions can arise from higher-order calculations of pulse sequences7. A more elegant approach is to remove the higher-order terms by pulse sequence design to invoke a response from the spin system that is simple to model according to first-order AHT results. The construction of "compensated" pulse sequences is often performed by use of composite pulses.[62,64,65] Although the design of such pulse sequences may require a large investment of time and computational effort (both analytical and numerical), the payoff is easily interpretable data that may be compared readily from one experimental result to the next. With sufficiently well compensated pulse sequences, working in an approximately ideal AHT limit is reasonable, and throughout this thesis, several examples will demonstrate this to be true for ^{13}C-^{13}C and ^{1}H-^{13}C systems under CMR7, T-MREV, and similar sequences.

Analytical models are refined and exercised in two-spin systems, but have broader implications. The availability of simple analytical forms for the two spin case implies that

extension to multiple spin models is computationally feasible, because the multi-spin behavior can then be described by one diagonalization of a large matrix, rather than creation of small step propagators. The standard approach of greatest convenience is to use the analytical model and expand the Hamiltonian into multiple spin states where necessary, always taking advantage of the "ideal" evolution approximation. Calculation of evolution is only necessary at the completion of each cycle as defined by the RF excitation. The time cost of including multiple spins in the simulation (matrix size is proportional to 2^n, and matrix diagonalization takes time units proportional to the third power of the matrix dimensionality) can be comparable to, or smaller than, the number of time steps that would have been required without the analytical expression. Thus, interactive fitting schemes over several parameters may be practical even for systems of 4-6 spins encountered in some instances. The crucial distinction is that diagonalization occurs only once per crystallite modeled, rather than hundreds of times over the course of a rotor cycle as required for the entirely numerical methods.

References

(1) Wüthrich, K. *NMR of Proteins and Nucleic Acids*; John Wiley and Sons: New York, **1986**.

(2) Wüthrich, K. "The second decade--into the third millennium," *Nat. Struct. Biol.* **1998**, *5*, 492-495.

(3) McDowell, L. M.; Schaefer, J. "High-resolution NMR of biological solids," *Curr. Opin. Struct. Biol.* **1996**, *6*, 624-629.

(4) Sussman, J. L.; Lin, D.; Jiang, J.; Manning, N. O.; Prilusky, J.; Ritter, O.; Abola, E. E. "Protein Data Bank (PDB): Database of three-dimensional structural information of biological macromolecules," *Acta Cryst.* **1998**, *D54*, 1078-1084.

(5) Abola, E. E.; Sussman, J. L.; Prilusky, J.; Manning, N. O. "Protein Data Bank archives of three-dimensional macromolecular structures," In *Methods in Enzymology*; C. W. Carter, Jr. and R. M. Sweet, Ed.; Academic Press: San Diego, **1997**; Vol. 227; 556-571.

(6) Bennett, A. E., *Dipolar Decoupling and Recoupling in Solid State Nuclear Magnetic Resonance Spectroscopy*, Ph. D. Thesis, Massachusetts Institute of Technology, **1995**.

(7) Bennett, A. E.; Ok, J. H.; Griffin, R. G.; Vega, S. "Chemical shift correlation spectroscopy in rotating solids: Radio-frequency dipolar recoupling and longitudinal exchange," *J. Chem. Phys.* **1992**, *96*, 8624-8627.

(8) Bennett, A. E.; Rienstra, C. M.; Griffiths, J. M.; Zhen, W.; Lansbury, P. T., Jr.; Griffin, R. G. "Homonuclear radio frequency-driven recoupling in rotating solids," *J. Chem. Phys.* **1998**, *108*, 9463-9479.

(9) Bennett, A. E.; Becerra, L. R.; Griffin, R. G. "Frequency-selective heteronuclear recoupling in rotating solids," *J. Chem. Phys.* **1994**, *100*, 812-814.

(10) Bennett, A. E.; Rienstra, C. M.; Lansbury, P. T., Jr.; Griffin, R. G. "Frequency-selective heteronuclear dephasing by dipole couplings in spinning and static solids," *J. Chem. Phys.* **1996**, *105*, 10289-10299.

(11) Bennett, A. E.; Rienstra, C. M.; Auger, M.; Lakshmi, K. V.; Griffin, R. G. "Heteronuclear decoupling in rotating solids," *J. Chem. Phys.* **1995**, *103*, 6951-6958.

(12) Costa, P. R., *Spins, peptides, and Alzheimer's disease: Solid-state nuclear magnetic resonance investigations of amyloid peptide conformation*, Ph.D. Thesis, Massachusetts Institute of Technology, **1996**.

(13) Costa, P. R.; Sun, B. Q.; Griffin, R. G. "Rotational resonance tickling: Accurate internuclear distance measurements in solids," *J. Am. Chem. Soc.* **1997**, *119*, 10821-10830.

(14) Costa, P. R.; Gross, J. D.; Hong, M.; Griffin, R. G. "Solid-state NMR measurement of psi in peptides: a NCCN 2Q-heteronuclear local field experiment," *Chem. Phys. Lett.* **1997**, *280*, 95.

(15) Sun, B. Q.; Costa, P. R.; Kocisko, D. A.; Lansbury, P. T., Jr. ; Griffin, R. G. "Internuclear distance measurements in solid state nuclear magnetic resonance: Dipolar recoupling via rotor sychronized spin locking," *J. Chem. Phys.* **1995**, *102*, 702-707.

(16) Sun, B. Q.; Costa, P. R.; Griffin, R. G. "Broadband heteronuclear cross polarization in rotating solids," *J. Magn. Reson. A* **1995**, *112*, 191-198.

(17) Sun, B. Q.; Rienstra, C. M.; Costa, P. R.; Williamson, J. R.; Griffin, R. G. "3D 15N-13C-13C chemical shift correlation spectroscopy in rotating solids," *J. Am. Chem. Soc.* **1997**, *119*, 8540-8546.

(18) Gross, J. D., *Measurements of segmental order parameters and torsion angles in solid state nuclear magnetic resonance*, Ph.D. Thesis, Massachusetts Institute of Technology, **1998**.

(19) Hong, M.; Gross, J. D.; Griffin, R. G. "Site-resolved determination of peptide torsion angle phi from the relative orientations of backbone N-H and C-H bonds by solid-state NMR," *J. Phys. Chem. B* **1997**, *101*, 5869-5874.

(20) Hong, M.; Gross, J. D.; Rienstra, C. M.; Griffin, R. G.; Kumashiro, K. K.; Schmidt-Rohr, K. "Coupling amplification in 2D MAS NMR and its application to torsion angle determination in peptides," *J. Magn. Reson.* **1997**, *129*, 85-92.

(21) Hohwy, M.; Jakobsen, H. J.; Edén, M.; Levitt, M. H.; Nielsen, N. C. "Broadband dipolar recoupling in the nuclear magnetic resonance of rotating solids: A compensated C7 pulse sequence," *J. Chem. Phys.* **1998**, *108*, 2686-94.

(22) Hohwy, M.; Rienstra, C. M.; Jaroniec, C. P.; Griffin, R. G. "Fivefold symmetric homonuclear dipolar recoupling in rotating solids: Application to double quantum spectroscopy," *J. Chem. Phys.* **1999**, *110*, 7983-7992.

(23) Hohwy, M.; Jaroniec, C. P.; Reif, B.; Rienstra, C. M.; Griffin, R. G. "Local structure and relaxation in solid-state NMR: Accurate measurement of amide N-H bond lengths and H-N-H bond angles," *J. Am. Chem. Soc.* **1999**, submitted.

(24) Hohwy, M.; Jaroniec, C. P.; Lansing, J.; Rienstra, C. M.; Griffin, R. G. "13C-1H Recoupling in the HCCH torsion angle experiment in solid-state NMR," *Chem. Phys. Lett.* **1999**, in preparation.

(25) Schmidt-Rohr, K.; Spiess, H. W. *Multidimensional Solid-State NMR and Polymers*; Academic Press: London, **1994**, pp 478.

(26) Gerstein, B. C.; Dybowski, C. R. *Transient Techniques in NMR of Solids*; Academic Press: Orlando, **1985**.

(27) Munowitz, M. *Coherence and NMR*; Wiley: New York, **1988**.

(28) Cavanagh, J.; Fairbrother, W. J.; Palmer, A. G.; Skelton, N. J. *Protein NMR Spectroscopy: Principles and Practice*; Academic Press: San Diego, **1996**, pp 587.

(29) Ernst, R. R.; Bodenhausen, G.; Wokaun, A. *Principles of Nuclear Magnetic Resonance in One and Two Dimensions*; Clarendon Press: Oxford, **1991**; Vol. 14.

(30) Augustine, M. P., *Theoretical treatment of time dependent phenomena and the investigation of highly magnetized systems*, Ph.D. Thesis, Yale University, **1995**.

(31) Hohwy, M.; Nielsen, N. C. "Systematic design and evaluation of multiple-pulse experiments in nuclear magnetic resonance spectroscopy using a semi-continuous Baker-Campbell-Hausdorff expansion," *J. Chem. Phys.* **1998**, *109*, 3780-3791.

(32) Griffiths, J. M.; Griffin, R. G. "Nuclear-magnetic-resonance methods for measuring dipolar couplings in rotating solids," *Anal. Chim. Acta* **1993**, *283*, 1081-1101.

(33) Bennett, A. E.; Griffin, R. G.; Vega, S. "Recoupling of Homo- and Heteronuclear Dipolar Interactions in Rotating Solids," In *Solid State NMR IV: Methods and Applications of Solid-State NMR*; B. Blumich, Ed.; Springer-Verlag: Berlin, **1994**; Vol. 33; 1-77.

(34) Griffin, R. G. "Dipolar recoupling in MAS spectra of biological solids," *Nat. Struct. Biol.* **1998**, *5*, 508-512.

(35) Doty, F. D.; Inners, R. R.; Ellis, P. D. "A multinuclear double-tuned probe for applications with solids or liquids utilizing lumped tuning elements," *J. Magn. Reson.* **1981**, *43*, 399-416.

(36) Doty, F. D.; Connick, T. J.; Ni, X. Z.; Clingan, M. N. "Noise in high-power, high-rrequency double-tuned Probes," *J. Magn. Reson.* **1988**, *77*, 536-549.

(37) Doty, F. D. "Probe design and construction," In *Encyclopedia of Magnetic Resonance* **1996**; 3753-3761.

(38) Doty, F. D. "Solid state probe design," In *Encyclopedia of Magnetic Resonance* **1996**; 4475-4485.

(39) McKay, R. A., "Double-tuned single coil probe for nuclear magnetic resonance spectrometer," USA Patent #4,446,431, **1984**.

(40) Holl, S. M.; McKay, R. A.; Gullion, T.; Schaefer, J. "Rotational-echo triple-resonance NMR," *J. Magn. Reson.* **1990**, *89*, 620-626.

(41) McKay, R. A. "Probes for special purposes," In *Encyclopedia of Magnetic Resonance* **1996**; 3768-3771.

(42) Schaefer, J.; McKay, R. A., "Multi-tuned single coil transmission line probe for nuclear magnetic resonance spectrometer," USA Patent #5,861,748, **1999**.

(43) Nielsen, N. C.; Bildsøe, H.; Jakobsen, H. J.; Levitt, M. H. "Double-quantum homonuclear rotary resonance: Efficient dipolar recovery in magic-angle spinning nuclear magnetic resonance," *J. Chem. Phys.* **1994**, *101*, 1805-1812.

(44) Lee, Y. K.; Kurur, N. D.; Helmle, M.; Johannessen, O. G.; Nielsen, N. C.; Levitt, M. H. "Efficient dipolar recoupling in the NMR of rotating solids. A sevenfold symmetric radiofrequency pulse sequence," *Chem. Phys. Lett.* **1995**, *242*, 304-309.

(45) Abragam, A. *Principles of Nuclear Magnetism*; Oxford University Press: New York, **1961**.

(46) Haeberlen, U. "NMR Basic Principles and Progress," *NMR Basic Principles and Progress* **1990**, *25*, 143.

(47) Haeberlen, U. *High Resolution NMR in Solids: Selective Averaging*; Academic Press: New York, **1976**.

(48) Mehring, M. *Principles of High Resolution NMR in Solids;* 2nd ed.; Springer-Verlag: Berlin, **1983**.

(49) Slichter, C. P. *Principles of Magnetic Resonance;* 3rd ed.; Springer-Verlag: Berlin, **1990**.

(50) Bovey, F. A. *Nuclear Magnetic Resonance Spectroscopy*; Academic Press: San Diego, **1988**.

(51) de Dios, A. C.; Oldfield, E. "Recent progress in understanding chemical shifts," *Solid State NMR* **1996**, *6*, 101-125.

(52) Oldfield, E. "Chemical shifts and 3-dimensional protein structures," *J. Biomol. NMR* **1995**, *5*, 217-225.

(53) Spiess, H. W. "Dynamic NMR Spectroscopy," In *NMR Basic Principles and Progress*; P. Diehl; E. Fluck and E. Kosfeld, Ed.; Springer: Berlin, **1978**; Vol. 15; 58-214.

(54) Sakurai, J. J. *Modern Quantum Mechanics*; Cummings Publishing: Menlo Park, **1985**.

(55) Maricq, M. M.; Waugh, J. S. "NMR in rotating solids," *J. Chem. Phys.* **1979**, *70*, 3300.

(56) Haeberlen, U.; Waugh, J. S. "Coherent averaging effects in magnetic resonance," *Phys. Rev.* **1968**, *175*, 453-467.

(57) Hohwy, M.; Nielsen, N. C. "Elimination of high order terms in multiple pulse nuclear magnetic resonance spectroscopy: Application to homonuclear decoupling in solids," *J. Chem. Phys.* **1997**, *106*, 7571-7586.

(58) Bak, M.; Nielsen, N. C. "REPULSION, a novel approach to efficient powder averaging in solid-state NMR," *J. Magn. Reson.* **1997**, *125*, 132-139.

(59) Hohwy, M.; Bildsøe, H.; Jakobsen, H. J.; Nielsen, N. C. "Efficient spectral simulations in NMR of rotating solids. The γ-COMPUTE algorithm," *J. Magn. Reson.* **1999**, *136*, 6-14.

(60) Eden, M.; Lee, Y. K.; Levitt, M. H. "Efficient simulation of periodic problems in NMR. Application to decoupling and rotational resonance," *J. Magn. Reson. A* **1996**, *120*, 56-71.

(61) Blümich, B.; Spiess, H. W. "Quaternions as a practical tool for the evaluation of composite rotations," *J. Magn. Reson.* **1985**, *61*, 356-362.

(62) Counsell, C.; Levitt, M. H.; Ernst, R. R. "Analytical theory of composite pulses," *J. Magn. Reson.* **1985**, *63*, 133-141.

(63) Barbara, T. M. "Simulation of multipulse tune-up sequences," *J. Magn. Reson. A* **1994**, *106*, 188-194.

(64) Levitt, M. H.; Freeman, R. "Population inversion using a composite pulse," *J. Magn. Reson.* **1979**, *33*, 473.

(65) Levitt, M. H.; Freeman, R. "Composite pulse decoupling," *J. Magn. Reson.* **1981**, *43*, 502-507.

Chapter 2. Analog RF Electronics for NMR

Introduction

Here we summarize the necessities of analog RF electronics required to understand some common NMR circuits, composed of lumped elements and transmission lines. The goal of this Chapter is to provide the reader with assistance in designing, tuning, debugging, and repairing NMR probe circuits. Not all of the engineering details for probe construction will be considered here, although reference to some design considerations will be made where relevant. Detailed theoretical discussions of these issues have been published by Doty,[1-3] and many additional practical issues in books by Gerstein and Dybowski,[4] and Fukishima and Roeder.[5] Emphasis here will be on the practical aspects of designing NMR probes for both high efficiency and power handling, by providing basic tools for probe circuit analysis and then evaluating some common solid state NMR probe designs.

Many essential theoretical results will be derived, to illustrate concepts in a cohesive manner; some other results will simply be stated with reference to the appropriate literature. A basic understanding of RF electronics is assumed, as available in review articles[6,7] and/or electronics textbooks.[8] Beyond the typical introductory treatment, many of the crucial assumptions regarding component modeling will be reexamined here. In particular, the parasitics associated with lumped elements at high frequency must be included in probe analysis in order for many fundamental features of designs to be properly understood. The excellent review of component modeling at high frequency by Rhea will be relied upon heavily.[9] Digital components will not be discussed.

Basic Approach

Most of RF circuit design for NMR can be reduced to a simple problem: provided a fixed level of transmission power, how can the largest possible coil current be generated? To answer this question, both the circuit efficiency and power-handling capabilities must be understood and accounted for. Both the peak B_1 field and maximum duty cycle must be specified, appropriate to achieve the >100-250 kHz nutation frequencies (γB_1) for each spin. Throughout this thesis, there will be examples of the direct impact that higher available B_1 fields have upon the quality of spectra. Because the amplitude of γB_1 and the internal terms in the SSNMR Hamiltonian are comparable in magnitude, increases in sensitivity and resolution may often be derived directly from higher applied field strengths. As the level of sophistication of the RF pulse sequences increases, so too does the value of quality hardware. In practice, order of magnitude improvements in NMR signal strength may often be achieved from ~75 to 150 kHz increases in ^{1}H decoupling fields, in combination with TPPM decoupling. Therefore under no circumstance may the solid state probe designer sacrifice power-handling capability solely in favor of circuit efficiency; no circuit can produce signals from fully dephased magnetization. Clearly many other probe issues—such as B_0 and B_1 field homogeneity, multi-channel tunability, temperature range of operation, maximum MAS rates, sample volume, and system stability—must be considered. But the hard RF pulse is the *sine qua non* of SSNMR, and all other design issues must be considered only in this context.

In terms of circuit analysis, we view the problem primarily from the transmission viewpoint. Current generates transverse B_1 field over the coil volume, which can be easily measured in NMR experiments. In practice, nutation of nuclear spins about the applied B_1 field is much simpler and reproducible than sensitivity measurements, as the latter depend on receiver noise figure, relaxation properties of the sample under study, and B_0 homogeneity, among many other potential factors. The reciprocity of transmit-receive efficiency ensures that this level of analysis is sufficient.[10] A circuit that generates B_1 with high efficiency will also effectively couple the

induced current from transverse magnetization (the source voltage from nuclear spins) into the pre-amplifier and receiver—that is, probes with high transmit efficiency will also have high receive sensitivity. (This assumes that receiver noise figure, electromagnetic shielding, and other such mundane issues are properly accounted for; in all modern spectrometers, the probe efficiency and noise temperature are the determinants of sensitivity.)

Although the principle of reciprocity implies that the choice of impedance reference frame for circuit analysis is arbitrary, transmit mode is a more natural choice. The transmit mode characteristic impedance—i.e., 50 Ω—is a common frame of reference for all circuit designs. In most instances transmit-receive switching circuits, amplifiers, and other components will be power-matched at 50 Ω. Transforming the coil impedance at a given frequency to this impedance is conceptually reasonable, and given the rules of impedance transformation in lumped and distributed circuit elements, can be achieved with standard methods. In receive mode, the appropriate reference frame is that of the highly inductive impedance (approximately $(1+j100)\Omega$) of the tuned, noise-matched pre-amplifier; this frame is significantly less intuitive. Therefore for all of the following discussion, we assume transmit mode but realize by reciprocity that the opposite perspective is equally valid, albeit more cumbersome.

With this assumption, the problem can be broken down into two parts. First, deliver as much power as possible to the coil. This is our measure of overall circuit efficiency—i.e., what percentage of amplifier power finds its way to the coil? We define this overall efficiency as:

$$\eta = \frac{P_{coil}}{P_{amplifier}}. \tag{1}$$

Second, generate as much current as possible from the power delivered to the coil. This is a function of coil quality factor (Q):

$$I_{coil} = k\sqrt{QP_{coil}} = k\sqrt{Q\eta P_{amplifier}} \tag{2}$$

Here and in all subsequent work Q, whether referring to a single component, collection of lumped elements, or the entire circuit, is defined as:

$$Q = \frac{\mathrm{Im}[Z]}{\mathrm{Re}[Z]} = \frac{X}{R} = \frac{stored\ energy}{dissipated\ energy} \tag{3}$$

This is equivalent to the effective rate of energy dissipation (or ring down) which is

$$\tau_{ringdown} = \frac{Q}{\omega} \tag{4}$$

Some of the factors that contribute to overall coil Q, and geometrical factors defining k, will be considered below, although our focus will be primarily on Eq. 1. Although the choice of coil geometry is most certainly an important consideration in probe design, we note that in practice the requirements for MAS rate and sample volume dictate the length and diameter of the solenoid coil. This restriction implies that there is not as much flexibility in choice of inductor geometry (which primarily determines coil Q) as there is in the design of circuits used to isolate frequencies from each other and to transform the impedance (tune and match) each frequency to 50 Ω. For this reason the majority of the discussion here will focus on impedance transformation and isolation circuits, which can readily accommodate any coil design within typical ranges of inductance and Q for NMR; very low inductance resonators and superconducting coils are the exceptions.

An additional caveat must be delivered at this point. One issue that is often confused in the probe literature is that of the relevance of circuit Q to overall probe performance. Although it is perfectly legitimate to discuss the "probe Q", in terms of the ringdown of a pulse delivered to the probe, in many instances—and in fact most circuits beyond single resonance—this value has little direct influence on sensitivity or overall transmission efficiency. The measured input port Q value on a probe channel is a function that depends upon the arrangement of isolation circuits, the electrical phase relating coil to tuning circuit, the type of impedance transformation scheme used for tuning and matching, and the relative Q values of components. "Probe Q" can, by

coincidence, be the same as the coil Q, but more likely will be very different. In well characterized circuits, the coil Q can be *back-calculated* from the input port ("probe") Q, and so the value of probe Q is not entirely meaningless. However, on its own, "probe Q" says *absolutely nothing* directly about the conversion of electrical power to magnetic field in a probe circuit. The steady state resonant coil current depends on only two factors: (1) how much power is delivered from amplifier to coil? (2) how effectively does the coil convert this power into current, and subsequent transverse B_1? Analysis that does not directly address these questions is irrelevant. This statement does not quarrel with the fact that circuit topology, electrical phase, and impedance transformation may effect the transient characteristics of circuits, and these transients may compromise performance in some pulse sequences; in addition, inordinately long probe ringdown times may obscure broad features in spectra. These concerns may dictate eventual use of Q-switching circuits, or place restrictions on types of pulse sequences used, but have only secondary importance.

In order to answer the questions above, a brief review of some basic RF electronics is required, which will precede discussion of specific probe circuits.

RF Circuit Components

Inductors

Ideal limit

Inductors are, by convention, conductors designed to increase magnetic flux linkage, and thereby energy storage:

$$E = \frac{1}{2} LI^2 \tag{5}$$

From the circuit viewpoint, in the ideal limit, inductance generates a positive, purely reactive impedance that is linear with frequency:

$$Z = j\omega L \tag{6}$$

For unit conversion, note that 1 nH at ~160 MHz is $+1j\ \Omega$ (reactive). Inductance for a single-layer solenoid (neglecting leads) is well approximated by

$$L = \frac{n^2 r^2}{9r + 10l} 10^{-3} \tag{7}$$

where the inductance is in nH, n is the number of turns, r the radius in inches to the wire center and l is the solenoid length (wire center to wire center) in inches.[9] (p. 59) This formula is correct to within 1% if the length-to-diameter ratio is greater than 0.33.[11] NMR solenoid inductance is generally in the 50-200 nH range, and frequencies in the hundreds of MHz.

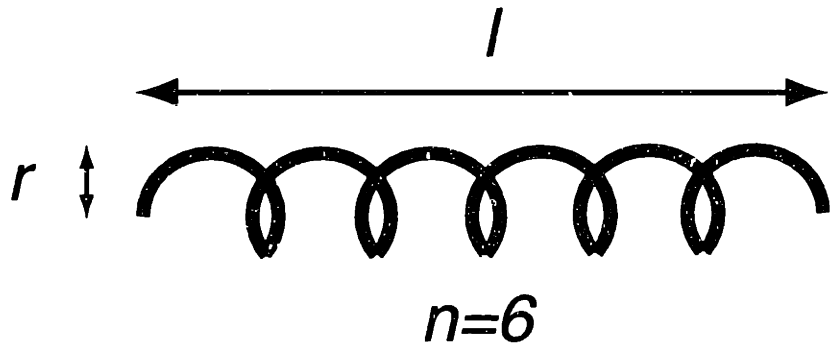

Figure 2-1. Single layer solenoid geometry.

Typical lead inductance is ~20 nH per inch for #22 gauge wire, and decreases with lead width. Circular rings (horseshoe loops) of wire have an inductance (nH)

$$L = \frac{a}{10^5}\left(7.353 \log\frac{16a}{d} - 6.386\right), \tag{8}$$

where a is the mean radius of the ring and d the wire diameter (in inches). Both lead and loop inductance values must be minimized relative to coil inductance for optimal magnetic field. Two

leads on either side of a solenoid are best modeled as a continuous loop that begins at the bottom of one lead and loops over the top of the coil to the end of the second lead.

Parasitic Model

In addition to the ideal inductance, solenoids have finite resistance and capacitance. The stray capacitance, including both inter-turn capacitance and that between the solenoid and ground plane, can be estimated based on the geometry. For most NMR sample coil geometries compatible with common MAS spinner designs (i.e., coil length to diameter ratio of 0.5-2.0), the stray capacitance can be estimated by

$$C_e \approx 1.22d, \tag{9}$$

where d is the coil diameter (wire center to center) in inches, assuming air dielectric ($\varepsilon \sim 1$). Additional dielectric material on or near the coil can be considered by multiplying Eq. 8 by the cross-sectional average dielectric between coil and ground plane.

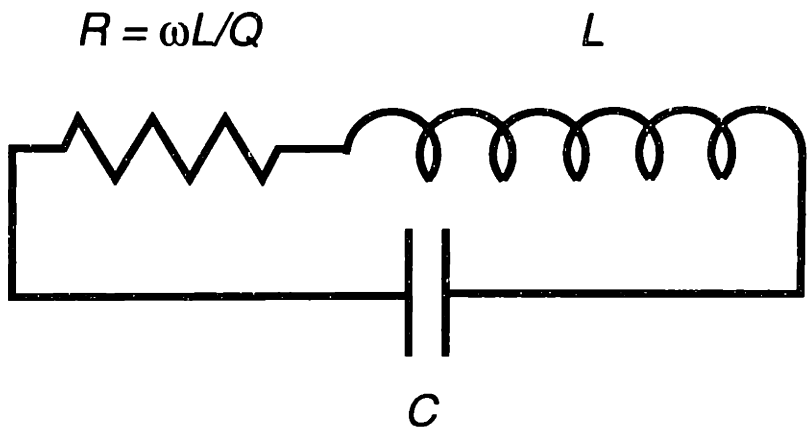

Figure 2-2. Solenoid parasitic model.

Self-resonance occurs when the inductive and capacitive reactances are equal:

$$f_{res} = \frac{1}{2\pi\sqrt{LC}} \tag{10}$$

As the frequency approaches self-resonance, a greater fraction of the energy is stored in the capacitance of sample and its surroundings. In other words, more energy is stored as electric than magnetic field. This may be particularly undesirable if the sample itself is a lossy dielectric, such as a salt solution. Therefore the coil self-resonance frequency should normally be significantly higher than the ^{1}H frequency. Note that Rhea discusses the coil "effective Q" (p. 63),[9] which is the expression relating the total coil complex impedance to the frequency relative to self-resonance, i.e.

$$Q_{eff} = Q_{coil}\left[1 - \left(\frac{f}{f_{res}}\right)^2\right] \tag{11}$$

For this reason, a coil with zero effective Q, as formally defined, can still generate magnetic field. Self-resonance by definition merely states that the total coil impedance is purely real (resistive). Energy may still be delivered to this resonant tank circuit, and will be shared between magnetic field (inductance) and electric field (capacitance). If the dissipation of energy in the capacitance is slow compared to the dissipation in the inductor itself (i.e., the fictitious coil Q, due to conductor resistance alone, is much less than the capacitor Q, determined by dielectric loss), the coil will function quite well for NMR. For solution NMR, this scenario is not typical, as aqueous solutions will be lossy. For solids, it may be possible (though probably not ideal) to work in a regime at or near self-resonance.

The unloaded coil Q is determined primarily by the finite resistance of copper wire at room temperature and high frequency. The resistivity at low frequency is described by the expression: (Rhea, p. 54)[9]

$$R_{dc} = \frac{10.37 \times 10^{-6} \rho_r}{d^2} \tag{12}$$

in ohms per foot of a round conductor, where d is the conductor diameter (in inches) ρ_r is the resistivity (relative to copper). At high frequency for an isolated conductor, current density in concentrated on the surface of the conductor, resulting in increased resistivity due to the skin effect. The skin depth δ (in inches) is

$$\delta = 2.6\sqrt{\frac{\rho_r}{f}} \tag{13}$$

where f is the frequency in Hz. As a point of reference, at 6.76 MHz the skin depth of copper is 1 mil (i.e., 1/1,000th inch); at 1 GHz, 0.082 mils. This implies that a (smooth) surface plating of a few mil of copper or silver is sufficient to ensure high conductivity at RF frequencies of 100-750 MHz, since 99%+ of the current is carried within 5 $\delta$of the surface. The AC resistance, assuming that the thickness of material is much greater than the skin depth, is

$$R_{ac} = 1 \times 10^{-6} \frac{\sqrt{\rho_r f}}{d} \tag{14}$$

per foot (where f is in Hz, d in inches).

Coil Quality Factor (Q)

Equations (3), (6), and (14) together show that the isolated conductor Q should increase as $\sqrt{f}$. This general functional form is also true for solenoids well below self-resonance. However, the absolute Q value of a single-layer solenoid depends upon the turn geometry and size, as explored in detail by Medhurst[12] and Grover.[13] Optimal wire spacing is determined primarily by proximity effects between turns.[12,14] Several additional factors contribute to coil Q,

as discussed in greater detail by Rhea (p. 60-70).[9] The results indicate that the overall diameter, and ratio of length to diameter, are the primary determinants of coil Q:

$$Q_{unloaded} \approx 190 d \psi \sqrt{f} \tag{15}$$

where d is the coil diameter (wire center to wire center) in inches, f is the frequency (MHz), and

$$\psi_{optimal} = 0.9121 - \frac{0.4964}{\sqrt{l/d}} + \frac{0.0709}{l/d}, \tag{16}$$

is a dimension-less parameter that expresses the dependence of Q upon turn density, due primarily to proximity effects. Because the parameters d and l are generally determined by the choice of magic-angle spinner apparatus (based on desired maximum MAS rate), the range of Q over the remaining degrees of freedom is relatively modest. Eq. 15 assumes the optimal inter-turn spacing (one-half the wire thickness between edges of adjacent turns of wire for a length to diameter ratio of 2-4). The parameter ψ may decrease by ~15-20% if the inter-turn spacing is changed to one-quarter the wire thickness or the full wire thickness, the typical extrema in winding geometry with constant diameter wire for SSNMR coils. (See Rhea p. 62, Table 3-2 for more details.) Because the total number of turns is also constrained somewhat in order to avoid self-resonance (due to higher inductance, not capacitance, in Eq. 10), generally this range of adjustment is not feasible and the practical deviation in coil Q for a fixed diameter, length, and ^{1}H operating frequency is on the order of 5-10%, assuming standard single-layer solenoid geometry. Nevertheless, it is desirable to ensure that the total inductance of the coil is dominated by the solenoid itself, and not the leads; this implies that the majority of magnetic flux is concentrated within the active sample volume.

B_1 Homogeneity

Although coil Q—given a fixed overall coil length, diameter, and material—is not expected to deviate by large amounts with modest changes in turn spacing and wire diameter or shape, the homogeneous portion of the B_1 field depends more strongly on these parameters. As discussed by Haeberlen and co-workers,[15] the roll-off in B_1 as a function of coil length (i.e., axial inhomogeneity) may be compensated by increasing the turn density at the ends of the coil (Figure 2-3(b)). Alternatively, the coil diameter may be tapered (Figure 2-3(c)) to achieve a very similar axial profile.[16] The shortcoming of both designs may be reduced radial homogeneity, which is determined primarily by spacing between turns. Coil geometries designed to reduce radial inhomogeneity without large increases in inductance (and decreasing self-resonance frequency) are: flattened wire (Figure 2-3(d)), variable width ribbon (Figure 2-3(e)), or loop-gap resonators (Figure 2-3(f)). Variable width ribbon designs may improve radial homogeneity relatively while maintaining a moderate inductance,[17] whereas loop-gap resonators appear to provide the best overall homogeneity of any resonator design but suffer from the extremely low inductance, which is hard to tune with high efficiency, especially to multiple frequencies, in the RF frequency range.[18]

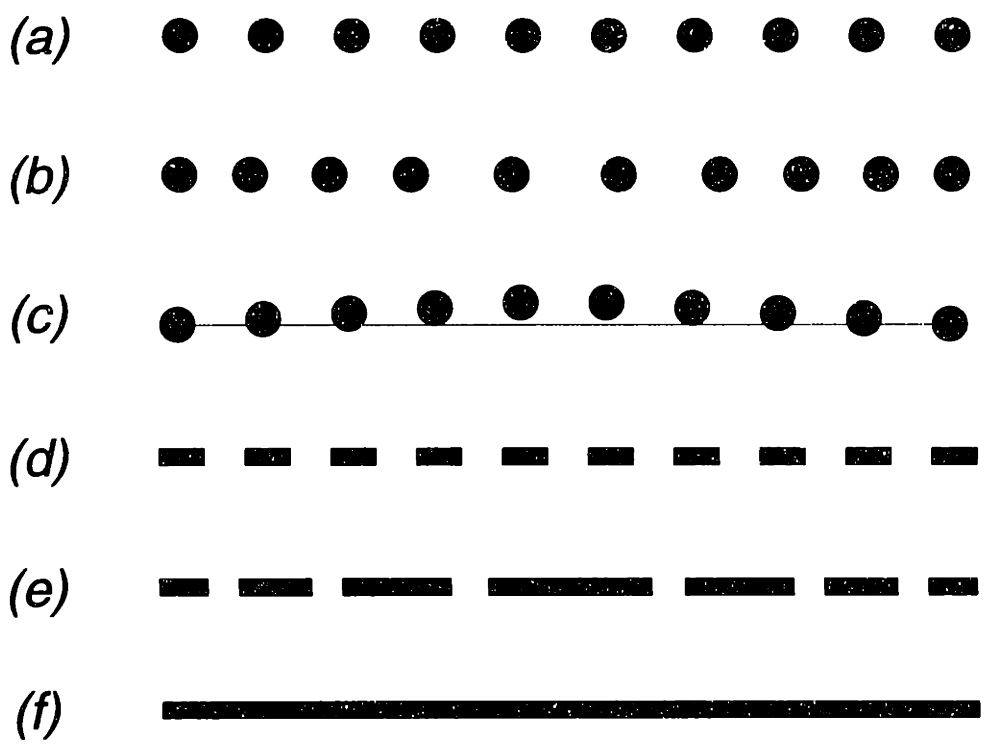

Figure 2-3. Cross sections of several inductor geometries.

One side of the coil is depicted at constant x, as a function of y and z. (a) Standard solenoid. (b) Variable pitch solenoid (Haeberlen).[15] (c) Tapered solenoid. (d) Flattened wire. (e) Variable ribbon width.[17] (f) Loop-gap resonator.[18,19]

Optimization of coil geometry can be performed by numerical integration of the Biot-Savart law,[20]

$$B(r) = \frac{1}{c} I_s \oint \frac{d\boldsymbol{r}_s \times \boldsymbol{r}_{fs}}{|r_{fs}|^3} \tag{17}$$

which assumes uniform current density over the path of the conductor surface and is found to predict field profiles well in the low frequency regime (i.e., where overall coil size is small compared to the wavelength). Normally the path is defined in analogy to the treatment of Haeberlen:[15]

$$B_{1z}(x,y,z)=\frac{I}{c}\int_{-n2\pi}^{+n2\pi}\frac{r^2-r(x\cos\varphi+y\sin\varphi)}{\left[(x-r\cos\varphi)^2+(y-r\sin\varphi)^2+(z-a\varphi)^2\right]^{3/2}}d\varphi \tag{18}$$

In this formalism, the path is swept out over φ, and coil geometry parameterized accordingly. Variable pitch is accounted for by the functionality of a, variable diameter by r. Variable width and shape of ribbon or wire is described by additional parameters, as in Ref. 17. Optimization by numerical integration of Eq. 18, and analysis of some homogeneity profile (usually by second moment methods) over a desired coil volume may yield improvements. Implementation is another matter, possibly requiring coil forms, which reduce filling factor and may arc under high voltage. An improved coil geometry that address all of these theoretical and practical issues may yield significant improvements in overall sensitivity and probe performance in the future.

Capacitors

Ideal limit

Energy may be stored in electric field according to:

$$E=\frac{1}{2}CV^2 \tag{19}$$

In the circuit modeling viewpoint, capacitive reactance is negative, inversely proportional to frequency:

$$Z=\frac{1}{j\omega C}=\frac{-j}{\omega C} \tag{20}$$

The simplest capacitor is a parallel plate, with capacitance (in pF)

$$C=\frac{0.2248\,\varepsilon A}{S} \tag{21}$$

where ε is the dielectric constant, A is the area (square inches) and S the plate spacing (inches).

Parasitic Model

Two non-ideal aspects of capacitors in the RF are associated lead inductance and dielectric loss, as shown in the following figure. The inductance L and series resistance R_s result from the finite lead lengths, and are modeled as if short segments of isolated wire. The parallel resistance, R_p, is due to dielectric loss, and determines the capacitor Q well below self-resonance. Self-resonance of small chip capacitors (American Technical Ceramics series B and C) will typically be above 1 GHz for small (~1-5 pF) values, although the voltage-handling specification of chip capacitors of this type and capacitance range is typically not sufficient for high power probe applications. Variable capacitors (Polyflon, Jennings-ITT, etc.) typically are self-resonant in the 100-500 MHz range, with the exception of physically small quartz dielectric models, which again have difficulty achieving voltage specifications of use for solids probes.

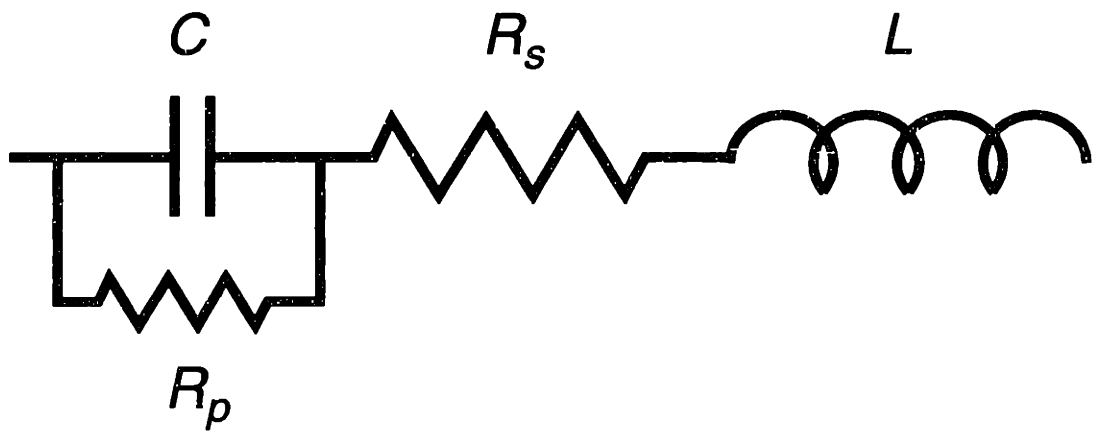

Figure 2-4. Capacitor model.

Capacitor Q

Because capacitor Q is, below self-resonance, a function of the dielectric loss,

$$Q = \frac{1}{\tan\delta}, \tag{22}$$

where tan δ is the dielectric loss constant. The primary consideration in choice of commercial capacitor, or design of custom capacitive elements, is the dielectric material. For fixed capacitors, a large dielectric constant is desired, in order to maximize capacitance in a small space. Most chip capacitors (e.g., ATC) use synthetic ceramics similar to porcelain, for example. Cylindrical capacitors with relatively high voltage specifications usually have teflon (e.g., Polyflon) or gas/vacuum (e.g., Jennings) dielectric. Transmission line supports and other insulators must have low loss and high breakdown voltage, but with lower dielectric constant to minimize stray capacitance, and again teflon is the best choice unless low ^{19}F background (or extremely low ^{1}H) is required. Clearly no other dielectric performs as well as air, which is therefore our preference whenever space allows.

Table 2-1. Material Dielectric Properties[a]

Material	ε (dielectric constant)	Loss tangent (100 MHz)	Loss tangent (3 GHz)
Air	1.0006	0	0
Teflon	2.1	0.0002+	0.0028
Polyethylene	2.26	0.0002	0.00031
Kel-F	2.5	0.001	
Vespel	3.5	0.004	
Epoxy	3.6	0.03	
Nylon	3.7		
Quartz (fused)	3.78	0.0002	0.00006
G-10	4.9	0.008	
Pyrex	5		
Silicon nitride	8	0.001+	
Porcelains	5-8	0.0002+	
Sapphire	9.9	0.0002	
Water	78	0.005	0.157

[a]from Doty (p. 4475)[3] and Rhea (p. 78)[9]

Transmission Lines

Distributed properties

Volumes have been written on transmission line theory, and it is recommended that one of several texts be consulted for a complete derivation of the transmission line equations, which is beyond the scope of the present discussion.[7,21-24] A transmission line is any pair of parallel conductors, which can be represented by uniform distributed capacitance, inductance, conductance, and resistance:

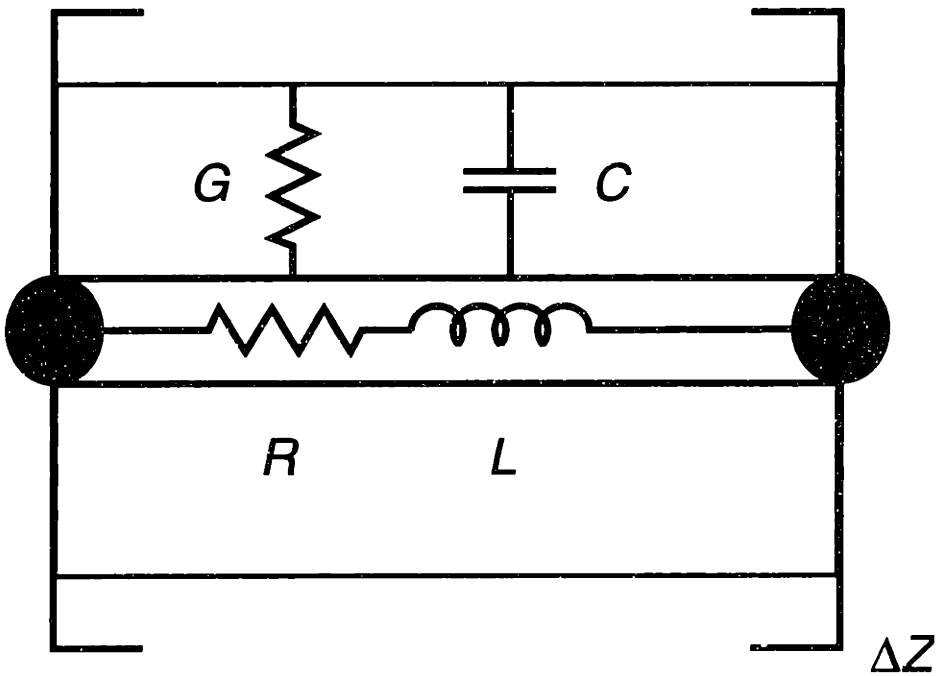

Figure 2-5. Transmission line distributed properties

The two conductors may be arranged in many configurations, though coaxial is standard. The field representation of a coaxial line is the transverse electromagnetic (TEM) mode, in which fields are always transverse to the direction of conductor length.

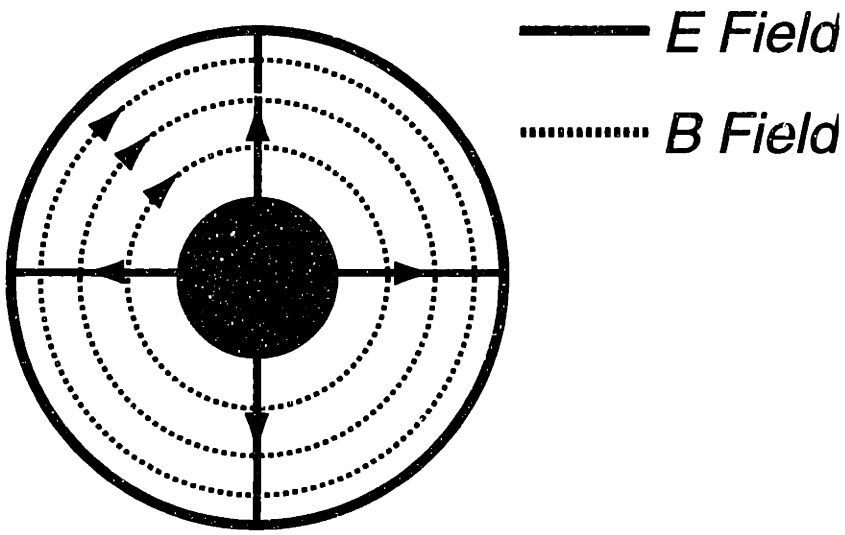

Figure 2-6. TEM mode for coaxial transmission line.

Applying Kirchhoff's law to the circuit for instantaneous voltages and currents and simplifying expressions (see, for example, Chipman p. 22)[21] results in the differential equations:

$$\frac{dV}{dz} = -(R + j\omega L)I$$
$$\frac{dI}{dz} = -(G + j\omega C)V \qquad (23)$$

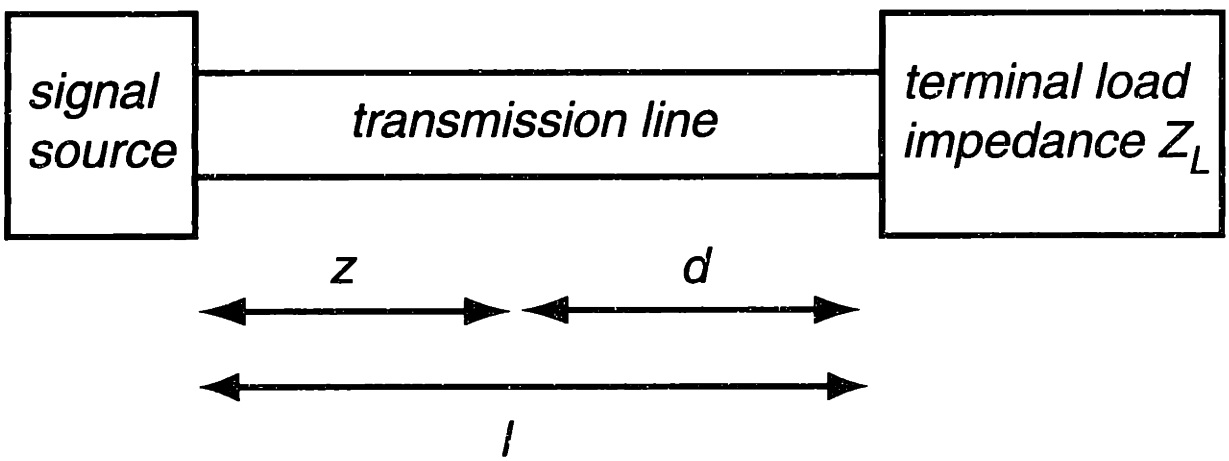

Figure 2-7. General transmission line circuit

The solution to Eq. 23 is:

$$V(z) = V_1 e^{-\gamma z} + V_2 e^{\gamma z}$$
$$I(z) = I_1 e^{-\gamma z} + I_2 e^{\gamma z} \tag{24}$$

where the propagation constant is

$$\gamma = \alpha + j\beta = \sqrt{(R + j\omega L)(G + j\omega C)}. \tag{25}$$

The complex factor can be decomposed into the attenuation coefficient α and the phase factor β. Eq. 24 shows that for any given point along the line, the ratio of V to I must be constant. This value is referred to as the characteristic impedance:

$$Z_0 = \frac{V}{I} = R_0 + jX_0 = \sqrt{\frac{R + j\omega L}{G + j\omega C}} \tag{26}$$

For all problems of interest for modern NMR, the high frequency approximation is valid, where

$$\omega L >> R, \omega C >> G. \tag{27}$$

The attenuation α is primarily due to the surface resistance R (assuming air dielectric), and the characteristic impedance is a simple function of line geometry for coaxial lines:

$$\alpha = \frac{R}{2Z_0} + \frac{GZ_0}{2} = 0.00164\left(\frac{1}{a} + \frac{1}{b}\right)\frac{\sqrt{f}}{Z_0} np/m, \tag{28}$$

$$Z_0 = \sqrt{\frac{L}{C}} = \frac{60}{\sqrt{\varepsilon}} \ln\frac{b}{a} = \frac{138}{\sqrt{\varepsilon}} \log\frac{b}{a}, \tag{29}$$

where a and b are the inner and outer conductor diameters (in inches), and f is in MHz. Examination of the functional dependence of Z_0 and α on coaxial line geometry (specifically, by keeping the outer conductor diameter b constant and varying the inner conductor diameter a)

reveals some interesting trends (Figure 2-8). The minimal attenuation is observed at the *b:a* ratio of 3.6:1, resulting in Z_0 of 77 Ω. At constant *b*, significant changes in the geometrical ratio, from 1.6:1 to 12.7:1 (corresponding to Z_0 of 29 to 152 Ω), can be tolerated with at most a 50% increase in α; more aggressive alteration of *a*, resulting in ratios of 1.4:1 to 20.8:1 (Z_0 of 20 to 182 Ω), causes only a doubling of the attenuation constant relative to the optimal result. The implication of this result—that Z_0 can be varied over an extreme range without large penalty in attenuation—may be useful for improved transmission line designs. This additional degree of freedom in probe design permits novel impedance transformation strategies for higher efficiency and power handling in multi-channel circuits.

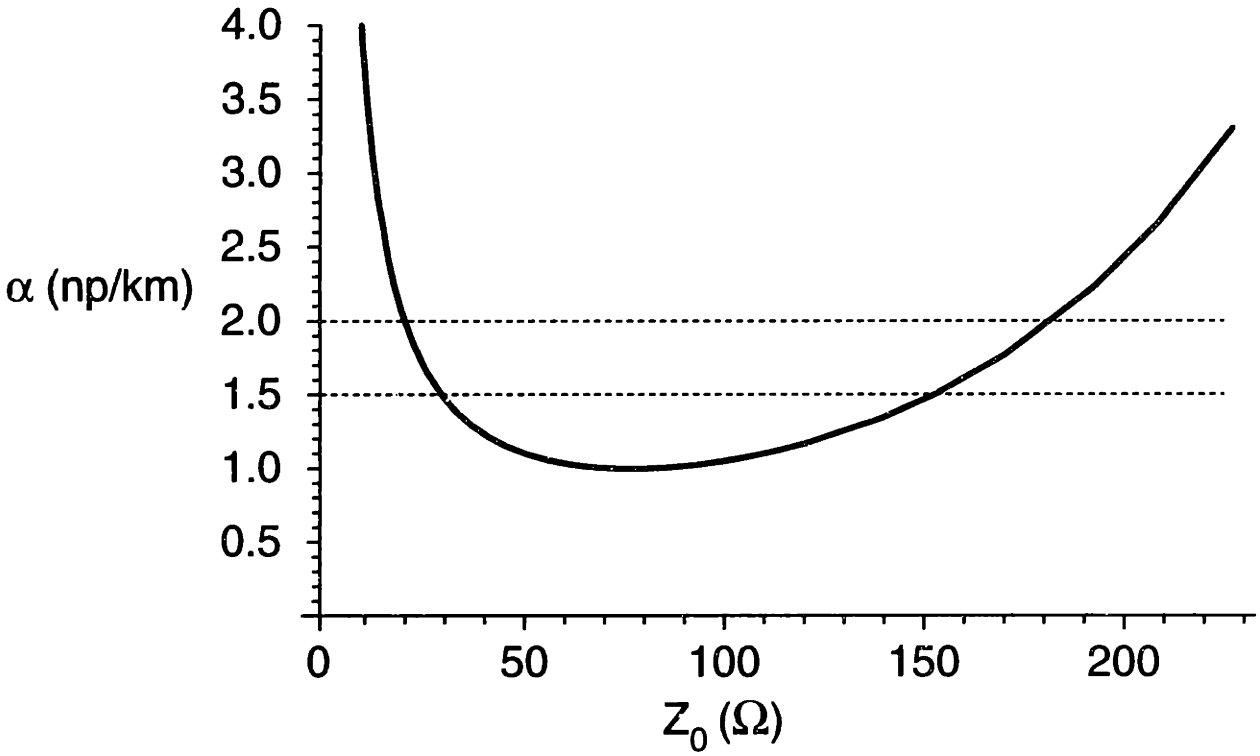

Figure 2-8. Transmission Line Attenuation as a Function of Impedance.

Attenuation is determined at 500 MHz by assuming 2.2" outer conductor and varying the inner conductor diameter, with air dielectric.

Eqs. 23, 24, and 26 can be combined to yield an expression for phasor current on the line at position *z*,

$$I = \frac{1}{Z_0}\left(V_1 e^{-\gamma z} - V_2 e^{\gamma z}\right) = I_1 e^{-\gamma z} + I_2 e^{\gamma z}, \tag{30}$$

implying that

$$I_1 = V_1/Z_0 \text{ and } I_2 = -V_2/Z_0. \tag{31}$$

From Eqs. 24 and 30, a general expression for impedance as a function of position can be derived:

$$Z(z) = \frac{V(z)}{I(z)} = Z_0\left[\frac{V_1 e^{-\gamma z} + V_2 e^{\gamma z}}{V_1 e^{-\gamma z} - V_2 e^{\gamma z}}\right] \tag{32}$$

Where $z = l$, the impedance is constrained to be the load impedance by definition, therefore

$$Z(l) = Z_L = Z_0\left[\frac{V_1 e^{-\gamma l} + V_2 e^{\gamma l}}{V_1 e^{-\gamma l} - V_2 e^{\gamma l}}\right] \tag{33}$$

The ratio of Z_L to Z_0 corresponds to the physical phenomenon of a reflected wave, implying that V_1 and V_2 are not necessarily equal. V_1 is the incident voltage wave, V_2 the reflected voltage wave. The ratio of these quantities is encountered frequently, and referred to as the reflection coefficient:

$$\rho = \frac{V_2}{V_1} e^{2\gamma l} = \frac{Z_L - Z_0}{Z_L + Z_0} \tag{34}$$

A related quantity, the voltage standing wave ratio (often denoted VSWR), expresses the ratio of maximum to minimum voltage along the line (at positions one-quarter wavelength apart):

$$S = \frac{1 + |\rho|}{1 - |\rho|} \tag{35}$$

Conversely,

$$|\rho| = \frac{S - 1}{S + 1}. \tag{36}$$

Substituting Eq. 34 into Eq. 30 to eliminate V_1 and V_2, converting the exponential to hyperbolic functions, and simplifying results in the following expression:

$$Z_{in} = Z_0 \frac{Z_L + Z_0 \tanh \gamma l}{Z_0 + Z_L \tanh \gamma l}, \tag{37}$$

where, as above, Z_L is the load impedance, and Z_{in} the input impedance at a position length l from the load. This is the famous transmission line impedance transformation equation, and can be used directly for computation of impedance at any point along the line, provided the line parameters and the impedance at some other point is known.

A convenient graphical depiction of Eqs. 34 and Eq. 37 is the Smith chart (Figure 2-9),[25,26] which is a linear polar coordinate display of the function

$$\rho = |\rho| e^{j\phi}. \tag{38}$$

The radius represents the reflection coefficient (ρ): 0 at the middle and 1 at the outer edge. Smith charts are commonly used in RF engineering because all possible impedance transformations in passive circuits can be expressed on the graph, and for real values of Z_0 (i.e., the high frequency limit) the representation has several intuitive aspects of use in tuning resonant circuits. Its original role was as a tool to calculate the complex exponential and hyperbolic functions necessary to determine impedance transformations; this was particularly useful to engineers in the field, and obviated the need for consulting mathematical tables. With the common representation as in Figure 2-9, real and imaginary components of impedance can be determined to better than 1%, usually sufficient for practical problems in RF circuits.

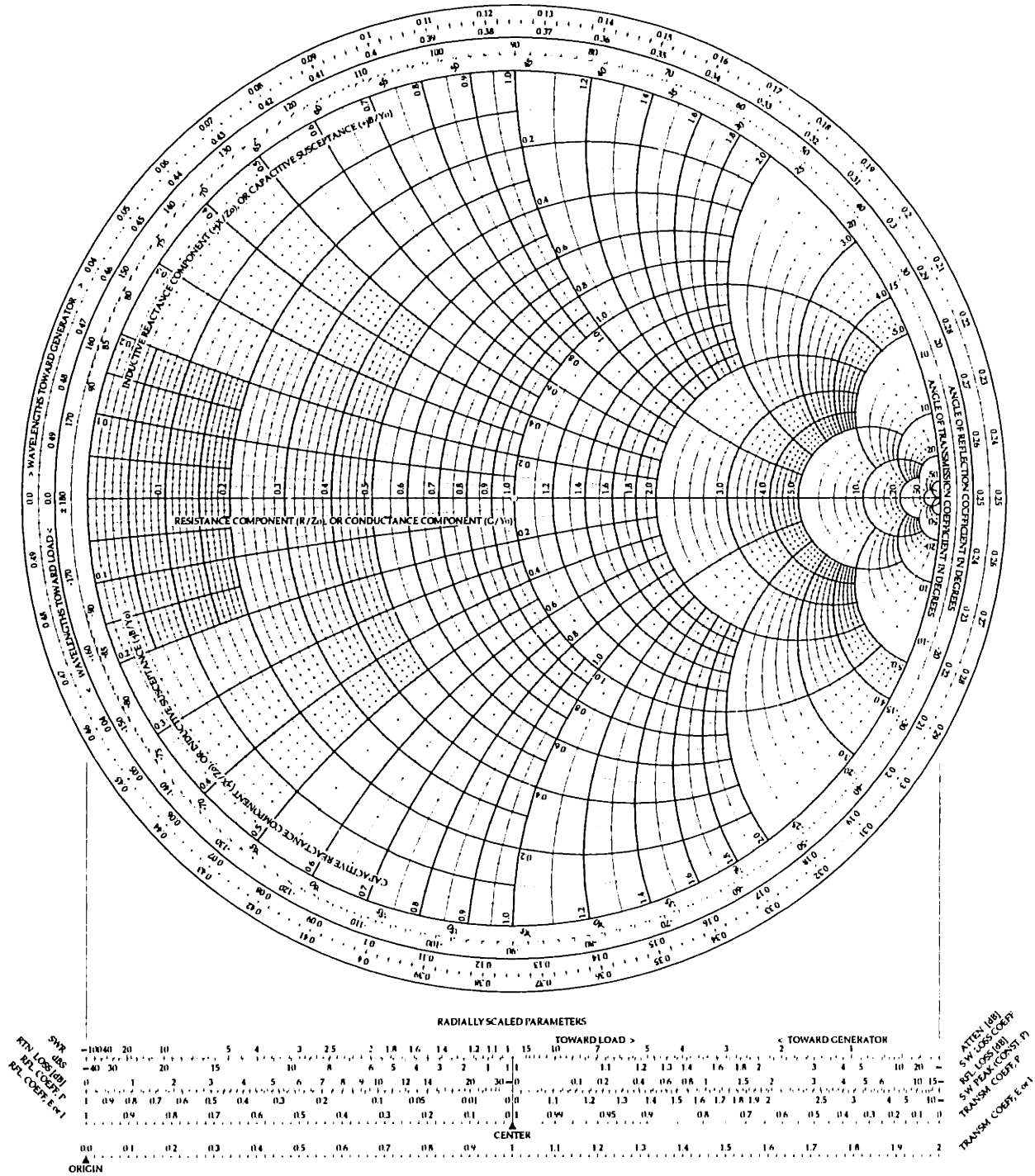

Figure 2-9. The Smith Chart.

Even now that fast calculators are readily available, and exact calculation of Eq. 37 poses no significant difficulty, the Smith chart is essential for developing an understanding of impedance transformation strategies in probe circuits. Several examples will illustrate this point.

Upon examining the Smith chart more closely, the curvilinear coordinates of normalized impedance may be appreciated. Circles, centered on points along the x-axis, map out positions of constant resistance (Figure 2-10(a)); arcs originating at the infinite impedance point denote positions of constant reactance (Figure 2-10(b)). (Derivations of the parametric expressions describing the circles and arcs can be found in, for example, Chipman p. 185-187.[21]) Thus, the change in impedance properties due to addition of series resistance or reactance can be followed by tracing a path along a circle or arc, respectively.

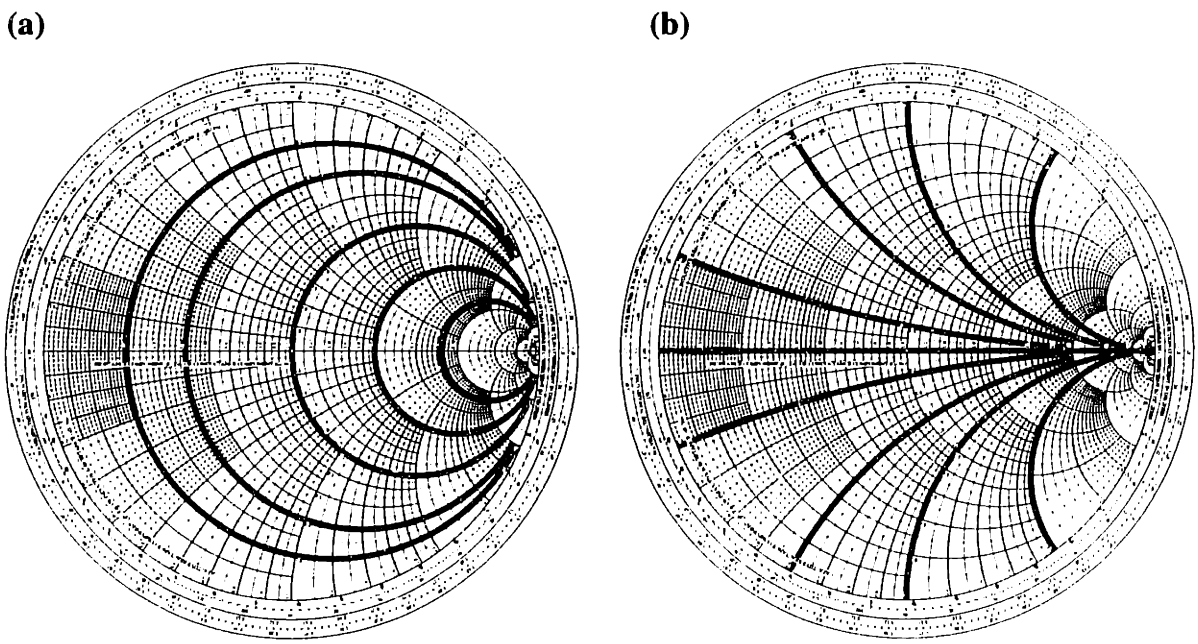

Figure 2-10. Smith charts emphasizing (a) constant resistance circles and (b) constant reactance arcs.

Of course, plotting lumped element impedance values on curvilinear coordinates is not the primary purpose of the Smith chart, and in fact can be quite awkward at first, if the only interest is to conceptualize a normalized impedance. The motivation of the Smith chart, and the value of

the polar coordinate plot, becomes more apparent when considering how impedance changes along the length of the transmission line. The procedure for doing so follows: First, we plot the load impedance ($Z_L=R_L+jX_L$) on the chart by finding the intersection of the appropriate resistance (R_L) and reactance (X_L). This amounts to a transformation from lumped element space to transmission line space. The radius at this point indicates the reflection coefficient, and the phase angle ϕ determines the "distance" (electrical length) from the nearest voltage nodes (local minima) and anti-nodes (maxima). Now, we want to determine the impedance at some point down the line. "Down" the line, here and in the following, will refer to locations further away from the load. (This is in the context of our usual load impedance, the probe sample coil, being on the "top" of our main transmission line entering the magnet.) To do so, some electrical phase ϕ is added, by sweeping around the chart clockwise, a full rotation for every $\lambda/2$ length at the relevant frequency. At this point, the electrical phase and impedance values can be extracted from the intersection of resistance circles and reactive arcs, and this impedance reintroduced into the context of a lumped element circuit if desired. More likely, once the reader has gained some familiarity with the Smith chart, it will be more natural to stay on the Smith chart for all subsequent calculations.

The periodicity of reactive impedance function is perhaps more obvious upon study of the high Q transmission line limit. In such a limit, where both lumped elements and transmission lines possess only very small distributed resistance, most impedances will fall on the outer edge of the Smith chart, where $\rho \approx 1$. This implies a high (>100) standing wave ratio S, whose exact value primarily effects efficiency, but not the impedance itself (discussed in more detail below). In this purely reactive limit, it is usually sufficient to dispense with the resistive term (α) for purposes of calculating impedance. For bookkeeping purposes in calculating circuit efficiency, this term must be remembered, but generally it is only necessary to worry about this term upon first designing a circuit; for day-to-day circuit debugging and tuning, knowledge of the reactive impedance alone is sufficient. In the reactive limit, Eq. 37 can be simplified to:

$$Z_{in} = Z_0 \frac{Z_L + jZ_0 \tan(\beta l)}{Z_0 + jZ_L \tan(\beta l)} = Z_0 \frac{Z_L + jZ_0 \tan\left(2\pi \frac{l}{\lambda}\right)}{Z_0 + jZ_L \tan\left(2\pi \frac{l}{\lambda}\right)} \tag{38}$$

This limit also provides a simple expression for the standing wave ratio as a function of the load impedance Q and magnitude (X=Im[Z_L]), which is derived directly from Eq. 35, neglecting terms of order 1/Q according to the assumption Q>>1:

$$S = Q\left(\frac{Z_0}{X} + \frac{X}{Z_0}\right) \tag{39}$$

It is important to recognize that although ρ, and therefore S, do not change with electrical phase evolution (in the low attenuation limit), the "effective Q" (i.e., the relationship Im[Z_{in}] / Re[Z_{in}]) does. This can be seen by thinking of the change in X as electrical phase is added. By sweeping around the transmission line at constant radius, the impedance passes from one constant reactance arc to another. One might wonder whether the change in resistance compensates for the change in reactance, but indeed it does not. Because S and Z_0 are constant, Q must change to satisfy Eq. 39. This result is an example of why the Q of a transformed impedance is, on its own, quite a meaningless and often misleading quantity.

Impedance transformation examples

To bring the preceding theoretical discussion into perspective, here we work three common examples of impedance transformations: (1) the shorted λ/4 line; (2) the open λ/4 line; and (3) the capacitively shortened ~λ/4 line. The shorted line corresponds to the case where Z_L=0 ideally, though typically some fraction of an ohm is associated with the shorting mechanism, solder, etc. From Eqs. 34 and 35, and the basic standing wave concept, it is clear that for a purely real load impedance, the following relations hold:

$$S = \frac{Z_0}{Z_L}, Z_L < Z_0$$
$$S = \frac{Z_L}{Z_0}, Z_0 < Z_L \tag{40}$$

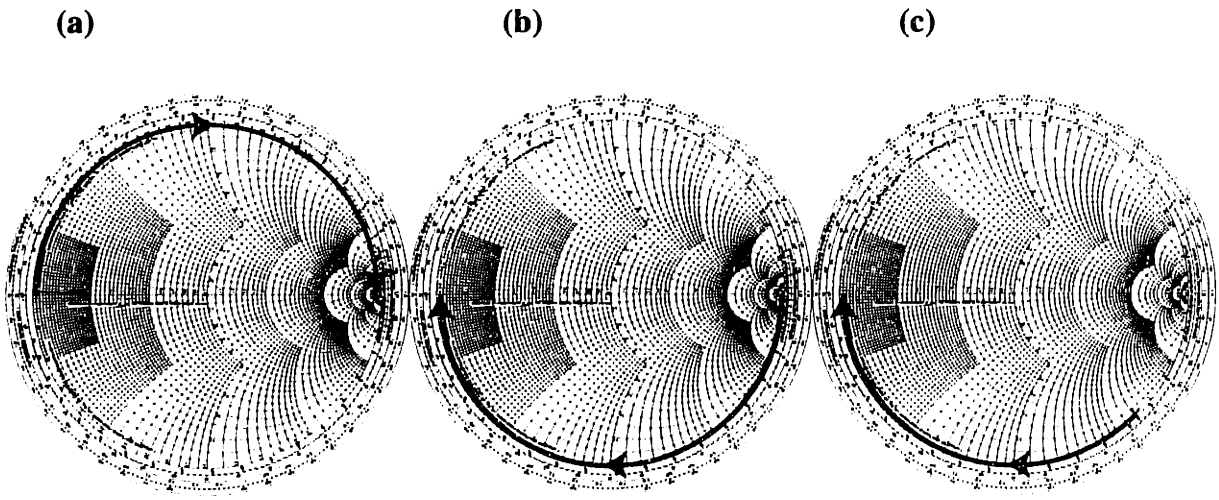

Figure 2-11. Smith chart depictions of (a) shorted λ/4 line, (b) open λ/4 line, and (c) capacitively shortened λ/4 line.

From Eq. 40, it is straightforward to calculate the impedance of the lossless shorted λ/4 line with finite resistance load as

$$Z_{in} = \frac{Z_0^2}{Z_L}, \tag{41}$$

or ~10 kΩ for a 50 Ω line shorted with a finite, 0.25 Ω load. Conversely, with an open load, the impedance transformation relations are the opposite. In practice, using a capacitor to ground in favor of an open load allows the effective electrical line length to be pruned to the exact frequency desired, without need to adjust the physical parameters of the line. This approach also reduces fringing at the open (discontinuous) end of the line, where the ideal transmission line behavior is no longer observed. Because the exact values of the short and open circuit loads are

difficult to assess, often we assume ideal load impedances and then calculate the effective input impedance based on a real (lossy) transmission line with well-known attenuation coefficient. Examples of this approach will be shown when we analyze the Cross-Hester-Waugh circuit below.

Power Transfer

Transmission lines

Up to this point, we have focused on the issue of impedance transformation, which will be generally useful both for probe design and tuning. However, we also require an understanding of power transfer in these circuits. These functions are most essential at the design stage, and for the user are secondary in importance to the fundamental impedance transformation principles above. Nevertheless, these relationships should not be ignored in the design stage. Often power transfer properties in transmission lines are discounted, because the low loss limit is assumed. It is clear that such an assumption is not misleading with respect to impedance transformation, but if quantitative power transfer is assumed, even with large air dielectric coaxial lines at relatively low frequencies, circuit performance may be compromised.

The two results of greatest use were derived first by Macalpine.[27] Here they will simply be stated and illustrated with relevant examples. First, in the "locally tuned" limit, where the load circuit has been approximately tuned and matched to the sending impedance (e.g., along the line between amplifier and tuned probe), it is shown that if S is less than 10, the following results are accurate to within 1% (error goes as ~S/1000):

$$S_2 = \frac{1}{\tanh\left(\alpha + \tanh^{-1}\frac{1}{S_1}\right)}, \tag{42}$$

and the efficiency of power delivery to the load is

$$\eta = \frac{S_2 - 1/S_2}{S_1 - 1/S_1}. \tag{43}$$

Here S_1 is the standing wave ratio at the load, S_2 at the input port; therefore S_1 must always be less than S_2 (in a passive circuit, as assumed here), in agreement with Eq. 42. For typical values of attenuation in flexible coax (α for RG-58 cable is approximately ~0.01 np/ft at 500 MHz, RG-214 cable is ~0.005 np/ft), we see that the power transfer is only moderately improved by tuning a probe from 10% to 0.1% reflection. Under these conditions the loss is primarily determined by the cable attenuation alone.

Table 2-2. Attenuation in low VSWR limit.

ρ (% reflect V)	dB[ρ]	S(1)	efficiency (%)		
			αl (np) 0.010	0.100	0.500
0.1%	-60.0	1.0020	98.0%	81.9%	36.8%
1.0%	-40.0	1.0202	98.0%	81.9%	36.8%
3.0%	-30.5	1.0619	98.0%	81.8%	36.8%
5.0%	-26.0	1.1053	98.0%	81.8%	36.7%
10.0%	-20.0	1.2222	98.0%	81.6%	36.5%
25.0%	-12.0	1.6667	97.8%	80.1%	34.8%
50.0%	-6.0	3.0000	96.8%	73.8%	28.6%
75.0%	-2.5	7.0000	93.3%	57.5%	17.4%

This general result accounts for the fact that probe performance depends only moderately upon the exact tuning. In fact, pulse widths often improve upon slight detuning of the probe because steady state power transfer is unaffected but ringdown and transient effects are reduced. This is especially true in moderately overcoupled,[28] high Q circuits.

The second limit that is often useful for probe analysis is the so-called remotely tuned limit, where S>>1. This corresponds to the behavior within a probe where the impedance of the

sample coil is not transformed prior to entry into the transmission line. Remote tuning refers to the fact that tuning and matching elements may be placed at some point down the transmission line (perhaps at the end of the first line), at which point the transformation to 50 Ω is achieved. This brute force approach relies upon the extremely low attenuation of the line to preserve efficiency of power transfer. However, this assumption is problematic with high Q loads, even in extremely large lines. If S is greater than 10, the following expression is accurate to within 1% (error term proportional to ~$1/S^2$):

$$\eta = \frac{1}{1 + S\alpha L} \tag{44}$$

The following table expresses the power efficiency as a function of S for a few typical frequencies (assuming ~2.2" outer conductor, 77 Ω, air dielectric transmission line at 100 and 500 MHz, 1.1" OD for 750 MHz—scaled according to typical available magnet geometries).

Table 2-3. Transmission efficiency in the high VSWR limit.

		VSWR				
Frequency	**αl**	**1000**	**500**	**250**	**100**	**50**
750 MHz	**0.00245**	29.0%	44.9%	62.0%	80.3%	89.1%
500 MHz	**0.00100**	50.0%	66.7%	80.0%	90.9%	95.2%
100 MHz	**0.00045**	69.1%	81.7%	89.9%	95.7%	97.8%

Voltage source

Here we review some of the fundamental result of power matching in a series circuit. The results are quite well known but the derivation serves to illustrate some differences between a voltage source (e.g., amplifier) and a fictitious power source.

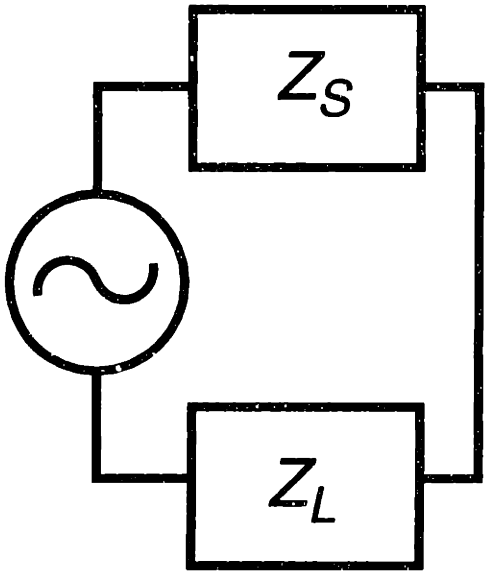

Figure 2-12. Voltage source with associated impedance, connected to load.

Assuming that the signal (voltage) source of (V_S) with some associated, fixed impedance (Z_S), is loaded with another impedance (Z_L):

$$Z_S = R_S + jX_S; Z_L = R_L + jX_L \tag{45}$$

This approximates an amplifier circuit. For purely real load impedances, by definition

$$I = \frac{V}{Z_S + Z_L} = \frac{V}{R_S + R_L} \tag{46}$$

Solving for the power dissipated in load:

$$V_L = IZ_L = \frac{V_S Z_L}{Z_S + Z_L} \tag{47}$$

$$P_L = IV_L = I^2 Z_L = Z_L \left(\frac{V_S}{Z_S + Z_L} \right)^2 = R_L \left(\frac{V_S}{R_S + R_L} \right)^2 \tag{48}$$

Maximum power dissipation is achieved at *matched* impedance:

$$\frac{dP_L}{dR_L} = 0 = \left(\frac{V_S}{R_S + R_L} \right)^2 + \frac{R_L {V_S}^2}{\left(R_S + R_L\right)^3} \longrightarrow R_S = R_L \tag{49}$$

Because the current passing through each element is the same, half the power is dissipated in the source and half in the load.

For complex impedances, power *dissipated* is the real part of the power function, power *stored* the imaginary part:

$$P_L = \mathrm{Re}\left(I^* V_L\right) = \mathrm{Re}\left(II^* Z_L\right) \tag{50}$$

Solving for the current

$$\begin{aligned} I &= \frac{V_S}{Z_S + Z_L} = \frac{V_S}{R_S + R_L + j\left(X_S + X_L\right)} \\ I &= \frac{V_S\left(R_S + R_L - j\left(X_S + X_L\right)\right)}{R_S + R_L + j\left(X_S + X_L\right)} \end{aligned} \tag{51}$$

Now the power dissipated is:

$$P_L = \mathrm{Re}\left(Z_L II^*\right) \frac{R_L V_S^2}{\left(R_S + R_L\right)^2 + \left(X_S + X_L\right)^2} \tag{52}$$

And solving for maximum power:

$$\frac{dP_L}{dX_L} = 0 \longrightarrow X_S = -X_L \tag{53}$$

$$\frac{dP_L}{dR_L} = 0 \longrightarrow R_S = R_L \tag{54}$$

That is, power transfer is maximized when the complex load impedance is the conjugate of the source impedance.

Power source

The problem of power transfer from a voltage source to matched load is appropriate to calculate how much power arrives at the input port of the probe. Once within a probe circuit, analysis of power transfer requires the consideration of a fictitious power source. The main

concern is to determine the fraction of power that is stored in the coil, in order to determine the steady state coil current. We assume that the power delivered (not the voltage) is a constant, and we want to maximize the power in the load:

$$P_L + P_S = P \tag{55}$$

Using Eq. 46 and the analogous result for the load power,

$$\frac{P_S}{P_L} = \frac{R_S}{R_L} = 0 \longrightarrow R_S = 0 \tag{56}$$

This result is not physically possible for an amplifier, because the amplifier must have some associated impedance. However, this is the desired case in probe circuits, and corresponds to the physical picture of avoiding resistance everywhere but at the coil itself. This implies that use of relatively low Q inductors elsewhere in the circuit should be avoided if at all possible.

More generally, for two elements in series (labeled 1 and 2), the percentage of power delivered to the "load" is

$$\eta_{series} = \frac{P_1}{P_1 + P_2} = \frac{1}{1 + \frac{Q_1|Z_2|}{Q_2|Z_1|}} \tag{57}$$

If one element is purely resistive (a situation not commonly encountered within the probe circuit):

$$\eta_{series} = \frac{P_1}{P_1 + P_2} = \frac{1}{1 + \frac{Q_1 R_2}{|Z_1|}} \tag{58}$$

For two parallel elements a similar analysis yields:

$$\eta_{parallel} = \frac{P_1}{P_1 + P_2} = \frac{1}{1 + \frac{Q_1|Z_1|}{Q_2|Z_2|}} \tag{59}$$

This applies to a coil in parallel with a tuning capacitor, one probe channel in parallel with another at a junction, etc. If one element is purely resistive (e.g., a transmission line junction at a voltage node, a resonant trap circuit in parallel with a second tuning circuit):

$$\eta_{parallel} = \frac{P_1}{P_1 + P_2} = \frac{1}{1 + \frac{Q_1|Z_1|}{R_2}} \tag{60}$$

These results of Eqs. 57-60 are rather intuitive; for example, Eqs. 57-58 express voltage division across a series circuit where current is the same in each element, and Eqs. 59-60 are the complex load impedance equivalent of "following the path of least resistance". Note that according to these expressions, a low coil (load) Q would always increase the percentage of power *dissipated* in the coil. However, this is at odds with the goal of probe design, which is to generate high coil *current*. This always requires as high coil Q as possible. Therefore it is not acceptable to reduce coil Q in order to improve efficiency. In practice, this calls for a separation of coil geometry design from circuit design. First the coil is optimized, perhaps experimentally using a simple tuning circuit. Then the multi-channel circuit is built.

Converting Coil Voltage to Current

By reciprocity, calculation of the B_1 field as a function of incident voltage is sufficient to understand both transmit and receive efficiency.[10] We take a convenient form of the expression most closely related to that of Stringer[29] and Doty (p. 3757-8):[2]

$$B_1 = \sqrt{\frac{\mu_0 \eta P Q_{coil}}{\pi \xi f V_{coil}}} \tag{61}$$

where μ_0 is the permittivity of free space ($4\pi \times 10^{-7}$), η is the overall probe circuit efficiency (input to coil), the frequency f is in Hz, V_{coil} is in m^3, P is in watts, and ξ is defined as

$$\xi = \frac{\frac{1}{2\mu_0}\int dV\, \boldsymbol{B}\cdot\boldsymbol{B}}{B_{\max}^2 V_{coil}} \qquad (62)$$

The value of Eq. 62 is unity for an infinite solenoid (i.e., the B_1 field is contained entirely within the coil). For most coil geometries this value is slightly less than unity, but in short coils with <5 turns can be much less. Greater insight is primarily gained by numerical integration of the Biot-Savart law, as discussed earlier. Such analysis is sometimes used for designing compensated coils of higher homogeneity, and the overall average field within the coil may be changed significantly upon modification of relative turn spacing, wire shape, etc. However, we will not consider these issues further at this point. We will therefore collect the constants and this geometric term into a constant β (realizing that this distinction is somewhat arbitrary and that Q_{coil} is also a function of geometry):

$$B_1 = \beta\sqrt{\frac{\eta P Q_{coil}}{f V_{coil}}} \qquad (63)$$

It is comforting that Eq. 63 gives a physically reasonable result. We assume here a ^{1}H frequency of 300 MHz, Q_c (loaded) of 200, 100 W incident power, and a standard ~5.5-mm inner diameter, ~15-mm long coil geometry, we consider only the transverse projection of B_1:

$$B_{1,xy} = \sin(\theta_m)B_1 \qquad (62)$$

If we divide by two to correct for the conversion of linear to circular polarization, the result is

$$\gamma B_{1,xy} \cong 125 \text{ kHz} \qquad (63)$$

This is within ~20% of the experimentally measured value in such probe circuit with approximately 200-250 W incident power from the amplifier. Absolute differences are due to our assumptions about coil geometry factors, the true loaded Q of the coil, and the overall efficiency of the circuit (~35-40% in this case). Relative differences between probe circuits where other parameters are (to first order) the same provide information about η.

Summary of Equations for Probe Design

$$\gamma = \alpha + j\beta = \sqrt{(R + j\omega L)(G + j\omega C)}$$

$$\alpha = \frac{R}{2Z_0} + \frac{GZ_0}{2} = 0.00164\left(\frac{1}{a} + \frac{1}{b}\right)\frac{\sqrt{f}}{Z_0} np/m \quad (25)$$

$$Z_0 = \sqrt{\frac{L}{C}} = \frac{60}{\sqrt{\varepsilon}} \ln\frac{b}{a} = \frac{138}{\sqrt{\varepsilon}} \log\frac{b}{a} \quad (28)$$

$$S = \frac{1 + |\rho|}{1 - |\rho|} \quad (29)$$

$$|\rho| = \frac{S - 1}{S + 1} \quad (35)$$

$$Z_{in} = Z_0 \frac{Z_L + Z_0 \tanh\gamma l}{Z_0 + Z_L \tanh\gamma l} \quad (36)$$

(37)

$$Z_{in} = Z_0 \frac{Z_L + jZ_0 \tan(\beta l)}{Z_0 + jZ_L \tan(\beta l)} = Z_0 \frac{Z_L + jZ_0 \tan\left(2\pi \frac{l}{\lambda}\right)}{Z_0 + jZ_L \tan\left(2\pi \frac{l}{\lambda}\right)} \quad (38)$$

$$S = Q\left(\frac{Z_0}{X} + \frac{X}{Z_0}\right)$$

$$S = \frac{Z_0}{Z_L} \text{ if } Z_L < Z_0, S = \frac{Z_L}{Z_0} \text{ if } Z_0 < Z_L \quad (39)$$

$$\eta_{line} = \frac{1}{1 + S\alpha L} \quad (40)$$

$$\eta_{series} = \frac{P_1}{P_1 + P_2} = \frac{1}{1 + \frac{Q_1|Z_2|}{Q_2|Z_1|}} \quad \eta_{series} = \frac{P_1}{P_1 + P_2} = \frac{1}{1 + \frac{Q_1 R_2}{|Z_1|}} \quad (44)\ (57\text{-}58)$$

$$\eta_{parallel} = \frac{P_1}{P_1 + P_2} = \frac{1}{1 + \frac{Q_1|Z_1|}{Q_2|Z_2|}} \quad \eta_{parallel} = \frac{P_1}{P_1 + P_2} = \frac{1}{1 + \frac{Q_1|Z_1|}{R_2}} \quad (59\text{-}60)$$

Analysis of Some Common SSNMR Probe Circuits

Now that the fundamentals have been established, the analysis of several popular solid state NMR circuits will be presented. In order to simplify the calculations, some assumptions about circuit components will be assumed:

1. All capacitors will be assumed to be ideal (i.e., have infinite Q). For most commercial capacitors at low frequency, and custom-built air dielectric capacitors at high frequency, it is safe to regard the capacitor Q as much larger than the inductor loaded Q (<500), our frame of reference.
2. All "short" and "open" circuit terminations are also ideal; i.e., short circuits have vanishing impedance, open circuits infinite impedance.
3. Lead inductance and stray capacitance will be ignored.
4. Inductors will be used far (>100 MHz) below self-resonance, and therefore have an effective Q that is proportional to the $\sqrt{f}$. Inductors other than the sample coil will be assumed to have at least twice the Q of the sample coil. This is justified because the sample coil is generally smaller and in a more constrained geometrical configuration (e.g., length to diameter and total number of turns constrained by the inductance required in the tuning circuit and MAS spinner considerations).
5. Transmission lines may be terminated in ideal "short" or "open" circuits; however, the characteristics of the transmission line itself, including attenuation, will be assumed to be in agreement with well-accepted values as indicated in the summary above. Therefore shorted or open $\lambda/4$ cables will have finite resistance.

All of these assumptions favor locally tuned circuits.

Practical Considerations

In projecting the modeled circuit into reality, we note that all the assumptions above give the benefit of the doubt to locally tuned circuits. In practice, it is not always possible to design traps with Q's twice the sample coil Q, and numerous parasitics (stray capacitance, lead inductance, etc.) contribute to locally tuned circuits more than transmission line circuits. Capacitors have a finite Q (and breakdown voltage); leads have finite length; solder junctions have resistance. With each additional lumped element component, the reality of the constructed circuit deviates further from the idealized world of computer simulations. In transmission line circuits this is not necessarily the case. Provided the coil inductance, stray capacitance, and lead lengths are characterized, all other impedance transformations and power dissipation can be modeled with extremely high precision, reproducibility and confidence, based simply on the equations in the preceding summary.

For this reason, all practical factors favor transmission line (ala McKay) probes, provided the design is compatible with magnet geometry. Despite this uneven playing field, we will find that even in theory many locally tuned, lumped element circuits are less efficient than transmission line circuits. The few locally tuned circuits that exceed the efficiency of remotely tuned probes actually incorporate transmission line tuning elements within the magnet.

High Voltage Breakdown (Arcing)

In practice, the high voltage breakdown can prevent certain designs from functioning at all. Therefore when attempting to optimize efficiency, the following issues must be considered. This concise guide may potentially save months of agony and burned capacitors. These principles will be described further in the proper context.

1. If possible, avoid creating voltages higher than the coil voltage, except within a transmission line. The cyclindrical symmetry of the transmission line results in breakdown voltages of at least 100 kV, and therefore arcing within a well constructed line is extremely unlikely in most probe circuits. High voltage at the coil (given a coil Q) is unavoidable if very large B_1 fields are required, as addressed in the next point.

2. Use a free standing coil with bare copper (or silver-plated) wire with adequate spacing between turns. In some instances, high quality dielectric (i.e., virgin teflon) will assist in insulating the coil wire, but causes irreversible damage if corona discharge occurs. For many applications, insulation on the coil wire itself is not permitted because of the broad ^{13}C background from teflon and/or polyimides. Mounting the coil on a form should be avoided, as the form may compromise filling factor; most forms are not capable of withstanding the required voltages.

3. Attempt to tune and match circuits at low voltages if possible. In many instances tuning and matching circuits can be placed at positions of lower voltage than the coil itself. In other words, the impedance transformation of the transmission line, which protects the high voltage point, presents a lower effective inductance to be tuned and matched. The decrease in voltage can be an order of magnitude.

4. Avoid parallel resonant traps. Parallel resonance causes high voltages to be stored across fixed capacitors in which significant power may be dissipated; although we assume infinite capacitor Q for design purposes, in practice the very high resonant currents in the

tank will cause significant dissipation in the capacitor. Most fixed capacitors (e.g., American Technical Ceramics chip capacitors) will drift quite significantly with small changes in temperature, and therefore the characteristics of the trap circuit change with high duty cycle pulsing. This necessitates empirical optimization of the trap tuning, and may severely compromise duty cycle specifications. In addition, at any high voltage point, capacitive coupling to the ground plane is increased, and dissipation through the probe body dielectric increases.

Single Resonance Circuit

The basic resonant circuit most commonly employed in NMR is the parallel tuned, series matched circuit (Figure 2-13a). Although the distinction between "tuning" and "matching" capacitor is sometimes arbitrary, in this circuit the tuning capacitor generates an impedance with approximately 50 Ω real component, and a large inductive reactance. The matching capacitor removes the reactive component (Figure 2-13b). Inductive tuning schemes are also feasible, but often cause a decrease in Q relative to capacitive tuning.

(a) **(b)**

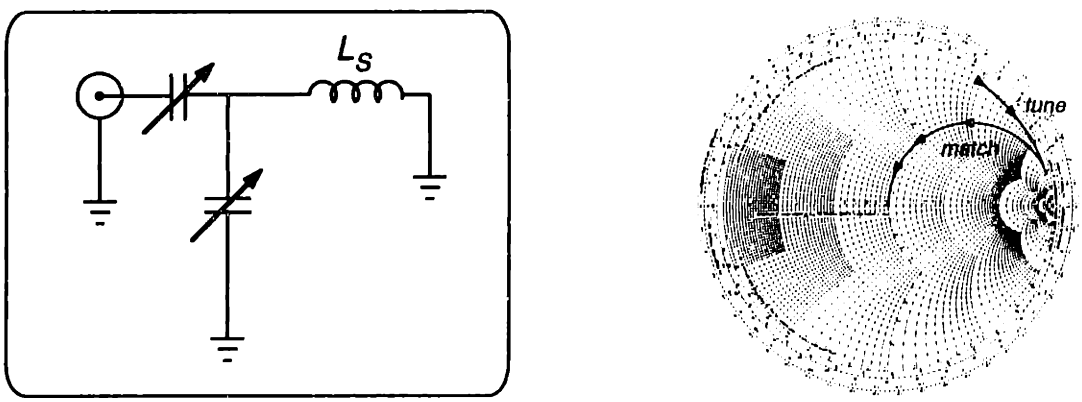

Figure 2-13. Single resonance tank circuit and impedance transformation.

We assume in all calculations in this section that capacitors have infinite Q and lead losses are ignored; therefore, the capacitively tuned single resonance circuit is theoretically 100% efficient. For purposes of spin-1/2 SSNMR, single resonance circuits are limited to use in ^{1}H CRAMPS experiments.

Double Resonance Circuits

Because most heteronuclear (^{1}H-^{13}C, ^{1}H-^{15}N, ^{13}C-^{15}N, etc.) CP experiments require the field amplitudes within each region of the coil volume to be correlated between channels, the use of a single coil tuned to both frequencies is generally preferred in SSNMR. In addition to concerns about homogeneity, more essential practical concerns such as high-voltage breakdown have thus far severely limited the applicability of multiple coil designs for high power applications. Therefore we require a means to tune and match a single coil to at least two frequencies, while delivering the majority of power to the sample coil and avoiding cross-talk between circuits. Typically 100-500 W ^{1}H decoupling pulses are applied while microvolt signals are being observed at the ^{13}C frequency. In order to avoid saturation of the ^{13}C (our default "X", or low frequency, channel) pre-amplifier from the ^{1}H frequency RF, at least 90-120 dB total isolation must be achieved between ^{1}H input and the ^{13}C pre-amplifier. Approximately 20-30 dB must come from the probe circuit itself, preferably more.

One of the earliest circuits proposed to satisfy the requirements of efficiency and isolation in a two-channel configuration was by Cross, Hester, and Waugh (Figure 2-14).[30] The circuit exploits short- and open-circuited $\lambda/4$ lines at the ^{1}H frequency to create virtual ground points on opposite sides of the coil for the ^{1}H and ^{13}C frequencies. Qualitatively, this produces approximate circuits as shown in Figure 2-14b (^{1}H frequency) and 2-14c (X frequency). In order to determine the theoretical efficiency, we assume: 400 MHz ^{1}H frequency, 100 nH, $Q_S = 10\sqrt{f}$ (f in MHz), and 0.250" OD, 50 Ω teflon-dielectric semi-rigid coaxial lines ($\alpha = 5.7 \times 10^{-4}\sqrt{f}\, np/m$, or 0.0114 np/m if loss is dominated by conductivity, not dielectric,

loss). The λ/4 lines are 13 cm, L_1 and L_2 40 cm each (approximate length to remove final matching capacitors from the magnet, as typically configured in these circuits). The equivalent component values for the λ/4 lines must be calculated at each frequency.

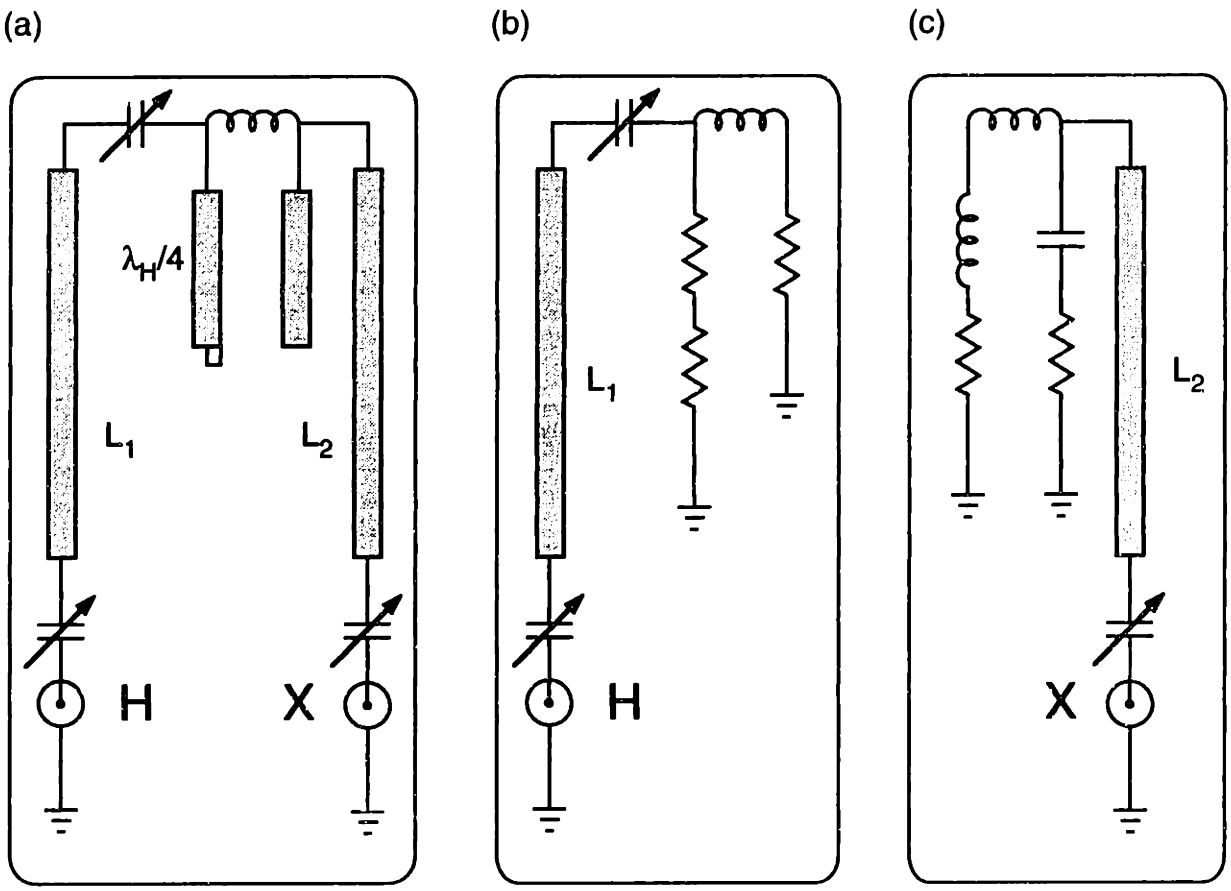

Figure 2-14. Cross Hester Waugh Double Resonance Circuit.

The ideal short-circuited λ/4 line has infinite impedance at ^{1}H; with finite α, we calculate the input impedance as

$$Z_{in} = Z_0 \frac{Z_L + Z_0 \tanh \gamma l}{Z_0 + Z_L \tanh \gamma l} = Z_0 \tanh\left(\alpha l + i\frac{\pi}{2}\right) \tag{64}$$

The first order term in the Taylor series expansion is a good approximation when $\alpha l << 1$:

$$Z_{in,\lambda/4}^{short} = Z_0\left(\frac{1}{\alpha l} + \frac{\alpha l}{3} - \frac{(\alpha l)^3}{45} + \ldots\right) \cong \frac{Z_0}{\alpha l} = \frac{50}{1.5\times 10^{-3}} = 33k\Omega \qquad (65)$$

Likewise, the open circuit is calculated to be $Z_{in,\lambda/4}^{open} = Z_0\alpha l = 0.075\Omega$. From Eqs. 58 and 60 we can directly calculate, based on the coil Q of 200 and reactance of 250 Ω, series and parallel efficiencies of 0.94 and 0.40. Now Eq. 44 can be used to calculate the loss along the transmission line length L_l, assuming the standing wave ratio S can be determined. First we determine the impedance of the sample coil (1.25 + *j* 250) with equivalent series and parallel resisitors to be 3.2 + *j* 250 (or X=250, Q=78). Ignoring the capacitor in series would result in a standing wave ratio $S = Q(Z_0/X + X/Z_0) \cong 78(5.2) = 405$. Note that this is already significant reduced relative to the standing wave ratio of the coil alone (~5.2 x 200 = ~1,040), in agreement with the qualitative view that the coil is Q-damped by the equivalent resistors and therefore all subsequent losses should be reduced. With S=405, the transmission efficiency along length L_l is

$$\eta_{line} = \frac{1}{1 + S\alpha L} = \frac{1}{1 + 405\cdot 1.1\times 10^{-2} np/m \cdot 0.4m} = 0.36 \qquad (66)$$

However, this neglects "partial" tuning by the series capacitor, which in the best case would cancel all of the reactive component of the coil impedance (i.e., series resonate the coil and associated resistances), thereby reducing S to 50 / 3.2 = ~16 and improving η_{line} to 0.93. Note that in order to complete the capacitive matching at the bottom of transmission line, L_l must be slightly more than an integer multiple of λ/2; i.e., the input impedance at the bottom of L_l must be inductive, and preferably small compared to Z_0 to minimize voltage in the tuning circuit. Therefore, the ^{1}H channel efficiency may be determined by a combination of line loss in the shorted λ/4 and L_l sections, and depending on the degree of series tuning performing with the variable capacitor, overall efficiency may range from 14% to 35%. (Table I of Ref. 30 considers only the efficiency along the main (L_l) transmission line, assuming perfect isolation and

efficiency throughout the rest of the circuit.) Overall efficiency could be improved significantly by increasing the line diameter of the shorted λ/4 and/or L_i lines, as suggested in similar circuits by Stringer.[29] For example, replacing the shorted λ/4 line with 1/2" coax would increase efficiency at that junction to ~53%, and overall circuit efficiency to ~45%.

The X channel (^{13}C assumed here) efficiency depends upon the equivalent values at 100 MHz. For the shorted line, $\alpha = 0.0057$ np/m, and $l = 0.13$, so

$$Z_{in} = Z_0 \tanh \gamma l \cong Z_0\left(\alpha l\left(1+\tan\frac{\pi}{8}\right)+j\tan\frac{\pi}{8}\right) = (0.043+j20.7)\Omega \qquad (67)$$

And similarly for the open line we find $(0.25 - j\ 121)\ \Omega$. In both cases the effective Q *of the input impedance* (which is *not* necessarily the same as the "transmission line Q") is ~500. The shorted line in series with the coil (X=62, Q=100 at 100 MHz) causes ~6% loss (i.e., η_{series}=0.94); the parallel component causes 9% loss. The additional high Q impedance in series with the coil results in a series impedance of (0.62 + 0.04) + j (62 + 21) = ~0.66 + 83 (or X = 83, Q = 125), which is placed in parallel with 0.25 – j 121, yielding "partially tuned" impedance of ~7.8 + j 261. [31-33] This is a modest change from the original coil VSWR (~205), but avoids the increase to 280 that would have been caused by the series line alone. The transmission efficiency along L_2 is therefore ~71%, and the total circuit efficiency ~62%. Under these assumptions, increasing the line size would assist the ^{13}C performance significantly; the exact improvement depends upon the degree of partial tuning actually exhibited in the circuit, which may depend on coil parasitics, etc. For example, doubling the L_2 line diameter would improve transmission along that length to ~85%, and total circuit efficiency to ~75%. A few percent additional gain would come from a similar replacement in the λ/4 line to ground on the ^1H side.

Doty has proposed modifications to the Cross-Hester-Waugh circuit that increase the tunable bandwidth on the X channel (Figure 2-15).[34] These changes involve replacing both λ/4 lines with lumped elements, a blocking inductor on the ^1H side of the coil, and a capacitor to ground on the X side.

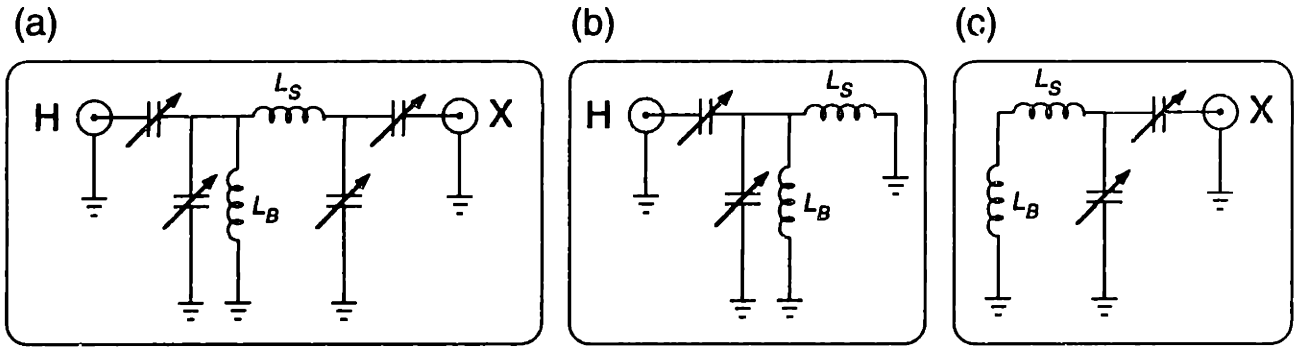

Figure 2-15. Doty Lumped Element Double Resonance Circuit

Again assuming ideal capacitors of extreme reactances (such that the X frequency views the capacitances on the H circuit as open loads, and the H frequency views the X channel shunt capacitor as a short to ground), the circuit in Figure 2-15(a) reduces to simple single resonance models as in Figure 2-15(b) and (c). Analysis of the circuit efficiency at each channel can be performed directly with Eqs. 57 and 59, and are summarized in Table 2-4. (The assumption of $Q_b / Q_s = 1.5$ agrees with Table 2 of Ref. 34) The direct tradeoff in efficiency based upon ratio of sample and blocking coil inductances and quality factors results from the use of lumped elements in this circuit. Replacing the open $\lambda/4$ line with a capacitor to ground is perhaps prudent, provided voltage specifications can be met. However, the replacement of the shorted $\lambda/4$ line with inductor has limited value in this instance. If dramatically improved Q values for the blocking inductor equivalent can be achieved, overall efficiency on both channels rises considerably and the constraint on sample coil inductance is lifted. This could result from the use of a 1/2-1" OD transmission line stub.

Table 2-4. Doty Double Resonance Circuit Efficiency

(Q_b / Q_s)	(L_s / L_b)			
1.0	1	2	3	4
HF efficiency	0.500	0.333	0.250	0.200
LF efficiency	0.500	0.667	0.750	0.800
1.5	1	2	3	4
HF efficiency	0.600	0.429	0.333	0.273
LF efficiency	0.600	0.750	0.818	0.857
2.0	1	2	3	4
HF efficiency	0.667	0.500	0.400	0.333
LF efficiency	0.667	0.800	0.857	0.889
10.0	1	2	3	4
HF efficiency	0.909	0.833	0.769	0.714
LF efficiency	0.909	0.952	0.968	0.976

A fair comparison of the Cross-Hester-Waugh and Doty circuits must mention that open-circuited $\lambda/4$ lines are in practice often difficult to implement, due to fringing fields and the ill-defined position of the voltage node. For this reason Doty has proposed a capacitively shortened coaxial resonator to replace the open $\lambda/4$ line. Nevertheless, the direct tradeoff in efficiency between the two channels based on the ratio of blocking to sample coil inductance is a clear shortcoming of the lumped element design, and could be quite easily remedied by a shorted, high Q air-dielectric transmission line (~1") for large increases in efficiency on ^{1}H without compromising the X channel. The remaining practical difficulty is that the ^{1}H side of the coil is at a relatively high impedance, so that although it is theoretically possible to define a parallel transmission line circuit of much higher impedance than the coil, this junction is by definition at very high voltage, and arcing at this point may occur.

The next step in the evolution of the Cross-Hester-Waugh approach, conceptually if not chronologically, is a design which has been employed by Chemagnetics (presently a division of Varian Analytical Instruments, Fort Collins, CO) and Bruker Instruments. (The details of the design analyzed here are in best agreement with the Chemagnetics version, and therefore we will refer to the circuit according to this company name.) Instead of generating a high impedance point with the ~$\lambda/4$ line on the ^{1}H side of the coil (in order to prevent power dissipation into the

line, as discussed above), this design assumes the transmission line stub to be a tunable element (Figure 2-16). The stub inductance is used to tune the transformed (capacitive) coil impedance.

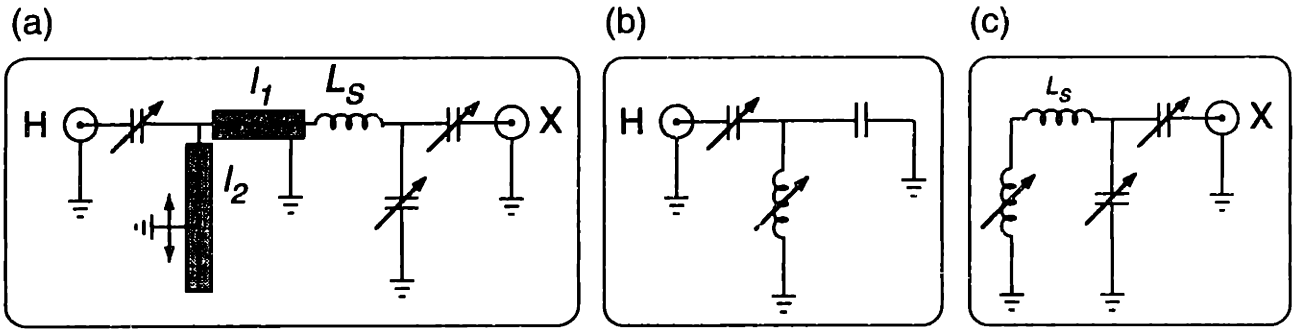

Figure 2-16. Chemagnetics Double Resonance Circuit

The attenuation of the stub here, assuming the 83 Ω, 1/8" ID, 1/2" OD air dielectric line typically used in this design, is 0.0039 np/m at 400 MHz. The tunability of the transmission line is achieved in practice by insertion of a high-conductivity, movable contact between outer and inner conductor of the air dielectric coaxial line. The sample coil inductance (Q=200, 200 nH, yielding Z = (3.5 + j 700) Ω) is transformed by the short (~1") section of line to be approximately (3.5 – j 700) Ω at the capacitor/stub junction. (Attenuation along this short section is ignored.) Assuming this capacitive impedance needs to be tuned in parallel by the stub, l_2 must be ~16.8 cm, slightly less than λ/4 at the ^{1}H frequency, producing an impedance of ~(2.0 + j 500) Ω. To first approximation, energy is distributed between the stub and transformed coil impedance according to:

$$\eta_{parallel} = \frac{P_1}{P_1 + P_2} = \frac{1}{1 + \frac{Q_1|Z_1|}{Q_2|Z_2|}} \cong \frac{1}{1 + \frac{200 \cdot 700}{250 \cdot 500}} = 0.47 \qquad (68)$$

That is, 47% of the power is delivered to the coil. Although the overall efficiency is comparable to the Doty circuit, in practice the Chemagnetics circuit permits substantially higher sample coil inductances to be used without greatly sacrificing efficiency. We assumed a sample

coil inductance here of 200 nH, producing a high reactive impedance (~700) at the coil. This could be further increased without greatly compromising the circuit efficiency. The larger number of turns consistent with this permissible coil inductance provides improved radial homogeneity relative to lower inductance coils (assuming constant wire diameter).

In addition to efficiency and homogeneity improvements, this circuit is noted to perform well with high ^{1}H power, because the voltage maximum (anti-node) in the ^{1}H circuit is within the transmission line stub. The tuning capacitor need only cancel the reactive component of the impedance generate by the transformed coil and stub impedances in parallel, which is ~1.8 kΩ here and can be reduced by increasing the ratio of l_1 to l_2. This results in essentially identical efficiencies, with decreasing tuning voltages, as the location of the matching capacitor is moved further down from the coil. This further enhances the performance at high power on the ^{1}H circuit. In practice the details of stub line characteristic impedance and matching capacitor location may be optimized for frequency, but the general result is unchanged; in all cases the efficiency is higher, and the voltage across the matching capacitor is lower, than in the Doty circuit under similar assumptions.

The Chemagnetics circuit X channel performance is now considered in double resonance mode. We assume ^{13}C operation at 100 MHz. Because the matching capacitor in the ^{1}H circuit appears to be a very high impedance to ^{13}C, the entire line on the ^{1}H side can be modeled as $\lambda/4$ at the ^{1}H frequency, or $\lambda/16$ at ^{13}C. With line loss of 0.002 np/m at 100 MHz, we find an impedance of approximately $0.036 + j\,34$ for the stub. The effective Q is therefore ~1,000, equivalent to the high Q limit of the reduced Doty X channel circuit shown in Table 2-4, where the ratio of Q's is ~10, and the ratio of inductances L_x:L_b is ~4. therefore X channel efficiency in the double resonance configuration is ~97% . As with the Doty circuit, the X channel efficiency would improve with higher coil inductance.

A final circuit for double resonance was introduced by McKay, and exploits the low loss characteristics of air dielectric transmission lines in a different manner (Figure 2-17).[35-37] The basic idea is to transform the coil impedance by a long section of low loss air dielectric

transmission line, to a nodal point (*b*) outside of the magnet. We show these impedance transformations in detail (Figure 2-18) because this is our first non-trivial example of such an approach. Assuming a 200 MHz ^{1}H frequency, the length from the magnet sweet spot to the bottom of the magnet is approximately 37.5 cm, which is λ/4 at 200 MHz in air. Therefore transformation from the coil (*a*) to the first voltage node (*b*) is convenient. In practice, the coil impedance (~240 nH, Q = 200 at 200 MHz) is approximately λ/16 from the nearest anti-node (on a 75 Ω line), and the total length (l_1) from *a* to *b* is 5/16 λ (~47 cm). An additional length (~λ/8, ~19 cm) is required to create an inductive impedance at point *c* which is capacitively tuned and matched to 50 Ω. The transformation via the tuning and matching capacitors can be suited to any characteristic impedance at the probe input port (usually 50 Ω), which has no necessary relationship to the impedance of the air dielectric lines.

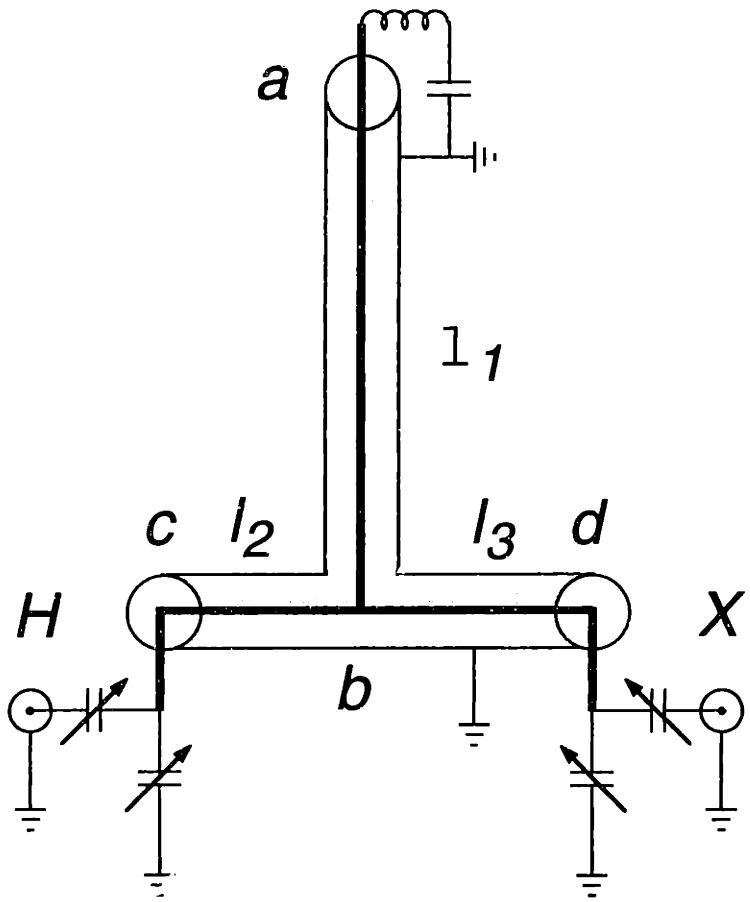

Figure 2-17. McKay Double Resonance Circuit

On Figure 2-18, the conversion from 75 to 50 Ω line is implied, at the point of tuning and matching. Because the junction point in this circuit (point *b*) occurs at a voltage node, it is unnecessary to consider the low frequency branch at all when computing the efficiency of the ^{1}H circuit. We can safely ignore the effect of the large series capacitance (~65 pF) on the high ^{1}H frequency, and determine the standing wave ratio at point *a* to be 850. The total line length from coil to tuning and matching circuit is ~66 cm, and the line characteristics are assumed to be: 1" OD, 75 Ω, 0.0014 np/m. Thus the ^{1}H efficiency is:

$$\eta_{line} = \frac{1}{1 + S\alpha L} = \frac{1}{1 + 850 \cdot 0.0014 \cdot 0.66} = 0.56 \tag{69}$$

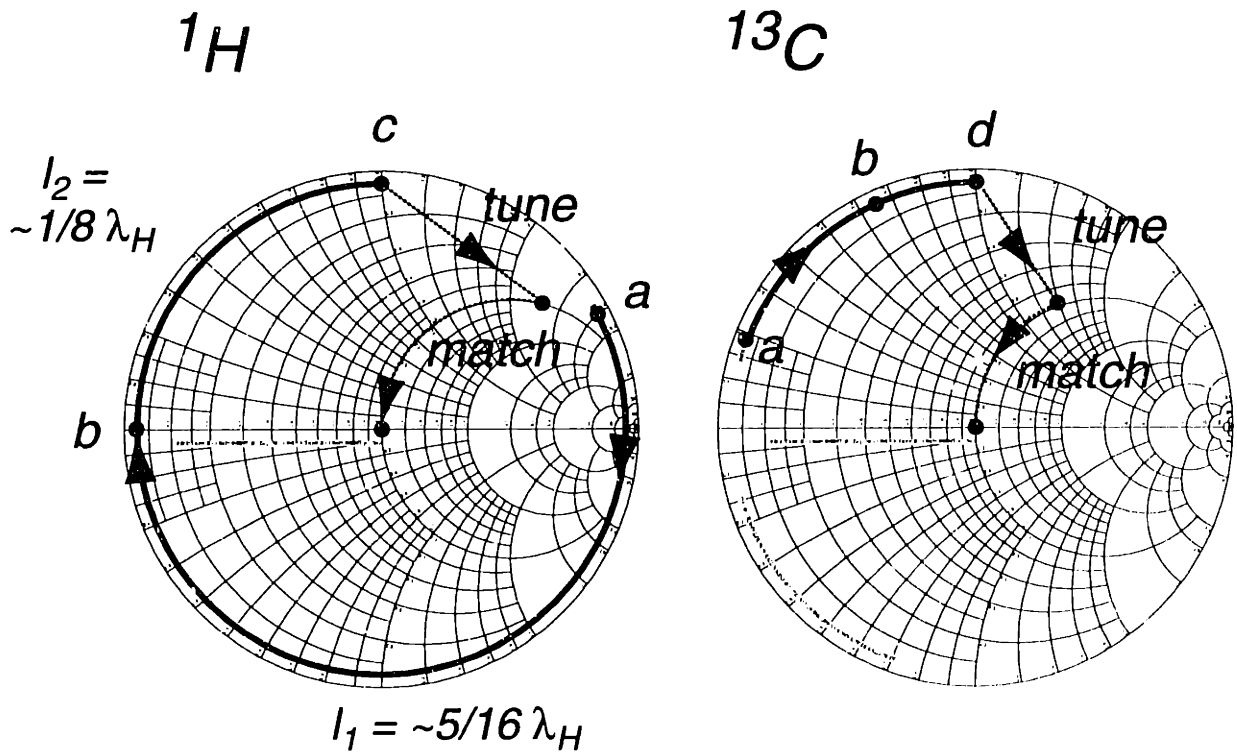

Figure 2-18. Smith chart illustration of standard impedance transformations in double resonance McKay topology probe.

A significant improvement may be derived from using larger diameter transmission line even at this relatively low frequency; 2" outer conductor would yield 72%, rather than 56%. By varying l_2, the tuning circuit voltages can be optimized according to desired power-handling specifications. For convenience (but slightly lower efficiency) the segment l_2 may be replaced with a high Q, low inductance lead. A 200 MHz circuit based on this approach has been demonstrated to achieve long decoupling bursts of 200-300 kHz in a 5 mm coil, and has facilitated numerous high power decoupling studies throughout this thesis.

At 400 MHz, the requisite length from the magnet sweet spot to bottom dictates the choice of l_1 to be an additional $\lambda/2$, and the attenuation coefficient increases with frequency. Otherwise the basic impedance transformation (for ^{1}H) is similar. We must reduce the coil inductance to 120 nH to avoid an increase in standing wave ratio. Assuming the Q remains the same as in the other circuits (200 at 400 MHz), the standing wave ratio again is ~850, and the line efficiency is (assuming a slightly shorter ~50 cm total length from coil to tuning circuit) ~54%. If a higher coil inductance (as in the Chemagnetics example above, 200 nH) is used, the standing wave ratio increases to 1360, and efficiency decreases (43%). In practice, parasitic reactances around the coil may further increase the standing wave ratio, and efficiency may drop further. Increasing the outer conductor line diameter by a factor of two may be feasible in a wide bore magnet, increasing the previous efficiency values from 54% to 70% for the low inductance, 43% to 60% for the high inductance.

The ^{13}C channel efficiency for both 200 and 400 MHz ^{1}H (50 and 100 MHz ^{13}C) can be analyzed with similar principles. At 50 MHz ^{13}C, the tuning circuit voltages are reduced at point *d* by placing a capacitor in series with the coil. This capacitor partially tunes the ^{13}C frequency, reducing the impedance from ~$(0.75 + j\,75)\ \Omega$ to ~$(0.75 + j\,15)\ \Omega$, thereby reducing S from 150 to ~100. From the efficiency standpoint, this partial tuning is not required, because both the standing wave ratio and line attenuation are significantly lower at 50 MHz, and theoretical efficiency exceeds 90% with (96%) or without (94%) the partial tuning. Non-idealities in the lead lengths, finite Q's in the tuning capacitors, etc. contribute to the dominant losses in the

circuit, which are minimal overall. At 100 MHz ^{13}C frequency, the efficiency of line transmission (without partial tuning) is, for the 200 nH coil (Q = 100, S = 225, α = 0.001 np/m, l = 70 cm), 86%; with 1" line, 76%. (At 100 MHz, series resonance of the coil with fixed capacitor is not advised, because the impedance transformation for ^{13}C is somewhat different than shown in Figure 2-18, resulting from the line length now being a significant fraction of $\lambda/4$ at 100 MHz; we will discuss this more thoroughly in the next section, in the context of triple resonance circuits.)

To summarize the results in double resonance circuits, we have shown that at least two topologies (Chemagnetics/McKay) permit >90% efficiencies on the low frequency channel to be achieved. The unnecessary introduction of inductors into tuning circuits (Doty) is extremely costly with respect to overall circuit efficiency. Improved performance in the Cross-Hester-Waugh topology, at least on paper, could readily be provided by slightly larger transmission lines. In all circuits thus far, ^{1}H efficiency is less than ideal and becomes more problematic as frequency increases. In the next section, we will see that as the number of channels increase, so do the benefits of transmission line tuning and matching. Improved tuning strategies within the McKay topology may recover a large fraction of the losses in ^{1}H efficiency.

Triple Resonance Circuits

The primary advantage of transmission line isolation circuits is in probes with three or more channels, as the isolation among low frequency circuits is improved considerably relative to locally tuned circuits. Here we will compare the Chemagnetics triple resonance circuit with the McKay-style transmission line circuit.

Analysis of the ^{1}H portion of the Chemagnetics is unchanged relative to double resonance, because the same high value capacitances in the X and Y circuits provide a convenient, low impedance path to ground on the X/Y side of the sample coil. Incorporation of a third channel, however, requires in addition to the additional tuning and matching capacitors, a fixed capacitor

in series with the coil and a parallel resonant trap circuit (Figure 2-19). The junction *a* between the two low frequencies X and Y presents a significant potential for power loss.

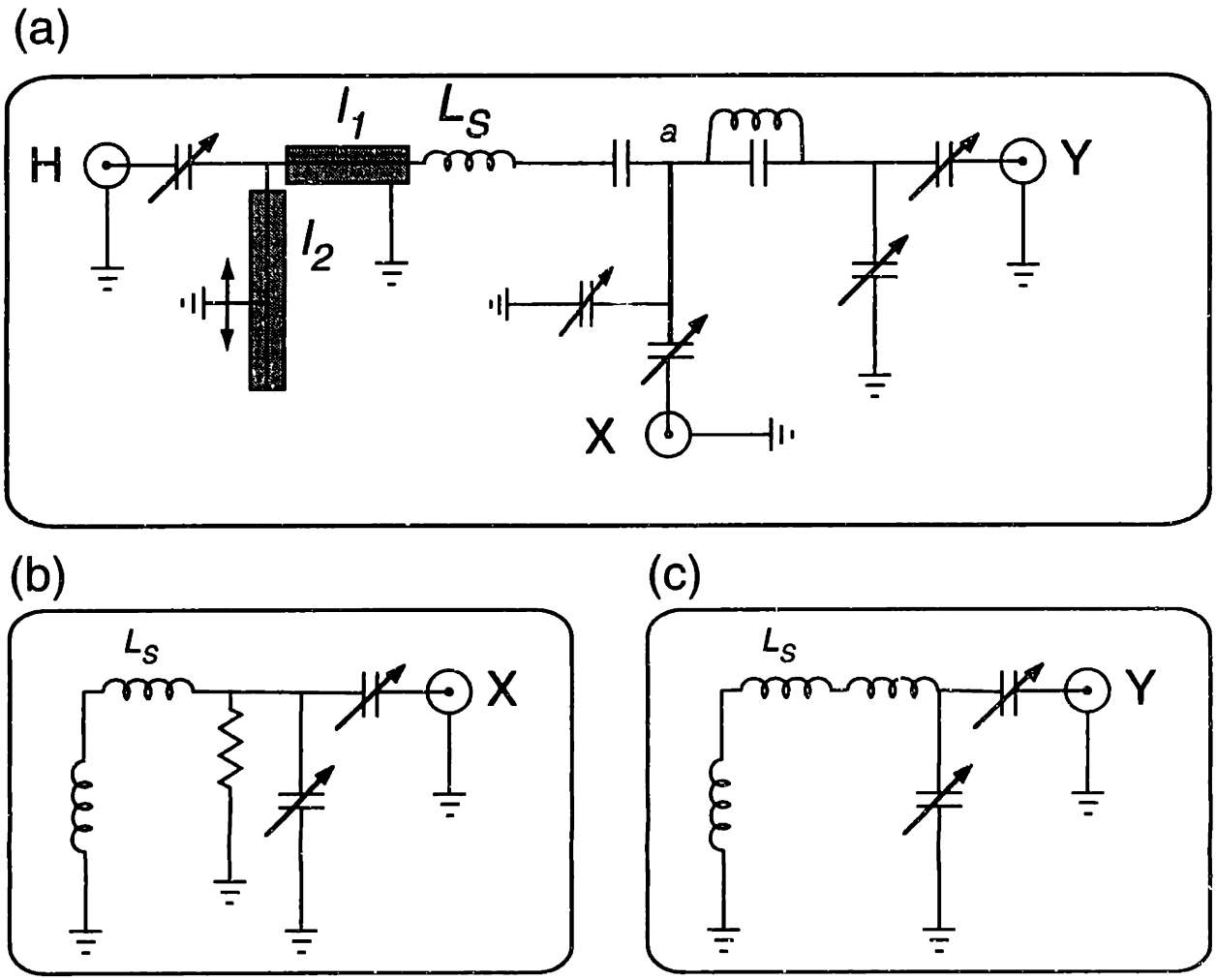

Figure 2-19. Chemagnetics Triple Resonance Circuit

The X channel (the higher of the two low frequencies; in this case we assume ^{13}C at 100 MHz) must be blocked from entry into the Y channel by a high impedance trap circuit. At 100 MHz, the sample coil Q is 100, with inductance 200 nH (i.e., (1.25 + j 125) Ω). The lines l_1 and l_2, as above, together represent a λ/16 length (at 100 MHz) to ground, providing an effective impedance of (0.036 + j 34.4) Ω on the 83 Ω line. So at the junction *a*, the impedance in the direction of the coil is ~1.3 + j 160 (Q=~125). If we assume a trap coil Q of 200 (i.e., twice the

sample coil), with the same 200 nH inductance as the coil, resonated with the appropriate capacitance (in this case, ~12-13 pF), the effective parallel resistance of this trap is theoretically well approximated by Q x X = 200 * 125 = 25 kΩ. Under these conditions, the efficiency of power delivery to the coil at junction *a* is 56%. Thus the overall efficiency of the ^{13}C channel is slightly over 50%, and the majority of losses are due to the trap circuit. In practice, in order to decrease heating and subsequent detuning in this trap circuit, the trap resonance frequency may be a few MHz higher than the ^{13}C frequency, so the trap impedance would appear inductive and energy would be stored primarily as magnetic, not electric, field in the trap circuit. Although power dissipation in the trap will always be dominated by the lower Q inductor, storing the bulk of energy in the magnetic field further reduces the possibility of heating and detuning of the trap capacitor. This is in practice the strategy employed in the Chemagnetics triple resonance design, and results in essentially identical overall efficiency in the circuit as for the exact frequency match trap circuit. The deviation from exact frequency match is limited by concerns for X-Y isolation.

Here we have implicitly ignored the effect of the series capacitor on the X (^{13}C) channel, because the value of this capacitor is chosen to approximately series resonate the Y channel frequency. Assuming ^{15}N, at 40 MHz, we must calculate the coil and stub impedance to determine the appropriate value for the series capacitor. The coil Q is again assumed to be proportional to the $\sqrt{f}$, so here it is ~63, with a total impedance of $0.8 + j\,50\ \Omega$. The stub has α = 0.0013 np/m at 40 MHz, and an electrical phase of $\pi/20$, resulting in $0.02 + j\,13\ \Omega$. Therefore power delivery to the coil is 97.5% efficient. To cancel the reactive component of the total load impedance prior to junction *a*, a capacitance of ~63 pF must be used. Assuming the circuit is series resonant according to this capacitance, the net impedance at junction *a* is ~0.82 Ω. Clearly concern for dissipation into the X circuit is minimal, as the relatively small capacitances required to tune and match ^{13}C appear to be at least 50-100 times larger in impedance magnitude than 0.82 Ω. Now the ^{15}N frequency sees, to first order, only the inductance of the ^{13}C frequency trap,

which is at 40 MHz ~0.4 + j 50 Ω, resulting in a loss of ~33%. Therefore total ^{15}N circuit efficiency is 65% (67% x 97.5%).

We see that both ^{15}N and ^{13}C efficiency (65% and 50%) suffer due to the triple resonance configuration. This is generally the case for the middle frequency in most triple resonance circuits. We note that the 63 pF capacitor would reduce the reactance of the ^{13}C impedance at junction *a* by ~25 Ω, and therefore improve efficiency slightly relative to the number quoted above (say, from ~50% to about 60%). If a lower value capacitance is used (~30-40 pF), ^{13}C efficiency at junction *a* may be improved further (to ~70%) but at significant cost to the ^{15}N isolation and efficiency.

The final circuit to be analyzed in this section will be the triple resonance configuration of McKay (Figure 2-20). This circuit is essentially identical to the previous McKay circuit shown, with the exception of an additional junction point *d* and line length l_5 for the ^{15}N channel.

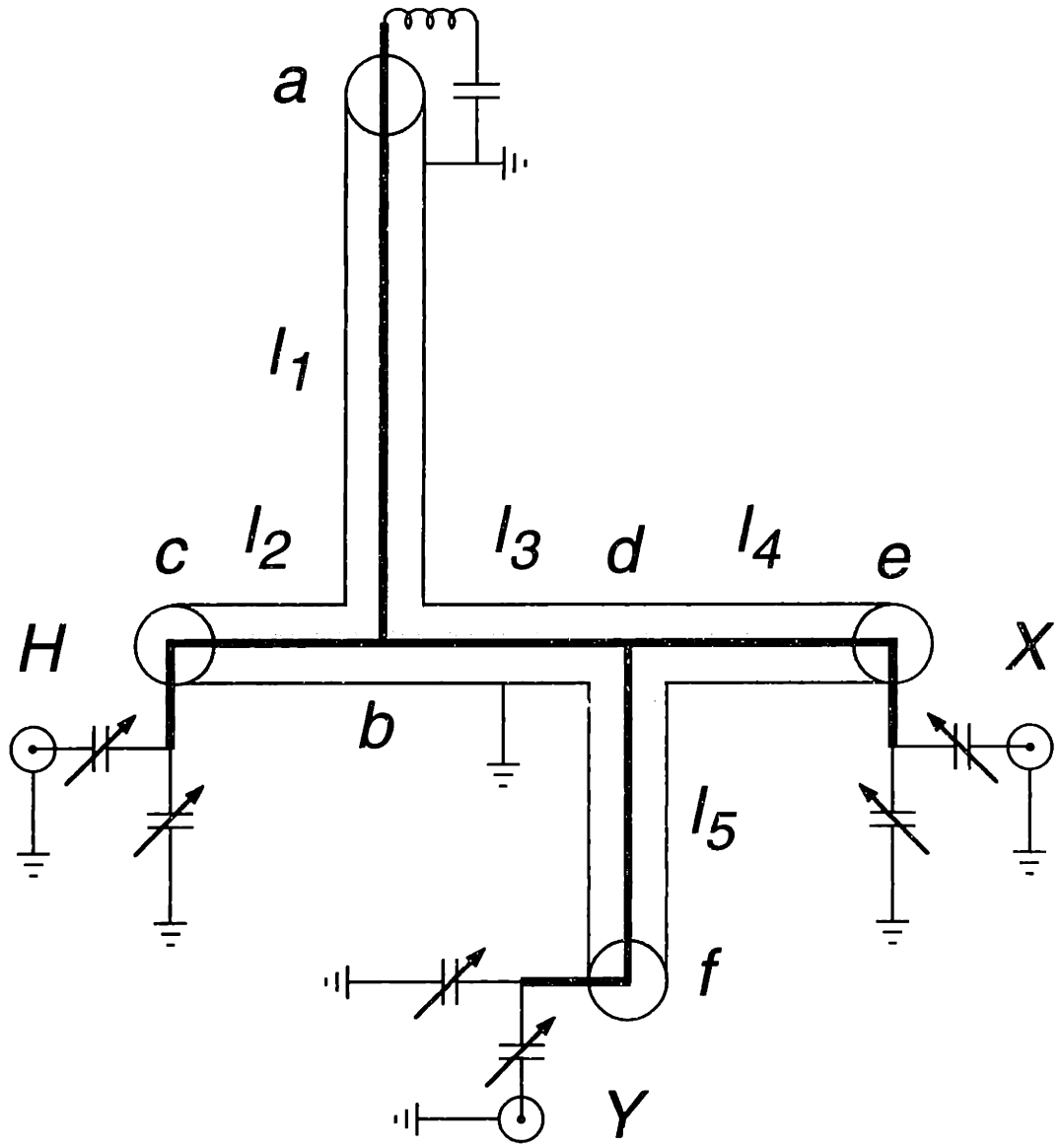

Figure 2-20. McKay Triple Resonance Transmission Line Circuit

To analyze this circuit, first we consider the impedance transformations, as shown in Figure 2-21. The ^{1}H circuit is identical to the McKay double resonance circuit, with the exception of the additional $\lambda/2$ total line length. (Here we again assume 400 MHz ^{1}H frequency.) The ~19 cm $\lambda/4$ length implies that the first voltage node, ~22-23 cm down from the coil, will be within the magnet bore. The second node, a total of 13/16 λ = ~61 cm from the coil, is outside of the magnet and therefore used for the ^{1}H tuning circuit junction. (In practice, small amounts of dielectric within the line shift the node position up by 3-5 cm.) The circuit tuning and matching

is identical to the previous circuit, and efficiency of power delivery to the 200 nH coil with 1" or 2" outer conductor line is 43% or 60%, respectively.

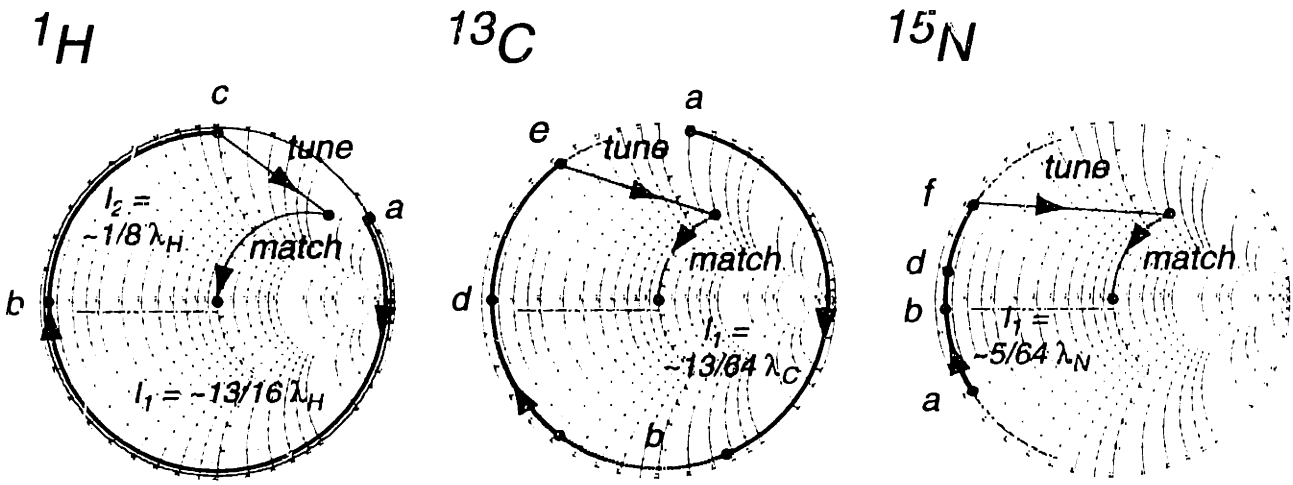

Figure 2-21. Impedance Transformations for McKay Triple Resonance Circuit.

In the triple resonance circuit, the choice of capacitance in series with the coil is dictated by the lowest frequency. This capacitance is not essential in this circuit, but helps to create a convenient, low voltage at point f, and reduce dissipation into the ^{1}H and ^{13}C channels by positioning the ^{15}N voltage node between points *b* and *d*. The capacitance should not be so small that the ^{15}N VSWR is raised; this is true if the reactance of the series capacitor is at most twice the reactance of the coil, in this case (200 nH, 50 Ω inductive at 40 MHz) ~80 pF. Slightly lower capacitances compromise ^{15}N efficiency, and the higher stored voltage may cause detuning and/or arcing at the series capacitor.

With a capacitor chosen, the analysis of the low frequency circuits is straightforward. The ^{13}C coil reactance is partially cancelled by the capacitor, resulting in a 20% reduction of VSWR (from 225 to 180). The ^{13}C channel impedance passes through an anti-node prior to point *b*, at which position the parallel capacitance of the ^{1}H tuning circuit is placed in parallel with the coil impedance. To first order the shunt impedance can be modeled by the transformed reactance of the ^{1}H capacitors, or simply as an open circuit line of length l_2. Adding l_2 to the total

transmission path approximates (to within ~1%) the efficiency of ^{13}C power transfer to the coil. The length l_3 transforms ^{13}C from a small capacitive reactance to a voltage node at position d. It is not essential that this is an exact node (isolation can be improved with external filters without loss of efficiency, provided the probe provides >20 dB), but here we assume so. The length l_4 (~λ/12 at ^{13}C) transforms the ^{13}C node impedance to a small inductance so that tuning and match can be performed at low voltage. The entire current path of the ^{13}C circuit consists of segments l_1 through l_4, with a total length of ~90 cm. The VSWR along this line is 180, and attenuation 0.001 np/m for the 2" line, resulting in overall efficiency of 86%. (This is identical to the double resonance circuit analyzed above without series capacitor, because the reduction in VSWR coincidentally compensates for the increased effective line length.)

The ^{15}N channel has a direct path to the coil, because at all junction points the impedance is near zero. Therefore computing the length (~90 cm), attenuation (0.0006 np/m for 2" line), and VSWR (~135), we find a total efficiency of 93%. Reduction of line diameter to 1" would reduce efficiency to 87%.

Conclusions

Table 2-5 reviews the efficiency of most circuit models presented in this Chapter. In comparison to the locally tuned, single resonance coil, which is assumed to be perfectly tuned and matched, we find that ^{1}H channel efficiency varies considerably among the double resonance designs, and in all cases is relatively poor compared to locally tuned, single resonance. This is not a fundamental problem in cases where ^{13}C or ^{15}N are observed, provided the ^{1}H channel can withstand sufficiently high input power (~200-500 Watts) to generate the required B_1 fields for long pulses.

Table 2-5. Summary of Modeled Circuit Efficiencies.[a]

Circuit Type and Configuration	^{1}H	^{13}C	^{15}N[b]
Single resonance ^{1}H	100%	(100%)	(100%)
Cross-Hester-Waugh, 1/4" coaxial line[b]	35%	62%	>62%
Cross-Hester-Waugh, 1/2" coaxial line[b]	45%	75%	>75%
Doty, $L_s / L_b = 2$, $Q_b / Q_s = 2$	43%	75%	75%
Chemagnetics, 1/2" coaxial line, double res.	47%	97%	97%
McKay, 1" outer conductor, high inductance	43%	76%	>90%
McKay, 2" outer conductor, high inductance	60%	86%	>95%
Chemagnetics, 1/2" coaxial line, triple res.	47%	50%	65%
McKay, 1" OC, high inductance, triple res.	43%	76%	87%
McKay, 2" OC, high inductance, triple res.	60%	86%	93%

[a]All circuits modeled at 400 MHz ^{1}H frequency. [b]In double resonance configuration, X channel could be returned to the ^{15}N frequency, perhaps requiring a change of component, but resulting in comparable or higher efficiency than ^{13}C. [c]Assumes proper partial tuning of ^{1}H circuit.

A more fundamental concern for ^{13}C and ^{15}N observe are the efficiencies of those low frequency channels. Low frequency efficiency varies by significant margins among the designs, but in all cases is above 60% in double resonance mode. Analysis has been performed assuming ^{13}C in the double resonance configuration; a lower frequency X channel would be expected to perform with superior efficiency (although we note that sample coil Q at the lowest frequency is non-ideal because Q is usually optimized for ^{1}H). In the triple resonance circuits, ^{13}C and ^{15}N performance is degraded significantly in the Chemagnetics design as modeled here. (Doty triple resonance designs were not considered in detail, because of the inferior performance in double resonance mode and the unnecessary complexity of the circuits.) For triple resonance, clearly the McKay topology presents substantial improvements relative to the locally tuned probes, because no inductors other than the sample coil are present in the circuit, and low loss transmission line is used. The additional advantages of robust performance, high duty cycle operation, and compatibility with very low temperatures make the McKay topology the circuit of choice for multiple resonance experiments. The one shortcoming is the declining ^{1}H performance at high frequency.

References

(1) Doty, F. D.; Connick, T. J.; Ni, X. Z.; Clingan, M. N. "Noise in high-power, high-rrequency double-tuned Probes," *J. Magn. Reson.* **1988**, *77*, 536-549.

(2) Doty, F. D. "Probe design and construction," In *Encyclopedia of Magnetic Resonance* **1996**; 3753-3761.

(3) Doty, F. D. "Solid state probe design," In *Encyclopedia of Magnetic Resonance* **1996**; 4475-4485.

(4) Gerstein, B. C.; Dybowski, C. R. *Transient Techniques in NMR of Solids*; Academic Press: Orlando, **1985**.

(5) Fukushima, K.; Roder, S. B. W. *Experimental Pulse NMR, a Nuts and Bolts Approach*; Addison-Wesley: Reading, MA, **1981**.

(6) Traficante, D. D. "Impedance: what it is, and why it must be matched," *Concepts Magn. Reson.* **1989**, *1*, 73.

(7) Traficante, D. D. "Introduction to transmission lines," *Concepts Magn. Reson.* **1989**, *5*, 57.

(8) Senturia, S. D.; Wedlock, B. D. *Electronic circuits and applications*; Krieger Publishing Company: Malabar, FL, **1993**, pp 623.

(9) Rhea, R. W. *HF Filter Design and Computer Simulation*; McGraw-Hill, Inc.: New York, **1995**, pp 432.

(10) Hoult, D. I.; Richards, R. E. "The signal-to-noise ratio of the nuclear magnetic resonance experiment," *J. Magn. Reson.* **1976**, *24*, 71-85.

(11) Wheeler, H. A. "Simple inductance formulas for radio coils," *Proc. IRE* **1928**, *Oct.*, 1398.

(12) Medhurst, R. G. "High frequency resistance and self-capacitance of single-layer solenoids," *Wireless Eng.* **1947**, *Feb-Mar*, 35, 80.

(13) Grover, F. W. *Inductance Calculations: Working Formulas and Tables*; D. Van Nostrand Company, Inc.: New York, **1946**, pp 286.

(14) Terman, F. E. *Radio Engineer's Handbook*; McGraw-Hill: New York, **1943**.

(15) Idziak, S.; Haeberlen, U. "Design and construction of a high homogeneity RF coil for solid-state multiple-pulse NMR," *J. Magn. Reson.* **1982**, *50*, 281-288.

(16) Gentzler, M.; Reimer, J. A. "High-homogeneity rf coils for solid-state NMR," *NMR Newsletter* **1995**, *437*, 51-53.

(17) Privalov, A. F.; Dvinskikh, S. V.; Vieth, H.-M. "Coil design for large-volume high-B1 homogeneity for solid-state NMR applications," *J. Magn. Reson.* **1996**, *123*, 157-160.

(18) Larsen, F. H.; Daugaard, P.; Jakobsen, H. J.; Nielsen, N. C. "Improving rf field homogeneity in solid-state MAS NMR using a loop-gap resonator," *J. Magn. Reson. A* **1995**, *115*, 283-286.

(19) Froncisz, W.; Hyde, J. S. "The loop-gap resonator: a new microwave lumped element circuit ESR sample structure," *J. Magn. Reson.* **1982**, *47*, 515-521.

(20) Westgard, J. B. *Electrodynamics: a Concise Introduction*; Springer: New York, **1997**.

(21) Chipman, R. A. *Theory and Problems of Transmission Lines*; McGraw-Hill Book Company: New York, **1968**.

(22) Blake, L. V. *Transmission Lines and Waveguides*; John Wiley & Sons, Inc.: New York, **1969**, pp 315.

(23) Gardiol, F. E. *Lossy Transmission Lines*; Artech House: Norwood, MA, **1987**, pp 384.

(24) Grivet, P. *The Physics of Transmission Lines at High and Very High Frequencies*; Academic Press: New York, **1970**; Vol. 1.

(25) Smith, P. H. "Transmission line calculator," *Electronics* **1939**, *12*, 29-31.

(26) Smith, P. H. "An improved transmission line calculator," *Electronics* **1944**, *17*, 130-133, 318-325.

(27) Macalpine, W. W. "Computation of impedance and efficiency of transmission line with high standing-wave ratio," *Electrical Comm.* **1953**, 238-246.

(28) Chingas, G. C. "Overcoupling NMR probes to improve transient response," *J. Magn. Reson.* **1983**, *54*, 153-157.

(29) Stringer, J. A.; Drobny, G. P. "Methods for the analysis and design of a solid state nuclear magnetic resonance probe," *Rev. Sci. Instrum.* **1998**, *69*, 3384-3391.

(30) Cross, V. R.; Hester, R. K.; Waugh, J. S. "Single coil probe with transmission-line tuning for nuclear magnetic double resonance," *Rev. Sci. Instrum.* **1976**, *47*, 1486.

(31) Walton, J. H.; Conradi, M. S. "Probe tuning adjustments: Need they be in the probe?," *J. Magn. Reson.* **1989**, *81*, 623-627.

(32) Rath, A. R. "Efficient remote transmission line tuning," *Magn. Reson. Med.* **1990**, *13*, 370-377.

(33) Rath, A. R., "Efficient remote transmission line probe tuning for NMR apparatus," USA Patent #4,916,398, **1990**.

(34) Doty, F. D.; Inners, R. R.; Ellis, P. D. "A multinuclear double-tuned probe for applications with solids or liquids utilizing lumped tuning elements," *J. Magn. Reson.* **1981**, *43*, 399-416.

(35) McKay, R. A., "Double-tuned single coil probe for nuclear magnetic resonance spectrometer," USA Patent #4,446,431, **1984**.

(36) McKay, R. A. "Probes for special purposes," In *Encyclopedia of Magnetic Resonance* **1996**; 3768-3771.

(37) Schaefer, J.; McKay, R. A., "Multi-tuned single coil transmission line probe for nuclear magnetic resonance spectrometer," USA Patent #5,861,748, **1999**.

Section II: Primary Structure (Assignments)

Chapter 3. Efficient Multi-Spin Homonuclear Double-Quantum Recoupling for Magic-Angle Spinning NMR: ^{13}C-^{13}C Correlation Spectroscopy of Erythromycin A

Note: This chapter is based upon a manuscript that appeared in the Journal of the American Chemical Society, 120:10602-10612 (1998), in collaboration with Mary E. Hatcher, Leonard J. Mueller, Boqin Sun, and Stephen W. Fesik.

Abstract

We introduce a radiofrequency (RF) pulse sequence for efficient homonuclear double-quantum dipolar recoupling under magic-angle-spinning NMR. The sequence is optimized for two-dimensional (2D) double-quantum ^{13}C-^{13}C chemical shift correlation spectroscopy in multiple spin systems, such as the U-^{13}C-labeled antibiotic erythromycin A. Spin systems like this display a wide range of isotropic and anisotropic chemical shifts and therefore require a broadband dipolar recoupling sequence that minimizes the errors arising from the interaction of chemical shifts and RF inhomogeneity. The sequence should also preserve the theoretical efficiency advantage over the powder average provided by the C7 experiment of Levitt and co-workers (Lee, Y.K.; Kurur, N.D.; Helmle, M.; Johannessen, O.G.; Nielsen, N.C.; Levitt, M.H. *Chem. Phys. Lett.* **1995,** *242*, 304-309). We satisfy these criteria by combining the standard C7 ($2\pi_{\phi}$-$2\pi_{\phi+180}$) elements with π-pulse permuted elements (π_{ϕ}-$2\pi_{\phi+180}$-π_{ϕ}, in analogy to the MLEV decoupling scheme), in order to remove error terms over a ±10% range of RF amplitude. The new sequence, which we refer to as CMR7 (*C*ombined *M*LEV-*R*efocusing and C7), yields for two-spin systems broadband double-quantum filtering efficiencies above 70% (near the theoretical maximum of ~73%). For multi-spin systems, the improved polarization transfer efficiency results in greater crosspeak intensities, facilitating assignment of U-^{13}C-labeled molecules in the solid state.

Introduction

In recent years, solid-state NMR has witnessed a rapid development of techniques aimed at measuring anisotropic interactions in the presence of magic-angle spinning (MAS).[1,2] These techniques provide valuable structural information via site-resolved measurements of interatomic distances[3-5] and the relative orientations of dipole vectors[6-11] and/or chemical shift tensors.[12-16] Such interactions are normally averaged effectively by MAS[17,18] in the context of the CP/MAS experiment,[19,20] which combines cross-polarization[21] and high-power ^{1}H decoupling[19,22] to provide chemical shift spectra of high sensitivity and resolution. This spectral dimension provides site resolution but little direct structural information. The latter is usually measured in indirect dimension(s), where radiofrequency (RF) perturbations are applied to recover NMR observables that are correlated with structural parameters.

The behavior of the spin system under RF modulations that interfere with MAS-assisted averaging is customarily described by coherent averaging theory.[23,24] In principle any term in the Hamiltonian with unique spin and/or spatial symmetry can be measured independently of other terms. However, accomplishing this in a manner that is efficient and free of contamination is a continuing challenge, particularly for the class of experiments that recover homonuclear dipole-dipole couplings. For example, the first RF-driven homonuclear recoupling experiments, such as DRAMA[25,26] and RFDR,[27,28] were designed solely with rotor-synchronized $\pi/2$ and π pulses. Even in the ideal pulse limit these sequences depend on chemical shifts, both isotropic and anisotropic, to the detriment of dipolar recoupling efficiency. The spin dynamics responsible for this compromised efficiency may be understood with the fictitious spin-1/2 theory,[29,30] where in the appropriate dipolar subspace[31] the residual chemical shifts are orthogonal to the recovered

dipolar interaction. The exact dipolar evolution is described by spin decoupling theory, whereby large residual chemical shifts quench the dipolar interactions.[32]

The dependence on chemical shifts is to some extent inherent in the laboratory frame spin dynamics, and several sequences have been proposed to avoid this shortcoming by using a continuous (windowless) RF irradiation field that is large compared to the chemical shifts. Under these conditions chemical shift spin terms are, to first approximation, averaged to zero. This approach was first applied to dipolar recoupling with the MELODRAMA sequence,[33] which generates a pure double-quantum (DQ) dipolar Hamiltonian without interference from chemical shifts terms. Similarly the DRAWS sequence[34-36] effectively averages chemical shifts, albeit at the cost of introducing a zero-quantum (ZQ) component which is undesirable for some applications.

An additional theoretical consideration for sequences of this type, demonstrated by Levitt and co-workers,[37,38] shows that individual spatial components can be selected so that recoupling occurs independent of rotor phase (specifically the azimuthal angle relating the principal axis frame of the dipolar interaction to the rotor-fixed frame). Over the powder average, elimination of the rotor-phase dependence increases the theoretical double-quantum filtration (DQF) efficiency from ~52% (with MELODRAMA[33] or DRAWS[34]) to ~73% (with HORROR[37] or C7[38]). This increased efficiency is particularly useful for applications such as correlation spectroscopy and DQF of strongly coupled spin pairs, where the sensitivity of the experiment depends upon the mixing efficiency.

However, the often-unavoidable presence of RF errors, especially inhomogeneity, complicates this picture. Although some recent probe designs[39] based on loop-gap resonators[40] can provide extremely high RF homogeneity over the full sample volume (<1-2% full width at half maximum

(FWHM) in the nutation[41] dimension), most solid-state NMR probes use solenoid coil geometries that have distributions of RF field amplitude of 5-10% over the sample volume. In addition, amplifier and/or probe instabilities can contribute to short- or long-term fluctuations in RF amplitude. Therefore in the development of recoupling sequences, it is necessary to consider explicitly the effects that RF inhomogeneity has upon the recoupling dynamics; these effects are usually not explained fully by basic theoretical treatments.

For example, it has been observed experimentally that the C7 sequence works most effectively when the RF carrier is centered between the two signals of interest,[7] where the chemical shift in the DQ subspace[29,30] vanishes. When this condition is not satisfied, a residual offset appears as a cross-term between the RF inhomogeneity and chemical shift (described below), producing an effective quenching field orthogonal to the recoupled interaction. This results in spin dynamics analogous to rotational resonance[12,42,43] and frequency-selective heteronuclear dipolar recoupling (FDR[44,45]). In such selective sequences, the quenching field may be exploited to eliminate the effects of strong couplings in order to measure weaker interactions in a multi-spin system.[43-48] However, when the goal is to recouple many spins with high efficiency for correlation spectroscopy or DQF, it is desirable to eliminate the effects of chemical shift offset entirely. This goal has motivated the development of an improved version of the MELODRAMA sequence which uses phase-compensated π pulses superimposed upon the basic sequence to provide correction for RF errors.[49] The result is comparable to the DRAWS sequence,[34-36] with the additional advantage of maintaining a pure DQ Hamiltonian.

Despite the experimental reliability of these two sequences, each promises only ~52% maximum theoretical DQF efficiency. Clearly development of a robust compensation scheme, similar to that for MELODRAMA or DRAWS, would be highly useful for the more efficient C7

sequence. Yet to retain this efficiency advantage, the solution must be not introduce rotor-phase dependence or otherwise disrupt the sequence symmetry. In the following sections, we will demonstrate theoretically how RF field inhomogeneity directly affects the averaging of chemical shift terms in the C7 sequence and propose a method for minimizing the residual shifts on a short timescale. The compensation scheme places minimal restrictions on the sampling interval, while effectively scaling cross-terms between RF errors and chemical shift offsets to provide broadband performance under typical experimental conditions. Because the compensation involves implementation of MLEV-type composite rotations and supercycles[50] to refocus error terms, we refer to the new sequence as *C*ombined *M*LEV *R*efocusing and C*7* (CMR7). The utility of this broadband sequence is demonstrated in a 2D correlation spectrum of the U-^{13}C-labeled antibiotic erythromycin A.

Experimental Methods

NMR Experiments

NMR spectra were acquired on custom-designed spectrometers operating at ^{1}H frequencies of 397.8 MHz (9.4 T), 317.4 MHz (7.4 T), or 198.3 MHz (4.7 T) with custom-designed triple- or quadruple-resonance MAS probes implementing transmission line isolation and tuning circuits.[51-53] At the high frequency, standing wave losses are minimized by periodically altering the characteristic impedance along the main transmission line. This approach allows the final tuning and matching to be removed from the magnet bore, leaving space for high-voltage fixed capacitors (American Technical Ceramics, Huntington Station, NY) and high-voltage variable capacitors (Polyflon Company, Norwalk, CT or Jennings Technology Company, San Jose, CA),

while maintaining optimal overall circuit efficiency. Solenoid sample coils wrapped from teflon-coated wire were mounted in spinner modules (4 mm for the 397.8 and 317.4 MHz probes, 5 mm for the 198.3 MHz probe) from Chemagnetics/Otsuka Electronics USA (Fort Collins, CO). Unless indicated otherwise, rotors were packed with enough sample to fill the entire usable volume as specified by the manufacturer. This resulted in RF inhomogeneity of 5-10% FWHM. Recycle delays were 2-4 s.

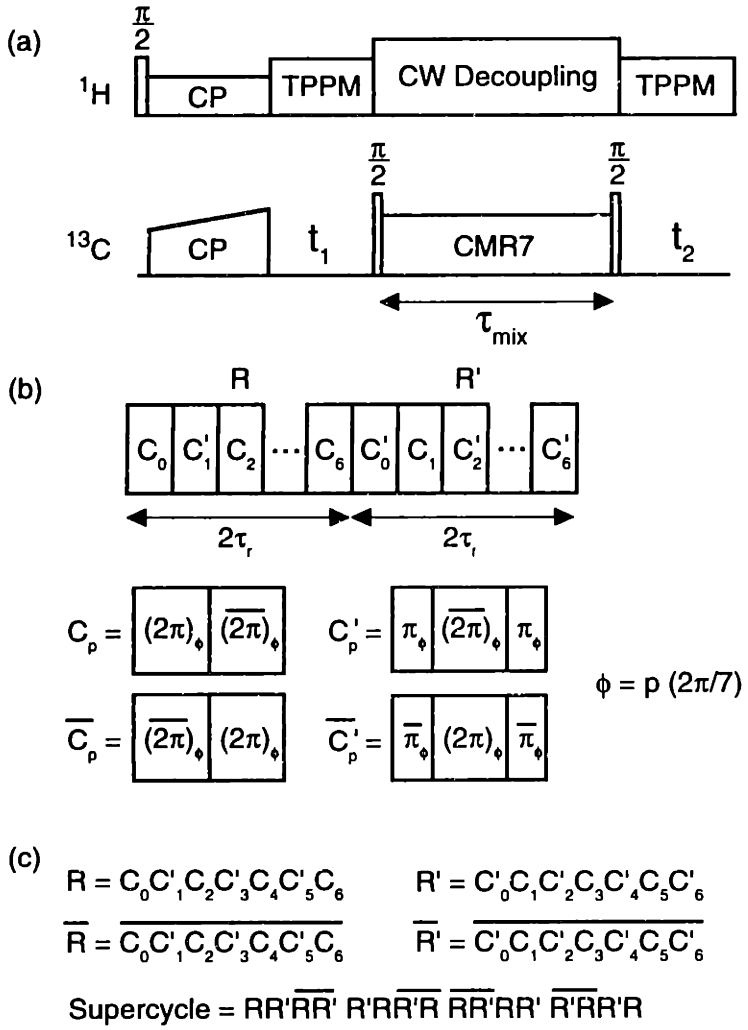

Figure 3-1. CMR7 RF pulse sequence.

(a) General sequence for double quantum dipolar recoupling in the framework of CP-MAS spectroscopy. Following ramp CP and an optional period of chemical shift evolution, sum polarization is stored longitudinally and the mixing sequence initiated. After mixing, observable coherence is read out with a $\pi/2$ pulse. During the evolution and acquisition periods, TPPM ^{1}H decoupling[22] is implemented; during the mixing period, high power resonant CW decoupling is used. (b) Basic CMR7 mixing sequence, constructed from C_p units of various symmetry. Notation is consistent with Lee et al.[38] The complete sequence is composed in a manner that most rapidly refocuses large, isotropic error terms. (c) Full supercycling of the compensation scheme for achieving quantitative long-time results. Phase inversions and cyclic permutations of the basic CMR7 sequence help to maximize coherence of the appropriate order. References to C7 and CMR7 indicate the N=2, n=7 sequence unless explicitly stated otherwise.

All experiments employed some version of the pulse sequences presented in Figure 1. Ramped CP[54] from ^{1}H to ^{13}C created the initial transverse polarization. In the two-dimensional (2D) version of the sequence, a period of evolution under TPPM decoupling[22] is used to encode chemical shifts in the indirect dimension. In the one-dimensional (1D) experiment, transverse magnetization is immediately stored longitudinally with a $\pi/2$ pulse. In either case, mixing is performed according to the phase modulation scheme presented in Figure 1, where compensation for residual RF errors is accomplished by alternation of C_p and C_p' sub-cycles. The basic C_p elements are combined to provide a complete CMR7 cycle over four rotor periods. Improved long-time behavior (not discussed in detail here) is obtained by expanding the basic unit with phase inversions and cyclic permutations to create the supercycle as indicated in Figure 1. For the 2D experiment, the total mixing time was chosen to be a multiple of $4\tau_r$, so that residual errors between the CSA and RF inhomogeneity would be refocused most effectively. Spectral intensities in all cases are computed by integration of the lineshape, and include correction for natural abundance background.

Phase cycles for the DQF experiments followed standard procedures for selection of DQ coherence,[55] in addition to spin temperature alternation of the ^{1}H reservoir. The 2D chemical shift correlation experiment incorporated phase cycles for pure phase detection in both dimensions developed by Ruben and co-workers.[56]

^{13}C-Labeled Samples

All U-^{13}C,^{15}N-labeled amino acids (Cambridge Isotope Laboratories, Andover, MA) were, where indicated, diluted in natural abundance material and recrystallized by slow evaporation from aqueous solution. U-^{13}C-oxalic acid (also from CIL) was dissolved with one equivalent NH_4OH in aqueous solution and recrystallized by slow evaporation.

U-^{13}C-erythromycin A was prepared by fermentation of *Saccharopolyspora erythraea* strain ER598 in a salt medium containing 1% D-glucose-U-$^{13}C_6$ as the sole source of carbon. Two liters of the medium were dispensed at 50 mL in 500 mL Erlenmeyer flasks. Vegetative inoculum grown in a rich organic medium was washed and used at 1%. The flasks were incubated at 32 °C on a rotary shaker operating at 225 rpm for 6 days. U-^{13}C-erythromycin was purified from 1500 mL of beer from two separate shake flask experiments by extracting twice with equal volumes of CH_2Cl_2 at pH 9. The extracts were pooled, dried, and digested into 2.5 mL of a solvent system consisting of n-hexane:ethyl acetate:aqueous potassium phosphate (0.02 M, pH 7) (3:7:5). The mixture was subject to countercurrent chromatography in an Ito multilayer Planet Coil centrifuge, with the upper phase mobile. Fractions were monitored based on bioactivity against *S. aureus* and from ^1H NMR spectra. U-13C-erythromycin was crystallized using ethyl acetate and n-hexane to yield 39 mg with >98% labeling efficiency based on an analysis of the C-1' resonance.

Background

Homonuclear recoupling sequences are readily described within the formalism of average Hamiltonian theory (AHT).[23,24] For simplicity we assume that the abundant ^{1}H spins are removed from the dynamics completely by high-power decoupling. (This assumption is not always justified, but we will demonstrate that such a limit can be achieved experimentally in the spinning speed regimes used here.) The rotating-frame Hamiltonian therefore consists of terms corresponding to the low-γ spin chemical shifts, dipole-dipole couplings, and an applied RF field:[57]

$$H = H_{int} + H_{rf}, \tag{1a}$$

$$H_{int} = \omega_j(t)S_{jz} + \omega_k(t)S_{kz} + \omega_{D_{jk}}(t)(3S_{jz}S_{kz} - \boldsymbol{S}_j \cdot \boldsymbol{S}_k) \tag{1b}$$

$$H_{rf} = \omega_1(t)\left[\left(S_{jx} + S_{kx}\right)\cos\varphi(t) + \left(S_{jy} + S_{ky}\right)\sin\varphi(t)\right] \tag{1c}$$

where the time-dependence of the coefficients of (1b) are expressed as

$$\omega_j(t) = \sum_{m=-2}^{2} \omega_0 \delta_j^{(m)} e^{im\omega_r t}, \tag{2}$$

and

$$\omega_{D_{jk}}(t) = \sum_{m=-2}^{2} \omega_{D_{jk}}^{(m)} e^{im\omega_r t}. \tag{3}$$

Complete expressions for the chemical shift anisotropy $\omega_0 \delta_j^m$ may be found in Ref. 38, although the coefficients are not important in the following, where averaging is designed to eliminate their effects. The time-dependent forms for the dipole-dipole coupling, however, will be used further and therefore are defined (assuming MAS[17,18]) as

$$\omega_{D_{jk}}^{(0)} = 0, \tag{4a}$$

$$\omega_{D_{jk}}^{(\pm 1)} = -\frac{\omega_{D_{jk}}}{2\sqrt{2}} \sin(2\beta_{PR}) e^{\pm i\gamma_{PR}}, \tag{4b}$$

$$\omega_{D_{jk}}^{(\pm 2)} = \frac{\omega_{D_{jk}}}{4} \sin^2(\beta_{PR}) e^{\pm 2i\gamma_{PR}}, \tag{4c}$$

where the angles β_{PR} and γ_{PR} describe the transformation from the principal axis system of the dipole vector to the rotor-fixed coordinate system.[58] The dipolar coupling constant in angular units is

$$\omega_{D_{jk}} = -\frac{\mu_0}{4\pi} \frac{\gamma_j \gamma_k \hbar}{r_{jk}^3} \tag{5}$$

When the time-dependence of H_{rf} involves non-orthogonal RF phases, the Cartesian basis may be cumbersome for purposes of calculating the interaction frame Hamiltonian. Therefore in the following we use irreducible spherical tensor operators in the convention of Spiess.[58] This notation permits both the spatial and spin parts of the Hamiltonian to be expressed in similar forms and in particular simplifies the calculation of spin terms that arise upon general (i.e., non-orthogonal) phase shifts of the RF irradiation. Thus, the phases of all terms of the Hamiltonian may be described together in a convenient form. In this basis, single spin operators are expressed as

$$T_{10}^{j} = S_{jz}, \tag{6a}$$

and the two-spin operators as

$$T_{20}^{jk} = \frac{1}{\sqrt{6}}\left(3S_{jz}S_{kz} - \boldsymbol{S}_j \cdot \boldsymbol{S}_k\right), \tag{6b}$$

$$T_{2\pm2}^{jk} = \frac{1}{2}S_j^{\pm}S_k^{\pm}. \tag{6c}$$

Substituting these terms into Eq. 1 and following the treatment of Lee et al.[38] we examine the Hamiltonian in the interaction frame of the RF field

$$\tilde{H}(t) = U_{rf}^{-1}H_{int}U_{rf} = \sum_{Q}\sum_{\lambda\mu lm}\tilde{\omega}_{\lambda\mu lm}^{Q}\left(t - t_p^0\right)\exp\left[i2\pi(Nm - \mu)p/n\right]T_{\lambda\mu}^{Q}, \tag{7}$$

defined over the time of the pth sub-cycle, $t_p^0 \le t < t_{p+1}^0$. The variable Q refers to the type of interaction, l the rank with respect to spatial modulation, m the spatial rotational component ($m = \{-l, -l+1, ...l\}$), λ the rank with respect to spin modulations, and μ the spin rotational component ($\mu = \{-\lambda, -\lambda+1, ...\lambda\}$).

The values of the coefficients

$$\tilde{\omega}_{\lambda\mu lm}^{Q}(\tau) = i^{\mu} d_{\mu 0}^{\lambda}\left(\beta_{rf}(\tau)\right)\tilde{\omega}_{\lambda 0 lm}^{Q} \exp\left[im\omega_r\left(\tau + t^0\right)\right] \tag{8}$$

are given in general by the reduced Wigner functions $d_{\mu 0}^{\lambda}$ [59] and the overall spin rotation angle β_{RF}, which is a function of time, dependent on the sequence being investigated.

For the Cn class of experiments, where n phase-shifted elements are implemented over N rotor periods (e.g., for C7, n = 7 and N = 2), the RF field is chosen to match an appropriate multiple of the spinning speed as defined by

$$\omega_1 = \frac{2n}{N}\omega_r. \tag{9}$$

However, in practice this match is only approximately true across the entire sample volume due to RF inhomogeneity, and some effort must be made to understand the effects of deviation from the ideal value. One approach to analyzing the effect of an inhomogeneous RF field is to partition H_{rf} into a large term $|\omega_1(t)|$, which defines the interaction frame, and a smaller RF inhomogeneity term, $|\Delta\omega_1(t)|$, included in H_{int}. Analysis of the effective Hamiltonian

$$\bar{\tilde{H}} = \bar{\tilde{H}}^{(0)} + \bar{\tilde{H}}^{(1)} + \bar{\tilde{H}}^{(2)} + \ldots, \tag{10}$$

through second order, defined as

$$\bar{\tilde{H}}^{(0)} = \frac{1}{\tau_c}\int_0^{\tau_c} \tilde{H}(t)dt, \tag{11a}$$

$$\bar{\tilde{H}}^{(1)} = \frac{-i}{2\tau_c}\int_0^{\tau_c} dt_1 \int_0^{t_1} \left[\tilde{H}(t_1), \tilde{H}(t_2)\right] dt_2, \tag{11b}$$

$$\bar{\tilde{H}}^{(2)} = \frac{-1}{6\tau_c}\int_0^{\tau_c} dt_1 \int_0^{t_1} dt_2 \int_0^{t_2} dt_3 \left(\left[\tilde{H}(t_1), \left[\tilde{H}(t_2), \tilde{H}(t_3)\right]\right] + \left[\tilde{H}(t_3), \left[\tilde{H}(t_2), \tilde{H}(t_1)\right]\right]\right), \tag{11c}$$

results in error terms which arise in $\bar{\tilde{H}}^{(1)}$ and $\bar{\tilde{H}}^{(2)}$ involving $|\Delta\omega_1(t)|$ and $(\omega_j + \omega_k)$. This is a general approach to calculating the relative magnitude of various higher-order contributions to the total effective Hamiltonian, and has been used to derive another compensated C7 sequence.[60]

In the present context we are primarily concerned with the effect of RF inhomogeneity on the spin terms, so we choose an alternative form of analysis that is well suited for excitations with symmetry such as the elements from which CMR7 is composed. Because each sub-cycle (C_p or C_p') consists of rotations with phases ϕ and $\phi+\pi$,constructed as in Figure 1b, the sequence is periodic over the element (U_{rf}=1), independent of the exact RF amplitude. This allows the average spin terms to be conveniently incorporated into $\bar{\tilde{H}}^{(0)}$ without making any assumptions

about the relative magnitude of the RF inhomogeneity by including explicit dependence on a RF field scaling factor,

$$s = \omega_{1,actual} \Big/ \omega_{1,ideal}. \tag{12}$$

We proceed with direct calculation of the coefficients and find, after algebraic simplification, that each term has the general form

$$\bar{\omega}^{Q}_{\lambda\mu lm} = \Phi(p) c^{Q} k_{\lambda l\mu} \left(a_{\lambda l\mu m} + b_{\lambda l\mu m} \right), \tag{13}$$

where the first factor

$$\Phi(p) = \exp\left[i2\pi (Nm - \mu) p / n \right] \tag{14}$$

is a phase depending on several variables. Incrementing p from one sub-cycle to the next provides a means for selecting desired spin (μ) and spatial (m) components by choice of the pulse sequence parameters N and n. Upon summation of the phases over the complete cycle, we find the function

$$\sum_{p=0}^{n-1} \frac{\Phi(p)}{n} = \begin{cases} 1 & Nm - \mu = n \times \text{integer} \\ 0 & Nm - \mu \neq n \times \text{integer} \end{cases}. \tag{15}$$

The second factor of Eq. 13 does not explicitly depend upon the spin component (μ):

$$c^{jk} = c_0 \omega_{D_{jk}}^{(m)}, \tag{16a}$$

$$c^{j} = c_0 \delta_j^{(m)} \omega_0 \tag{16b}$$

$$c^{jk} = \left[\frac{\exp[iNm\pi/n]}{\pi(Nm - 2\lambda ns)(Nm + 2\lambda ns)} \right] \tag{16c}$$

Table 3-1. Coefficients from AHT calculation ($\bar{\tilde{H}}^{(0)}$) for CMR7.[a]

$\lambda\mu l$	k	a	a'	b	b'
102	1	$Nmn\sin\left(\frac{Nm\pi}{n}\right)$	$Nmn\sin\left(\frac{Nm\pi}{n}\right)$	$-2n^2 s\sin(2\pi s)$	$-4n^2 s\sin(\pi s)\cos\left(\frac{Nm\pi}{2n}\right)$
222	$\sqrt{\frac{3}{2}}\frac{n^2 s}{Nm}$	$-4ns\sin\left(\frac{Nm\pi}{n}\right)$	$-4ns\sin\left(\frac{Nm\pi}{n}\right)$	$Nm\sin(4\pi s)$	$2Nm\sin(2\pi s)\cos\left(\frac{Nm\pi}{2n}\right)$

[a]The general windowless recoupling scheme is defined in Figure 1. The effect of RF inhomogeneity is explicitly included in the variable s, which expresses deviation from the ideal value (s=1). The coefficients a and b refer to the C_p sub-cycles, a' and b' to the C_p' sub-cycles. Note that all functions of the form $k(a+b)$ are even with respect to the s, so phase inversion alone does not remove the residual error. Through this level of AHT, all other spin components vanish according to Eq. 15.

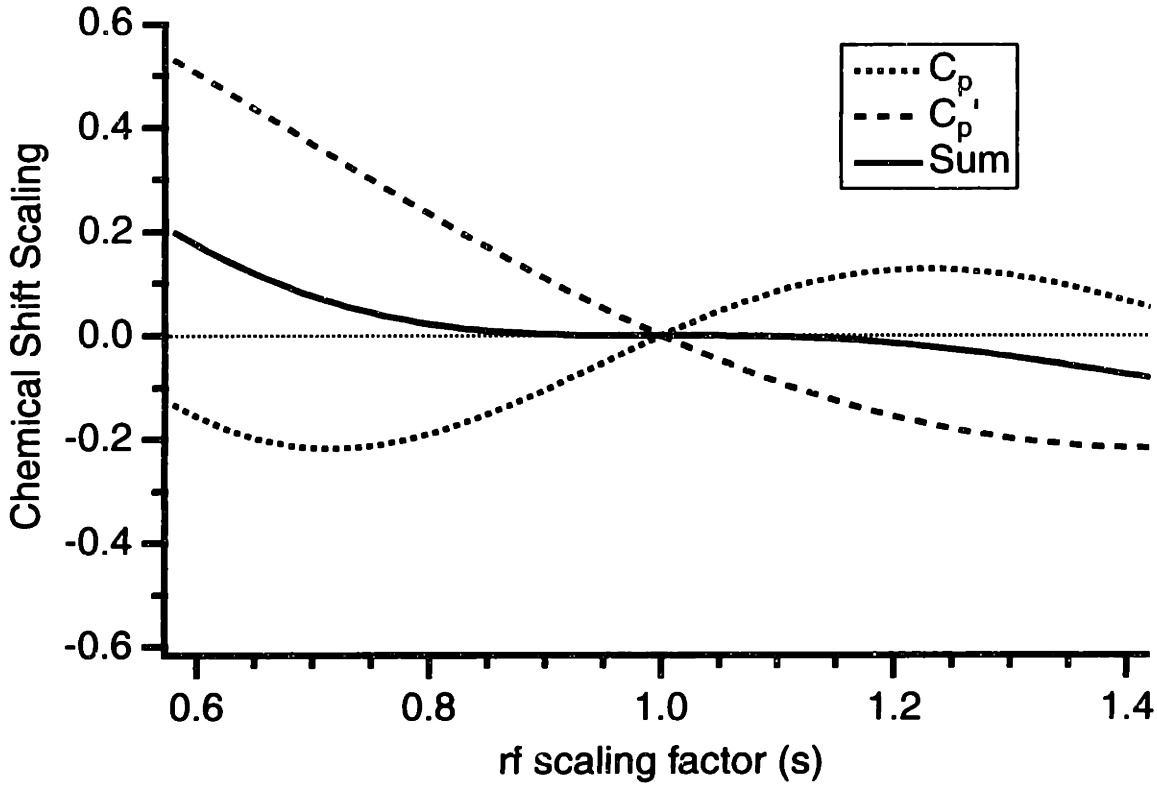

Figure 3-2. Residual isotropic chemical shift during CMR7 mixing.

Contributions due to RF inhomogeneity for the basic sub-cycle $C_p = 2\pi_\varphi 2\pi_{\varphi+\pi}$ and the cyclic permutation $C_p' = \pi_\varphi 2\pi_{\varphi+\pi}\pi_\varphi$. See Table 3-1 for analytical forms. Combination of the two in the manner shown in Figure 1 refocuses isotropic chemical shift error terms (to this level of approximation) over a time scale of $4/7\tau_r$, and anisotropic terms over $4\tau_r = 2\tau_c$.

The expressions for the spin components $k_{\lambda l\mu}\left(a_{\lambda l\mu m}+b_{\lambda l\mu m}\right)$, gathered in Table 3-1, contain the explicit dependence upon RF inhomogeneity as a function of s. The most important result is the significant error term that arises when $s\neq 1$ and the isotropic chemical shift (in the DQ-subspace, $\omega^{j}_{1020}+\omega^{k}_{1020}$) is non-zero. With the C_p element alone, the longitudinal term has a strong dependence upon s, as illustrated in Figure 2. The z-component can be inverted over the next element (C'_{p+1}) by cyclic permutation of a π rotation.[50,61] Combination of these two elements cancels the (large) isotropic error term (through $O(s-1)^2$) over the timescale of $\frac{4}{7}\tau_r$. The isotropic error term would not be averaged by the standard C7 phase-shifting alone (through the symmetry of Eq. 15) because the error term phase is invariant with respect to the shifts in RF phase (i.e., for $m=\mu=0$, $\Phi(p)=1$). Additional, smaller error terms due to the interaction of CSA with the inhomogeneity are averaged on a timescale of $4\tau_r$.

The analytic forms of Table 1 provide a simple method for calculating the magnitude of recoupled interactions in a general manner. The expression for $\overline{\omega}_{2\pm 22\pm 1}$ (with s=1, i.e., ideal RF irradiation) can be evaluated over the general Cn cycle as

$$\sum_{p=0}^{n-1}\frac{\overline{\omega}_{2\pm 22\pm 1}}{n}=\frac{i3\sqrt{2}}{3\pi}\frac{n^3\left(\exp[iN2\pi/n]-1\right)}{N\left(N^2-16n^2\right)}\omega_D^{jk}\sin 2\beta_{PR}. \qquad (17)$$

This expression allows convenient evaluation of the scaling factors for alternative formulations of the Cn sequences. For example, for $N=2$ and $n>6$ only a single spatial component is selected for each spin component ($m=\pm 1$ for $\mu=\pm 2$). The exact scaling factor depends on the value of n; for $n=7$, the familiar C7 scaling factor is recovered:

$$|\bar{\omega}_{2\pm22\pm1}| = \left| -\frac{343\left(i + e^{i\pi/14}\right)}{520\pi\sqrt{2}} \right| \cong 0.232\omega_D^{jk} \sin 2\beta_{PR}. \tag{18}$$

In the limit where $n \to \infty$, the dipolar scaling factor under double-quantum dipolar recoupling is

$$|\bar{\omega}_{2\pm22\pm1}| = \frac{3}{8\sqrt{2}} \cong 0.265\omega_D^{jk} \sin 2\beta_{PR}. \tag{19}$$

Therefore, when it is experimentally feasible, more rapid phase shifting (and correspondingly higher RF amplitudes) may be used to increase the scale factor by up to ~14% within this limit. This may be useful for the measurement of weak couplings in some circumstances.

Of more general use for correlation spectroscopy are the cases where n=7 and N=5 or N=9. These solutions satisfy the symmetry constraints in a manner similar to that of the N=2 case; i.e., only DQ spin terms (μ=±2) with a single spatial component ($m = \mp 1$ for N=5, $m = \pm 1$ for N=9) remain over the cycle. With respect to the sample rotation, the RF phases are shifted less rapidly as N increases, and the intuitive expectation of a less favorable dipolar scaling factor results:

$$|\bar{\omega}_{2\pm22\mp1}| = \left| \frac{343\left(i + e^{i\pi/14}\right)}{1265\pi\sqrt{2}} \right| \cong 0.095\omega_D^{jk} \sin 2\beta_{PR} \text{ for } N=5, \tag{20a}$$

$$|\bar{\omega}_{2\pm22\pm1}| = \left| -\frac{343\left(i + e^{i\pi/14}\right)}{2109\pi\sqrt{2}} \right| \cong 0.057\omega_D^{jk} \sin 2\beta_{PR} \text{ for } N=9. \tag{20b}$$

However, the reduction in scaling factor may be an acceptable compromise for applications at high MAS rates because the required RF field amplitude is decreased approximately by the same percentage as the dipolar scaling factor. In the MAS regime of 10-20 kHz and beyond, achieving $\omega_1 = \frac{2n}{N}\omega_r$ may not be experimentally feasible for N=2. In these cases, the sequences with N=5 or N=9 would allow more reasonable RF field amplitudes to be used. For ^{13}C-^{13}C chemical shift correlation spectroscopy in U-^{13}C-labeled samples, the higher N alternatives imply increasing the optimal mixing time for one-bond transfer from ~1 ms to 2.5 or 4 ms (for N=5 and N=9, respectively). Provided that appropriate ^{1}H decoupling conditions are maintained (see below), the additional mixing time is not expected to cause significant signal loss, allowing the full advantage of the C7 lineshape to be exploited at higher MAS rates. As discussed in more detail below, with the N=2 CMR7 sequence ~1 ms mixing provides strong one-bond correlations and many two-bond correlations in all U-^{13}C-labeled systems studied thus far. Similar behavior would be expected for the higher N alternatives with proportionately longer mixing times. Here we also note that the form for the ω_{222m} component in Table 1 indicates a scaling of the dipolar coupling which is explicitly dependent on the RF amplitude. The implications of this effect with respect to quantitative distance measurements with CMR7 will be discussed in a forthcoming publication.[62]

For the MELODRAMA[33] pulse sequence (where n=4, N=2) although the overall symmetry of the sequence does not cause terms such as μ=0, m=±2 to vanish, the symmetry described in Lee et al.[38] (Eq. 15) is a sufficient but not necessary condition for removal of all CSA terms. Direct examination of the terms a_{102m} and b_{102m} in Table 1 shows that the sub-cycle averaging of all

chemical shift terms in the MELODRAMA sequence is accomplished on half rotor period timescale, rather than the two-rotor period timescale of the full C7 averaging. For μ=0, this is identically true, as the term a_{102m} vanishes when $Nm = n \times \text{integer}$. The residual chemical shift interactions (b_{102m}) (for $s \neq 1$) can be minimized by improved compensation schemes.[49] The remaining shortcoming of the MELODRAMA sequence is that both m=1 and m=−1 spatial components are recoupled, leading to a $\sin\gamma_{PR}$ dependence in the average recoupled interaction. Integration over γ_{PR} then reduces the maximum double-quantum filtering efficiency from ~73% to ~52%. (For C7/CMR7 the phase, but not the magnitude, of the recoupled interaction depends on γ_{PR}.)

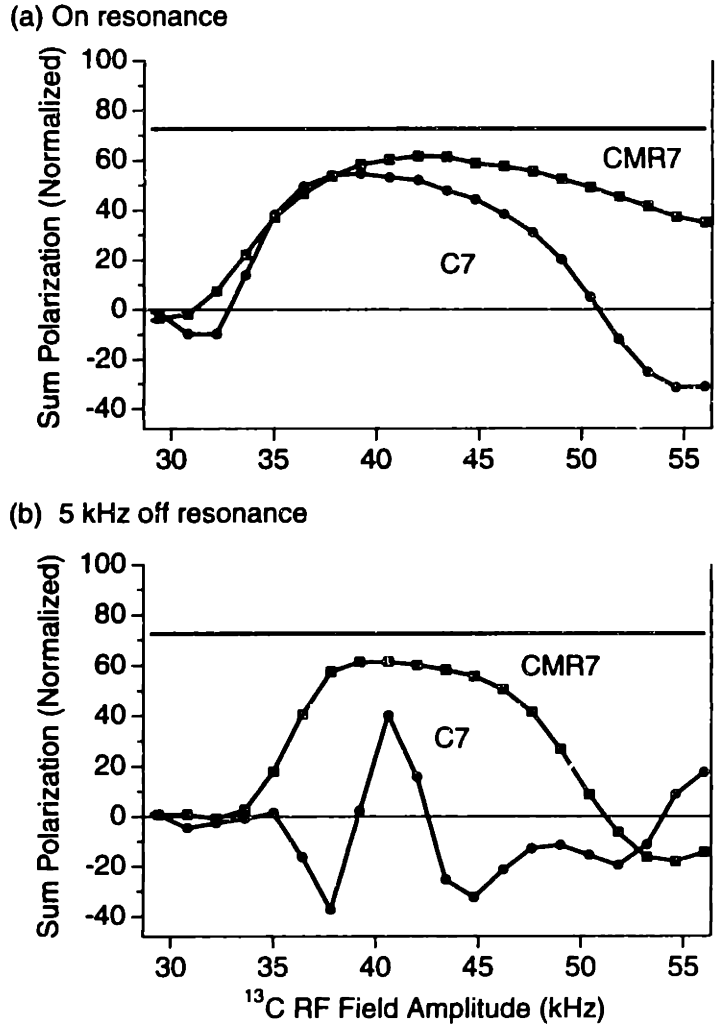

Figure 3-3. Experimental ^{13}C CMR7 double-quantum filtration (DQF) efficiencies in U-^{13}C,^{15}N-glycine.

Experiments were performed at 397.8 MHz ^{1}H frequency and 5.95 kHz (±5 Hz) MAS rate, with 670 μsec double-quantum excitation (τ_{mix} = 1.34 ms) under 125 kHz resonant CW ^{1}H decoupling. Decoupling power was reduced to 80 kHz TPPM (5.8 μsec, ±7.5°) during acquisition. The sample (~10 mg) was packed in the middle ~20% of the 4-mm rotor (Chemagnetics/Otsuka Electronics USA) sample volume to ensure optimal RF homogeneity. (Steady-state RF field amplitudes and homogeneity (2-3% FWHM) were determined with standard nutation experiments.[41]) The solid horizontal line indicates the maximum theoretical C7/CMR7 DQF efficiency. (a) Carrier frequency centered between the two peaks of interest. (b) Carrier frequency offset by 5 kHz from center.

Results and Discussion

RF error compensation and ^{1}H-^{13}C decoupling dynamics

Figure 3 illustrates the dependence of C7 and CMR7 DQF efficiency on RF amplitude for two different chemical shift offsets. The total mixing time, consisting of one-half double-quantum excitation and one-half reconversion, is chosen to maximize the theoretical DQF efficiency (~73%). For a 2 kHz dipolar coupling, this maximum occurs at ~1.3 ms, which in this case is approximately equal to $4\tau_c$ ($8\tau_r$). The even integer multiple of the pulse sequence cycle is used to ensure that all anisotropic chemical shifts are averaged as completely as possible. Sampling within the cycle yields small oscillations due to the combination of CSA and RF error.

The results presented in Figure 3 were obtained under circumstances that are optimized beyond what is typical for standard solenoid sample coils. Only the center portion of the available sample volume was used, yielding a small RF field inhomogeneity (~±1-2%). In Figure 3a, the carrier is positioned on resonance (in the DQ subspace, where the sum of the two shifts is zero). The basic C7 sequence shows some sensitivity to error in the RF field amplitude, although the DQF efficiency is 40% or better over the range of 35-45 kHz. The optimal RF amplitude is slightly less than predicted by theory (in part due to a ^{1}H decoupling effect discussed below), but in general the performance is acceptable for this two-spin system. Here the CMR7 sequence offers improvement at higher RF field amplitude, a maximum of 62% DQF efficiency.

When the carrier is moved off resonance by 5 kHz, the differences are even more pronounced. A severe sensitivity to the RF field amplitude is observed for the C7 sequence. Even when the nominal field amplitude is matched to the theoretical value (42 kHz), only 40% DQF efficiency is

realized. Several effects may be responsible for this discrepancy, two of which are substantially more pronounced with C7 sequence than with CMR7. First, because the chemical shift error term is proportional to $\sin 2\pi s$ (which in the region of $s \approx 1$ is well approximated by $2\pi(s-1)$) the sign of the residual shift depends upon the exact RF amplitude. This is relevant even when the error is small ($\left|\bar{\omega}^{j}_{1020} + \bar{\omega}^{k}_{1020}\right| \sin 2\pi s << \left|\bar{\omega}^{jk}_{2221}\right|$), due to a shift in the phase of the resulting DQ coherence. Over the entire sample, the distribution of phases results in destructive interference of the DQ coherence. Secondly, crystallites with small effective dipolar couplings (due to the $\sin 2\beta_{PR}$ dependence) may be fully decoupled by the chemical shift, resulting in little or no DQ coherence produced in those crystallites.

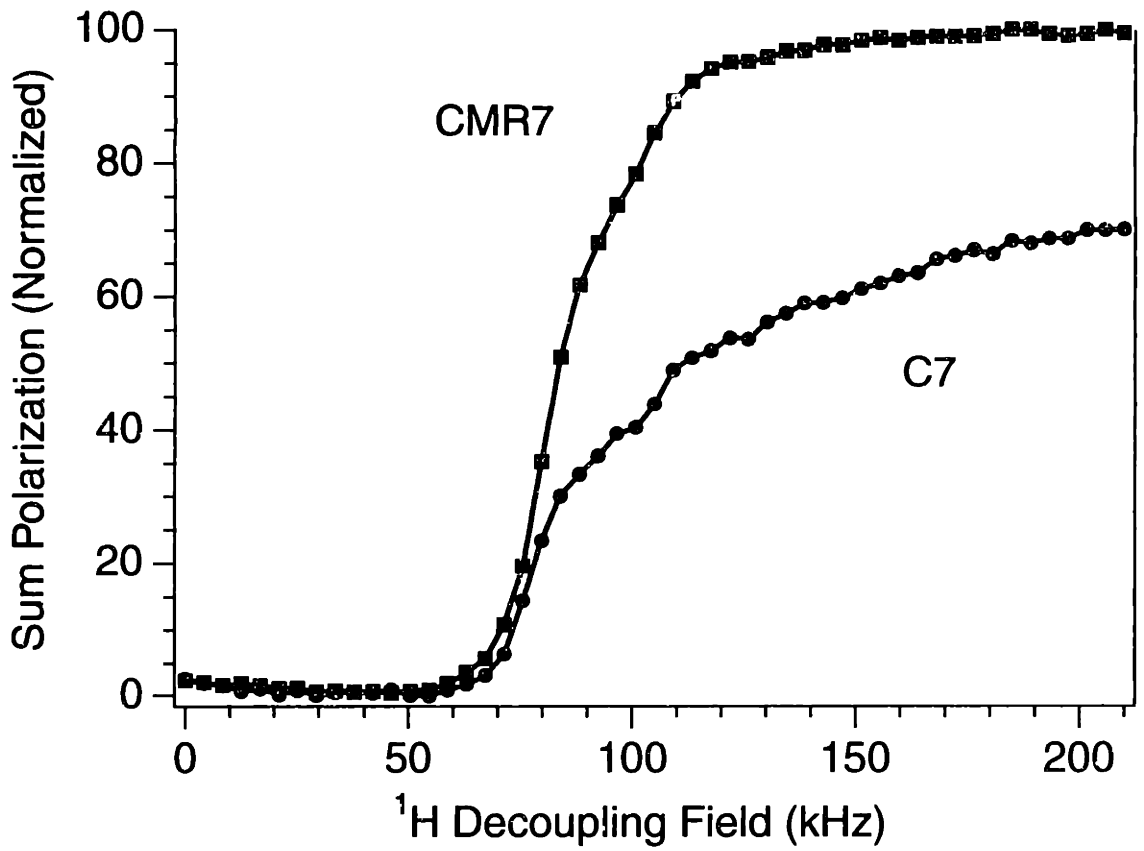

Figure 3-4. Dependence of DQF efficiency on ^{1}H CW decoupling field.

Experiments are performed at 198.3 MHz ^{1}H frequency and 6.053 kHz (±5 Hz) MAS rate, with 668 μsec double-quantum excitation (τ_{mix} = 1.3216 ms). In this case, a 5-mm rotor (Chemagnetics) is filled with ~120 mg of sample, providing an RF inhomogeneity of 6-8% FWHM. The decoupling field is incremented from 0 to >210 kHz in steps of approximately 2.2 kHz, and ^{13}C carrier frequency is approximately centered between the two signals. Signal due to natural abundance background is subtracted prior to calculation of DQF efficiency. The y-axis is normalized to the maximum observed CMR7 DQF efficiency (65% of total intensity observed with CP-MAS experiment).

Finally and perhaps of greatest significance, the heteronuclear decoupling dynamics exhibit strong dependence on mismatch of ^{1}H and ^{13}C RF field amplitudes.[28,63,64] This effect causes essentially irreversible loss of ^{13}C coherences into the ^{1}H bath, as illustrated in Figure 4. For the case of rotor-synchronized π pulses, mismatch of the RF field amplitudes by a factor of three greatly reduces the depolarization effect due to interference between the two RF fields. Although the theoretical approximation of π pulses is not directly applicable to windowless mixing sequences due to the timescale of ^{1}H-^{1}H interactions,[65] we find experimentally that the DQF filtration efficiency for CMR7 rapidly increases as a function of ^{1}H field until the factor of three is achieved (at ~125 kHz), at which point the rate of increase reduces substantially. This suggests that in cases where decoupling fields are hardware-limited, substantial increases in DQF efficiency may be achieved by decreasing the MAS spinning rate (ω_r) or implementing sequences that require a lower multiple of ω_1:ω_r.[66]

Referring back to Figure 3, with a ^{1}H decoupling field of 125 kHz, a more subtle demonstration of the ^{1}H-^{13}C interference effect is observed as an asymmetry in DQF efficiency as a function of ^{13}C RF field about the ideal theoretical value. In Figure 3a, the C7 DQF efficiency slopes downward at ^{13}C RF amplitudes higher than 35-45 kHz. Likewise in Figure 3b, the CMR7 DQF efficiency is lower when the ^{13}C RF amplitude errs on the high side. Separate experiments (not shown here) indicate that lowering the decoupling field exacerbates this effect, and raising the decoupling field reduces the asymmetry. This result suggests an another possible strategy for improved decoupling when ^{1}H field amplitudes are limited, namely reducing the ^{13}C field a few percent below the correct value; under these circumstances the CMR7 compensation

effectively removes the RF error and chemical shift terms, and the required ^{1}H field is reduced three times as rapidly as the ^{13}C field. Such an intentional reduction of RF field is particularly well tolerated for a two-spin system when the carrier is centered between the resonances, for the aforementioned reasons.

Figure 5 demonstrates broadband DQ excitation under the CMR7 sequence. With a ^{13}C RF field of 42 kHz, 50% or better DQF efficiency (3 dB below the theoretical maximum) is observed over a bandwidth of ±10.5 kHz; in contrast, the C7 sequence behaves selectively. Both sequences exhibit a slight frequency offset from zero chemical shift due to an asymmetric phase transient effect, which cancels a portion of the chemical shift due to rotation error . This effect is more pronounced in high Q probes and higher RF field strengths, and similar behavior has been observed in frequency-selective heteronuclear experiments[45] Probe overcoupling[67] and/or optimization of the carrier frequency are essential only for C7, where slight difference from ideal conditions can lead to non-trivial DQF efficiency losses. However, the bandwidth of CMR7 implies that such empirical optimization is unnecessary.

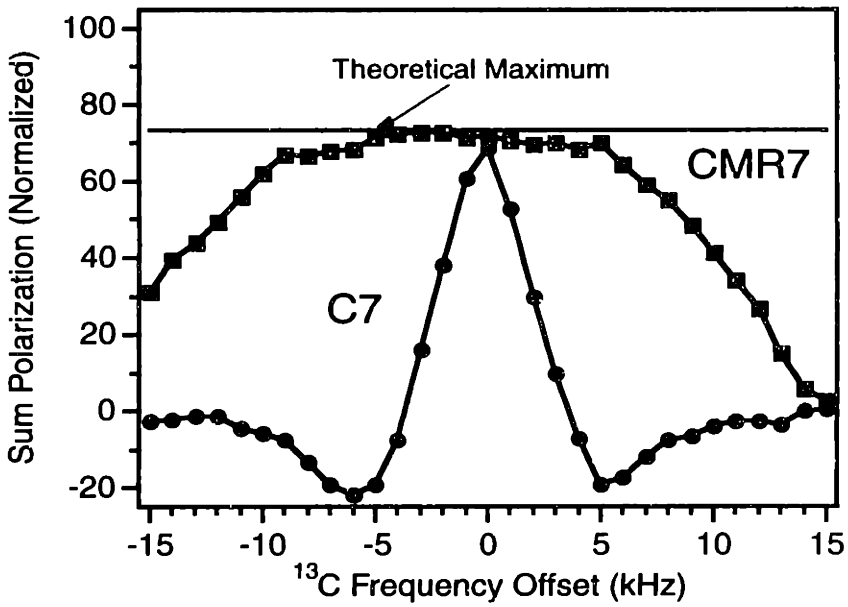

Figure 3-5. Bandwidth comparison for ^{13}C DQF of U-^{13}C,^{15}N-glycine.

Sample is diluted to 10% with natural abundance material. The ^{1}H CW decoupling field during mixing is 160 kHz. Otherwise, experimental conditions are identical to those in Figure 4. The y-axis is renormalized to the signal obtained with CP-MAS experiment.

Multi-spin double-quantum filtration.

Assuming that the two-spin DQ Hamiltonian is created over the CMR7 cycle with minimal dependence on chemical shift, additional spins can be considered within the approximation that each two-spin interaction is recoupled according to the zeroth-order theory. Multi-spin numerical simulations indicate that orientation-dependent effects in multi-spin chains may be observable.[48,68] However, in the present context we are primarily concerned with the efficient excitation of DQ coherence for purpose of DQF experiments, with the intent of removing natural

abundance background in cases where labeled clusters of spins are inserted within larger molecules.

Figure 6 demonstrates the three- and four-spin cases in the U-^{13}C-labeled amino acids Ala and Thr. At short times polarization is shared almost equally between each spin in the DQ state. With 290 μsec DQ excitation, the integrated intensities of ω-, α-, and β-^{13}C signals of Ala (normalized to the reference spectrum) are 22%, 43%, and 27% respectively. The approximate 1:2:1 ratio is the result of equal distribution between spin pairs at short time, neglecting higher-order coherences and weak couplings (e.g., ω to β). The significant CSA of the ω-^{13}C signal causes a slight reduction of intensity relative to the β. However, this asymmetry is reduced upon longer mixing, due to the additional compensation for higher-order CSA effects provided by the CMR7 supercycle. At 580 μsec DQ excitation, the intensities of 30%, 57%, and 34% correspond to higher total efficiency, and the 1:2:1 ratio is still approximately correct.

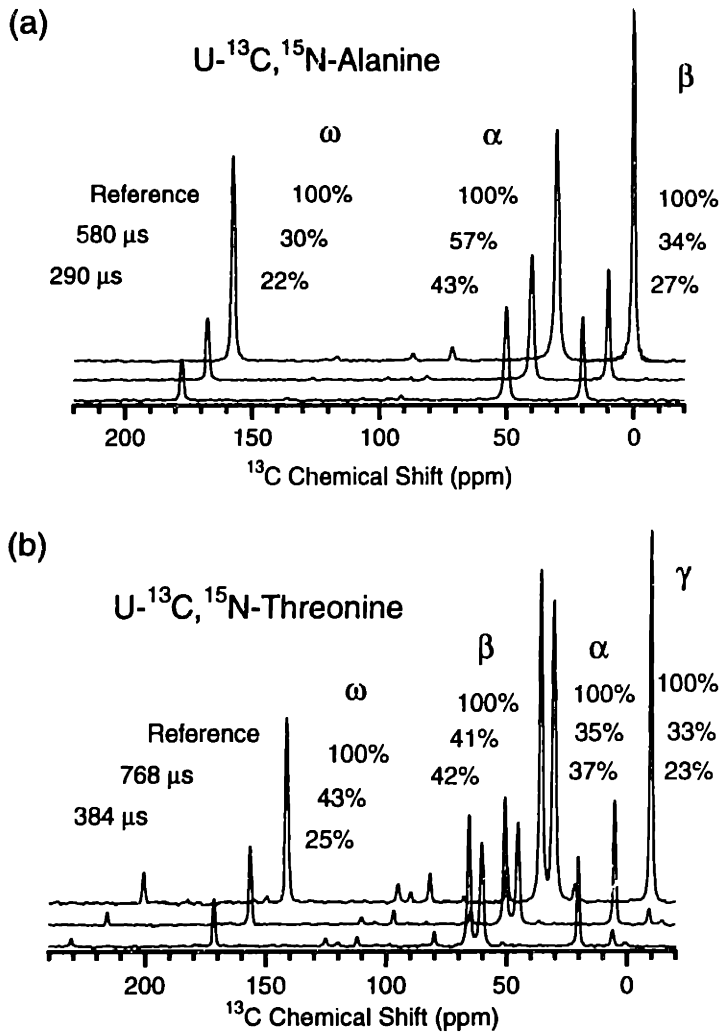

Figure 3-6. Experimental DQF spectra for multi-spin systems.

In both cases the RF carrier frequency is placed at approximately 100 ppm, and the DQ excitation time annotated for comparison with the reference spectrum. The reference spectra are scaled to correct for natural abundance background signal. (a) U-^{13}C-Ala spectra were acquired at 317.4 MHz ^{1}H frequency, with 6.896 kHz (±5 Hz) MAS rate. CW ^{1}H decoupling (135 kHz) was used during the mixing period, and TPPM (100 kHz, 4.8 μsec/15°) during acquisition. (b) U-^{13}C-Thr spectra were acquired at 397.8 MHz ^{1}H frequency, with 5.952 kHz (±5 Hz) MAS rate and 115 kHz CW ^{1}H decoupling during mixing. TPPM decoupling (80 kHz, 5.8 μsec/15°) was used during the acquisition period. Short-time behavior can be approximated by the excitation and reconversion of DQ coherence between neighboring spin pairs. Longer filtering times result in more even distribution of polarization.

In the four-spin system of U-^{13}C-Thr, the corresponding behavior is observed at short mixing time. With 384 μsec DQ excitation, the relative integrated intensities (from left to right in the spectra shown) for ω, β, α, and γ are 25%, 42%, 37%, and 23%. Here the intensity ratio of 1:2:2:1 is approximately correct, although more polarization is distributed to the outer spins than in the three-spin case. At longer mixing time (768 μsec DQ excitation), the outer spins increase in intensity (ωto 43%, γ to 33%) while the inner spins remain almost constant (β at 41%, α at 37%). We have explored this behavior in larger spin systems as well, where the effects are qualitatively similar. Experiments with larger U-^{13}C-labeled amino acids and peptides suggest the existence of a multi-spin limit of 40-45% for spins within a continuous chain and slightly less for spins at or near the end of chains. In general the optimal total mixing time for DQF in multi-spin ^{13}C systems is slightly less (~0.8-1.0 ms total excitation and reconversion time) than in the two-spin case (1.3 ms). At longer mixing times (1.2-1.5 ms) the total polarization is distributed to the ends of the chain more evenly, although the total integrated intensity decreases rapidly. This signal loss may be due to the creation of higher order coherences (four-quantum, six-quantum) which relax more rapidly than the DQ states. Yet we also observe rapid signal loss in cases where the DQ relaxation is significantly slower than the timescale of polarization transfer. Because total coherence order is not conserved, in contrast to the analogous ZQ experiments,[69] not all polarization is reconverted to observable coherence for detection and cancellation may occur during reconversion of DQ coherences in a multi-spin environment. These considerations suggest that in the present context shorter mixing times are most appropriate for DQF experiments in multi-spin systems.

Two-dimensional ^{13}C-^{13}C chemical shift correlation spectroscopy.

Several sequences, including RFDR,[27,28] MELODRAMA[33,49] DRAWS,[34-36] and RIL[70,71] have been applied to ^{13}C-^{13}C chemical shift correlation spectroscopy. Although the latter three sequences also offer dipolar recoupling which is insensitive to chemical shift and tolerant of RF errors, the CMR7 DQ mixing scheme does so with the significant improvement in theoretical crosspeak intensity. With 73% polarization transfer, the ratio of crosspeak to diagonal intensity would be expected to be almost 3:1, and in two-spin cases such as U-^{13}C,^{15}N-Gly, we have observed better than 2:1 relative intensities in 2D spectra (not shown). However, as demonstrated in the three- and four-spin DQF experiments above, the full theoretical DQF efficiency is not realized in multi-spin systems, and similar behavior is observed in correlation spectra with respect to crosspeak intensities. Nevertheless, in many cases crosspeak intensities exceed the diagonal peaks, and in favorable instances the ratio of intensities is greater than 2:1, even in the multi-spin limit.

Although 2D correlation spectra can be implemented with DQF,[68] there are several advantages to constant DQ phase mixing. In either implementation crosspeaks arise only from pairs of ^{13}C spins. However, with the filter, half of the selected DQ coherence is reconverted to the diagonal peak (in the two-spin case). For many applications this diagonal peak intensity provides little additional information and may obscure crosspeaks near the diagonal, in particular when crosspeaks have the same sign (as is the case for the standard DQF 2D implementation). In addition, we have observed that multiple-bond crosspeaks appear with greater relative intensity without the DQ filter. Filtration does of course scale the natural abundance background signal, and therefore may be of use for applications to spin labels within larger molecules, despite the

fact that sensitivity in the information-rich crosspeak region is reduced. Yet for smaller molecules the constant phase DQ mixing provides superior spectra in our experience.

An illustrative example of these effects and the improvement in resolution observed upon extending to a second ^{13}C chemical shift dimension is provided by the 2D correlation spectrum of U-^{13}C-labeled erythromycin A (Figure 7). Erythromycin A is a macrolide antibiotic that inhibits protein synthesis by binding to bacterial ribosomes. A number of structural studies have been performed on this molecule using solution-state NMR[72-77] and x-ray crystallography.[78] The erythromycin-ribosome complex exhibits a solid-state NMR spectrum even in solution and motivates the solid-state studies of free erythromycin A.

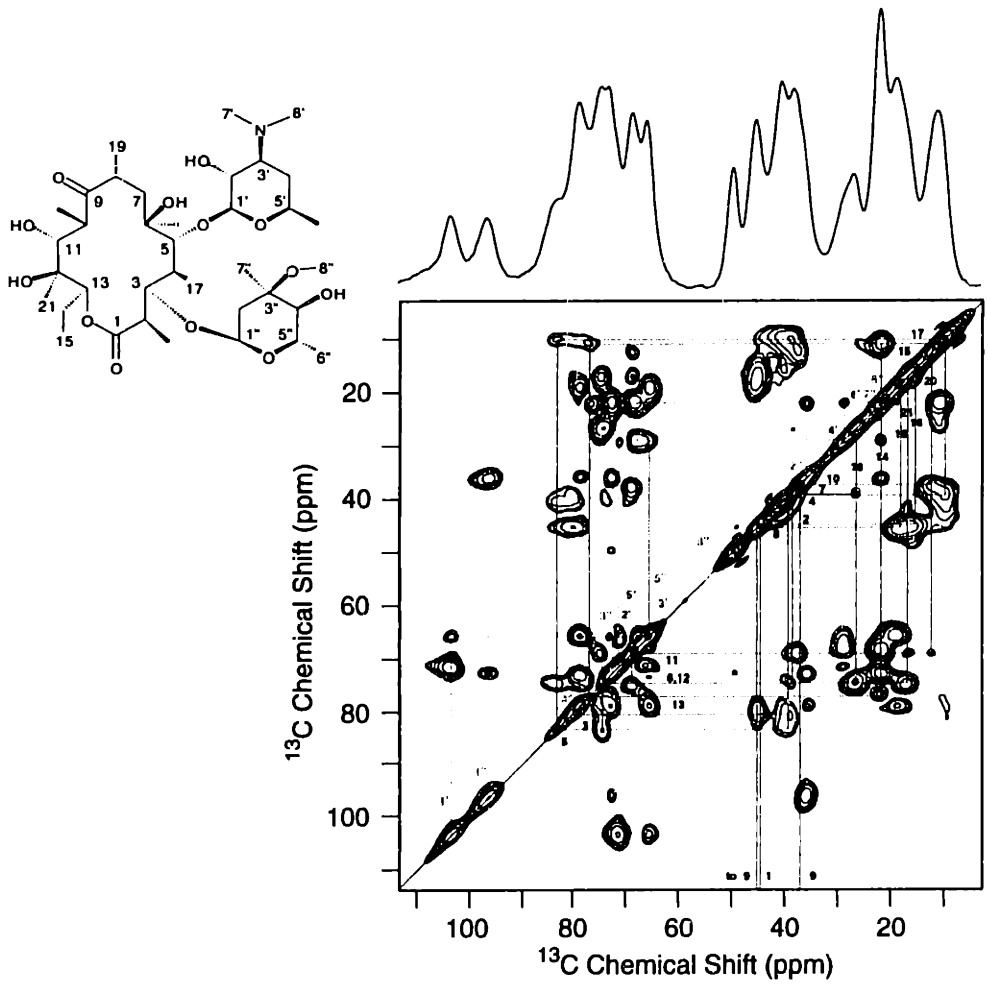

Figure 3-7. Chemical structure and 2D CMR7 ^{13}C-^{13}C chemical shift correlation spectrum of U-^{13}C-erythromycin A (EA).

EA consists of a 14-member lactone ring with desosamine (labeled prime) and cladinose (labeled double prime) sugar substituents. Experimental conditions for DQ mixing are the same as in Figure 3, with the following exceptions: (1) the MAS rate is 8.00 kHz (±5 Hz); (2) mixing time is 1.0 ms; and (3) rotor volume is fully utilized with ~30-35 mg sample; (4) the phase of the DQ Hamiltonian is constant throughout the mixing period. Two-dimensional data processing includes sine bell and exponential apodization functions in each dimension. Ten contour levels are logarithmically spaced over the range of 1% to 100% of maximum peak amplitude (positive in blue, negative in red). The diagonal peaks are numbered and crosspeaks labeled with a color-coded scheme as follows: black for the macrocyclic ring, magenta for the desosamine, and green for the cladinose.

The spectrum shown in Figure 7b allows the unambiguous assignment of all resonances which have directly bonded ^{13}C neighbors, and represents an important first step for future structural studies. Of particular utility are the regions of crosspeaks near the diagonal (65-85 ppm), corresponding to the hexose rings where chemical shift dispersion is minimal. The resolution in this region is significantly better than that observed with ZQ mixing methods such as RFDR and ^{1}H-driven spin diffusion[79] (data not shown). In part this is due to improved polarization transfer efficiency between spins of small chemical shift difference. However, an additional important consideration is the improved contrast and dynamic range implied by the DQ transfer. A minority of the total polarization remains on the diagonal, and so this uninformative part of the spectrum is de-emphasized; also because the diagonal and crosspeak differ in sign, a sharp delineation is observed between the two. Cancellation of crosspeaks due to degeneracies of opposite sign are not significant in this spectrum, although partial cancellation can lead to slight distortions of the lineshape and uncertainties in chemical shift (in the absence of explicit lineshape simulations). Note that in one case (C-3' to C-5') a two-bond DQ transfer of resonances of small chemical shift difference provides a lineshape similar to that observed under ZQ transfer. This is manifested as a broadening of the diagonal that is often experimentally indistinguishable from the lineshape asymmetries that arise due to uneven initial polarization and non-ideal ^{1}H decoupling conditions.[80]

An additional advantage of the DQ mixing scheme lies in the identification of two-bond crosspeaks (e.g., from C-1' to C-3' and C-1" to C-3"); these peaks are valuable for confirming the assignment in the congested hexose region, and are unambiguously distinguished from one-bond transfers due to the sign difference. Significant polarization transfer through weaker couplings

(e.g., the 500 Hz two-bond couplings of C-3 to C-1", C-5 to C-1', C-3' to C-7' and C-8', etc.) is not observed when multi-step transfer pathways through strong (~2-2.2 kHz) couplings exist.[43,46,47] However, in one case where a strong-coupling pathway is not available, direct transfer through a 500-Hz coupling is observed (C-3" to C-8"). The intensity of this crosspeak is substantially weaker than many of those that arise due to two-step transfers (e.g., C-1' to C-3', C-1" to C-3", C-3 to C-16, C-5 to C-17, etc.), but the direct transfer is unambiguous due to the sign of the crosspeak. Only the C-7' and C-8' resonances are not assigned from the 2D spectrum, due to motional averaging of the C-3' to C-7' and C-3' to C-8' couplings.[81,82]

Table 3-2. Chemical shifts for U-^{13}C-erythromycin A.[a]

Position	Chemical Shift (ppm)	Position	Chemical Shift (ppm)
9	221.2	1	176.1
1	176.1	2	44.8
1'	102.7	3	79.4
1"	95.8	4	39.2
5	83.1	5	83.1
3	79.4	6	73.8
4"	78.5	7	38.7
13	76.7	8	45.3
12	74.3	9	221.0
6	73.8	10	37.2
3"	72.4	11	68.4
2'	71.1	12	74.3
11	68.4	13	76.7
5'	68.2	14	21.6
3'	65.5	15	10.6
5"	65.3	16	15.7
8"	49.2	17	9.6
8	45.3	18	26.2
2	44.8	19	17.9
4	39.2	20	12.1
7	38.7	21	16.5
10	37.2	1'	102.7
2"	35.7	2'	71.1
4'	28.9	3'	65.5
18	26.2	4'	28.9
14	21.6	5'	68.2
7"	21.6	6'	21.3
6'	21.3	1"	95.8
6"	18.9	2"	35.7
19	17.9	3"	72.4
21	16.5	4"	78.5
16	15.7	5"	65.3
20	12.1	6"	18.9
15	10.6	7"	21.6
17	9.6	8"	49.2

[a]Shifts were assigned via the 2D CMR7 ^{13}C-^{13}C correlation spectrum. Peaks are referenced to the 2-^{13}C resonance of glycine at 43.5 ppm. Digital resolution is 0.25 ppm. (The 7' and 8' signals are not observed in the correlation spectrum, due to the rapid two-site hops of the dimethyl-amino group at room temperature.[81,82])

Conclusions

We have demonstrated that the theoretical advantages of the C7 sequence of Lee et al.[38] may be applied in a more experimentally robust manner. By refocusing the dominant error terms due to chemical shifts and RF errors, a DQ dipolar Hamiltonian can be created under MAS conditions with high efficiency over a bandwidth of approximately ±10 kHz. This allows for potential applications of CMR7 up to ^{1}H frequencies of at least 400 MHz in multi-spin systems experiencing a large range of chemical shifts, both isotropic and anisotropic. The ability to excite and filter DQ coherence with high efficiency in such multi-spin systems facilitates the use of U-^{13}C-labeled molecules within a large natural abundance background. In addition, correlation spectroscopy of similar systems permits more expedient and cost-effective determination of chemical shifts and allows the unambiguous assignment of spin labels.

The 2D ^{13}C-^{13}C correlation spectrum of erythromycin A provides a vivid example of the enhanced resolution by extension to a second chemical shift dimension. Although other DQ[33,34,36,49,80] and/or ZQ[27,28,70,71,83] recoupling methods may also produce correlation spectra of high quality, the improved crosspeak intensities observed with the CMR7 method are a significant advantage in larger spin systems where sensitivity is problematic. In addition, the alternation of crosspeak intensities from negative to positive, etc. (characteristic of DQ mixing) is a valuable tool in the assignment process in cases such as erythromycin A, where multiple degeneracies exist in the 1D ^{13}C spectrum and one-bond correlations alone are not sufficient to make unambiguous assignments.

Beyond the assignment and filtering applications, extensions of dipole-dipole correlation experiments are possible with the CMR7 sequence. By incorporating a third dimension of

heteronuclear dipolar evolution (e.g., ^{1}H-^{13}C or ^{13}C-^{15}N) into the chemical shift correlation experiment, each correlated pair in the 2D ^{13}C-^{13}C spectrum may be constrained with respect to the relative orientation of the attached ^{1}H or ^{15}N spins. Such an experiment could constrain several ^{1}H-^{13}C-^{13}C-^{1}H[6,7] or ^{15}N-^{13}C-^{13}C-^{15}N[8,11] torsion angles in a single experiment.

Finally, we note that the compensation scheme presented here is generally applicable, and does not perturb the symmetry inherent to C*n* sequences, where each unit has time-reflection symmetry and the overall sequence is organized according to the coherence order desired. (This in general, is not true in sequences that superimpose π or $\pi/2$ pulses over the basic unit.) Therefore we anticipate that similar compensation schemes will facilitate applications with other types of windowless mixing sequences.

Acknowledgments

The authors wish to thank M. Jackson, D. Zeidner, and R. Summers for the preparation of U-^{13}C-erythromycin A and to acknowledge NIH support of this research via grants RR-00995, GM-36810, GM-23403, and GM-23289 and a post-doctoral fellowship for MEH. LJM is an American Cancer Society Postdoctoral Fellow, and CMR is a Howard Hughes Medical Institute Predoctoral Fellow. Insightful discussions with John D. Gross and Dr. Marc A. Baldus are appreciated, as are the critical reading of the manuscript by Prof. Judith Herzfeld (Brandeis University) and the technical expertise of Dr. David J. Ruben.

References

(1) Griffiths, J. M.; Griffin, R. G. "Nuclear-magnetic-resonance methods for measuring dipolar couplings in rotating solids," *Anal. Chim. Acta* **1993**, *283*, 1081-1101.

(2) Bennett, A. E.; Griffin, R. G.; Vega, S. "Recoupling of Homo- and Heteronuclear Dipolar Interactions in Rotating Solids," In *Solid State NMR IV: Methods and Applications of Solid-State NMR*; B. Blumich, Ed.; Springer-Verlag: Berlin, **1994**; Vol. 33; 1-77.

(3) Thompson, L. K.; McDermott, A. E.; Raap, J.; van der Wielen, C. M.; Lugtenberg, J.; Herzfeld, J.; Griffin, R. G. "Rotational resonance NMR study of the active site structure in bacteriorhodopsin: Conformation of the schiff base linkage," *Biochem.* **1992**, *31*, 7931-7938.

(4) Christensen, A. M.; Schaefer, J. "Solid-state NMR determination of intramolecular and intermolecular P-31-C-13 distances for shikimate 3-phosphate and [1-C-13]glyphosate bound to enolpyruvylshikimate-3-phosphate synthase," *Biochem.* **1993**, *32*, 2868-2873.

(5) Lansbury, P. T., Jr.; Costa, P. R.; Griffiths, J. M.; Simon, E. J.; Auger, M.; Halverson, K. J.; Kocisko, D. A.; Hendsch, Z. S.; Ashburn, T. T.; Spencer, R. G. S.; Tidor, B.; Griffin, R. G. "Stuctural model for the β amyloid fibril: Interstrand alignment of an antiparallel β sheet comprising a C-terminal peptide," *Nat. Struct. Biol.* **1995**, *2*, 990-998.

(6) Feng, X.; Lee, Y. K.; Sandström, D.; Edén, M.; Maisel, H.; Sebald, A.; Levitt, M. H. "Direct determination of a molecular torsional angle by solid-state NMR," *Chem. Phys. Lett.* **1996**, *257*, 314-320.

(7) Feng, X.; Verdegem, P. J. E.; Lee, Y. K.; Sandström, D.; Edén, M.; Bovee-Geurts, P.; de Grip, W. J.; Lugtenburg, J.; de Groot, H. J. M.; Levitt, M. H. "Direct determination of a molecular torsion angle in the membrane protein rhodopsin by solid-state NMR," *J. Am. Chem. Soc.* **1997**, *119*, 6853-6857.

(8) Feng, X.; Eden, M.; Brinkmann, A.; Luthman, H.; Eriksson, L.; Graslund, A.; Antzutkin, O. N.; Levitt, M. H. "Direct determination of a peptide torsional angle psi by double-quantum solid-state NMR," *J. Am. Chem. Soc.* **1997**, *119*, 12006-12007.

(9) Hong, M.; Gross, J. D.; Griffin, R. G. "Site-resolved determination of peptide torsion angle phi from the relative orientations of backbone N-H and C-H bonds by solid-state NMR," *J. Phys. Chem. B* **1997**, *101*, 5869-5874.

(10) Hong, M.; Gross, J. D.; Rienstra, C. M.; Griffin, R. G.; Kumashiro, K. K.; Schmidt-Rohr, K. "Coupling amplification in 2D MAS NMR and its application to torsion angle determination in peptides," *J. Magn. Reson.* **1997**, *129*, 85-92.

(11) Costa, P. R.; Gross, J. D.; Hong, M.; Griffin, R. G. "Solid-state NMR measurement of psi in peptides: a NCCN 2Q-heteronuclear local field experiment," *Chem. Phys. Lett.* **1997**, *280*, 95.

(12) Levitt, M. H.; Raleigh, D. P.; Creuzet, F.; Griffin, R. G. "Theory and simulations of homonuclear spin pair systems in rotating solids," *J. Chem. Phys.* **1990**, *92*, 6347-64.

(13) Tycko, R.; Weliky, D. P.; Berger, A. E. "Investigation of molecular structure in solids by two-dimensional NMR exchange spectroscopy with magic angle spinning," *J. Chem. Phys.* **1996**, *105*, 7915-7930.

(14) Weliky, D. P.; Tycko, R. "Determination of peptide conformations by two-dimensional magic angle spinning NMR exchange spectroscopy with rotor synchronization," *J. Am. Chem. Soc.* **1996**, *118*, 8487-8488.

(15) Schmidt-Rohr, K. "Torsion angle determination in solid C-13-labeled amino acids and peptides by separated-local-field double-quantum NMR," *J. Am. Chem. Soc.* **1996**, *118*, 7601-7603.

(16) Bennett, A. E.; Weliky, D. P.; Tycko, R. "Quantitative conformational measurements in solid state NMR by constant-time homonuclear dipolar recoupling," *J. Am. Chem. Soc.* **1998**, *120*, 4897-4898.

(17) Andrew, E. R.; Bradbury, A.; Eades, R. G. "Nuclear magnetic resonance spectra from a crystal rotated at high speed," *Nature (London)* **1958**, *182*, 1659.

(18) Lowe, I. J. "Free induction decays of rotating solids," *Phys. Rev. Lett.* **1959**, *2*, 285-287.

(19) Schaefer, J.; Stejskal, E. O. "13C-NMR of Polymers Spinning at the Magic Angle," *J. Am. Chem. Soc.* **1976**, *98*, 1031.

(20) Maricq, M. M.; Waugh, J. S. "NMR in rotating solids," *J. Chem. Phys.* **1979**, *70*, 3300.

(21) Pines, A.; Gibby, M. G.; Waugh, J. S. "Proton-enhanced NMR of dilute spins in solids," *J. Chem. Phys.* **1973**, *59*, 569-590.

(22) Bennett, A. E.; Rienstra, C. M.; Auger, M.; Lakshmi, K. V.; Griffin, R. G. "Heteronuclear decoupling in rotating solids," *J. Chem. Phys.* **1995**, *103*, 6951-6958.

(23) Haeberlen, U.; Waugh, J. S. "Coherent averaging effects in magnetic resonance," *Phys. Rev.* **1968**, *175*, 453-467.

(24) Haeberlen, U. *High Resolution NMR in Solids: Selective Averaging*; Academic Press: New York, **1976**.

(25) Tycko, R.; Dabbagh, G. "Measurement of nuclear magnetic dipole-dipole couplings in magic-angle spinning NMR," *Chem. Phys. Lett.* **1990**, *173*, 461-465.

(26) Tycko, R.; Smith, S. O. "Symmetry principles in the design of pulse sequences for structural measurements in magic-angle spinning nuclear magnetic resonance," *J. Chem. Phys.* **1993**, *98*, 932-943.

(27) Bennett, A. E.; Ok, J. H.; Griffin, R. G.; Vega, S. "Chemical shift correlation spectroscopy in rotating solids: Radio-frequency dipolar recoupling and longitudinal exchange," *J. Chem. Phys.* **1992**, *96*, 8624-8627.

(28) Bennett, A. E.; Rienstra, C. M.; Griffiths, J. M.; Zhen, W.; Lansbury, P. T., Jr.; Griffin, R. G. "Homonuclear radio frequency-driven recoupling in rotating solids," *J. Chem. Phys.* **1998**, *108*, 9463-9479.

(29) Wokaun, A.; Ernst, R. R. "Selective excitation and detection in multilevel spin systems: Application to single transition operators," *J. Chem. Phys.* **1977**, *67*, 1752.

(30) Vega, S. "Fictitious spin 1/2 operator formalism for multiple quantum NMR," *J. Chem. Phys.* **1978**, *68*, 5518-27.

(31) Munowitz, M. *Coherence and NMR*; Wiley: New York, **1988**.

(32) Waugh, J. S. "Heteronuclear Spin Decoupling," *J. Magn. Reson.* **1982**, *50*, 30.

(33) Sun, B. Q.; Costa, P. R.; Kocisko, D. A.; Lansbury, P. T., Jr. ; Griffin, R. G. "Internuclear distance measurements in solid state nuclear magnetic resonance: Dipolar recoupling via rotor sychronized spin locking," *J. Chem. Phys.* **1995**, *102*, 702-707.

(34) Gregory, D. M.; Mitchell, D. J.; Stringer, J. A.; Kiihne, S.; Shiels, J. C.; Callahan, J.; Mehta, M. A.; Drobny, G. P. "Windowless dipolar recoupling--The detection of weak dipolar couplings between spin-1/2 nucleic with large chemical-shift anisotropies," *Chem. Phys. Lett.* **1995**, *246*, 654.

(35) Mehta, M. A.; Gregory, D. M.; Kiihne, S.; Mitchell, D. J.; Hatcher, M. E.; Shiels, J. C.; Drobny, G. P. "Distance measurements in nucleic acids using windowless dipoalr recoupling solid state NMR," *Solid State Nucl. Magn. Reson.* **1996**, *7*, 211-288.

(36) Gregory, D. M.; Mehta, M. A.; Shiels, J. C.; Drobny, G. P. "Determination of local structure in solid nucleic acids using double quantum nuclear magnetic resonance spectroscopy," *J. Chem. Phys.* **1997**, *107*, 28-42.

(37) Nielsen, N. C.; Bildsøe, H.; Jakobsen, H. J.; Levitt, M. H. "Double-quantum homonuclear rotary resonance: Efficient dipolar recovery in magic-angle spinning nuclear magnetic resonance," *J. Chem. Phys.* **1994**, *101*, 1805-1812.

(38) Lee, Y. K.; Kurur, N. D.; Helmle, M.; Johannessen, O. G.; Nielsen, N. C.; Levitt, M. H. "Efficient dipolar recoupling in the NMR of rotating solids. A sevenfold symmetric radiofrequency pulse sequence," *Chem. Phys. Lett.* **1995**, *242*, 304-309.

(39) Larsen, F. H.; Daugaard, P.; Jakobsen, H. J.; Nielsen, N. C. "Improving rf field homogeneity in solid-state MAS NMR using a loop-gap resonator," *J. Magn. Reson. A* **1995**, *115*, 283-286.

(40) Froncisz, W.; Hyde, J. S. "The loop-gap resonator: a new microwave lumped element circuit ESR sample structure," *J. Magn. Reson.* **1982**, *47*, 515-521.

(41) Bax, A. *Two-Dimensional Nuclear Magnetic Resonance in Liquids*; Delft University Press: Dordrecht, Holland, **1980**.

(42) Raleigh, D. P.; Levitt, M. H.; Griffin, R. G. "Rotational resonance in solid state NMR," *Chem. Phys. Lett.* **1988**, *146*, 71-76.

(43) Costa, P. R.; Sun, B. Q.; Griffin, R. G. "Rotational resonance tickling: Accurate internuclear distance measurements in solids," *J. Am. Chem. Soc.* **1997**, *119*, 10821-10830.

(44) Bennett, A. E.; Becerra, L. R.; Griffin, R. G. "Frequency-selective heteronuclear recoupling in rotating solids," *J. Chem. Phys.* **1994**, *100*, 812-814.

(45) Bennett, A. E.; Rienstra, C. M.; Lansbury, P. T., Jr.; Griffin, R. G. "Frequency-selective heteronuclear dephasing by dipole couplings in spinning and static solids," *J. Chem. Phys.* **1996**, *105*, 10289-10299.

(46) Costa, P. R., *Spins, peptides, and Alzheimer's disease: Solid-state nuclear magnetic resonance investigations of amyloid peptide conformation*, Ph.D. Thesis, Massachusetts Institute of Technology, **1996**.

(47) Costa, P. R.; Sun, B.-Q.; Griffin, R. G. **1998**, manuscript in preparation.

(48) Munowitz, M. "Exact simulation of multiple-quantum dynamics in solid-state NMR: implications for spin counting," *Mol. Phys.* **1990**, *71*, 959-978.

(49) Rienstra, C. M.; Sun, B.-Q.; Hu, J. G.; Hatcher, M. E.; Herzfeld, J.; Griffin, R. G. "Rotating frame double-quantum MAS spectroscopy," *manuscript in preparation* **1998**,

(50) Levitt, M. H.; Freeman, R.; Frenkiel, T. "Supercycles for broadband heteronuclear decoupling," *J. Magn. Reson.* **1982**, *50*, 157-160.

(51) Holl, S. M.; McKay, R. A.; Gullion, T.; Schaefer, J. "Rotational-echo triple-resonance NMR," *J. Magn. Reson.* **1990**, *89*, 620-626.

(52) McKay, R. A., "Double-tuned single coil probe for nuclear magnetic resonance spectrometer," USA Patent #4,446,431, **1984**.

(53) McKay, R. A., Personal communication.

(54) Wu, X.; Zilm, K. W. "Cross polarization with high-speed magic angle spinning," *J. Magn. Reson. A* **1993**, *104*, 154-165.

(55) Wokaun, A.; Ernst, R. R. *Chem. Phys. Lett.* **1977**, *52*, 407.

(56) States, D. J.; Haberkorn, R. A.; Ruben, D. J. "A two-dimensional nuclear Overhauser experiment with pure absorption phase in four quadrants," *J. Magn. Reson.* **1982**, *48*, 286-292.

(57) Mehring, M. *Principles of High Resolution NMR in Solids;* 2nd ed.; Springer-Verlag: Berlin, **1983**.

(58) Spiess, H. W. "Dynamic NMR Spectroscopy," In *NMR Basic Principles and Progress*; P. Diehl; E. Fluck and E. Kosfeld, Ed.; Springer: Berlin, **1978**; Vol. 15; 58-214.

(59) Sakurai, J. J. *Modern Quantum Mechanics*; Cummings Publishing: Menlo Park, **1985**.

(60) Hohwy, M.; Jakobsen, H. J.; Edén, M.; Levitt, M. H.; Nielsen, N. C. "Broadband dipolar recoupling in the nuclear magnetic resonance of rotating solids: A compensated C7 pulse sequence," *J. Chem. Phys.* **1998**, *108*, 2686-94.

(61) Waugh, J. S. "Systematic procedure for constructing broadband decoupling sequences," *J. Magn. Reson.* **1982**, *49*, 517-21.

(62) Rienstra, C. M.; Mueller, L. J.; Hohwy, M. H.; Jaroniec, C. P.; Hatcher, M. E.; Griffin, R. G. "Quantitative distance measurements with gamma-encoded double-quantum dipolar recoupling," *manuscript in preparation* **1998**,

(63) Ishii, Y.; Ashida, J.; Terao, T. "13C-1H dipolar recoupling dynamics in 13C multiple-pulse solid-state NMR," *Chem. Phys. Lett.* **1995**, *246*, 439-445.

(64) Bennett, A. E., *Dipolar Decoupling and Recoupling in Solid State Nuclear Magnetic Resonance Spectroscopy*, Ph. D. Thesis, Massachusetts Institute of Technology, **1995**.

(65) Rienstra, C. M.; Bennett, A. E.; Hohwy, M. H.; Sun, B. Q.; Griffin, R. G. "Phase-modulated heteronuclear decoupling in rotating solids," *manuscript in preparation* **1998**,

(66) Hohwy, M.; Rienstra, C. M.; Jaroniec, C. P.; Griffin, R. G. "Fivefold symmetric homonuclear dipolar recoupling in rotating solids: Application to double quantum spectroscopy," *J. Chem. Phys.* **1999**, *110*, 7983-7992.

(67) Burum, D. P.; Linder, M.; Ernst, R. R. "A New "Tune-Up" NMR Pulse Cycle for Minimizing and Characterizing Phase Transients," *J. Magn. Reson.* **1981**, *43*, 463-471.

(68) Geen, H.; Gottwald, J.; Graf, R.; Schnell, I.; Spiess, H. W.; Titman, J. T. "Elucidation of dipolar coupling networks under magic-angle spinning," *J. Magn. Reson.* **1997**, *125*, 224-227.

(69) Bruschweiler, R.; Ernst, R. R. "A cog-wheel model for nuclear-spin propagation in solids," *J. Magn. Reson.* **1997**, *124*, 122-126.

(70) Baldus, M.; Tomaselli, M.; Meier, B. H.; Ernst, R. R. "Broad-band polarization-transfer experiments for rotating solids," *Chem. Phys. Lett.* **1994**, *230*, 329-336.

(71) Baldus, M.; Meier, B. H. "Broadband polarization transfer under magic-angle spinning: application to total through-space-correlation NMR spectroscopy," *J. Magn. Reson.* **1997**, *128*, 172-193.

(72) Barber, J.; Gyi, J. I.; Morris, G. A.; Pye, D. A.; Sutherland, J. K. "Isomerization of erythromycin A in deuterium-oxide and [H-2(6)]dimethyl-sulfoxide solutions - A H-1 and C-13 NMR study," *J. Chem. Soc., Chem. Comm.* **1990**, *15*, 1040-41.

(73) Barber, J.; Gyi, J. I.; Lian, L.; Morris, G. A.; Pye, D. A.; Sutherland, J. K. "The structure of erythromycin-A in [H-2(6)]DMSO and buffered D2O--full assignments of the H-1 and C-13 NMR spectra," *J. Chem. Soc., Perk. Trans. 2* **1991**, *10*, 1489-1494.

(74) Barber, J.; Gyi, J. I.; Pye, D. A. "Specific, weak binding of erythromycin-A (ketone) and chloramphenicol to 50S subunits of escherichia-coli ribosomes--a H-1 NMR study," *J. Chem. Soc., Chem. Comm.* **1991**, *18*, 1249-1252.

(75) Cane, D. E.; Hasler, H.; Taylor, P. B.; Liang, T.-C. "Macrolide biosynthesis-II: origin of the carbon skeleton and oxygen atoms of the erythromycins," *Tetrahedron* **1983**, *39*, 3449-3455.

(76) Pye, D. A.; Gyi, J. I.; Barber, J. "Tautomeric recognition of erythromycin A by ribosomes: A H-1 nuclear magnetic resonance study," *J. Chem. Soc., Chem. Commun.* **1990**, *17*, 1143-1145.

(77) Everett, J. R.; Tyler, J. W. "The conformational analysis of erythromycin A," *J. Chem. Soc. Perkin Trans. II* **1987**, 1659-1667.

(78) Perun, T. J.; Egan, R. S. "The conformation of erythromycin aglycones," *Tetrahedron Lett.* **1969**, *5*, 387-390.

(79) Kubo, A.; McDowell, C. A. "Spectral spin diffusion in polycrystalline solids under magic-angle spinning," *J. Chem. Soc., Faraday Trans. 1* **1988**, *84*, 3713-3730.

(80) Sun, B. Q.; Rienstra, C. M.; Costa, P. R.; Williamson, J. R.; Griffin, R. G. "3D 15N-13C-13C chemical shift correlation spectroscopy in rotating solids," *J. Am. Chem. Soc.* **1997**, *119*, 8540-8546.

(81) Stephenson, G. A.; Stowell, J. G.; Toma, P. H.; Pfeiffer, R. R.; Byrn, S. R. "Solid-state investigations of erythromycin A dihydrate: Structure, NMR spectroscopy, and hygroscopicity," *J. Pharm. Sci.* **1997**, *86*, 1239-1244.

(82) McGeorge, G., "ENC Conference Poster."

(83) Böender, G. J.; Raap, J.; Prytulla, S.; Oschkinat, H.; de Groot, H. J. M. "MAS NMR structure refinement of uniformly C-13 encriched chlorophyll-A water aggregates with 2D dipolar correlation spectroscopy," *Chem. Phys. Lett.* **1995**, *237*, 502-508.

.

Chapter 4. RFDR Recoupling for Correlation and Assignment of Backbone and Sidechain ^{13}C Resonances in Peptides

Note: This chapter is excerpted from a manuscript that appeared in the Journal of Chemical Physics, 108(22):9463-9479 (1998), in collaboration with Andrew E. Bennett, Janet M. Griffiths, Weiguo Zhen, and Peter T. Lansbury, Jr.

Abstract

We discuss some aspects of homonuclear recoupling and longitudinal exchange using rotor-synchronized spin echo sequences in solid state magic angle spinning (MAS) experiments. These include the effects of insufficient proton decoupling during π pulse echo sequences and chemical shift correlation spectroscopy via polarization exchange. In order to avoid rapid polarization losses during π pulses, at least a factor of three mismatch between ^{1}H and ^{13}C RF fields must be achieved, even if ^{1}H decoupling fields are in excess of 200 kHz. Obeying this rule leads to improved two-dimensional correlation spectra, based on dipolar exchange among proximate nuclei. The principles are illustrated with amino acids and a uniformly $^{15}N,^{13}C$-labeled sample of the tetrapeptide achatin-II (Gly-L-Phe-L-Ala-L-Asp).

Introduction

Dipole-dipole couplings are an important avenue for investigating molecular structure via distance measurements between or among nuclear spins.[1,2] The magnitudes of relatively large dipole-dipole interactions are sometimes revealed directly in one-dimensional (1D) solid state NMR spectra.[3] However, weak dipole-dipole couplings, which contain important information

about relatively long internuclear separations, are frequently obscured by larger interactions in the spin Hamiltonian, and in these cases it is necessary to apply special techniques to enhance and observe the weaker interactions selectively. In static samples, various approaches to enhancing dipole-dipole couplings in the presence of other interactions have been developed for both homonuclear[4] and heteronuclear interactions.[5-8] Solid state NMR spectra, however, are often acquired with magic-angle spinning (MAS) in order to improve sensitivity and resolution.[9-11] This method employs mechanical rotation to eliminate dipole-dipole couplings and other second-rank anisotropic interactions. In order to measure the attenuated dipolar couplings, they must be reintroduced into MAS experiments with rotor-driven[12-14] or RF-driven recoupling techniques.[1,2]

The recoupling of heteronuclear interactions in rotating samples is relatively straightforward to achieve with π pulse sequences.[15,16] The spin Hamiltonian for coupled homonuclear spins, however, is complicated by the non-commutation among the chemical shifts of the nuclei and their dipole-dipole interactions.[17] For weak couplings, the chemical shift interactions dominate, and recoupling (in the absence of radiofrequency irradiation) occurs only at special "rotational resonance" conditions, where the chemical shift difference between two spins matches a multiple of the spinning frequency, $\Delta\delta = m\omega_r$.[12-14] Rotational resonance provides a means of accurately measuring distances in these cases, [1,18,19] most conveniently for spins with significant (>50 ppm) chemical shift differences.

Homonuclear recoupling with less sensitivity to the chemical shift is desired for many applications, such as distance measurements between spins of small (<50 ppm) chemical shift differences and correlation spectroscopy of multiple spins over a broad range of chemical shifts.[20,21] To achieve this goal it is necessary to spoil the coherent averaging of MAS by

imposing additional modulations on the spin Hamiltonian with multiple pulse RF irradiation.[2] The general approach employs applications of rotor-synchronized π and/or $\pi/2$ pulses, [21-25] continuous (windowless) phase-switched RF fields, [26 27 28] or combinations of the two[29,30] to recouple dipolar interactions. In the more recent experiments,[26-28,30] recoupling occurs independent of chemical shift terms, albeit with some sensitivity to RF pulse imperfections.

On the other hand, multiple pulse sequences based on π pulses are very robust with respect to RF errors, yet have some remaining dependence on the chemical shift differences among spins. These experiments, monitoring either the transverse[23] or longitudinal evolution[21,31] of spin magnetization, have been applied to several biophysical applications. [32,33] Furthermore, the RF-Driven Recoupling (RFDR) approach of π pulse longitudinal exchange is a promising method to measure very long internuclear distances accurately, and it is easily integrated into two-dimensional correlation NMR with multiply-^{13}C-labeled samples.[21,33] In particular, this general approach tolerates pulse errors, and the data is easy to simulate and interpret under typical MAS conditions with the methods described below.

Here we consider the general theory of π pulse recoupling in greater detail, examining specifically the dynamics of polarization decay during longitudinal mixing as a function of ^{1}H decoupling conditions, and principles of polarization transfer in multi-spin systems, as demonstrated in the uniformly-^{13}C,^{15}N-labeled tetrapeptide, Gly-Phe-Ala-Asp. The application of homonuclear recoupling has a promising future in applications to non-oriented biological samples and other systems. The RFDR experiment has already been utilized to examine the retinal-Schiff base linkage[32] and the analysis of highly ^{13}C-enriched chlorophyll/water aggregates using two-dimensional correlation spectroscopy. [33]

Theory

Effect of Insufficient Proton Decoupling

A simple model which is useful in understanding the influence of proton decoupling on the performance of a π pulse consists of the basic Hamiltonian:

$$H = \omega_I I_x + \omega_S S_x + d_{IS} \cdot 2I_z S_z \,, \tag{1}$$

where ω_I and ω_S are the RF field amplitudes applied to the heteronuclear spin pair. The S spin, whose echo intensity is observed, is coupled to the I spin via d_{IS}. With sample rotation, this discussion applies to the case where $\tau_r >> \tau_p$. Although the decoupling field ν_I is typically applied continuously, the S spin RF field is active only for a short time τ_p in order to stimulate a π pulse rotation. During these intervals, the decoupling efficiency is generally reduced because of interference between the two fields. Moreover, in the case of strong ^{1}H-^{1}H interactions, spin coherences involving the protons experience irreversible dephasing within a short time interval,[34,35] strongly limiting the efficiency of phase-alternated echo sequences in compensating for insufficient proton decoupling. Consequently, it is important to apply strong decoupling on the short time scale τ_p.

The mechanism of decoupling degradation can be understood by examining the time evolution operator during the short interval τ_p when the S spin pulse is applied. The spin operators are transformed into the toggling frame in order to investigate their joint behavior

under the two RF fields. To evaluate the time evolution operator, the AHT approximation is employed under the reasonable assumption that both RF fields dominate the dipolar coupling:

$$U(\tau_p,0) \approx \exp\left\{-i\omega_I \tau_p I_x\right\}\exp\left\{-i\omega_S \tau_p S_x\right\} \times \exp\left\{-i\tilde{H}_D^{(0)}\tau_p\right\}. \tag{2}$$

where:

$$\tilde{H}_D^{(0)} = \frac{1}{\tau_p}\int_0^{\tau_p} dt\, d_{IS}\cdot 2\tilde{I}_z(t)\tilde{S}_z(t). \tag{3}$$

The evaluation of Eq. 6-1 leads to the following expression:

$$\begin{aligned}
\tilde{H}_D^{(0)} = {} & d_{IS}\cdot I_z S_z\left\{\frac{\sin\left\{(\omega_I+\omega_S)\tau_p\right\}}{(\omega_I+\omega_S)\tau_p} + \frac{\sin\left\{(\omega_I-\omega_S)\tau_p\right\}}{(\omega_I-\omega_S)\tau_p}\right\} \\
& + d_{IS}\cdot I_z S_y\left\{\frac{1-\cos\left\{(\omega_I+\omega_S)\tau_p\right\}}{(\omega_I+\omega_S)\tau_p} - \frac{1-\cos\left\{(\omega_I-\omega_S)\tau_p\right\}}{(\omega_I-\omega_S)\tau_p}\right\} \\
& + d_{IS}\cdot I_y S_z\left\{\frac{1-\cos\left\{(\omega_I+\omega_S)\tau_p\right\}}{(\omega_I+\omega_S)\tau_p} + \frac{1-\cos\left\{(\omega_I-\omega_S)\tau_p\right\}}{(\omega_I-\omega_S)\tau_p}\right\} \\
& + d_{IS}\cdot I_y S_y\left\{\frac{\sin\left\{(\omega_I+\omega_S)\tau_p\right\}}{(\omega_I+\omega_S)\tau_p} - \frac{\sin\left\{(\omega_I-\omega_S)\tau_p\right\}}{(\omega_I-\omega_S)\tau_p}\right\}.
\end{aligned} \tag{4}$$

Three particular cases deserve attention. First, when the RF fields are matched in amplitude at the Hartmann Hahn (HH) condition $\omega_S = \omega_I$,[36] the coherent averaging effect is spoiled by interference between the simultaneous modulations of the I and S spin operators. This resonance condition is fulfilled in cross polarization experiments[37] in order to permit rotating frame magnetization exchange. In order to minimize dephasing of the signal in spin echo experiments, this HH condition $\omega_S \approx \omega_I$ must clearly be avoided. However, in the case of a π pulse applied to

the S spin, where $\omega_S \tau_p = \pi$, an especially large mismatch is required in order to reduce signal losses to an acceptable level. For example, if $\omega_I = 2\omega_S$, then the dipole-dipole interaction is still not eliminated:

$$\tilde{H}_D^{(0)} = -\frac{2}{3\pi} d_{IS} \cdot I_z S_y + \frac{4}{3\pi} d_{IS} \cdot I_y S_z \,. \tag{5}$$

In order to eliminate $\tilde{H}_D^{(0)}$ over the course of a π pulse, the condition $\omega_I = 3\omega_S$ must be fulfilled, leading to $\tilde{H}_D^{(0)} = 0$.[38,39] In contrast, over an entire 2π rotation, $\omega_I = 2\omega_S$ is sufficient to ensure $\tilde{H}_D^{(0)} = 0$. Although sharp resonance effects are not observed in practice because of strong proton-proton interactions and sample spinning, this simple model implies that additional decoupling power is required for the case of π pulses compared to windowless ^{13}C RF excitations which switch phase less frequently.[26,28] Over a single cycle τ_p of the decoupling field such that $\omega_I \tau_p = 2\pi$, the coupling vanishes in the absence of the S spin RF field. Since the efficiency of the decoupling field is therefore reduced roughly according to the expression $\omega_I \rightarrow \omega_I - \omega_S$, it is necessary to apply particularly strong proton RF fields during double resonance echo experiments to minimize the decay of S spin coherences. According to Eq. (6-4), the signal losses should be reduced continuously as the decoupling field and the ratio ω_I/ω_S are increased in the limit $\omega_I >> \omega_S$.

As will be demonstrated below, it is possible to achieve this limit under some experimental conditions, in which case the rates of coherence loss are extremely small. However, it is not always possible to achieve vanishingly small relaxation rates, either due insufficient available decoupling power or the presence of molecular motion. Therefore, the quantitative interpretation of recoupling experiments usually requires incorporation of the time scale of coherence losses

into numerical calculations.[14] To account for the attenuation of coherences, the exponential framework for describing coherence decay is employed in the π pulse recoupling simulations. An effective rate of decay Γ_p, which is taken to be the same for the longitudinal and transverse spin magnetization, is chosen to describe dephasing from heteronuclear couplings and random fluctuations in mechanical rotation and RF power. Likewise, an effective T_2 is also selected to match the observed rates of decay in transverse echo recovery experiments. The exponential model accounts for the observed multiple pulse echo intensities reasonably well in polycrystalline solids, and it provides a route to incorporating these influences explicitly into the analysis of dipolar evolution.

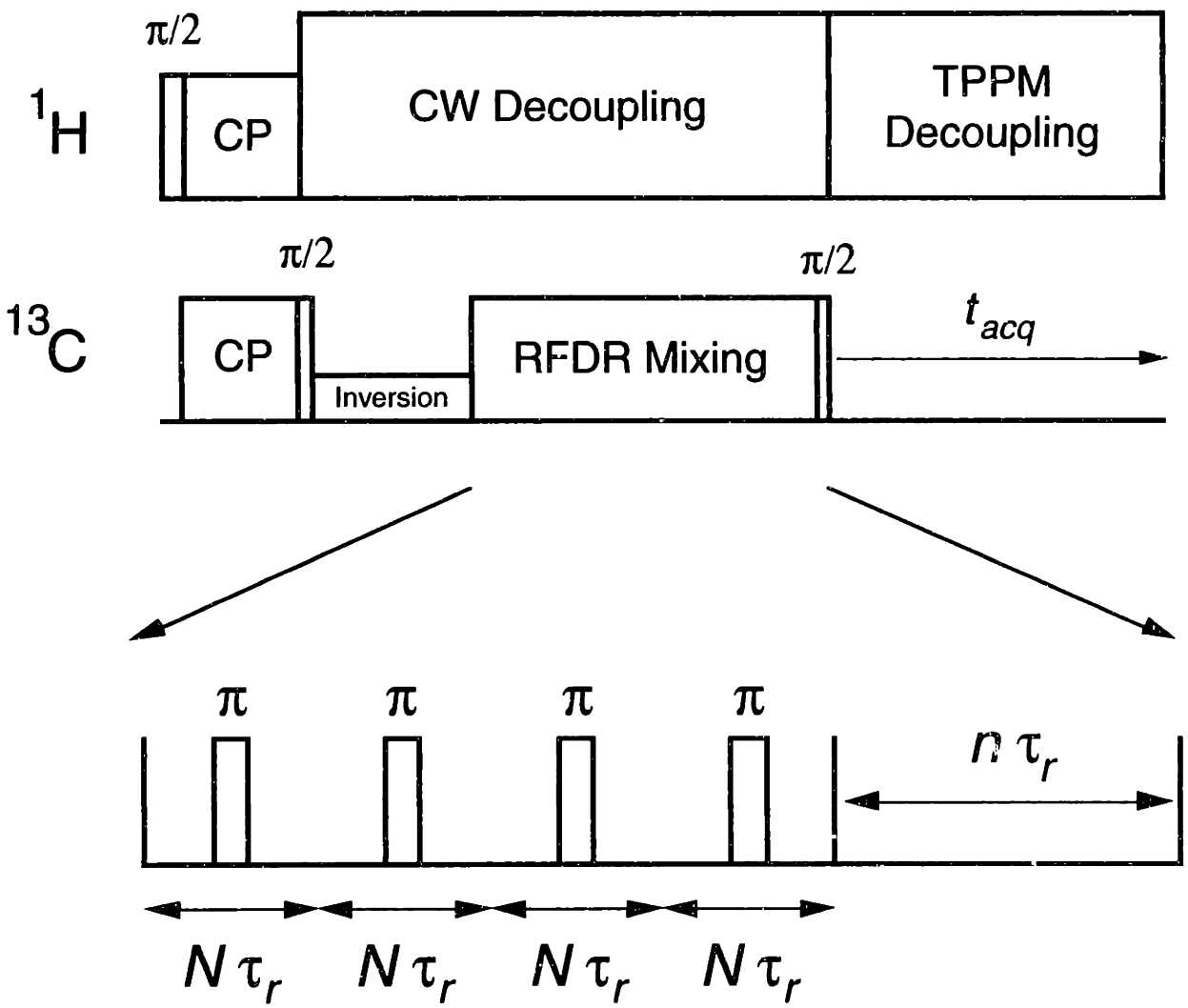

Figure 4-1. RFDR pulse sequence for spin echo recoupling.

One π pulse is applied per *N* rotor periods in a one-dimensional inversion exchange experiment.

The standard RFDR experiment is performed with N=1 and n=0. Pulses during mixing are phase cycled according to the *XY*-16 scheme.[40] The frequency-selective analog of the mixing sequence employs a non-zero value for n. For two-dimensional chemical shift correlation spectroscopy, an evolution period is inserted (between the ^{13}C CP pulse and π/2 storage pulse) and the inversion period removed.

Results

Polarization Decay During RFDR Mixing

A primary experimental consideration in attempting to measure weak dipole-dipole couplings with RFDR is the minimization of signal loss due to insufficient ^{1}H decoupling. Although effective relaxation rates can easily be measured and included in numerical simulations, rapid signal loss obscures weak coupling information and reduces the precision with which distance measurements can be performed. The experiments presented in Figure 4-2 illustrate that signal losses due to insufficient decoupling can be almost entirely eliminated by appropriate mismatch of the RF field amplitudes. Here we examine the $^{13}CH_2$ signal of [2-^{13}C,^{15}N]glycine, which serves as an excellent test case for decoupling because both the heteronuclear and homonuclear couplings are large (~20 kHz).[41,42]

This sample is particularly difficult to decouple, but separate experiments indicate that under otherwise identical conditions, the directly observed ^{13}C linewidth converges to a constant value (with the lower bound determined by B_0 inhomogeneity and other inhomogeneous broadening) as the on-resonance CW ^{1}H decoupling field is raised to ~130-140 kHz. Furthermore, we do not observe an experimentally significant (~0.5 Hz) narrowing observed upon increasing the field from 140 to 250 kHz. This suggests a complete decoupling of the ^{1}H-^{13}C interactions, which is desirable in the periods between π pulses in order to separate the signal loss due to interference effects alone. Therefore in the experiments here (Figure 4-2) we employ a large (150 kHz) ^{1}H decoupling field between the ^{13}C π pulses. The remaining loss mechanisms are limited to (1) depolarization due to the interference effect and (2) relaxation through pathways which do not

involve the protons (the "true" T_2 in the limit of infinite decoupling, which is greater than 100 ms, as indicated by 95% echo refocusing at 12.8 ms under optimal decoupling conditions).

The presentation of Figure 3b shows that the 3:1 mismatch is a necessary but not sufficient condition for minimal signal loss. For example, at the lowest ^{13}C field shown here (25 kHz), a steep ascent in echo intensity is observed as the ^{1}H field is raised to ~75 kHz; then the intensity increases at a slower rate until the ^{1}H field approaches the 130-140 kHz limit. When the 3:1 mismatch already implies a ^{1}H field of >130-140 kHz, the secondary effect is not significant. Note that although the total signal loss at the higher ^{13}C fields (71 and 100 kHz) with a mismatch of 2-3 is not dramatic, an additional consideration is that the total depolarization contact time is inversely proportional to the ^{13}C field (because the number of π pulses is constant), so the *rate* of polarization decay is well approximated by a function of mismatch alone.

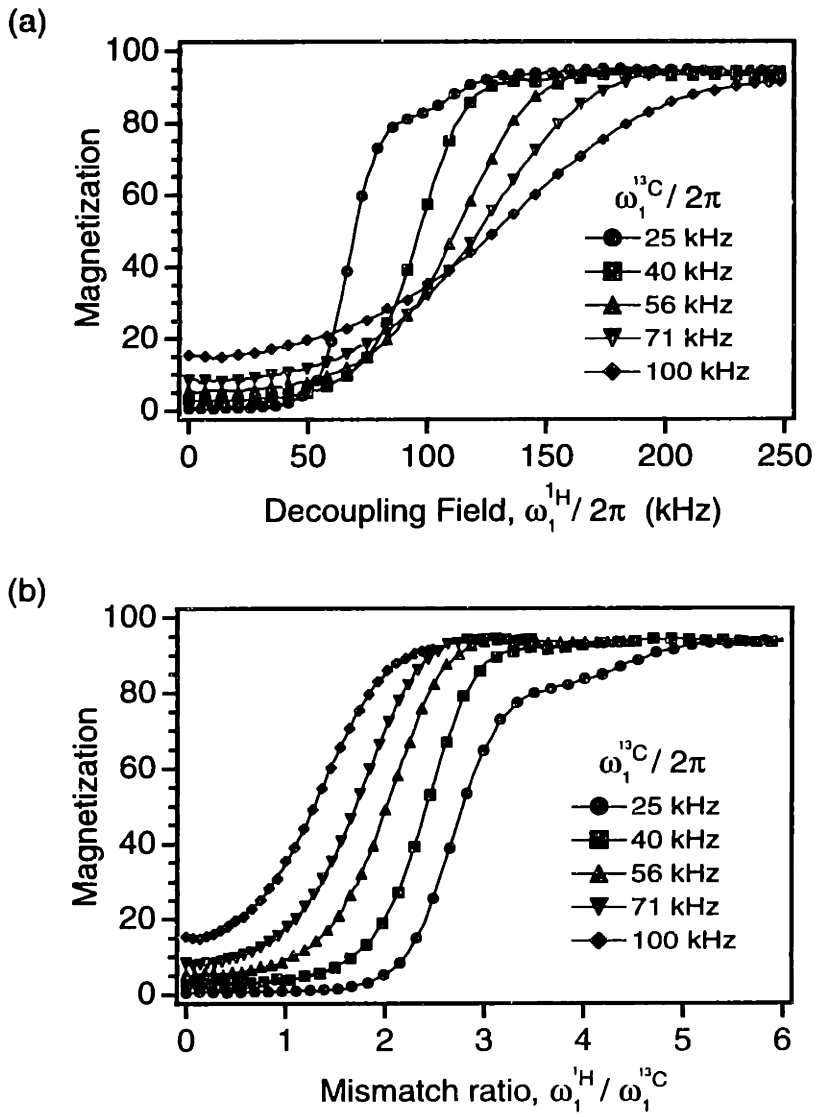

Figure 4-2. Experimental determination of magnetization loss under longitudinal RFDR mixing.

Total ^{13}C magnetization is monitored as a function of ^{13}C RF field (for the π pulses) and ^{1}H decoupling field (during the π pulses). The ^{1}H decoupling field between pulses is 150 kHz. Mixing time is 12.8 ms (64 τ_r at 5.000 kHz MAS) with one π pulse per rotor period. Curves are normalized to the signal obtained without a mixing period (CP and $\pi/2$ pulses alone). (a) Plotted as a function of ^{1}H RF amplitude. (b) Same data as (a), but plotted as a function of the ^{1}H to ^{13}C RF amplitude ratio. When $\omega_1^{1H}/\omega_1^{13C} \geq 3$, then minimal ^{13}C magnetization is lost due to depolarization to ^{1}H (see discussion in text).

Computationally, the results of Figure 3 can be described by a coherent three-spin model[43] in which all spin coherences involving the protons are eliminated between ^{13}C π pulses (simulation data not shown). This is a reasonable physical model because in most organic samples estimates of the correlation time for coherence decay within the proton reservoir ($\tau_c < 30\,\mu s$) are much shorter than the length of the rotor period (in this case, $\tau_r = 200\,\mu s$).[44] The simple three-spin model (without elimination of proton coherences between π pulses) predicts coherent behavior, such as refocusing of ^{1}H-^{13}C antiphase coherences via the *XY*-16 ^{13}C phase cycling and MAS averaging, which is not observed under the experimental conditions discussed here. Due to the complexity introduced by the large ^{13}C-^{1}H and ^{1}H-^{1}H couplings, additional resonance effects (where $\omega_1^{^1H}/\omega_1^{^{13}C} = 2n+1,\ n>1$) predicted by the zero-order theory of Eq. **(6-4)** do not lead to dramatic behavior in practice. Such effects may be more readily observed at high MAS rates or in samples where the ^{1}H-^{1}H couplings are weaker.

In experiments where the infinite decoupling limit is not practical, due to the combination of probe limitations and larger ^{1}H frequency offsets encountered at higher magnetic field, a compromise must be achieved which avoids the steep descent in echo intensity caused by the interference effect. This usually implies raising the ^{1}H decoupling field during the pulses alone to the maximum level which the probe can safely tolerate, and then strictly obeying the 3:1 mismatch in setting the ^{13}C π pulse.

Two-Dimensional RFDR ^{13}C-^{13}C Correlation Spectroscopy in Gly-Phe-Ala-Asp

Two-dimensional (2D) correlation spectra based on the recoupled interactions among neighboring ^{13}C spins can be acquired with π pulse longitudinal exchange because Zeeman polarizations are directly coupled via the zero-quantum coherences.[21] This is illustrated (Figure 8) in a 2D spectrum of the tetrapeptide achatin-II (Gly-Phe-Ala-Asp).[45,46] The relatively short mixing time of 1.55 ms produces crosspeaks between all directly bonded nuclei, including γ_{Phe} to the Phe aromatic ring (not shown). Only correlations within the Phe ring are not evident, due to the degeneracy in shifts and possibly motional effects.

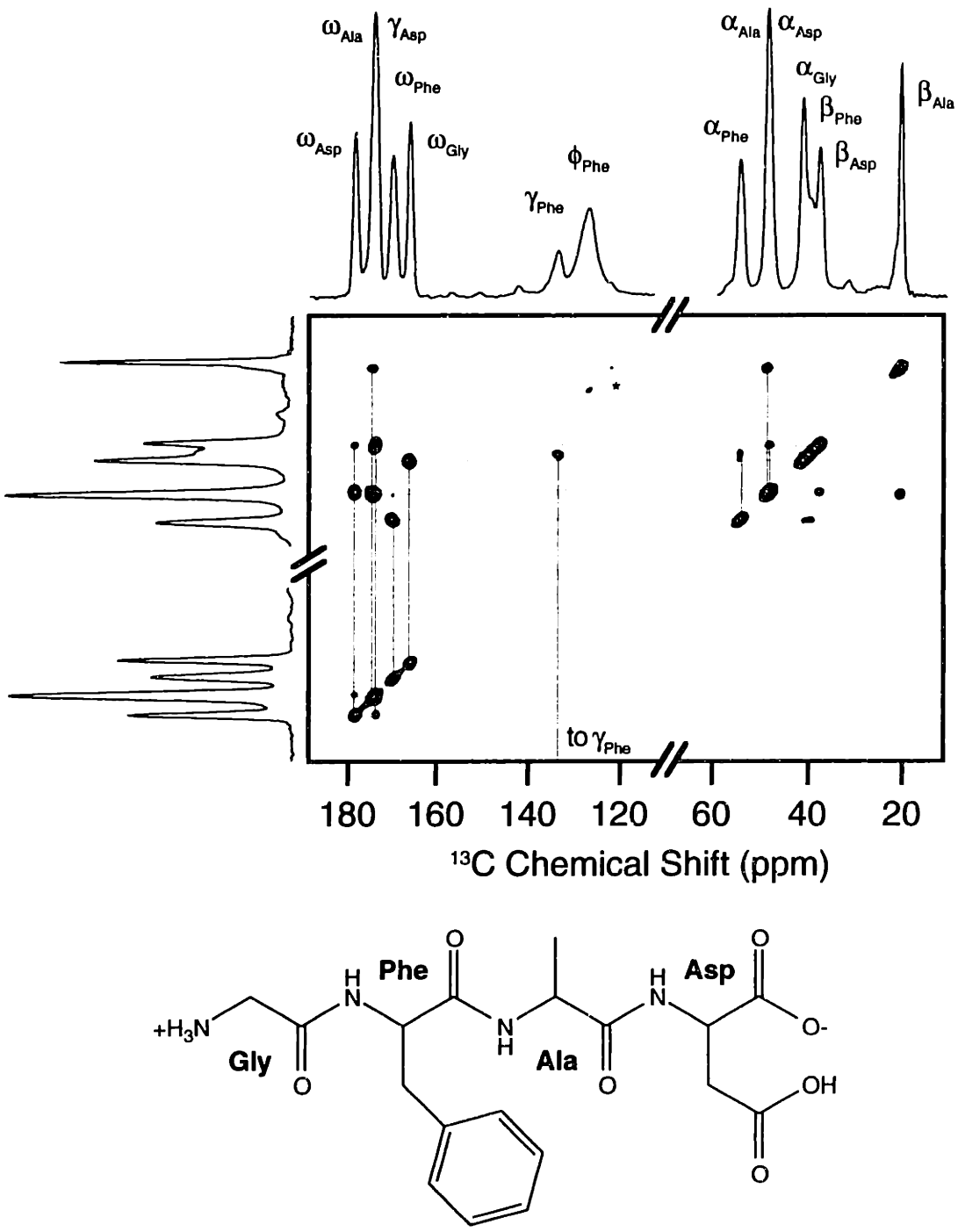

Figure 4-3. Two-dimensional ^{13}C-^{13}C chemical shift correlation spectrum and chemical structure of [U-^{13}C,^{15}N]achatin-II.

RFDR mixing time is 1.55 ms (16 π pulses). Contour levels are logarithmically spaced from 2% to 100% of the maximum peak height. The asterisk indicates a spinning sideband manifold.

Several interesting features of the spectrum are notable. First, ω-^{13}C to α-^{13}C and in one case (Asp) β-^{13}C to γ-^{13}C, correlations produce the largest crosspeaks (30-50% of the diagonal), owing to the proximity of these chemical shift differences to the m=1 rotational resonance condition. Although RFDR is most efficient in general at recoupling resonances separated approximately by rotational resonance conditions (e.g., ω-^{13}C to α-^{13}C at this MAS rate), one- and two-bond exchange also occurs in 1.55 ms between sidechain ^{13}C signals, because of differences in CSA tensor orientations among nearby resonances, as well as finite pulse recoupling effects. The latter effect dominates as the spinning speed increases, which increases the number of pulses applied per unit time. Some sidechain correlations (e.g., α_{Asp}-β_{Asp}, α_{Phe}-β_{Phe}) are substantially weaker (10-20% of diagonal) than the backbone correlations because the chemical shift differences are small; however, they are still easily distinguishable from the interresidue (ω_i-α_{i+1}) crosspeaks which arise at longer mixing times (not shown; a weak ω_{Phe}-α_{Ala} crosspeak rises just above the lower contour threshold in the spectrum shown). The α_{Ala}-β_{Ala} correlation is an intermediate case where the chemical shift difference is a substantial fraction of the MAS rate, and therefore the crosspeak is larger than the other sidechain correlations.

As the Asp motif illustrates, the rate of transfer through directly-bonded ^{13}C-^{13}C interactions is dominant, with a three-bond intraresidue correlation (ω_{Asp}-γ_{Asp}) easily discerned at contour levels where the interresidue three-bond correlations are not. We should emphasize that in no case do direct crosspeaks arise via weaker (<500 Hz) couplings when multi-step transfers

through intervening larger (500-2.2 kHz) couplings are feasible. Direct measurement of the weaker couplings requires the recoupling effect to be tailored so that the strong couplings are quenched, as in the selective sequence.[18,19,47]

In cases where uniformity of crosspeak intensities is desired, sequences which are less sensitive to chemical shift differences, such as DRAWS,[27,48,49] MELODRAMA,[26] and RIL[50,51] may be used for correlation spectroscopy. However, RFDR presents a very practical means of performing ^{13}C-^{13}C correlation spectroscopy because of its robust performance with respect to pulse errors, minimal loss of total polarization, and applicability at very high MAS rates (we have successfully performed such experiments at MAS rates of up to 19 kHz). In addition, the RFDR sequence (in the appropriate MAS regime) is ideally suited for emphasizing backbone ^{13}C-^{13}C correlations in peptides and proteins.

Experimental

NMR Spectroscopy

Experiments were performed with custom-designed NMR spectrometers and probes at several magnetic fields. Features common to all experiments discussed here are the application of *XY*-16 phase cycling[40] and maintenance of rotor-synchronization within ± 5 Hz with commercial spin rate controllers (Doty Scientific, Columbia, SC) unless indicated otherwise.

The ^{1}H and ^{13}C field-dependent echo intensity spectra presented in Figure 3 were acquired at 198.8 MHz ^{1}H frequency (50.0 MHz ^{13}C). A custom-designed triple resonance transmission line probe with a 5-mm Chemagnetics (Fort Collins, CO) spinner module was used. The transmission line design allows the tuning circuit voltages to be minimized so that maximum decoupling fields are not limited by high-voltage breakdown of circuit components.[52] The maximum decoupling field achievable with this probe for bursts of >25 ms is ~300 kHz with ~1 kW input power. Experiments presented in Figure 3 were carried out at 5 kHz MAS rate with a total of 64 π pulses (12.8 ms mixing time), and the intensities normalized to that acquired with cross polarization and $\pi/2$ pulses alone.

In the two-dimensional RFDR spectrum of achatin, the ^{1}H frequency is 397.8 MHz (100.0 MHz for ^{13}C); the spinning frequency was 10.309 kHz ± 5 Hz. A triple resonance transmission line probe with 4-mm Chemagnetics spinner module was used. During the mixing period (1.55 ms, 16 π pulses), continuous wave (CW) ^{1}H decoupling was implemented, with an amplitude of 110 kHz between pulses raised to 150 kHz during the pulses to achieve the appropriate 3:1 mismatch with the 10.0 μs ^{13}C π pulses. TPPM decoupling[42] at a reduced field amplitude (80

kHz, 5.8 μs pulse width and total phase difference of 15°) was used during the evolution and acquisition periods. The phase cycling method of Ruben and co-workers was used for pure phase detection in each dimension.[53]

The polycrystalline sample [2-^{13}C,^{15}N]glycine was diluted ten-fold in natural abundance material to reduce the influence of intermolecular dipole-dipole interactions, and recrystallized by slow evaporation from water. Labeled amino acids were purchased from Cambridge Isotope Laboratories (Andover, MA). The tetrapeptide achatin-II (Gly-L-Phe-L-Ala-L-Asp) [45,46,54] was synthesized via solution methods, which in this case provided far greater coupling efficiency and purity than solid phase methods. Free amino acids were protected with 9-fluorenylmethoxycarbonyl and then converted to their corresponding fluorides,[55] which were used in the stepwise solution synthesis. This method is efficient with high coupling yield, avoids potential difficulties with racemization, and allows purification with one-step preparative HPLC. The lyophilized U-^{13}C,^{15}N-achatin powder was packed in a 4-mm Chemagnetics rotor for NMR experiments.

Conclusions

The recoupling of homonuclear interactions using spin echo π pulse sequences and the observation of 1D and 2D exchange is a simple and accurate means of determining internuclear separations and correlations in many cases. Its advantages in measuring weak two-spin couplings include tolerance of the results with respect to RF pulse errors, such as the RF inhomogeneity (up to at least 5% in these experiments) and large CSA tensors, as well as the simplicity of analysis and implementation of experiments and analysis. For weak couplings, the

δ-function simulations are reasonably accurate and particularly easy to perform computationally. Compared to rotational resonance, two advantages of this method are that (1) inhomogeneous line-broadening does not reduce exchange or complicate its analysis,[1] and (2) spin inversion can be performed straightforwardly away from rotational resonance conditions. Although spin echo recoupling is most efficient near the m=1 and m=2 rotational resonance conditions, this range is quite suitable for many ^{13}C spectra, which correspond to a similar dispersion at typical magnetic field strengths. In the 2D experiments strong correlations are observed particularly between ω-^{13}C and α-^{13}C signals. Consequently, π pulse recoupling is a convenient way to obtaining two-dimensional correlation spectra, where spin polarization exchange proceeds via dispersion of magnetizations among neighboring spins. In two-dimensional correlation spectra, the migration of spin polarizations occurs via pathways dominated by the nearest neighboring dipole-coupled spins. In this way, a wealth of information concerning the molecular framework of molecules is obtained.

Acknowledgments

The authors wish to acknowledge support of this research by NIH grants RR-00995, GM-36810, GM-23403, and GM-23289. We also thank Prof. Shimon Vega for helpful discussions. Andrew E. Bennett would like to acknowledge predoctoral fellowship support from the National Science Foundation, and Janet M. Griffiths received postdoctoral fellowship support from the American Cancer Society.

References

(1) Griffiths, J. M.; Griffin, R. G. "Nuclear-magnetic-resonance methods for measuring dipolar couplings in rotating solids," *Anal. Chim. Acta* **1993**, *283*, 1081-1101.

(2) Bennett, A. E.; Griffin, R. G.; Vega, S. "Recoupling of Homo- and Heteronuclear Dipolar Interactions in Rotating Solids," In *Solid State NMR IV: Methods and Applications of Solid-State NMR*; B. Blumich, Ed.; Springer-Verlag: Berlin, **1994**; Vol. 33; 1-77.

(3) Pake, G. E. "NMR in Hydrated Crystals: Fine Structure of the 1H Line," *J. Chem. Phys.* **1948**, *16*, 327.

(4) van Willigen, H.; Griffin, R. G.; Haberkorn, R. A. "13C-13C Dipolar Spectra in Solids," *J. Chem. Phys.* **1977**, *67*, 5855.

(5) Herzog, B.; Hahn, E. L. "Spin echo double resonance," *Phys. Rev.* **1956**, *103*, 148.

(6) Stoll, M. E.; Vega, A. J.; Vaughn, R. W. "Heteronuclear dipolar modulated chemical-shift spectra for geometrical information in polycrystalline solids," *J. Chem. Phys.* **1976**, *65*, 4093-4098.

(7) Hester, R. K.; Ackerman, J. L.; Neff, B. L.; Waugh, J. S. *Chem. Phys. Lett.* **1976**, *36*, 1081.

(8) Haberkorn, R. A.; Stark, R. E.; van Willigen, H.; Griffin, R. G. "Determination of Bond Distances and Bond Angles by Solid State NMR: 13C and 14N NMR Study of Glycine," *J. Am. Chem. Soc.* **1981**, *103*, 2534.

(9) Andrew, E. R.; Bradbury, A.; Eades, R. G. "Nuclear magnetic resonance spectra from a crystal rotated at high speed," *Nature (London)* **1958**, *182*, 1659.

(10) Lowe, I. J. "Free induction decays of rotating solids," *Phys. Rev. Lett.* **1959**, *2*, 285-287.

(11) Schaefer, J.; Stejskal, E. O. "13C-NMR of Polymers Spinning at the Magic Angle," *J. Am. Chem. Soc.* **1976**, *98*, 1031.

(12) Meier, B. H.; Earl, W. "A double quantum filter for rotating solids," *J. Am. Chem. Soc.* **1987**, *109*, 7937-7942.

(13) Raleigh, D. P.; Levitt, M. H.; Griffin, R. G. "Rotational resonance in solid state NMR," *Chem. Phys. Lett.* **1988**, *146*, 71-76.

(14) Levitt, M. H.; Raleigh, D. P.; Creuzet, F.; Griffin, R. G. "Theory and simulations of homonuclear spin pair systems in rotating solids," *J. Chem. Phys.* **1990**, *92*, 6347-64.

(15) Munowitz, M. G.; Griffin, R. G. "Two-dimensional nuclear magnetic resonance in rotating solids: an analysis of line shapes in chemical shift-dipolar spectra," *J. Chem. Phys.* **1982**, *76*, 2848-2858.

(16) Gullion, T.; Schaefer, J. "Rotational-Echo Double-Resonance NMR," *J. Magn. Reson.* **1989**, *81*, 196-200.

(17) Maricq, M. M.; Waugh, J. S. "NMR in rotating solids," *J. Chem. Phys.* **1979**, *70*, 3300.

(18) Costa, P. R., *Spins, peptides, and Alzheimer's disease: Solid-state nuclear magnetic resonance investigations of amyloid peptide conformation*, Ph.D. Thesis, Massachusetts Institute of Technology, **1996**.

(19) Costa, P. R.; Sun, B. Q.; Griffin, R. G. "Rotational resonance tickling: Accurate internuclear distance measurements in solids," *J. Am. Chem. Soc.* **1997**, *119*, 10821-10830.

(20) Ok, J. H.; Spencer, R. G. S.; Bennett, A. E.; Griffin, R. G. "Homonuclear correlation spectroscopy in rotating solids," *Chem. Phys. Lett.* **1992**, *197*, 389-395.

(21) Bennett, A. E.; Ok, J. H.; Griffin, R. G.; Vega, S. "Chemical shift correlation spectroscopy in rotating solids: Radio-frequency dipolar recoupling and longitudinal exchange," *J. Chem. Phys.* **1992**, *96*, 8624-8627.

(22) Tycko, R.; Dabbagh, G. "Measurement of Nuclear Magnetic Dipole-Dipole Couplings in Magic Angle Spinning NMR," *Chem. Phys. Lett.* **1990**, *173*, 461-465.

(23) Gullion, T.; Vega, S. "A simple magic-angle spinning NMR experiment for the dephasing of rotational echoes of dipolar coupled homonuclear spin pairs," *Chem. Phys. Lett.* **1992**, *194*, 423-428.

(24) Joers, J. M.; Rosanske, R.; Gullion, T.; Garbow, J. R. "Detection of Dipolar Interactions by CROWN NMR," *J. Magn. Reson. A* **1994**, *106*, 123-.

(25) Klug, C. A.; Zhu, W.; Merritt, M. E.; Schaefer, J. "Compensated XY8-DRAMA Pulse Sequence for Homonuclear Dephasing," *J. Magn. Reson. A* **1994**, *109*, 134.

(26) Sun, B. Q.; Costa, P. R.; Kocisko, D. A.; Lansbury, P. T., Jr. ; Griffin, R. G. "Internuclear distance measurements in solid state nuclear magnetic resonance: Dipolar recoupling via rotor sychronized spin locking," *J. Chem. Phys.* **1995**, *102*, 702-707.

(27) Gregory, D. M.; Mitchell, D. J.; Stringer, J. A.; Kiihne, S.; Shiels, J. C.; Callahan, J.; Mehta, M. A.; Drobny, G. P. "Windowless dipolar recoupling--The detection of weak dipolar couplings between spin-1/2 nucleic with large chemical-shift anisotropies," *Chem. Phys. Lett.* **1995**, *246*, 654.

(28) Lee, Y. K.; Kurur, N. D.; Helmle, M.; Johannessen, O. G.; Nielsen, N. C.; Levitt, M. H. "Efficient dipolar recoupling in the NMR of rotating solids. A sevenfold symmetric radiofrequency pulse sequence," *Chem. Phys. Lett.* **1995**, *242*, 304-309.

(29) Fujiwara, T.; Ramamoorthy, A.; Nagayama, K.; Hioka, K.; Fujito, T. "Dipolar HOHAHA under MAS conditions for Solid-State NMR," *Chem. Phys. Lett.* **1993**, *212*, 84-84.

(30) Baldus, M.; Tomaselli, M.; Meier, B. H.; Ernst, R. R. "Broad-band polarization-transfer experiments for rotating solids," *Chem. Phys. Lett.* **1994**, *230*, 329-336.

(31) Sodickson, D. K.; Levitt, M. H.; Vega, S.; Griffin, R. G. "Broad band dipolar recoupling in the nuclear magnetic resonance of rotating solids," *J. Chem. Phys.* **1993**, *98*, 6742-6748.

(32) Griffiths, J. M.; Lakshmi, K. V.; Bennett, A. E.; Raap, J.; Vanderwielen, C. M.; Lugtenburg, J.; Herzfeld, J.; Griffin, R. G. "Dipolar correlation NMR spectroscopy of a membrane protein," *J. Am. Chem. Soc.* **1994**, *116*, 10178-10181.

(33) Böender, G. J.; Raap, J.; Prytulla, S.; Oschkinat, H.; de Groot, H. J. M. "MAS NMR structure refinement of uniformly C-13 encriched chlorophyll-A water aggregates with 2D dipolar correlation spectroscopy," *Chem. Phys. Lett.* **1995**, *237*, 502-508.

(34) Mehring, M. *Principles of High Resolution NMR in Solids;* 2nd ed.; Springer-Verlag: Berlin, **1983**.

(35) Slichter, C. P. *Principles of Magnetic Resonance;* 3rd ed.; Springer-Verlag: Berlin, **1990**.

(36) Hartmann, S. R.; Hahn, E. L. "Nuclear double resonance in the rotating frame," *Phys. Rev.* **1962**, *128*, 2042.

(37) Pines, A.; Gibby, M. G.; Waugh, J. S. "Proton enhanced nuclear induction spetroscopy," *J. Chem. Phys.* **1972**, *56*, 1776.

(38) Ishii, Y.; Ashida, J.; Terao, T. "13C-1H dipolar recoupling dynamics in 13C multiple-pulse solid-state NMR," *Chem. Phys. Lett.* **1995**, *246*, 439-445.

(39) Bennett, A. E., *Dipolar Decoupling and Recoupling in Solid State Nuclear Magnetic Resonance Spectroscopy*, Ph. D. Thesis, Massachusetts Institute of Technology, **1995**.

(40) Gullion, T.; Baker, D. B.; Conradi, M. S. "New, compensated Carr-Purcell sequences," *J. Magn. Reson.* **1990**, *89*, 479-484.

(41) Haeberlen, U. *High Resolution NMR in Solids: Selective Averaging*; Academic Press: New York, **1976**.

(42) Bennett, A. E.; Rienstra, C. M.; Auger, M.; Lakshmi, K. V.; Griffin, R. G. "Heteronuclear decoupling in rotating solids," *J. Chem. Phys.* **1995**, *103*, 6951-6958.

(43) Haeberlen, U. "NMR Basic Principles and Progress," *NMR Basic Principles and Progress* **1990**, *25*, 143.

(44) VanderHart, D. L.; Earl, W. L.; Garroway, A. N. "Resolution in 13C NMR of Organic Solids Using High-Power Proton Decoupling and Magic-Angle Sample Spinning," *J. Magn. Reson.* **1981**, *44*, 361-401.

(45) Ishida, T.; In, Y.; Inoue, M.; Yasuda-Kamatani, Y.; Minakata, H.; Iwashita, T.; Nomoto, K. "Effect of the D-Phe2 residue on molecular conformation of an endogenous neuropeptide achatin-I: Comparison of X-ray crystal structures of achatin-I (D form) and achatin-II (L form)," *FEBS Lett.* **1992**, *307*, 253-256.

(46) Ishida, T.; In, Y.; Doi, M.; Inoue, M.; Yasuda-Kamatani, Y.; Minakata, H.; Iwashita, T.; Nomoto, K. "Crystal structure and molecular conformation of achatin-I, an endogenous neuropeptide containing a D-amino acid residue," *Int. J. Peptide Protein Res.* **1992**, *39*, 258-264.

(47) Costa, P. R.; Sun, B.-Q.; Griffin, R. G. **1998**, manuscript in preparation.

(48) Gregory, D. M.; Mehta, M. A.; Shiels, J. C.; Drobny, G. P. "Determination of local structure in solid nucleic acids using double quantum nuclear magnetic resonance spectroscopy," *J. Chem. Phys.* **1997**, *107*, 28-42.

(49) Mehta, M. A.; Gregory, D. M.; Kiihne, S.; Mitchell, D. J.; Hatcher, M. E.; Shiels, J. C.; Drobny, G. P. "Distance measurements in nucleic acids using windowless dipoalr recoupling solid state NMR," *Solid State Nucl. Magn. Reson.* **1996**, *7*, 211-288.

(50) Baldus, M.; Meier, B. H. "Total correlation spectroscopy in the solid state. The use of scalar couplings to determine the through-bond connectivity," *J. Magn. Reson. A* **1996**, *121*, 65-69.

(51) Baldus, M.; Meier, B. H. "Broadband polarization transfer under magic-angle spinning: application to total through-space-correlation NMR spectroscopy," *J. Magn. Reson.* **1997**, *128*, 172-193.

(52) McKay, R. A., "Double-tuned single coil probe for nuclear magnetic resonance spectrometer," USA Patent #4,446,431, **1984**.

(53) States, D. J.; Haberkorn, R. A.; Ruben, D. J. "A two-dimensional nuclear Overhauser experiment with pure absorption phase in four quadrants," *J. Magn. Reson.* **1982**, *48*, 286-292.

(54) Kamatani, Y.; Minakata, H.; Iwashita, T.; Nomoto, K.; In, Y.; Doi, M.; Ishida, T. "Molecular conformation of achatin-I, an endogenous neuropeptide containing D-amino acid residue," *FEBS Lett.* **1990**, *276*, 95-97.

(55) Chaturvedi, N. C.; Fuller, W. D.; Sigler, D. F. *Biopolymers* **1983**, *22*, 2157.

Chapter 5. 2D and 3D ^{15}N-^{13}C-^{13}C NMR Correlation Spectroscopy for Chemical Shift Assignment in Solid Peptides

Abstract

We discuss strategies for resolving and assigning peptide backbone and sidechain resonances in solid peptides. New methods for 2D ^{13}C-^{13}C, ^{15}N-(^{13}C)-^{13}C and 3D ^{15}N-^{13}C-^{13}C chemical shift correlation spectroscopy are demonstrated in the tripeptide formyl-[U-^{13}C,^{15}N]-Met-Leu-Phe-OH (MLF). The combination of band-selective heteronuclear double cross polarization (DCP) and γ-encoded homonuclear double-quantum mixing generate crosspeak intensities 2-3 times greater than broadband heteronuclear transfers and γ-dependent homonuclear methods. The improved sensitivity of these experiments will facilitate application of 2D and 3D correlation methods to assignment of larger solid peptides and proteins.

Introduction

In recent years, many new techniques have emerged for use in the study of biomolecules by solid state NMR.[1] These methods have been applied to problems involving membrane proteins,[2,3] peptide aggregates such as β-amyloid,[4-7] and enzyme-substrate complexes,[8,9] revealing atomic level structural and dynamic information inaccessible to other techniques. In most cases such experiments have required the selective incorporation of isotopic labels (usually ^{13}C and/or ^{15}N) at particular residues, usually by site-directed mutagenesis or chemical synthesis. Certainly the value of such an approach lies in its ability to test specific biochemical hypotheses, provided that labels can be positioned appropriately. However, the same specificity that permits such focus also restricts measurements to portions of molecules that are presumed to have

functional relevance; this may possibly divert attention from other regions of unexpected importance. Moreover, site-specific labeling may be time-consuming and expensive, especially in the context of total structure determination, where multiple constraints per residue are required.

More general methods for efficient measurement of such constraints may be derived from experiments using uniformly-^{13}C,^{15}N-labeled (U-^{13}C,^{15}N) molecules. This strategy has been essential in the field of solution NMR.[10,11] The combination of biosynthetic labeling procedures and multidimensional correlation spectroscopy has led to more than 1,500 high resolution protein structures by solution NMR methods.[12,13] The first step in the structure determination procedure requires the use of relatively simple 2D experiments to assay resolution and chemical shift dispersion. Standard 2D methods, such as the ^{1}H-^{15}N HSQC,[14] permit rapid optimization of sample conditions, by assessing resolution before proceeding to more time-consuming 3D and 4D experiments. The 2D experiments also permit identification of important regions of molecules—such as portions involved in drug binding—by evaluating changes in chemical shifts of the entire protein in a single experiment.[15]

Clearly such methods would be useful in solids as well, in order to increase the rate at which structural and dynamic parameters can be measured. Interest has mounted in the problem of assignment and structure determination in U-^{13}C,^{15}N solid biological molecules. Some of the issues involved in assigning signals of solid proteins have been considered theoretically,[16] and partial assignments of selectively and uniformly labeled ubiquitin samples have been made via 2D methods at relatively low magnetic field strengths (300-400 MHz ^{1}H frequency).[17,18] Recently, high resolution (<0.5 ppm total linewidth) ^{13}C-^{13}C spectra of BPTI at high field (800 MHz) have been acquired, demonstrating the ability to resolve and assign many residues in a 2D experiment.[19] These developments indicate that assignment and subsequent structure determination of moderately sized solid proteins will be possible in the near future. In order to realize this potential, methods for correlation spectroscopy in solid U-^{13}C,^{15}N peptides and proteins must be refined. In particular, the issue of optimal polarization transfer must be

carefully addressed, because solid state experiments are inherently less sensitive than solution methods due to the present requirement of low-γ nucleus (usually ^{13}C or ^{15}N) observation.

Recently, we introduced 3D ^{15}N-^{13}C-^{13}C spectroscopy in solids, using the example of U-^{13}C,^{15}N-His.[20] Here we describe new approaches to solid state multi-dimensional chemical shift correlation spectroscopy, which are especially useful for resolving and assigning polypeptide backbone and sidechain resonances. We show that band-selective quasi-adiabatic heteronuclear DCP permits the efficient, directional transfer of polarization from amide ^{15}N signals to $^{13}C^{\alpha}$ or $^{13}C'$, yielding up to three-fold increases in sensitivity relative to the broadband experiments. This permits inter-residue (N[i]-C'[i-1]) and intra-residue (N[i]-C^{α}[i]) correlations to be measured in separate experiments, *both* of which may be performed faster and with higher sensitivity than the single broadband experiment. For homonuclear ^{13}C-^{13}C correlation, the recently developed SPC-5 sequence is employed.[21] SPC-5 provides broadband γ-encoded homonuclear double-quantum polarization transfer compatible with higher MAS rates than seven-fold sequences. [22-24] In the context of the ^{13}C-^{13}C correlation experiment, SPC-5 generates crosspeaks that often exceed the diagonal peak intensity, providing two- to three-fold improvements relative to γ-dependent methods. Combining SPC-5 homonuclear ^{13}C-^{13}C mixing with heteronuclear band-selective ^{15}N-^{13}C DCP transfer results in a 3D ^{15}N-^{13}C-^{13}C correlation experiment with greatly improved sensitivity. With this method, 3D spectra of the tripeptide formyl-Met-Leu-Phe-OH (MLF) have been acquired in 16-20 hours. Techniques described here should be useful for assaying conditions of optimal resolution in solid sample preparations, and for systematically improving chemical shift assignment procedures in solid state NMR.

Experimental

Tripeptide synthesis

Uniformly-^{13}C,^{15}N-labeled amino acids (Cambridge Isotope Laboratories, Andover, MA; ~96-99% ^{15}N, 98+% ^{13}C) were submitted to the American Peptide Company for custom synthesis of formyl-[U-^{13}C,^{15}N]-Met-Leu-Phe-OH,[25] using standard solid phase methods and HPLC purification. The lyophilized peptide was recrystallized by slow evaporation from isopropanol.

NMR Experiments

NMR spectra were acquired with a custom-designed spectrometer (courtesy of David Ruben) and triple-resonance MAS probe operating at ^{1}H frequency of 500.0 MHz (11.7 T). The probe design is based upon transmission line isolation and tuning circuits.[26-28] Final tuning and matching is achieved with custom-designed air-dielectric capacitors on the ^{1}H channel, and high-voltage fixed capacitors (American Technical Ceramics, Huntington Station, NY) and variable capacitors (Polyflon Company, Norwalk, CT) on the low frequency channels. One particularly relevant feature of this design is the fact the ^{13}C efficiency does not depend on whether the probe is double or triple tuned, implying a substantial sensitivity advantage in ^{13}C observe mode relative to most lumped element designs. Solenoid sample coils were mounted in a 4 mm spinner modules from Chemagnetics/Varian (Fort Collins, CO). The U-[^{13}C,^{15}N]-MLF sample (~15 mg, ~40 μmol) was packed in the center third of the rotor, over which the RF inhomogeneity was ~4-6% FWHM. Recycle delays were 2.5 s.

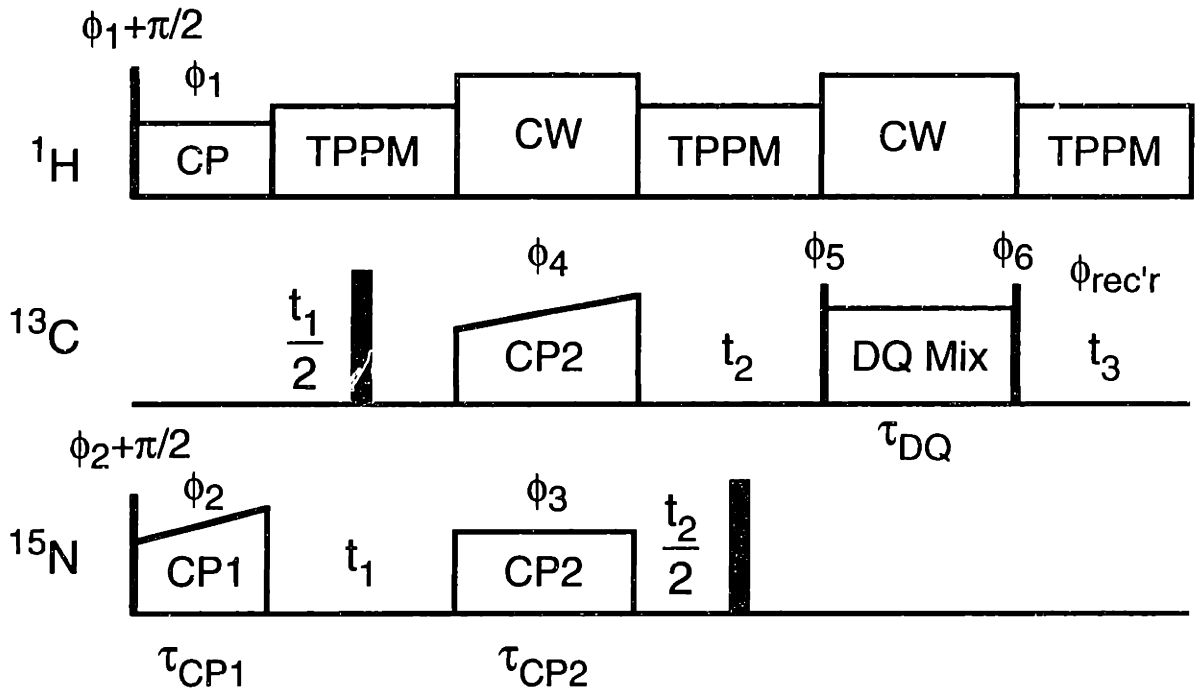

Figure 5-1. Pulse sequence for 3D ^{15}N-^{13}C-^{13}C correlation spectroscopy.

Narrow and wide solid rectangles represent $\pi/2$ and π pulses, respectively. Heteronuclear polarization transfer by quasi-adiabatic CP may be directed within or between residues by choice of ^{13}C RF frequency and field amplitude (see text for further details). The DQ mixing sequence (SPC-5,[21] POST-C7,[23] or CMR7[24]) is chosen for optimal performance at the desired MAS rate and decoupling conditions; SPC-5 was used in all cases shown here. Optional delays of one rotor period may be inserted between the DQ bracketing $\pi/2$ pulses and the DQ mixing, and the ^{1}H decoupling field reduced during this time, in order to attenuate residual transverse magnetization. Phase cycling is as follows: $\phi_1 = 1$, $\phi_2 = 13$, $\phi_3 = 1$, $\phi_4 = 11111111\ 33333333$, $\phi_5 = 2$, $\phi_6 = 11223344$, $\phi_{rec'r} = 13243142\ 31421324$, where 1 = X, 2 = Y, etc. Hypercomplex data is acquired by shifting ϕ_2 and ϕ_4 according to Ruben and co-workers.[29] Additional phase cycling of ϕ_3 and ϕ_5 may improve quadrature image suppression in cases where low-γ nuclei have rapid T_1 relaxation. Spin temperature alteration of ϕ_1 (13) is not necessary, and in practice results in 10-15% signal intensity losses compared to the scheme shown here.

All experiments employed some version of the pulse sequences presented in Figure 5-1, with an MAS rate of 8.9 kHz. Ramped CP from ^{1}H to ^{13}C or ^{15}N created the initial transverse polarization.[30] The direct ^{13}C or ^{15}N magnetization was spin-locked along the CP axis, and resulted in 10-15% increases in total signal intensity related to CP alone, due to the relatively short ^{13}C and ^{15}N T_1 and ^{1}H $T_{1\rho}$ relaxation. Spin locking fields were ~65 kHz for ^{1}H and ramped from 52-58 kHz for ^{15}N and ^{13}C; contact times were 700-850 μs. Total CP intensity demonstrated a strong dependence both on the amplitude of spin locking fields and the contact time in MLF at room temperature; particularly short (200-300 μs) $T_{1\rho}$ values in the Phe aromatic region resulted in non-optimal CP efficiency for those resonances. Chemical shift evolution periods incorporated TPPM decoupling[31] with typical values of pulse width and phase of 5.3 μs and 10°, using a ^{1}H rf setting corresponding to a 5.7 μs steady-state π pulse (~88 kHz).

The heteronuclear transfers were achieved with quasi-adiabatic ramped double cross polarization (DCP), using a constant ^{15}N rf field amplitude and a linear ramp of ±2.5-5 kHz on ^{13}C around the desired set of DCP conditions. In all cases the ^{15}N carrier was centered in the amide ^{15}N region at ~115-120 ppm. The ^{15}N amplitude, ^{13}C carrier frequency, and ^{13}C field amplitude were optimized to achieve particular DCP matching conditions, as shown in Table 5-1.

Table 5-1. Experimental Parameters for DCP Matching Conditions.[a]

Condition	Emphasis	^{15}N RF Amplitude (kHz)	^{13}C Carrier Frequency (ppm)	^{13}C RF Amplitude (kHz)	Downfield Match (ppm)[a]	Upfield Match (ppm)[a]
I	C^{α}-C'	34.0	115	43 to 38	95 to 275	135 to –45
II	C'-C^{α}	34.0	115	21.5 to 24.5	215 to 155	15 to 75
III	C^{α}-C^{β}	30.0	80	19 to 21.5	150 to 50	10 to 110
IV	C'	36.5	160	25.5 to 28.5	240 to 100	80 to 220

[a]Upfield and downfield match refer to the ranges of ^{13}C frequencies that satisfy the nearest appropriate dipolar (±1) DCP condition over the course of the ^{13}C ramp (described in more detail within text).

DCP conditions were selected first by considering the theoretical matching profile (as described below) and careful measurements of RF field distributions by nutation experiments[32] on both ^{15}N and ^{13}C. A relatively large ^{15}N field amplitude ($\omega_{1N} >> \Omega_N$) was chosen so that all ^{15}N resonances experienced the same effective field. The ^{13}C carrier frequency was approximately centered between the C' and C^{α} regions for the pseudo-broadband experiments (**I** and **II**) and offset by 30-50 ppm in the appropriate direction for band-selective experiments (**III** and **IV**). Enhanced selectivity could be achieved by larger asymmetry in the placement of ^{13}C carrier, but at the cost of reduced efficiency during the homonuclear DQ mixing period. Improved combinations of band-selective DCP and broadband SPC-5 may be achieved by coherent frequency switching during the mixing periods, but such schemes were not necessary here. The amplitude of the ^{13}C field was ramped so that a range of chemical shifts would be matched throughout the mixing period. Some empirical optimization of ramp range and amplitude is generally necessary, in order to account for the distribution of RF fields over the sample volume and to determine an optimal ramp range. Ramping the RF field implies that signals with chemical shifts in the middle of the range will experience the closest approximation to an effective field ramp through resonance.

Homonuclear DQ transfer was achieved by with the SPC-5 mixing sequence.[21] The DQ mixing time (τ_{DQ}) was either 8 or 12 τ_r; a multiple of 4 τ_r is required to compensate properly for CSA and RF inhomogeneity. Spectral intensities are determined by integration of the lineshape, and assume 100% ^{13}C and ^{15}N labeling efficiency, thereby underestimating the true CP and DQF efficiency due to imperfect isotopic enrichment (specifications for ^{15}N are ~96-99%, for ^{13}C 98+%). Standard phase cycles for the selection of double quantum (DQ) coherence were used.[33] Pure phase detection of the indirect dimensions was achieved with the algorithm or Ruben and co-workers.[29]

Sensitivity and Resolution in Multi-Dimensional Solid State Correlation Spectra

Successful implementation of correlation spectroscopy in solids requires optimal sensitivity and resolution. With improved decoupling methods,[31] total linewidths observed in dilute ^{13}C and ^{15}N spin systems at high field are determined primarily by inhomogeneous broadening due to chemical shift dispersion. In well ordered solids, such as microcrystalline powders, total ^{13}C and ^{15}N linewidths of <0.1-0.2 ppm have been observed at high field.[34-36] These linewidths compare well with typical ^{13}C and ^{15}N linewidths of proteins in solution, and suggest that sample preparation technique,[37] rather than the relaxation processes determining the homogeneous linewidth, may be the primary limitation to resolution in dilute-labeled solids. In U-^{13}C,^{15}N-labeled samples, several additional linebroadening mechanisms may contribute to the total linewidth: (1) heteronuclear scalar couplings; (2) residual homonuclear dipolar couplings (due to the proximity to rotational resonance conditions);[38] and (3) homonuclear scalar couplings. With use of heteronuclear decoupling and the appropriate choice of MAS rate, (1) and (2) are minimized, leaving primarily the homonuclear scalar couplings as the determinant of ^{13}C resolution in U-^{13}C,^{15}N-labeled samples. This contribution (30-60 Hz for one-bond couplings) is field independent and dominates the total linewidth in microscopically well-ordered materials,

provided that adequate ^{1}H decoupling fields and MAS rates are used. This implies that the *absolute* linewidth may often be independent of magnetic field: for ^{13}C, ~75-125 Hz; for ^{15}N, 25-50 Hz. Therefore *relative* linewidths of less than 1 ppm may be expected in many U-^{13}C,^{15}N-labeled solid proteins at high field (>600 MHz).

Provided that such resolution can be achieved, sensitivity will be the primary limitation to applying SSNMR methods in these systems. Increases in field strength assist in this matter as well, but sensitivity in solids is currently limited by the fact that no general technique for direct observation of high-resolution ^{1}H chemical shifts has yet been developed. The usual observation of ^{13}C rather than ^{1}H implies a decrease in sensitivity of approximately $(\gamma_H/\gamma_C)^{5/2}$, if the Boltzmann polarization is directly observed.[39] An additional factor of $(\gamma_H/\gamma_C)^{1/4}$ may be achieved if the sample coil quality factor is proportional to $\sqrt{\omega}$, as is often the case.[40] In practice, the use of CP from ^{1}H reduces the difference in sensitivity by a factor (γ_H/γ_C).[41] Therefore, in the case of ^{1}H versus ^{13}C observe, the difference may be $(\gamma_H/\gamma_C)^{3/2}$ to $(\gamma_H/\gamma_C)^{7/4}$, i.e., 8-11.3. For ^{1}H v. ^{15}N, the approximate factor is 32-56. The difference in sensitivity between ^{15}N and ^{13}C may be reduced somewhat by potentially narrower ^{15}N linewidths in U-^{13}C,^{15}N samples. In the MLF sample studied here, the ^{15}N linewidths are up to five times narrower than the ^{13}C linewidths; yet ^{13}C sensitivity is superior, as analyzed in more detail below. Figure 5-2 shows the 1D ^{15}N and ^{13}C spectra of MLF at 500 MHz ^{1}H frequency. Here we have not employed ^{15}N or ^{13}C decoupling during acquisition; the larger relative contribution of the ^{15}N-^{13}C scalar couplings to the ^{15}N linewidth suggests that the difference in overall sensitivity could be further reduced with such methods. Assignments for ^{13}C and ^{15}N (Table 5-2) in this peptide have been determined with a ^{15}N-labeled sample,[42] and are confirmed by experiments presented here. But our primary focus is the development of more sensitive methods for correlation spectroscopy, and for this purpose U-^{13}C,^{15}N-MLF serves as an excellent test case.

Table 5-2. MLF ^{13}C and ^{15}N Chemical Shift Assignments.[a]

Residue	N	C'	C^{α}	C^{β}	C^{γ}	C^{δ}
Met	125.5	172.2[b]	52.0	37.9	28.6	14.0
Leu	116.2	175.2	56.8	40.7	25.6	24.9, 19.6[c]
Phe	107.6	173.5	54.4	36.9	136.2	128.1[d]

[a]Chemical shifts are referenced to TMS using adamantane as a secondary ^{13}C standard (38.56 ppm $^{13}CH_2$ and 29.50 ^{13}CH).[43] The virtual liquid $^{15}NH_3$ zero point is calculated from the standardized gyromagnetic ratios of ^{15}N and ^{13}C.[44,45] Uncertainties are ±0.1 ppm. [b]The natural abundance formyl C' signal resonates at 165.3 ppm. [c]Leu $C^{\delta 1}$ and $C^{\delta 2}$ signals cannot be distinguished based on chemical shifts alone. [d]The broad, upfield portion of the Phe aromatic region is peaked at this value.

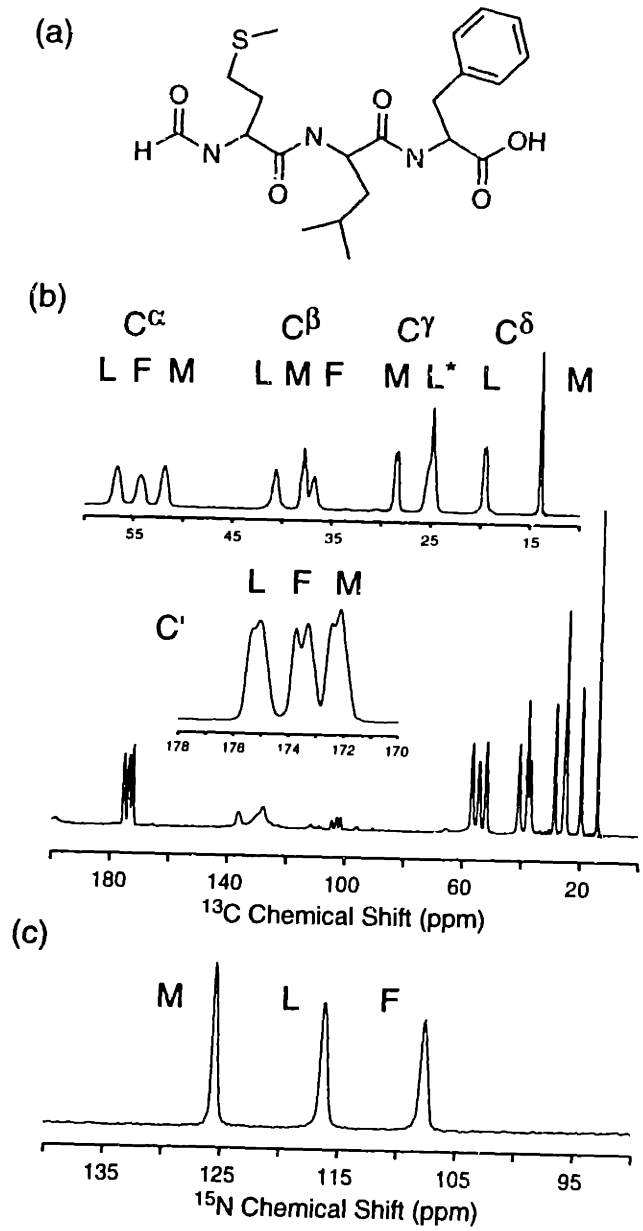

Figure 5-2. Primary structure and spectra of formyl-[U-^{13}C,^{15}N]Met-Leu-Phe-OH.

(a) Primary structure, (b) 1D ^{13}C and (c) ^{15}N CP-MAS spectra of formyl-[U-^{13}C,^{15}N]-Met-Leu-Phe-OH (MLF). Spectra were acquired at 500 MHz ^{1}H frequency with 128 transients (2.5 s recycle delay, 5 minutes total measurement time for each spectrum), using 88 kHz TPPM decoupling (5.3 usec pulse width, 10° total phase difference) at 8.9 kHz MAS rate. CP parameters were independently optimized for each spectrum. The ^{13}C spectrum was processed with 5 Hz (0.04 ppm) linebroadening in order to display all signals on the same vertical scale. The ^{15}N spectrum was processed without linebroadening.

In the context of multidimensional chemical shift correlation experiments, sensitivity is determined primarily by the efficiency of polarization transfers. Many high resolution 2D ^{13}C-^{13}C and ^{15}N-^{13}C chemical shift spectra in solids have been published. [46-51] In particular, 2D methods have been used to assign chemical shifts in solid peptides.[42,49,51,52] These experiments have incorporated some permutation of the pulse sequence shown in Figure 5-1, employing initial CP transfer from ^{1}H to one low-γ nucleus, and then one or two periods of indirect chemical shift evolution, connected by heteronuclear and/or homonuclear polarization transfer mixing periods. The substantive differences among the many implementations are primarily the polarization transfer method employed. The optimal choice may depend on MAS rate, available decoupling power, and desired bandwidth; most thus far have utilized broadband DCP or TEDOR-type heteronuclear polarization transfer and RFDR or spin diffusion for the homonuclear mixing.

These approaches have been successful in small molecules where sensitivity is not problematic. However, for application to larger molecules, improved transfer efficiency is essential. It is imperative to employ techniques that transfer the majority of polarization in each transfer step, in particular when multiple transfer steps are required. Otherwise extensions to multiple dimensions in solids have dubious value, due to the severe compromise in sensitivity made for purposes of increasing resolution. This requirement in solids is fundamentally no different than in solution, although achieving optimal transfer efficiency in solid state experiments is generally more demanding with respect to probe and spectrometer hardware (especially the available ^{1}H decoupling fields) and pulse sequence design.

An additional consideration that affects sensitivity in 2D and 3D solids experiments is the choice of observe nucleus, an issue not often debated in solution NMR because of the substantial advantages of ^{1}H observe. In solids, the choice between observing ^{15}N and ^{13}C in U-^{13}C,^{15}N peptides is not always clear, as discussed by Straus et al.[17] There the choice of ^{15}N observe in ^{13}C-^{15}N 2D experiments was motivated by the desire for improved resolution in the indirect ^{13}C dimension by homonuclear J decoupling.[48] Here we do not employ homonuclear decoupling,

and so consider primarily the sensitivity of the 1D ^{13}C and ^{15}N spectra (Table 5-3) under CP-MAS conditions. Despite the larger contributions of ^{13}C-^{13}C scalar couplings, resulting in absolute ^{13}C linewidths 2-5 times greater than ^{15}N (with the exception of the upfield Met C^{δ} signal, which does not have one-bond scalar couplings), sensitivity is usually at least a factor two better for ^{13}C than ^{15}N under the conditions explored here. With ^{13}C decoupling during ^{15}N observation, this difference may be reduced, since the heteronuclear ^{13}C-^{15}N scalar coupling accounts for a significant fraction of the total ^{15}N linewidth. However, we have chosen ^{13}C observe because the amide ^{15}N bandwidth is relatively narrow, and digitizing it in the indirect dimension minimizes the number of increments required for our 2D and 3D experiments, where phase cycling is rate-limiting. With gradients now available in solids probes,[53] this limitation may be alleviated and ^{15}N observe may prove favorable for some applications. But, because our probes presently do not include gradients, we have not directly compared ^{15}N versus ^{13}C observe in all 2D and 3D experiments. Instead we focus in the following on optimizing conditions for multi-dimensional ^{13}C observe experiments.

Table 5-3. MLF 1D ^{13}C and ^{15}N Spectral Resolution and Sensitivity

Signal	Linewidth (Hz, ppm)	Signal-to-Noise Ratio[a]	Linewidth (Hz) * S/N Ratio[b]
Met C^{α}	103, 0.82	600	61900
Leu C^{α}	110, 0.88	580	63600
Phe C^{α}	121, 0.97	460	55600
Leu C^{β}	86, 0.68	590	50200
Met C^{γ}	67, 0.54	860	57600
Leu $C^{\delta'}$	60, 0.48	1000	59900
Met C^{δ}	27, 0.22	2190	59700
Met N	25, 0.49	345	8450
Leu N	34, 0.67	265	8880
Phe N	35, 0.71	233	8260

[a]Signal-to-noise ratio for 128 shots CP-MAS experiment (2.5 s recycle delay, total measurement time of five minutes) at 8.9 kHz MAS rate. [b]For the ^{13}C listed here, the sensitivity factor is 58300 ± 4500 (one standard deviation); for ^{15}N, 8500 ± 300. The ratio of 6.85:1 is consistent with an overall receptivity proportional to $(\gamma_C / \gamma_N)^{2.1}$.

Heteronuclear Polarization Transfer in U-^{13}C,^{15}N-Peptides

Heteronuclear polarization transfer can be performed with π pulse methods such as TEDOR.[54] However, the maximum theoretical transfer efficiency with TEDOR is only ~52%, and in practice yields are typically less than 40%.[55,56] In addition, the recoupling of homonuclear dipolar couplings by multiple π pulses may cause irreversible loss of transverse ^{13}C polarization due to ZQ and DQ dephasing.[46,51,57] The effect of ^{13}C homonuclear couplings can be reduced by applying the majority of π pulses on the ^{15}N channel, but unless the principal axes of the ^{15}N CSA and ^{15}N-^{13}C dipolar couplings are co-linear, the recoupled ^{15}N CSA interaction

will also cause rapid dephasing of anti-phase coherence.[58] Usually in peptides, the ^{15}N CSA will be oriented 15-20° out of the ^{15}N-^{1}H vector, far from co-linear with the ^{15}N-$^{13}C^{\alpha}$ and ^{15}N-^{13}C' dipole vectors. In practice, the combination of ^{13}C-^{13}C homonuclear and/or ^{15}N CSA recoupling lead to inferior performance of TEDOR-based sequences in multi-spin systems.

A more appropriate choice for heteronuclear polarization transfer is DCP,[59,60] which is not effected, to first order, by the homonuclear coupling or CSA terms in the Hamiltonian. The original ^{15}N-^{13}C DCP experiments were developed by Schaefer and co-workers, for isolated spin pairs.[61,62] In order to apply DCP-like methods to 2D ^{15}N-^{13}C correlation spectroscopy, greater bandwidth was required, as first demonstrated with the RFDR-CP sequence.[63] Variable amplitude[64,65] and ramped[30] CP methods were designed primarily to improve ^{1}H-X transfer at high MAS, but have relevance to the ^{15}N-^{13}C problem as well. The use of ramped effective fields for ^{15}N-^{13}C transfer offers substantially improved efficiency (both theoretical and experimental) and compensation for RF inhomogeneity and chemical shift offset.[20,56] The dynamics of adiabatic heteronuclear transfer in low-γ two-spin systems have been investigated extensively in recent years, primarily by Ernst, Meier, and co-workers.[56,66-70] To briefly summarize the essential elements of the spin dynamics, we start with two-spin Hamiltonian in the rotating frame,[71]

$$H = \Omega_I I_z + \Omega_S S_z + \omega_{IS} 2 I_z S_z + \omega_{1I} I_x + \omega_{1S} S_x, \tag{1}$$

where in the general case all terms may be time-dependent. It proves convenient to transform the Hamiltonian into a tilted frame, as described by Baldus et al.[72],

$$H^T = U_T^{-1} H U_T \tag{2}$$

defined by the transformation operator

$$U_T = \exp\left[-i\left(\theta_I I_y + \theta_S S_y\right)\right], \tag{3}$$

where the inclination angle for each spin is determined by the applied RF field and the frequency offset according to

$$\theta_I = \arctan\left(\omega_{1I}/\Omega_I\right), \text{ and } \theta_I = \arctan\left(\omega_{1S}/\Omega_S\right). \tag{4}$$

The projection along the new z-axis is the effective field for each spin:

$$\omega_{I,eff} = \sqrt{\omega_{1I} + \Omega_I}\,, \text{ and } \omega_{S,eff} = \sqrt{\omega_{1S} + \Omega_S}\,. \tag{5}$$

The modulation of spin terms proceeds according to these effective fields, with a second transformation into the interaction frame

$$\tilde{H}^T = U^{-1} H^T U \tag{6}$$

where

$$U_T = \exp\left[-i\left(\omega_{I,eff} I_z + \omega_{S,eff} S_z\right)t\right] \tag{7}$$

This time modulation causes all terms to vanish (through first order in average Hamiltonian theory)[73] unless the time-dependence of spin terms resulting from Eq. 7 is cancelled by an equal spatial modulation frequency. This occurs when

$$\omega_{I,eff} - \omega_{S,eff} = n\omega_r. \tag{8}$$

In the context of peptide backbone polarization transfer from ^{15}N to ^{13}C, we assume that the ^{15}N carrier frequency is on resonance, and that matching conditions may be determined by selecting the ^{15}N (S spin) RF field amplitude, and ^{13}C (I spin) amplitude and frequency. Substituting the effective field expressions (Eq. 5) and solving for the ^{13}C RF amplitude, we find

$$|\omega_{1I}| = \sqrt{\left(n\omega_R + \omega_{1S}\right)^2 - \Omega_{1I}^2}\,,\ n = 0, \pm 1, \pm 2. \tag{9}$$

In the two-spin system, experimental sensitivity to the exact matching condition may be minimized by sweeping the carrier amplitude and/or frequency of each applied low-γ RF field to match a range of conditions. Small steps around the CP match condition compensate both for the distribution of RF within the coil and the distribution of couplings over the powder average, by passing through a range of matching conditions and inducing an effective composite rotation in the ZQ-subspace. If the change in effective field ranges from far off the CP condition in one direction, through resonance, and then to the other extreme, this amounts to adiabatic passage for a spin pair, as discussed by Meier and co-workers.[68]

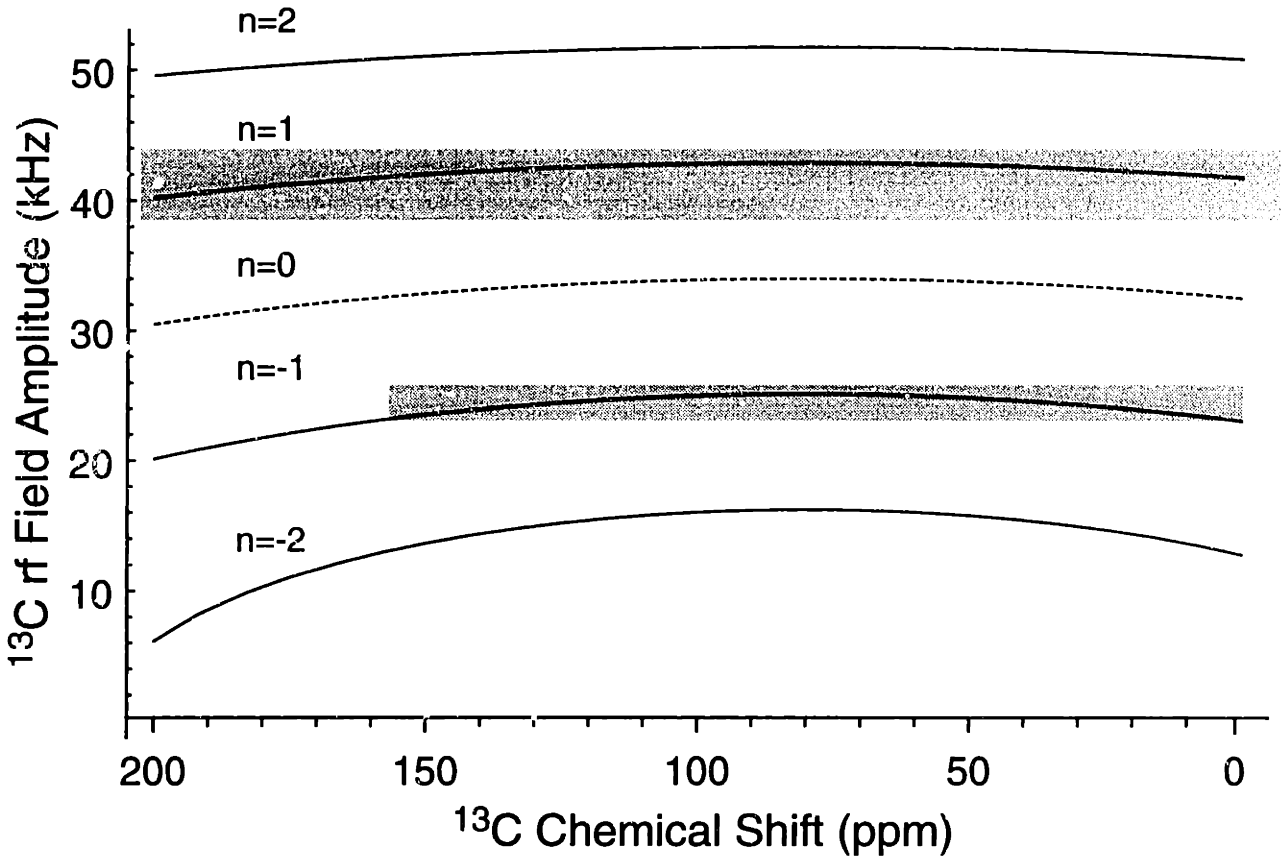

Figure 5-3. Broadband and band-selective DCP matching conditions.

The form of the DCP matching conditions are plotted as a function of the ^{13}C chemical shift offset. This example assumes a resonant ^{15}N RF field of 34 kHz and ^{13}C carrier frequency of 80 ppm. The desired range of ^{13}C chemical shifts to be matched defines the amplitude and carrier position to be used. The $n = 1$ condition is usually chosen when broadband matching is desired (i.e., larger amplitude ^{13}C RF), or the $n = -1$ condition (lower amplitude ^{13}C RF) is a narrower bandwidth is required. Here a 5 kHz ramp of ^{13}C RF field promotes transfer over the entire range of shifts. Narrower bandwidths can be selected by working in the SPECIFIC CP[72] limit of very low RF amplitude, with carrier positioned far off resonance, in order to maximize the slope of these curves; e.g., on the $n = -2$ curve near 200 ppm. (The dotted line (n=0 condition) represents transfer due to the scalar coupling.)[74]

However, in a multi-spin system, it is in general not possible to perform a truly adiabatic sweep through one matching condition without encountering another. We must consider multiple potential matching conditions, assuming that the total behavior can be described by a sum of two-spin effective Hamiltonians for each ^{13}C-^{15}N pair. In order to direct polarization from ^{15}N to $^{13}C^{\alpha}$ or $^{13}C'$ resonances, it is necessary to select only one bandwidth to satisfy the matching condition. At high (B_0) field, moderate RF fields (20-25 kHz) are sufficient to match the aliphatic or carbonyl regions separately; the entire bandwidth can be covered with ^{13}C fields of 35-45 kHz. An example, at 125 MHz ^{13}C frequency, is shown in Figure 5-3. Here the ^{15}N effective fields are assumed to be the same for all ^{15}N spins, which is reasonable based on the ~15-25 ppm (750-1,250 Hz at this field) range of ^{15}N chemical shifts in the amide region, which is much less than the assumed ^{15}N RF field (34 kHz). The ^{13}C RF amplitude and sweep size are chosen to match a range of chemical shifts, depicted by the boxes. Here we do not desire an extremely narrow bandwidth, so very weak applied ^{13}C fields are not necessary.

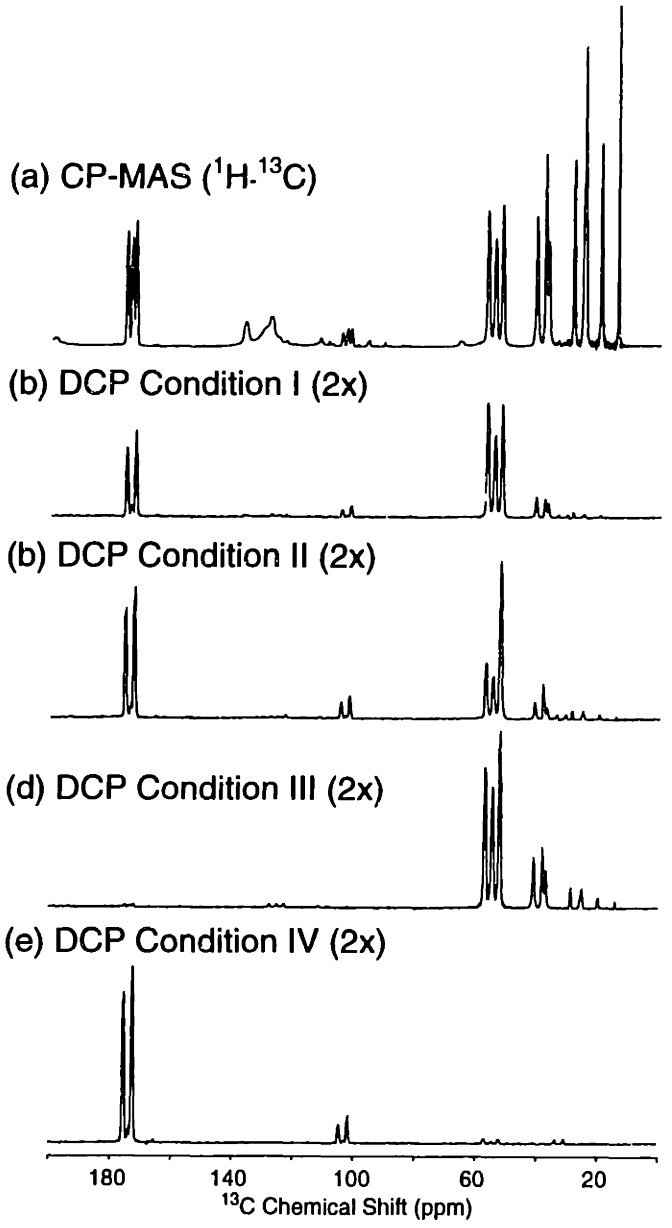

Figure 5-4. Comparison of various ^{15}N-^{13}C DCP conditions.

Different ^{15}N-^{13}C DCP matching conditions were chosen by setting ^{13}C carrier frequency and amplitude as described in the text. (a) CP-MAS reference spectrum (identical to Figures 1 and 3); (b) DCP condition **I** (6 ms), matching both C^{α} and C' regions with emphasis on C^{α}; (c) DCP condition **II** (8 ms), matching both C^{α} and C' regions but with emphasis on C'; (d) DCP condition **III** (10 ms), matching aliphatic region with the majority of transfer to C^{α} signals; and (e) DCP condition **IV** (8 ms), matching C' signals. The mixing times were optimized to give maximum intensity for each condition.

Experiments comparing the transfer efficiency using the various DCP conditions are shown in Figure 5-4. Normalized relative to direct ^{1}H-^{13}C CP, we find that the maximum total ^{15}N-^{13}C polarization transfer does not depend strongly on the direction of transfer; whether all C^{α} and C' resonances, only C', or only C^{α} are matched, the total intensity is similar. In cases where each ^{15}N source of polarization is matched to at least one directly bonded ^{13}C spin, the optimum polarization transfer in the ^{1}H-^{15}N-^{13}C (ramped) DCP experiment is ~14-17%, limited by the amount of polarization that can be transferred to ^{15}N. (Relative intensity data is summarized in Table 5-4.) However, the intensity of *individual* ^{13}C signals (from atoms directly bonded to ^{15}N) can be ~60-70% of the direct ^{1}H-^{13}C polarization, if each ^{15}N spin is matched to only a single ^{13}C. In order to compare the various implementations here, for all experiments the same series of optimization steps were performed. First, some suitable set of CP matching conditions was fulfilled (based on theory and known RF field profiles); second, rapid rotating frame depolarization due to CSA (rotary resonance recoupling)[75] and/or homonuclear ^{13}C-^{13}C (HORROR)[76] was avoided by shifting both ^{15}N and ^{13}C effective fields away from multiples of the MAS rate, with some empirical optimization; third, other experimental settings, such as decoupling field and mixing time, were optimized iteratively. Under these conditions, the ^{15}N source of polarization is limiting.

Whether this polarization is dispersed among all nearby spins, or focused in one direction, has clear implications for assignment strategy. In analogy with solution HN[i]-C^{α}[i]-C^{β}[i]/C'[i][77] and HN[i]-C'[i-1]-C^{α}[i-1][78,79] experiments, intra- or inter-residue correlations may be emphasized by choosing one range of CP conditions at a time. For the 2D ^{15}N-^{13}C and ^{15}N-(^{13}C)-^{13}C experiments, this band selectivity may decrease spectral overlap and increase sensitivity in the regions of greatest interest. For the 3D experiment, experiment time for a required digital

resolution is reduced, by minimizing the indirect ^{13}C dimension the bandwidth. The choice of N-C' or N-C^{α} CP conditions can generate spectra with >100:1 suppression of undesired C^{α} or C' signals, respectively. In addition, spectral editing procedures may suppress the undesired signal further.[80,81]

Table 5-4. Relative Intensity of 1D MLF Spectra (CP-MAS, DQF, DCP, and DQF-DCP).[a]

Experiment	C'	C^{α}	C^{β}	Upfield	Total
CP-MAS	100	100	100	100	100
DQF	31	50	46	28	35
DCP[b] I & DQF	10	13	6	<1	6
DCP I (C^{α}-C')	32	40	6	<1	14
DCP II (C'-C^{α})	49	33	7	<1	15
DCP III (C^{α})	<1	58	17	2	17
DCP IV (C')	68	<1	0	0	9

[a]Percentage of polarization observed relative to CP-MAS experiment with direct CP from ^{1}H. [b]For DCP, only $^{13}C'$ resonances directly bonded to ^{15}N nuclei are considered in the computation of relative efficiency. [c]These values consider all resonances, including the non-directly bonded CO resonance and the Phe aromatic ^{13}C signals.

Homonuclear Polarization Transfer

Solid state NMR methods for homonuclear polarization transfer and double-quantum filtering (DQF) have been developed extensively in recent years. Homonuclear methods benefit from rotating frame approaches such as C7,[22] which were discussed in Chapter 3 and in several recent publications.[21,23,24] Due to γ-encoding, the dependence on the powder distribution of crystallites is reduced relative to earlier methods, and POST-C7, CMR7, and SPC-5 have an upper threshold of ~73% total polarization transfer in two spin systems. Experimentally values of ~70% have been observed in U-^{13}C,^{15}N-Gly.[24] In examples presented here, DQF efficiencies

of up to 50% for spins with two neighbors are observed; this is a lower bound on the crosspeak intensity expected in the polarization transfer experiments, as discussed below. In principle, use of the scalar Hamiltonian can remove the dependence on orientation altogether, and techniques have been developed for isotropic scalar transfer, in analogy to TOCSY methods in solution.[82] However, the competition between scalar couplings of *c.* 50 Hz with typical rotating frame relaxation rates of ~50-100 s^{-1} limits the efficiency of scalar transfers relative to dipolar methods, which exploit dipolar couplings of >2 kHz. Even the *scaled* dipolar coupling (usually 400-500 Hz) derived from a typical windowless mixing sequence is an order of magnitude larger than the scalar coupling. In our hands (at 500 MHz ^{1}H frequency), under conditions explored here, we have observed optimal TOBSY transfer of approximately 10-15%, whereas polarization transfer mediated by the dipolar Hamiltonian may exceed 50-60%. The less favorable rotating frame relaxation rates typically observed for many applications (e.g., membrane proteins) may possibly exacerbate this differential efficiency of scalar- versus dipolar-mediated transfers.

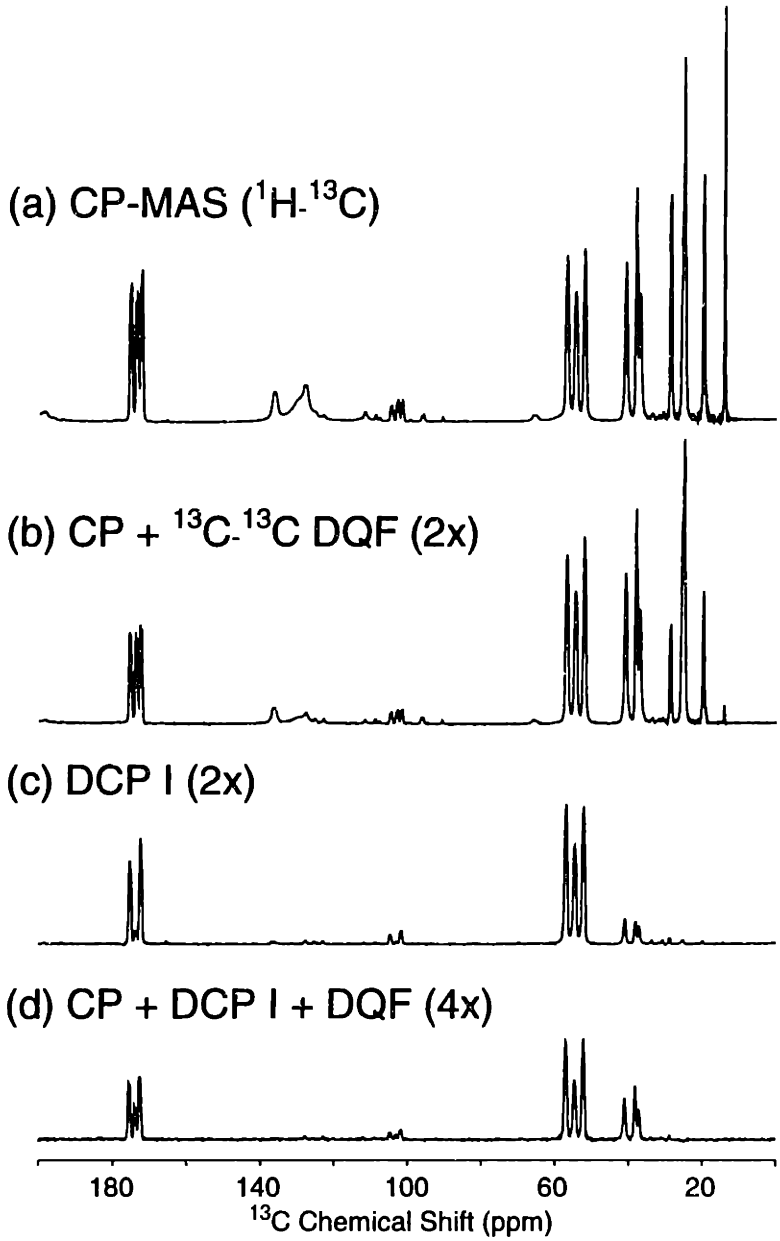

Figure 5-5. 1D ^{13}C DQF, DCP, and DQF-DCP spectra.

These spectra are used to optimize polarization transfer and estimate the crosspeak intensities expected in 2D and 3D spectra. (a) CP-MAS directly from ^{1}H, as in Figure 1; (b) CP with DQ filtration using SPC-5, with 4 τ_r (0.4446 ms) excitation time; (c) DCP condition **I** as described in text; (d) DCP condition **I** and SPC-5 DQF. The observed intensities of (b) and (c), relative to the reference spectrum in (a), approximate the crosspeak intensity expected in the 2D ^{13}C-^{13}C and ^{15}N-^{13}C spectra. The total intensity in (d) corresponds is a lower bound for crosspeak intensity in the 3D ^{15}N-^{13}C-^{13}C experiment (discussed in text). Integrated intensities for several signals are shown in Table 5-4.

The DQF spectrum in Figure 5-5(b) provides total intensity of ~35% relative to the direct ^{1}H-^{13}C CP reference. (See Table 5-4 for list of DQF efficiencies for each signal type.) The total DQ excitation time of 444.6 μs is chosen in order to minimize the cancellation of polarization due to multi-step evolution during the DQ reconversion process. These dynamics are explained in greater detail in Ref. 21. Figure 7 of that reference is an INADEQUATE spectrum of alanine, where weak negative crosspeaks to, for example, the C^{β} frequency in the direct dimension are correlated to the C'-C^{α} DQ coherence in the indirect dimension. This results from evolution of the C'-C^{α} DQ coherence under the three spin Hamiltonian during the reconversion block of the sequence. These dynamics are dominated by the directly bonded ~2.2 kHz interactions. If the indirect dimension of such an INADEQUATE spectrum is projected (as in the MLF DQF reference spectrum of Figure 5-5(b)), partial cancellation of the C^{β} peak in the direct dimension would occur. For this reason, the 1D DQF spectrum is a *lower* bound on the crosspeak intensity in the 2D ^{13}C-^{13}C correlation experiment, where both positive and negative crosspeaks are observed. Peaks that would be partially cancelled in the 1D DQF spectrum appear as two-bond crosspeaks in the 2D spectrum. The fact that particular types of correlations (e.g., C'-C^{β}, C'-C^{α}, C^{α}-C^{β}) occupy mostly separate portions of the 2D spectrum implies that cancellation will not occur in general.

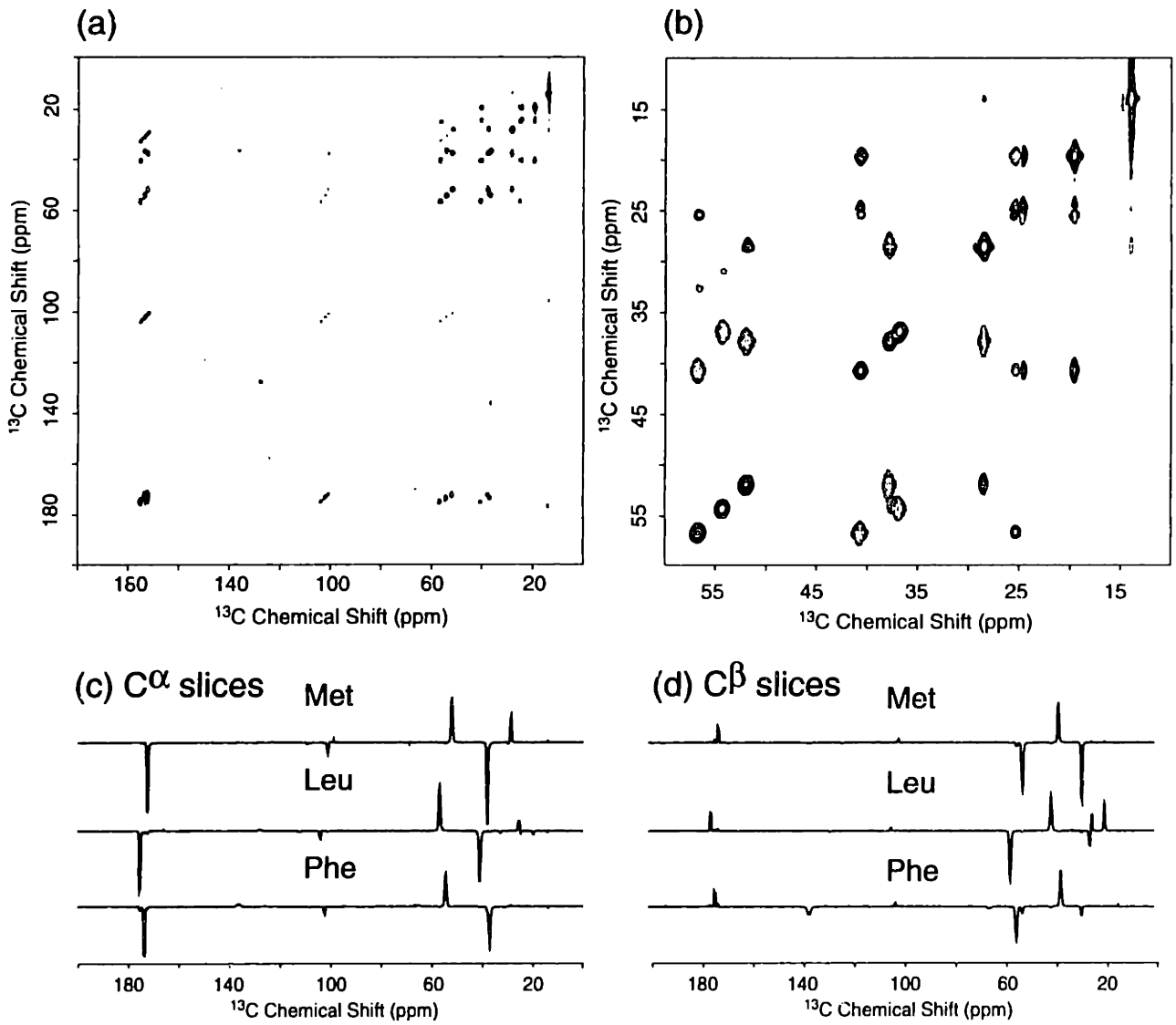

Figure 5-6. MLF 2D ^{13}C-^{13}C correlation spectrum with 12 τ_r (1.3488 ms) SPC-5 mixing time.

(a) Complete bandwidth; (b) expansion of aliphatic region; (c) slices through the C^{α} resonances in the indirect dimension for each residue (52.0 ppm for Met, 56.8 ppm for Leu, 54.4 ppm for Phe); (d) slices through the C^{β} resonances in the indirect dimension for each residue (37.9 ppm for Met, 40.7 ppm for Leu, 36.9 ppm for Phe). Sidechain spin topology can be determined by the sign and frequency of upfield resonances. For the Leu C^{β} slice, partial cancellation near 25 ppm occurs due to the overlap of C^{γ} and C^{δ}.

2D ^{13}C-^{13}C Spectra

Figure 5-6 shows the 2D ^{13}C-^{13}C correlation spectrum of MLF with 1.3488 ms mixing time. This mixing time, slightly longer than that used for the aforementioned DQF 1D spectrum, is used for the 2D experiment because negative crosspeaks do not overlap with positive ones, except in one case (Leu C^{γ}-C^{δ}). In general the spin topology in peptides implies that cancellation in the C'-C^{α} and C^{α}-C^{β} regions is not expected, because each first-order crosspeak lies in a distinctive region of the spectrum. Cancellation is more likely among upfield aliphatic resonances, where overlapping regions of the C^{β} and C^{γ} shifts are possible.

In comparison to laboratory frame 2D experiments in peptides,[51] superior crosspeak intensities are observed because of the efficiency of the γ-encoded DQ transfer. Some slices, such as the Met C^{α}, Met C^{β}, and Leu C^{β}, exhibit more than 80% of the remaining intensity in crosspeaks. (Signal loss due to insufficient decoupling is approximately 10%.) The high overall transfer efficiency is attributable to the fact that powder-average is over only β_{PR}; in the typical three-spin topology (e.g., C'-C^{α}-C^{β}), the ~120° C-C-C bond angle results in efficient C^{α}-C' transfer for most crystallites for which the C^{α}-C^{β} vector lies along the magic-angle (i.e., $\beta_{PR} = 0$), and vice versa. At this mixing time, connectivities over two bonds can easily be distinguished; approximately 5-10% of the remaining polarization in each slice has been transferred two bonds away. In addition to the total efficiency of polarization transfer, the sign of the crosspeaks leads to distinctive patterns that can be used to identify residue type. In cases where overlap of C^{α} and C^{β} shifts is possible, the sign of the crosspeaks to C' will remove ambiguity, provided cancellation does not occur. This feature will be useful in the 2D ^{15}N-(^{13}C)-^{13}C experiment as well.

2D ^{15}N-(^{13}C)-^{13}C Spectra

Combining the ^{15}N-^{13}C DCP and ^{13}C-^{13}C SPC-5 portions of the pulse sequence, with evolution only during t_1, results in the ^{15}N-(^{13}C)-^{13}C spectra depicted in Figure 5-7. The experiment here is implemented with three different mixing conditions. First, broadband DCP (condition **I**) is used in conjunction with the 8 rotor period SPC-5 mixing time. The DCP period is somewhat shorter (3 ms) than that used for Figure 5-4, but still results in greater than 90% of the optimal one-bond N-C transfer. This shorter mixing time is used in order to minimize transfer to intraresidue C^β and C', and interresidue C^α signals, which would complicate the appearance of each ^{15}N frequency slice. The ratio of C^α:C' polarization prior to ^{13}C-^{13}C mixing is ~3:2, which is appropriate because the C^α polarization transfer will be dispersed in two directions. At the ~900 μs mixing time used here, the C^α polarization is divided almost equally among C^α, C', and C^β. The C' resonances are coupled only to a single C^α and therefore on the timescale of mixing, less than half the C' polarization is transferred. The resulting spectrum shows, in each N[i] slice, positive crosspeaks to C'[i-1] and C^α[i], and negative crosspeaks to C^α[i-1], C'[i], and C^β[i]. The distinctive pattern of chemical shifts produced in this experiment should be useful for uniquely identifying residue types.[83,84]

The second implementation of the 2D ^{15}N-(^{13}C)-^{13}C experiment involves band selective transfer to C^α resonances, using DCP condition **III**. At the mixing time of 4 ms, little polarization is transferred to interresidue C^α signals, so each slice consists primarily of intra-residue C'-C^α-C^β shifts in the characteristic negative-positive-negative pattern. Transfer to C^γ at this SPC-5 mixing time (0.8992 ms) is minimal, but can be improved by increasing the mixing time to 1.3488 ms. This additional intensity permits slightly longer SPC-5 mixing times to be used without a sacrifice in sensitivity, relative to Figure 5-7(a). Transfer further out the sidechain at the same mixing time can be achieved by reducing the amplitude of the ^{13}C RF during SPC-5 (i.e., synchronizing the SPC-5 mixing period to three rotor periods).[21]

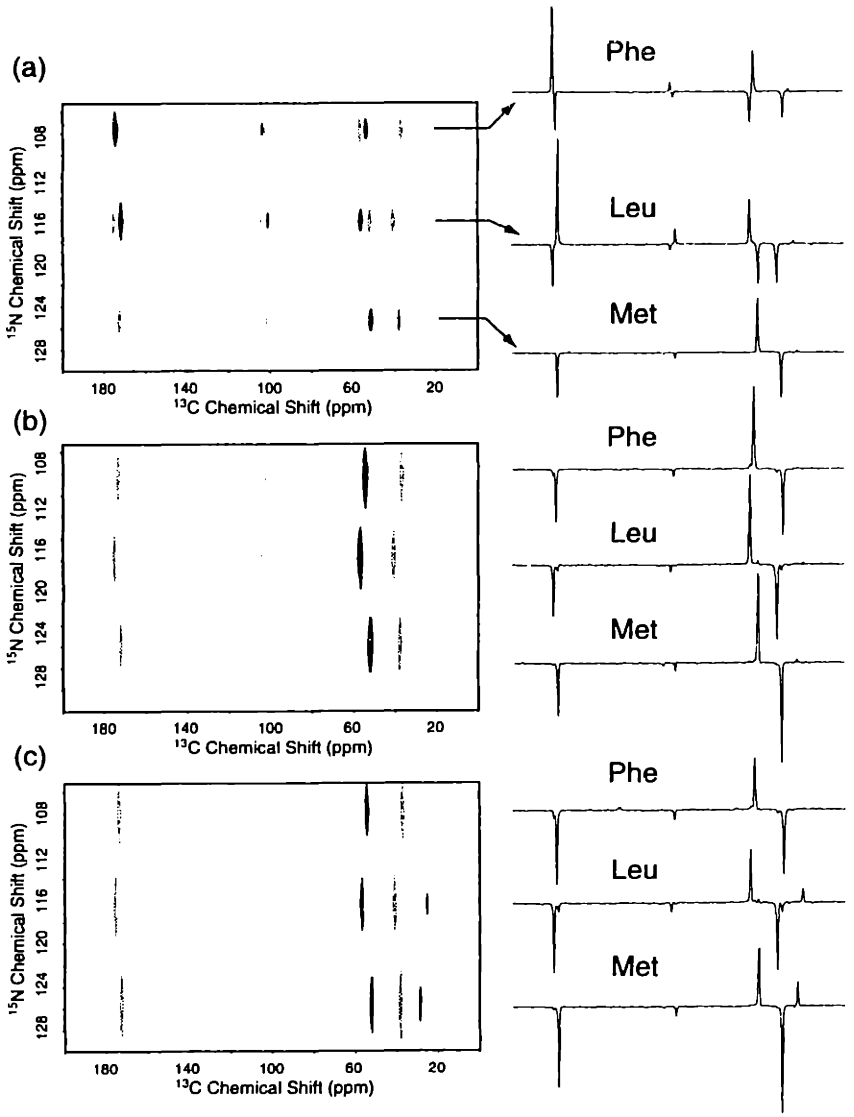

Figure 5-7. MLF 2D ^{15}N-(^{13}C)-^{13}C correlation spectra.

Various DCP and DQ mixing conditions are employed. (a) Broadband, C^{α}-emphasized CP (3 ms, condition **I**) with 0.8992 ms SPC-5 mixing; (b) C^{α}-only CP (4 ms, condition **III**) with 0.8992 ms SPC-5 mixing; (c) C^{α}-only CP (4 ms, condition **III**) with 1.3488 ms SPC-5 mixing. The relatively short, 3-4 ms ^{15}N-^{13}C DCP transfer times are used in order to minimize two-bond (interresidue N[i]-C^{α}[i-1] and intraresidue N[i]-C'[i]) transfer, which would cancel negative DQ-transferred polarization. The differences in ^{15}N linewidth between (a) and (b)-(c) are due to minor changes in the sampling and processing of the ^{15}N dimension; however, all spectra (a)-(c) have been scaled according to the same reference spectrum and therefore peak intensities in the slices may be compared directly.

3D ^{15}N-^{13}C-^{13}C Spectra

Complete 3D spectra were acquired for both the broadband DCP condition **I** (Figure 5-8) and for the band-selective DCP condition **III** (Figure 5-9). This required a difference in placement of the ^{13}C carrier frequency. Changing the carrier from 80 to 115 ppm was found to have only a modest effect on the homonuclear polarization transfer profile. Other than the DCP conditions and carrier frequency, all other experimental and processing parameters are identical. The appearance of the broadband 3D spectra can be appreciated by considering the strips in Figure 5-8(a) and Figure 5-9(a), in comparison to the 2D spectra shown in Figure 5-7. The 2D version of the experiment (or equivalently, the F2 projection of the 3D dataset) shows multiple ^{15}N frequency slices, each coupled to 3-5 ^{13}C signals. Intra- and inter-residue C^{α} and C' signals, though distinguishable by parity, may be nearly degenerate. Indeed, in a more congested spectrum overlapping positive and negative crosspeaks are likely.

In the 3D version of the experiment, each direct dimension ^{13}C slice at a given ^{15}N frequency is uniquely mapped to the $^{13}C^{\alpha}$ frequency to which the heteronuclear transfer took place. Therefore each plane in the 3D displays a single strong positive peak at the ^{15}N-$^{13}C^{\alpha}$-$^{13}C^{\alpha}$ frequency, along with negative peaks at ^{15}N-$^{13}C^{\alpha}$-$^{13}C^{\beta}$ and ^{15}N-$^{13}C^{\alpha}$-$^{13}C'$. Other than the small interresidue ^{15}N-$^{13}C^{\alpha}$ transfer resulting in weak crosspeaks, for example, at the Phe(^{15}N)-Leu($^{13}C^{\alpha}$)-Leu($^{13}C^{\alpha}$) frequency, the ^{15}N-^{13}C slices at each C^{α} frequency are dominated by intraresidue chemical shift patterns, and therefore are easily interpreted for this simple example. Similarly, interresidue connectivities are immediately evident in the C' planes. Again each ^{15}N frequency maps primarily to a single interresidue $^{13}C'$ frequency, and appears as a positive peak in the $^{13}C'$ plane, along with a negative peak at each ^{15}N-$^{13}C'$-$^{13}C^{\alpha}$ frequency.

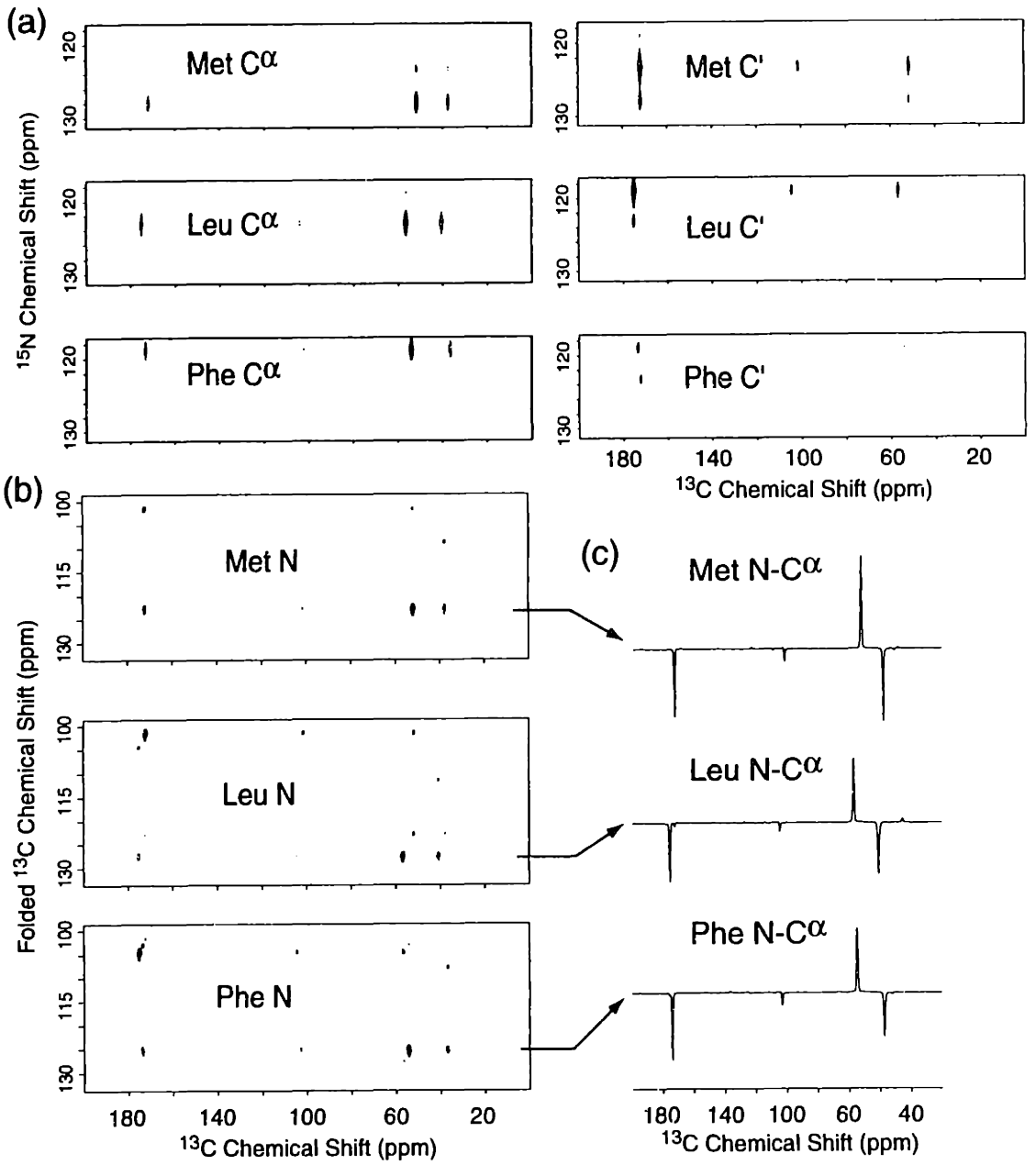

Figure 5-8. 3D ^{15}N-^{13}C-^{13}C Correlation Spectrum of MLF.

2D ^{13}C-^{13}C and ^{15}N-^{13}C planes are shown for several ^{15}N and ^{13}C chemical shifts. (a) ^{15}N-^{13}C planes at the Met, Leu, and Phe C$^{\alpha}$ and C' shifts in F2; (b) ^{13}C-^{13}C planes at Met, Leu, and Phe ^{15}N shifts in F1; (c) slices through the N-C$^{\alpha}$ frequencies in F1 and F2 for each residue. The (^{15}N-)^{13}C'-^{13}C' peaks appear in the upper left corner of each ^{13}C-^{13}C plane, due to the folding in t_2.

The ^{13}C-^{13}C planes at each ^{15}N chemical shift show the expected positive crosspeaks to the $C^{\alpha}[i]$ and $C'[i-1]$ signals, and negative crosspeaks to $C^{\alpha}[i-1]$, $C^{\beta}[i]$, and $C'[i]$. Each residue also shows a weak, positive crosspeak on the C^{β}-C^{β} diagonal frequency corresponding to intraresidue, two-bond transfer from ^{15}N to $^{13}C^{\beta}$. The ^{15}N-$^{13}C^{\alpha}$ slices shown in part (c) of each figure illustrate the absolute sensitivity of the experiments. Because the 3D processing routines include linebroadening and forward linear prediction, comparisons of signal-to-noise measurements between the 1D and 3D spectra are not valid, but relative signal-to-noise in the two 3D spectra are. We find that each N-C^{α}-C^{α} signal is enhanced by at least 10%, and in the case of Met, over 100%, in the N-C^{α}-C experiment relative to the N-C-C experiment, despite the fact that the longer mixing times of the former experiment transfer a larger fraction of the total polarization to C^{β} and $C^{\alpha}[i-1]$ signals.

Table 5-5. Relative Sensitivity of N-C^{α}-C^{α} Signals in 3D Spectra.[a]

Residue	Broadband N-C-C	Band-Selective N-C^{α}-C
Met	620	1280
Leu	490	550
Phe	580	770

The smaller enhancement of Leu C^{α} is largely due to the fact that a greater number of ^{13}C nuclei within 3-4 Å of the Leu ^{15}N nucleus (i.e., sidechain resonances) are within the bandwidth of DCP condition III. Lower RF fields, faster MAS, and/or shorter mixing times would reduce the distribution of ^{15}N polarization to the Leu sidechain.

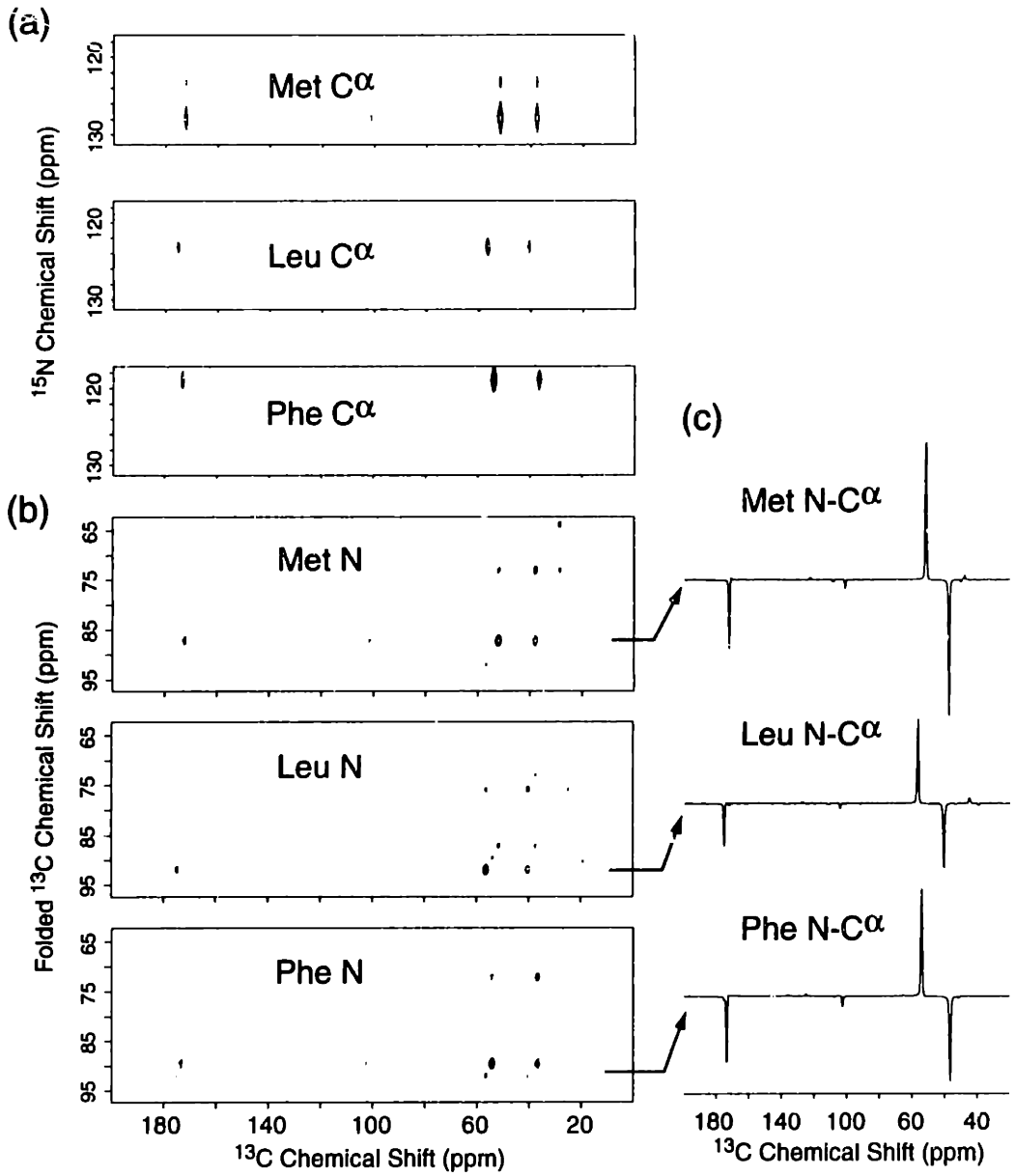

Figure 5-9. 3D ^{15}N-^{13}C$^{\alpha}$-^{13}C Correlation Spectrum of MLF.

(a) 2D ^{15}N-^{13}C planes at ^{13}C$^{\alpha}$ frequencies, (b) ^{13}C-^{13}C planes at ^{15}N frequencies, and (c) ^{13}C slices at ^{15}N-^{13}C$^{\alpha}$ frequencies from the 3D ^{15}N-^{13}C$^{\alpha}$-^{13}C experiment.. Conditions are identical to the broadband experiment shown in Figure 5-8, with the exception of the DCP condition, which in this case selectively transfers ^{15}N polarization to the aliphatic region (i.e, DCP condition **III**) with a mixing time of 10 ms. In addition to increases in C$^{\alpha}$ transferred polarization, C$^{\beta}$ resonances are polarized directly from ^{15}N. The ^{13}C carrier is placed at 80 ppm.

Conclusions

We have shown that polarization transfer efficiency in multi-dimensional solid state ^{15}N-^{13}C-^{13}C spectra can be enhanced significantly by the use of band-selective heteronuclear polarization transfer and the γ-encoded DQ homonuclear mixing sequence SPC-5. The improvements in the heteronuclear transfer step arise largely from the fact that total polarization is limited by the ^{1}H-^{15}N CP step, and in part because ^{15}N-^{13}C DCP conditions can be more carefully optimized when transfer to a narrower bandwidth is required. Greater selectivity may be achieved by using high MAS rates, lower amplitude RF fields, smaller ranges of effective field ramps, and shorter contact times. Directed transfers from ^{13}C to ^{15}N are likely to benefit less from band-selective methods, but any 3D experiment with two ^{13}C dimensions will require at least one ^{15}N to ^{13}C transfer, and therefore the principles demonstrated here will be essential for most 3D schemes. The ordering of ^{15}N-^{13}C-^{13}C permits one transfer step to be homonuclear, which is highly efficient due to γ-encoded SPC-5 step. The compatibility of SPC-5 with somewhat higher MAS rates than the compensated C7 analogs POST-C7 and CMR7 also assists in this matter.

To date, few 3D chemical shift correlation experiments have been implemented in solids, and none in larger peptides and proteins, despite the potential advantages of such methods for improving resolution and facilitating assignment, because of the time-consuming nature of these experiments. These restrictions may be alleviated by the improved polarization transfer efficiency demonstrated here. In addition to the increased signal amplitude of each increment, the overall time required for a 3D experiment may be reduced because only the C^{α} or C' bandwidth must be digitized in the indirect dimension. Here we used identical sampling of the indirect ^{13}C chemical shift dimension for both the 3D ^{15}N-^{13}C-^{13}C and ^{15}N-$^{13}C^{\alpha}$-^{13}C experiments, but this choice was strictly for purposes of making a direct sensitivity comparisons in these spectra. For most applications, the reduced bandwidth in the indirect dimension will permit faster acquisition of a desired digital resolution. In cases where sensitivity is limiting, as in

larger proteins, band-selective transfers will be an even greater advantage. Assuming that the ^{15}N bottleneck limits total transfer to $^{13}C^{\alpha}$ or $^{13}C'$, and that crosspeak intensity is reduced by a factor of two in the broadband experiment, two separate 3D experiments—^{15}N-$^{13}C^{\alpha}$-^{13}C and ^{15}N-$^{13}C'$-^{13}C—may be performed in the same amount of time, with $\sqrt{2}$ better sensitivity than the single ^{15}N-^{13}C-^{13}C experiment. The separate experiments emphasizing intra- and inter-residue connectivities can be recombined after acquisition, to yield data with reduced degeneracy and improved information content. These approaches are likely to be used extensively as solid state NMR becomes a mainstream method for structure determination in uniformly labeled proteins.

Acknowledgments

This work was performed in collaboration with Morten Hohwy. We thank Mei Hong for acquiring the U-^{13}C,^{15}N-MLF sample.

References

(1) Griffin, R. G. "Dipolar recoupling in MAS spectra of biological solids," *Nat. Struct. Biol.* **1998**, *5*, 508-512.

(2) Marassi, F. M.; Ramamoorthy, A.; Opella, S. J. "Complete resolution of the solid-state NMR spectrum of a uniformly 15N-labeled membrane protein in phospholipid bilayers," *Proc. Natl. Acad. Sci. USA* **1997**, *94*, 8551-8556.

(3) Marassi, F. M.; Opella, S. J. "NMR structural studies of membrane proteins," *Curr. Opin. Struct. Biol.* **1998**, *8*, 640-648.

(4) Lansbury, P. T., Jr.; Costa, P. R.; Griffiths, J. M.; Simon, E. J.; Auger, M.; Halverson, K. J.; Kocisko, D. A.; Hendsch, Z. S.; Ashburn, T. T.; Spencer, R. G. S.; Tidor, B.; Griffin, R. G. "Stuctural model for the β amyloid fibril: Interstrand alignment of an antiparallel β sheet comprising a C-terminal peptide," *Nat. Struct. Biol.* **1995**, *2*, 990-998.

(5) Griffiths, J. M.; Ashburn, T. T.; Auger, M.; Costa, P. R.; Griffin, R. G.; Lansbury, P. T., Jr. "Rotational resonance solid-state NMR elucidates a structural model of pancreatic amyloid," *J. Am. Chem. Soc.* **1995**, *117*, 3539-46.

(6) Benzinger, T. L. S.; Gregory, D. M.; Burkoth, T. S.; Miller-Auer, H.; Lynn, D. G.; Botto, R. E.; Meredith, S. C. "Propagating structure of Alzheimer's .beta.-Amyloid(10-35) is parallel .beta.-sheet with residues in exact register," *Proc. Natl. Acad. Sci. USA* **1998**, *95*, 13407-13412.

(7) Gregory, D. M.; Benzinger, T. L. S.; Burkoth, T. S.; Miller-Auer, H.; Lynn, D. G.; Meredith, S. C.; Botto, R. E. "Dipolar recoupling NMR of biomolecular self-assemblies: determining

inter- and intrastrand distances in fibrilized Alzheimer's beta-amyloid peptide," *Solid State Nucl. Magn. Reson.* **1998**, *13*, 149-166.

(8) Christensen, A. M.; Schaefer, J. "Solid-state NMR determination of intramolecular and intermolecular P-31-C-13 distances for shikimate 3-phosphate and [1-C-13]glyphosate bound to enolpyruvylshikimate-3-phosphate synthase," *Biochem.* **1993**, *32*, 2868-2873.

(9) McDowell, L. M.; Klug, C. A.; Beusen, D. D.; Schaefer, J. "Ligand geometry of the ternary complex of 5-enolpyruvylshikimate-3-phosphate synthase from rotational-echo double-resonance NMR," *Biochem.* **1996**, *35*, 5395-5403.

(10) Wüthrich, K. *NMR of Proteins and Nucleic Acids*; John Wiley and Sons: New York, **1986**.

(11) Wüthrich, K. "The second decade--into the third millennium," *Nat. Struct. Biol.* **1998**, *5*, 492-495.

(12) Abola, E. E.; Sussman, J. L.; Prilusky, J.; Manning, N. O. "Protein Data Bank archives of three-dimensional macromolecular structures," In *Methods in Enzymology*; C. W. Carter, Jr. and R. M. Sweet, Ed.; Academic Press: San Diego, **1997**; Vol. 227; 556-571.

(13) Sussman, J. L.; Lin, D.; Jiang, J.; Manning, N. O.; Prilusky, J.; Ritter, O.; Abola, E. E. "Protein Data Bank (PDB): Database of three-dimensional structural information of biological macromolecules," *Acta Cryst.* **1998**, *D54*, 1078-1084.

(14) Bodenhausen, G.; Ruben, D. J. "Natural abundance nitrogen-15 NMR by enhanced heteronuclear spectroscopy," *Chem. Phys. Lett.* **1980**, *69*, 185-189.

(15) Shuker, S. B.; Hajduk, P. J.; Meadows, R. P.; Fesik, S. W. "Discovering high-affinity ligands for proteins: SAR by NMR," *Science* **1996**, *274*, 1531-1534.

(16) Tycko, R. "Prospects for resonance assignments in multidimensional solid-state NMR spectra of uniformly labeled proteins," *J. Biomol. NMR* **1996**, *8*, 239-251.

(17) Straus, S. K.; Bremi, T.; Ernst, R. R. "Experiments and strategies for the assignment of fully 13C/15N-labelled polypeptides by solid state NMR," *J. Biomol. NMR* **1998**, *12*, 39-50.

(18) Hong, M. In *Experimental NMR Conference*; Orlando, FL, **1999**;

(19) McDermott, A. E.; Polenova, T.; Coker, G.; Montelione, G.; Zilm, K. W. "NMR resonance assignments of uniformly (13C,15N)-labeled proteins in the solid state," **1999**, manuscript in preparation.

(20) Sun, B. Q.; Rienstra, C. M.; Costa, P. R.; Williamson, J. R.; Griffin, R. G. "3D 15N-13C-13C chemical shift correlation spectroscopy in rotating solids," *J. Am. Chem. Soc.* **1997**, *119*, 8540-8546.

(21) Hohwy, M.; Rienstra, C. M.; Jaroniec, C. P.; Griffin, R. G. "Fivefold symmetric homonuclear dipolar recoupling in rotating solids: Application to double quantum spectroscopy," *J. Chem. Phys.* **1999**, *110*, 7983-7992.

(22) Lee, Y. K.; Kurur, N. D.; Helmle, M.; Johannessen, O. G.; Nielsen, N. C.; Levitt, M. H. "Efficient dipolar recoupling in the NMR of rotating solids. A sevenfold symmetric radiofrequency pulse sequence," *Chem. Phys. Lett.* **1995**, *242*, 304-309.

(23) Hohwy, M.; Jakobsen, H. J.; Edén, M.; Levitt, M. H.; Nielsen, N. C. "Broadband dipolar recoupling in the nuclear magnetic resonance of rotating solids: A compensated C7 pulse sequence," *J. Chem. Phys.* **1998**, *108*, 2686-94.

(24) Rienstra, C. M.; Hatcher, M. E.; Mueller, L. J.; Sun, B.-Q.; Fesik, S. W.; Herzfeld, J.; Griffin, R. G. "Efficient multispin homonuclear double-quantum recoupling for magic-angle spinning NMR: ^{13}C-^{13}C Correlation spectroscopy of U-^{13}C-erythromycin A," *J. Am. Chem. Soc.* **1998**, *120*, 10602-10612.

(25) Morfew, A. J.; Tickle, I. "Formyl-methionine-leucine-phenylalanine, C21H31N3O5S," *Cryst. Struct. Comm.* **1981**, *10*, 781.

(26) Holl, S. M.; McKay, R. A.; Gullion, T.; Schaefer, J. "Rotational-echo triple-resonance NMR," *J. Magn. Reson.* **1990**, *89*, 620-626.

(27) McKay, R. A., "Double-tuned single coil probe for nuclear magnetic resonance spectrometer," USA Patent #4,446,431, **1984**.

(28) Schaefer, J.; McKay, R. A., "Multi-tuned single coil transmission line probe for nuclear magnetic resonance spectrometer," USA Patent #5,861,748, **1999**.

(29) States, D. J.; Haberkorn, R. A.; Ruben, D. J. "A two-dimensional nuclear Overhauser experiment with pure absorption phase in four quadrants," *J. Magn. Reson.* **1982**, *48*, 286-292.

(30) Wu, X.; Zilm, K. W. "Cross polarization with high-speed magic angle spinning," *J. Magn. Reson. A* **1993**, *104*, 154-165.

(31) Bennett, A. E.; Rienstra, C. M.; Auger, M.; Lakshmi, K. V.; Griffin, R. G. "Heteronuclear decoupling in rotating solids," *J. Chem. Phys.* **1995**, *103*, 6951-6958.

(32) Bax, A. *Two-Dimensional Nuclear Magnetic Resonance in Liquids*; Delft University Press: Dordrecht, Holland, **1980**.

(33) Wokaun, A.; Ernst, R. R. *Chem. Phys. Lett.* **1977**, *52*, 407.

(34) Tounge, B. A., *High field solid state NMR: Assignment strategies and distance measurements using U-13C-labeled samples*, Ph.D. Thesis, Yale University, **1998**.

(35) Mehta, A. K., *High resolution 13C solid-state nuclear magnetic resonance: decoupling and recoupling under high speed magic angle spinning*, Ph.D. Thesis, Yale University, **1998**.

(36) McGeorge, G.; Alderman, D. W.; Grant, D. M. "Resolution enhancement in 13C and 15N magic-angle turning epxeriments with TPPM decoupling," *J. Magn. Reson.* **1999**, *137*, 138-143.

(37) Jakeman, D. L.; Mitchell, D. J.; Shuttleworth, W. A.; Evans, J. N. S. "Effects of sample preparation conditions on biomolecular solid-state NMR lineshapes," *J. Biomol. NMR* **1998**, *12*, 417-421.

(38) Levitt, M. H.; Raleigh, D. P.; Creuzet, F.; Griffin, R. G. "Theory and simulations of homonuclear spin pair systems in rotating solids," *J. Chem. Phys.* **1990**, *92*, 6347-64.

(39) Abragam, A. *Principles of Nuclear Magnetism*; Oxford University Press: New York, **1961**.

(40) Hoult, D. I.; Richards, R. E. "The signal-to-noise ratio of the nuclear magnetic resonance experiment," *J. Magn. Reson.* **1976**, *24*, 71-85.

(41) Bax, A.; Sparke, S. W.; Torchia, D. A. In *Methods in Enzymology*Academic Press: New York, **1989**; Vol. 176; 134-150.

(42) Hong, M.; Griffin, R. G. "Resonance assignments for solid peptides by dipolar-mediated C-13/N-15 correlation solid-state NMR," *J. Am. Chem. Soc.* **1998**, *120*, 7113-7114.

(43) Earl, W. L.; Vanderhart, D. L. "Measurement of C-13 chemical shifts in solids," *J. Magn. Reson.* **1982**, *48*, 35-54.

(44) Markley, J. L.; Bax, A.; Arata, Y.; Hilbers, C. W.; Kaptein, R.; Sykes, B. D.; Wright, P. E.; Wüthrich, K. "Recommendations for the presentation of NMR structures of proteins and nucleic acids - (IUPAC Recommendations 1998)," *Pure Appl. Chem.* **1998**, *70*, 117-142.

(45) Wishart, D. S.; Bigam, C. G.; Yao, J.; F., A.; Dyson, H. J.; Oldfield, E.; Markley, J. L.; Sykes, B. D. "H-1, C-13, and N-15 chemical-shift referencing in biomolecular NMR," *J. Biomol. NMR* **1995**, *6*, 135-140.

(46) Bennett, A. E.; Ok, J. H.; Griffin, R. G.; Vega, S. "Chemical shift correlation spectroscopy in rotating solids: Radio-frequency dipolar recoupling and longitudinal exchange," *J. Chem. Phys.* **1992**, *96*, 8624-8627.

(47) Böender, G. J.; Raap, J.; Prytulla, S.; Oschkinat, H.; de Groot, H. J. M. "MAS NMR structure refinement of uniformly C-13 encriched chlorophyll-A water aggregates with 2D dipolar correlation spectroscopy," *Chem. Phys. Lett.* **1995**, *237*, 502-508.

(48) Straus, S. K.; Bremi, T.; Ernst, R. R. "Resolution enhancement by homonuclear J decoupling in solid-state MAS NMR," *Chem. Phys. Lett.* **1996**, *262*, 709-715.

(49) Straus, S. K.; Bremi, T.; Ernst, R. R. "Side-chain conformation and dynamics in a solid peptide: CP-MAS NMR study of valine rotamers and methyl-group relaxation in fully C-13-labelled antamanide," *J. Biomol. NMR* **1997**, *10*, 119-128.

(50) Egorova Zachernyuk, T. A.; van Rossum, B.; Boender, G. J.; Franken, E.; Ashurst, J.; Raap, J.; Gast, P.; Hoff, A. J.; Oschkinat, H.; deGroot, H. J. M. "Characterization of pheophytin ground states in Rhodobacter sphaeroides R26 photosynthetic reaction centers from multispin pheophytin enrichment and 2-D C-13 MAS NMR dipolar correlation spectroscopy," *Biochem.* **1997**, *36*, 7513-7519.

(51) Bennett, A. E.; Rienstra, C. M.; Griffiths, J. M.; Zhen, W.; Lansbury, P. T., Jr.; Griffin, R. G. "Homonuclear radio frequency-driven recoupling in rotating solids," *J. Chem. Phys.* **1998**, *108*, 9463-9479.

(52) Zell, M. T.; Padden, B. E.; Grant, D. J. W.; Chapeau, M. C.; Prakash, I.; Munson, E. J. "Two-dimensional high-speed CP/MAS NMR spectroscopy of polymorphs. 1. Uniformly C-13-labeled aspartame," *J. Am. Chem. Soc.* **1999**, *121*, 1372-1378.

(53) Maas, W. E.; Laukien, F. H.; Cory, D. G. "Gradient, high resolution, magic angle sample spinning NMR," *J. Am. Chem. Soc.* **1996**, *118*, 13085-13086.

(54) Hing, A.; Vega, S.; Schaefer, J. "Transferred-echo double-resonance NMR," *J. Magn. Reson.* **1992**, *96*, 205-209.

(55) Sun, B. Q.; Costa, P. R.; Kocisko, D. A.; Lansbury, P. T., Jr. ; Griffin, R. G. "Internuclear distance measurements in solid state nuclear magnetic resonance: Dipolar recoupling via rotor sychronized spin locking," *J. Chem. Phys.* **1995**, *102*, 702-707.

(56) Baldus, M.; Geurts, D. G.; Hediger, S.; Meier, B. H. "Efficient N-15-C-13 polarization transfer by adiabatic-passage Hartmann-Hahn cross polarization," *J. Magn. Reson. A* **1996**, *118*, 140-144.

(57) Gullion, T.; Vega, S. "A simple magic-angle spinning NMR experiment for the dephasing of rotational echoes of dipolar coupled homonuclear spin pairs," *Chem. Phys. Lett.* **1992**, *194*, 423-428.

(58) Costa, P. R.; Sun, B. Q.; Griffin, R. G. "Rotational resonance tickling: Accurate internuclear distance measurements in solids," *J. Am. Chem. Soc.* **1997**, *119*, 10821-10830.

(59) Hartmann, S. R.; Hahn, E. L. "Nuclear double resonance in the rotating frame," *Phys. Rev.* **1962**, *128*, 2042.

(60) Pines, A.; Gibby, M. G.; Waugh, J. S. "Proton enhanced nuclear induction spetroscopy," *J. Chem. Phys.* **1972**, *56*, 1776.

(61) Schaefer, J.; Stejskal, E. O. "Double cross polarization NMR of solids," *J. Magn. Reson.* **1979**, *34*, 443-447.

(62) Stejskal, E. O.; Schaefer, J.; McKay, R. A. "Analysis of double cross-polarization rates in solid proteins," *J. Magn. Reson.* **1984**, *57*, 471-485.

(63) Sun, B. Q.; Costa, P. R.; Griffin, R. G. "Broadband heteronuclear cross polarization in rotating solids," *J. Magn. Reson. A* **1995**, *112*, 191-198.

(64) Peersen, O. B.; Wu, X.; Kustanovich, I.; Smith, S. O. "Variable amplitude cross-polarization MAS NMR," *J. Magn. Reson. A* **1993**, *104*, 334-339.

(65) Peersen, O. B.; Wu, X.; Smith, S. O. "Enhancement of CP-MAS signals by variable amplitude cross polarization. Compensation for inhomogeneous B1 fields," *J. Magn. Reson. A* **1994**, *106*, 127-131.

(66) Hediger, S.; Meier, B. H.; Ernst, R. R. "Cross-polarization under fast magic-angle sample-spinning using amplitude-modulated spin-lock sequences," *Chem. Phys. Lett.* **1993**, *213*, 627-635.

(67) Hediger, S.; Meier, B. H.; Kurur, N. D.; Bodenhausen, G.; Ernst, R. R. "NMR cross-polarization by adiabatic passage through the Hartmann-Hahn condition (APHH)," *Chem. Phys. Lett.* **1994**, *223*, 283-288.

(68) Hediger, S.; Meier, B. H.; Ernst, R. R. "Adiabatic passage Hartmann-Hahn cross-polarization in NMR under magic-angle sample-spinning," *Chem. Phys. Lett.* **1995**, *240*, 449-456.

(69) Hediger, S.; Meier, B. H.; Ernst, R. R. "Rotor-synchronized amplitude-modulated nuclear-magnetic-resonance spin-lock sequences for improved cross-polarization under fast magic-angle sample-spinning," *J. Chem. Phys.* **1995**, *102*, 4000-4011.

(70) Hediger, S.; Signer, P.; Tomaselli, M.; Ernst, R. R.; Meier, B. H. "A combination of slow and fast RF field modulation for improved cross polarization in solid-state MAS NMR," *J. Magn. Reson.* **1997**, *125*, 291-301.

(71) Mehring, M. *Principles of High Resolution NMR in Solids;* 2nd ed.; Springer-Verlag: Berlin, **1983**.

(72) Baldus, M. A.; Petkova, A. T.; Herzfeld, J. H.; Griffin, R. G. "Cross polarization in the tilted frame: assignment and spectral simplification in heteronuclear spin systems," *Mol. Phys.* **1998**, *95*, 1197-1207.

(73) Haeberlen, U.; Waugh, J. S. "Coherent averaging effects in magnetic resonance," *Phys. Rev.* **1968**, *175*, 453-467.

(74) Verhoeven, A.; Verel, R.; Meier, B. H. "J cross polarization in magic-angle-spinning NMR," *Chem. Phys. Lett.* **1997**, *266*, 465-472.

(75) Gan, Z. H.; Grant, D. M.; Ernst, R. R. "NMR chemical shift anisotropy measurements by RF driven rotary resonance," *Chem. Phys. Lett.* **1996**, *254*, 349-357.

(76) Nielsen, N. C.; Bildsøe, H.; Jakobsen, H. J.; Levitt, M. H. "Double-quantum homonuclear rotary resonance: Efficient dipolar recovery in magic-angle spinning nuclear magnetic resonance," *J. Chem. Phys.* **1994**, *101*, 1805-1812.

(77) Clubb, R. T.; Thanabal, V.; Wagner, G. "A constant-time 3-dimensional triple-resonance pulse scheme to correlate intraresidue H-1(N), N-15, and C-13(') chemical shifts in N-15-C-13 labeled proteins," *J. Magn. Reson.* **1992**, *97*, 213-217.

(78) Bax, A.; Ikura, M. "An efficient 3D NMR technique for correlating the proton and 15N backbone resonance with the alpha-carbon of the preceding residue in uniformly 15N/13C enriched proteins," *J. Biomol. NMR* **1991**, *1*, 99-104.

(79) Grzesiek, S.; Bax, A. "Improved 3D triple-resonance NMR techniques applied to a 31-kDa protein," *J. Magn. Reson.* **1992**, *96*, 432-440.

(80) Wu, X. L.; Zilm, K. W. "Complete spectral editing in CPMAS NMR," *J. Magn. Reson. A* **1993**, *102*, 205-213.

(81) Wu, X. L.; Burns, S. T.; Zilm, K. W. "Spectral editing in CPMAS NMR--generating subspectra based on proton multiplicities," *J. Magn. Reson. A* **1994**, *111*, 29-36.

(82) Baldus, M.; Meier, B. H. "Total correlation spectroscopy in the solid state. The use of scalar couplings to determine the through-bond connectivity," *J. Magn. Reson. A* **1996**, *121*, 65-69.

(83) Clubb, R. T.; Thanabal, V.; Wagner, G. "A new 3D HN(CA)HA experiment for obtaining fingerprint H(N)-H-alpha cross peaks in N-15-labeled and C-13-labeled proteins," *J. Biomol. NMR* **1992**, *2*, 203-210.

(84) Grzesiek, S.; Bax, A. "Correlating backbone amide and side-chain resonances in larger proteins by multiple relayed triple resonance NMR," *J. Am. Chem. Soc.* **1992**, *114*, 6291-6293.

Section III: Secondary Structure (Torsion Angles)

Chapter 6. 3D ^{1}H-^{15}N-^{13}C-^{1}H and ^{1}H-^{13}C-^{13}C-^{1}H Separated Local Field Spectroscopy for Simultaneous Determination of Multiple Torsion Angles in Rotating Solid Peptides

Abstract

Here we demonstrate the measurement of multiple ^{1}H-^{13}C-^{13}C-^{1}H and ^{1}H-^{15}N-^{13}C-^{1}H projection angles in a uniformly-^{13}C,^{15}N-labeled solid peptide (formyl-Met-Leu-Phe-OH) using three-dimensional separated local field spectroscopy (3D SLF) experiments under magic-angle spinning (MAS). The techniques employ two chemical shift dimensions for site resolution, along with one synchronous dimension of γ-encoded, constant time H-X and H-Y dipolar evolution with the newly developed T-MREV sequence. Heteronuclear and homonuclear polarization transfers are performed by quasi-adiabatic, band-selective cross polarization and SPC-5 double-quantum (DQ) mixing, respectively. The effects of multiple heteronuclear couplings, multi-spin polarization transfer dynamics, and differential relaxation are considered; these potential complications can be addressed with analytical models. The techniques provide several torsion constraints per residue, with high sensitivity and dynamic range, and can be applied directly to larger peptides and proteins.

Introduction

The measurement of relative dipole vector orientations in order to constrain molecular torsion angles is now a well established method for NMR structure determination. Principles that were first demonstrated in static solids[1-5] have been developed into experiments for rotating solids,[6-13] and related solution NMR techniques based on cross-correlated relaxation have recently been developed.[14] These torsion angle techniques have well-recognized advantages over distance measurements for determining secondary structure, particularly in peptides. An

additional advantage of the torsion angle techniques arises from the relative simplicity of the Hamiltonian; because the local fields (in examples here, heteronuclear dipolar couplings) commute with one another, extension to multiply-^{13}C,^{15}N-labeled samples should be possible. Combined with chemical shift assignment procedures, such techniques have potential to dramatically increase the rate with which structural constraints can be determined by solid state NMR.

Nevertheless, torsion angle experiments in solids have thus far been demonstrated primarily in systems with no more than two homonuclear low-γ spins. For example, the ^{1}H-^{13}C-^{13}C-^{1}H experiment has been performed with ^{13}C spin pairs only;[7,9] the ^{1}H-^{15}N-^{13}C-^{1}H experiment with ^{15}N-^{13}C pairs,[10,11] and both ^{15}N-^{13}C-^{13}C-^{15}N experiments with glycine residues.[12,13] Recently similar techniques were extended to U-^{13}C,^{15}N-labeled amino acids and peptides, using selective spin pair recoupling with R^2TR^{15} and selective Gaussian excitation pulses.[16] These results illustrate the abundant sensitivity of the methods to molecular geometry, and that torsion angle techniques can be applied to U-^{13}C,^{15}N-labeled molecules, but lack generality in terms of total structure determination. In all cases thus far, each torsion angle measurement has required a separate experiment.

Here we show that torsion angle measurement techniques can be applied to uniformly labeled molecules in a manner that produces many torsion angle constraints in a single 3D experiment. Several factors must be carefully considered in order to do so, while avoiding potential pitfalls and compromises of measurement precision. To be generally applicable, the experiment must be performed under conditions that are compatible with high resolution and sensitivity in U-^{13}C,^{15}N-labeled samples, the dipolar spectra must possess high dynamic range, and the data must be interpretable with tractable models for analysis of multi-spin dynamics. We have met these requirements by combining 2D ^{15}N-^{13}C and ^{13}C-^{13}C chemical shift correlation spectroscopy with T-MREV recoupling of ^{1}H-^{13}C and ^{1}H-^{15}N interactions. The experiment is performed at relatively high MAS rates, providing resolution and sensitivity. The superior dynamic range of the γ-encoded T-MREV sequence permits dipolar evolution to be projected onto a single

evolution dimension, permitting two dimensions of chemical shifts to be used for frequency labeling. Therefore many projection angle constraints, including important auto-correlated controls, may be derived from a single 3D data set. The precision of these constraints compares favorably with those measured in spin pairs, and the triangulation of each torsion angle by several measured projection angles breaks the degeneracy of solutions based on a single measurement.

Most methods for ^{1}H-X-Y-^{1}H SLF correlation spectroscopy thus far have been implemented in a manner that is incompatible with U-^{13}C,^{15}N-labeled compounds, or allows only one constraint to be determined per experiment. The schemes proposed here provide numerous constraints per residue, and are directly applicable to a wide variety of solid peptides and proteins.

Background & Theory

The basis of all torsion angle techniques is the dependence of the total coherent evolution upon relative orientation of at least two tensorial interactions. For our purposes, these interactions are assumed to be heteronuclear dipolar couplings, recovered under MAS by use of the T-MREV recoupling sequence:[17]

$$\tilde{H}_{IS}^{(1)} = \sum_{i,j}^{n} \omega_{ij} S_z^i I_\gamma^j, \qquad (1)$$

where S refers to the low-γ spins (usually ^{13}C or ^{15}N) and I to protons. T-MREV and MAS remove I_i-I_j and S_i-S_j couplings, respectively, from the effective Hamiltonian. The indices i and j refer to summation over all S and I spins, respectively. The pure heteronuclear Hamiltonian of Eq. 1 causes evolution of the initial S spin states

$$\rho(0) = \sum_i S_x^i, \qquad (2)$$

according to

$$\rho(\tau) = \sum_i \rho_i(\tau). \tag{3}$$

where

$$\rho_i(t) = S_x^i \prod_j \cos\omega_{ij}\tau + S_y^i \sum_j I_\gamma^j \sin\omega_{ij}\tau + \ldots \tag{4}$$

That is, each S spin evolves under the influence of many protons. This first term of Eq. 4 expresses the dephasing of observable coherence. Additional terms correspond to creation of anti-phase coherences between the S spin and each proton; higher order terms are possible due to evolution under multiple couplings. The relaxation of such coherences must be considered explicitly to fit the data with high precision (as discussed below), but the fundamental dephasing effect can be understood by considering the first term. Each coupling has an orientation dependence given by

$$\omega_{ij} = |\kappa| \frac{b_{IS}}{2\sqrt{2}} \sin 2\beta_{ij}, \tag{5}$$

where $|\kappa|$ is the magnitude of the complex scaling factor of the T-MREV sequence,[17] which depends upon the T-MREV symmetry number n and the exact RF amplitude due to rf-dipolar crossterms (the overall scaling is usually 45-0.48 in experiments here), b_{IS} is the dipolar coupling constant, and β_{ij} is the Euler angle relating the principal axis system of the dipolar vector to the rotor-fixed frame. The relative orientation of multiple dipole vectors of similar magnitude can be determined in SQ evolution experiments to extract bond angles; and in favorable cases projection angles between strong and weak ^{1}H-X dipole vectors can be determined, and this angle related to a torsion angle.[17] However, in order to maximize the dependence of the total evolution on the projection angle, it is generally preferable to create a

signal modulation that depends on the product of two separate S spin states. This can be performed by creating an initial condition of DQ coherence,

$$\rho(0) = S_x^{i1} S_x^{i2} - S_y^{i1} S_y^{i2} = S_x^{(14)i1i2}, \tag{6}$$

which evolves under the sum of heteronuclear couplings during a single SLF period.[7] Alternatively, two separate sets of local fields may be measured with independent dipolar evolution periods, which are connected by a polarization transfer step.[8] The latter case provides more flexibility in general, because polarization may be transferred over many bonds with ^{13}C-^{13}C or ^{15}N-^{13}C dipolar mixing schemes, whereas creation of DQ coherence between distant low-γ spins in a multi-spin cluster is more difficult. If the two SLF periods, a and b with mixing times τ_a and τ_b, are used to effect signal modulations according to Eq. 4, and the S_x coherences selected after each mixing period, the resulting observable coherence is modulated according to

$$\sigma_{nm}(\tau_a, \tau_b, \tau_{transfer}) = f_{nm}(\omega_{nm}, \tau_{transfer}) \prod_j \cos \omega_{nj} \tau_a \prod_j \cos \omega_{mj} \tau_b , \tag{7}$$

where $\sigma(t)$ is the observable coherence corresponding to the nth S spin during the first dipolar evolution period and the mth S spin during the second period (S_x selected from each dipolar evolution period), and $f_{ab}(\omega_{ab}, \tau_{transfer})$ is the function describing the polarization transfer from n to m. This expression can be extended to account for a third period dipolar evolution period (after a second polarization transfer period), with potentially much greater polarization transfer efficiency than in the corresponding triple quantum experiment.[18]

Although the resulting spectra can be quite complicated when all spins are considered explicitly, the dominant features can be appreciated by considering the two largest couplings (for example, in the ^{1}H-^{13}C-^{13}C-^{1}H system, which is I^1-S^1-S^2-I^2 in the notation here):

$$\sigma_{12}\left(\tau_a,\tau_b,\tau_{transfer}\right)=f_{12}\left(\omega_{12}^{SS},\tau_{transfer}\right)\cos\omega_{11}^{SI}\tau_a\cos\omega_{22}^{SI}\tau_b \tag{8}$$

The most dramatic effect occurs when the two strongest couplings are nearly co-linear (i.e, $\theta = 0^o$ or 180^o) and the ratio of mixing times is

$$\xi=\frac{\tau_b}{\tau_a}=\frac{\omega_{11}^{SI}}{\omega_{22}^{SI}} \tag{9}$$

This yields the signal:

$$\sigma\left(\tau_a\right)=\cos^2\omega_{22}^{SI}\tau_b \tag{10}$$

which has very distinctive features.[19] These spectral features vary widely with small deviations from co-linearity of the two I-S dipole vectors. Therefore this regime is where all projection angle techniques have optimal sensitivity.

Where in the *torsion* angle space this sensitivity lies depends upon molecular geometry. Therefore in determining structure with high precision, it is convenient to choose sets of angles that are naturally near co-linear (e.g., HN-$C^{\alpha}H$ in the β-sheet region of Ramachandran space), and then engineer either the isotopic labeling scheme or polarization transfer function so that near co-linear projection angles may be measured. However, there is no general solution for peptide structure if only one projection angle is measured. Alternatively, if we measure several projection angles, including some over multiple bonds, the combined dependence upon torsion angles will eliminate many of the degenerate solutions, and provide high precision, because at least one projection angle will be near 0^o or 180^o.

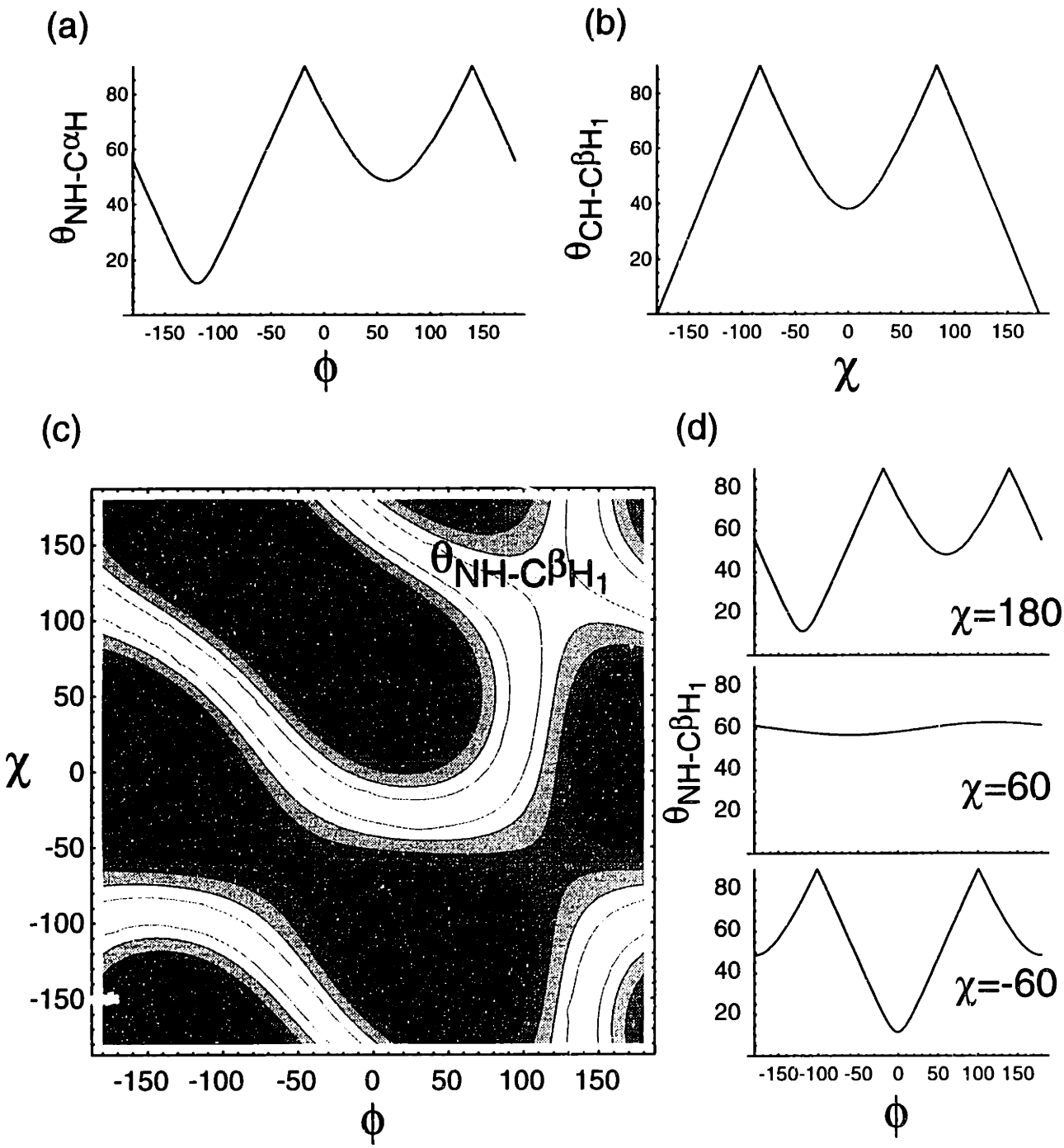

Figure 6-1. Dependence of Dipolar Projection Angles on Molecular Torsion Angles.

Only directly bonded protons are considered, assuming standard bond lengths and angles. (a) HN-$C^{\alpha}H$ dependence on ϕ; (b) HC^{α}-$C^{\beta}H$ dependence on χ; (c) HN-$C^{\beta}H_1$ dependence on ϕ and χ; (d) Slices through selected χ values from (c). The results suggest that multiple projection angle measurements will constrain the torsion angle space with highly non-linear convergence to the unique solution.

For example, Figure 6-1 shows a series of projection angle (θ) functions that are relevant to determination of ϕ and χ^1. If we assume that a very high precision measurement arises only when $\theta < 30^o$ (we will challenge this assumption later), this requires

$$-90 > \phi > -150 \tag{11}$$

or

$$|\chi| > 150. \tag{12}$$

Although useful for many cases, in general solutions will not always fall in these regions of high sensitivity. However, if the HN-C$^\beta$H projection angle is measured as well, an additional region of high sensitivity appears near χ = +60 and $|\phi| < 30$. This corresponds to the regime where the NH and C$^\beta$H dipole vectors are nearly co-linear, and produces a precise solution in the torsion angle space.

Requirements for Applying SLF Spectroscopy to U-^{13}C,^{15}N-Molecules.

The most expedient route to acquiring multiple projection angle constraints is to apply solid state SLF techniques to U-^{13}C,^{15}N-molecules. To do so without compromising the quality of each constraint, at least four *fundamental requirements* must be met: (1) low-γ sites must be resolved in at least two chemical shift dimensions; (2) MAS rates must be sufficiently fast to avoid sideband manifold overlap and rotational resonance (R^2) mediated broadening[20] between ^{13}C nuclei; (3) a suitable recoupling[21] scheme must be used to defeat MAS averaging of the desired local field (in this context, a H-X heteronuclear dipolar coupling); (4) pulse sequence elements that might cause recoupling of the ^{13}C-^{13}C dipolar interactions must be strictly avoided.

The requirement of site resolution through chemical shifts is essential for bookkeeping purposes. Both the source and destination of spin polarization must be known in order to correctly interpret the dipolar dephasing data and project the relative orientation measurement

onto the (primary) molecular structure. In some cases site resolution may be achieved in one dimension, and indeed this is the case for the examples shown here, but in general at least two dimensions will be required in order to resolve multiple U-^{13}C,^{15}N-labeled residues in a peptide or protein. Furthermore, in a multiply labeled sample, even if there is site resolution in the 1D spectrum, care must be exercised to avoid improper interpretation of the dephasing data. For example, in addition to S_2-S_3 DQ coherence, S_1-S_2 DQ coherence may be reconverted to S_3 observable coherence due to evolution through the strong homonuclear dipolar couplings, as discussed in Ref. 22. Therefore interpreting the modulated amplitude of the S_3 signal in terms of the local field evolution of the S_2-S_3 DQ coherence is incorrect in the general case. Labeling of both dipolar evolution periods with a unique chemical shift is necessary to avoid this type of ambiguity.

The second requirement, for fast MAS, arises from the need for optimal resolution in the 2D experiment. In peptides, severe R^2 broadening occurs if the MAS rate matches chemical shift differences between C^α (50-70 ppm) and C^β (10-70 ppm) resonances, or between C' (170-185 ppm) and C^α or C^β.[20,23-25] With site- or residue-specific labels it would possible to avoid some R^2 conditions by small changes in MAS rate, but in fully labeled samples it will be necessary to spin at a rate sufficient to overcome all R^2 conditions. In addition, increased MAS rates are required to average the large CSA at high field and provide significant narrowing due to the removal of interactions between CSA and homonuclear ^{13}C-^{13}C dipolar couplings (i.e., "near rotational resonance" broadening).[20] Recent results from Zilm and co-workers[26,27] and Munson and co-workers[28] provide the most persuasive evidence that faster MAS is highly beneficial for spectral resolution in U-^{13}C-labeled solids. For application to peptides, the MAS rate should be at least ~70 ppm for ^{13}C, preferably 85-95 ppm. At 125 MHz ^{13}C frequency (500 MHz ^{1}H), this is ~8.8 kHz or greater. Of the previous SSNMR torsion angle methods, only the NCCN ψ measurement technique of Costa and co-workers has been designed with this consideration in mind.[13]

The third requirement, recoupling of the heteronuclear dipolar interactions, is necessary so that the dynamic range and sensitivity of the experiment is not impaired by fast MAS. Recoupling is defined as the creation of a non-zero average Hamiltonian over a period of time, usually an integer *multiple number of rotor periods* ($n\,\tau_r$), in contrast to SLF methods applied at slow MAS rates (e.g., $\omega_D > \omega_r / 3$), which depend upon a dynamic phase accumulated *within a rotor period.* It is possible to amplify the H-X interaction by application of multiple π pulse sequences on the low-γ RF channel. This approach has been demonstrated in the context of HN-CH projection angle measurements for determination of the torsion angle ϕ.[11]

However, the application of multiple π pulse sequences for ^1H-^{13}C coupling amplification at MAS rates above ~5-6 kHz is highly problematic, especially in a U-^{13}C labeled environment, and violates the fourth requirement because the π pulses will cause irreversible dephasing of ^{13}C coherence due to SEDRA effects.[29] Even if appropriately high ^{13}C channel RF field strengths can be achieved to minimize finite pulse effects, and phase cycling devised to remove chemical shift and RF inhomogeneity artifacts, the signal loss due to the SEDRA effect may be insurmountable. Even more troublesome is the dependence of the SEDRA dephasing upon chemical shift parameters and the position of π pulses within the rotor period (see, for example, Eq. 18 of Ref. 30). As the π pulse timings are adjusted over the course of the doubling or quadrupling experiment, the variable dephasing effect causes oscillations in the acquired data which can be greater than those due to ^1H-X couplings. Interpretation of projection angle data in this context would require explicit calculation of the dependence upon S_1-S_2 chemical shift differences, CSA orientations, finite pulse amplitude, etc. Although this is possible in special cases, such a protocol would not be easily generalized. Therefore in general it is preferable to avoid this ^{13}C-^{13}C dephasing entirely, by applying minimal RF the ^{13}C channel during the heteronuclear dephasing portion of the experiment. Here we accomplish this with a constant time SLF period with a single ^{13}C π pulse to refocus chemical shifts.

Polarization Transfer Methods

Beyond the aforementioned fundamental concerns, it is also incumbent to maximize both sensitivity and resolution by means of adequate decoupling and optimal efficiency in all polarization transfer steps. This requires the use of γ-encoded recoupling for homonuclear polarization transfer steps, using homonuclear dipolar DQ recoupling sequences such C7,[31] POST-C7,[32] CMR7,[33] or SPC-5[22]. These sequences provide ~73% theoretical polarization transfer in a spin pair, and typical *experimental* results compare favorably with the *theoretical maximum* polarization transfer obtained by γ-dependent recoupling techniques such as RFDR,[34] RIL,[35] DRAWS,[36] and MELODRAMA[37] (i.e., ~52%). Ultimately, approaches based on polarization transfer through scalar couplings (e.g., TOBSY)[38] might prove superior to DQ-based dipolar methods, if sufficiently long rotating frame lifetimes can be achieved.

For the heteronuclear transfer steps, quasi-adiabatic polarization transfer pulse sequence elements are preferred.[39-46] Because sensitivity and resolution are the primary limitations to the general application of solid state MAS NMR to a wide range of biologically relevant problems, techniques that employ optimal polarization transfer steps are essential for application to large biomolecules. By combining highly efficient homo- and heteronuclear polarization transfer steps with appropriate MAS and decoupling (TPPM)[47] conditions, high resolution 3D ^{15}N-^{13}C-^{13}C experiments can be acquired in the MLF peptide.[48] Alternatively, for our purposes, the third dimension of chemical shift evolution can be replaced with synchronous dipolar evolution to retrieve structural information.

γ-Encoded Local Field Spectroscopy with T-MREV

Once all resonances are resolved and assigned, heteronuclear couplings may be recoupled to the desired coherences, in order to extract dipolar lineshapes that depend strongly on the relative orientation of the two (or more) strongest dipole-dipole vectors. Local-field spectroscopy has been demonstrated in a variety of contexts in recent years (by authors mentioned above). In general all of the experiments provide numerous degenerate or near degenerate solutions. The degeneracy may be reduced by measuring several torsion angles, as discussed above.

In addition, precision may be increased in regions of low sensitivity by using γ-encoded heteronuclear recoupling, such as T-MREV.[17] A comparison of γ-dependent and γ-encoded dephasing curves for a typical four spin, HC-CH system are presented in Figure 6-2. Although both dephasing trajectories display a strong dependence in the region from 140-180°, the γ-encoded trajectories display almost double the dynamic range in the time-domain, due to the larger depth of oscillation at ~100 μs. The various curves range in amplitude from –0.1 to 0.4 at approximately 125 μs, and show distinctive features at longer time (200-300 μs). In contrast, the γ-dependent curves show greater overlap in the time domain, has a dynamic range of only ~30% (at 150 μs), and contributes little additional information for mixing times beyond ~200 μs.

To place these qualitative observations in a more quantitative footing, we have calculated the dependence of the RMSD deviation between simulated dephasing trajectories for both the γ-encoded and γ-dependent cases, choosing four torsion angles from the trajectories shown above. The results are presented in Figure 6-3. Clearly once again the strong sensitivity of both techniques near *trans* geometry is evident, with a very large slope in the region $\chi > 140^{o}$. However, the γ-encoded SLF trajectory has approximately twice the sensitivity to torsion angle in the regions of $\chi < 140^{o}$.

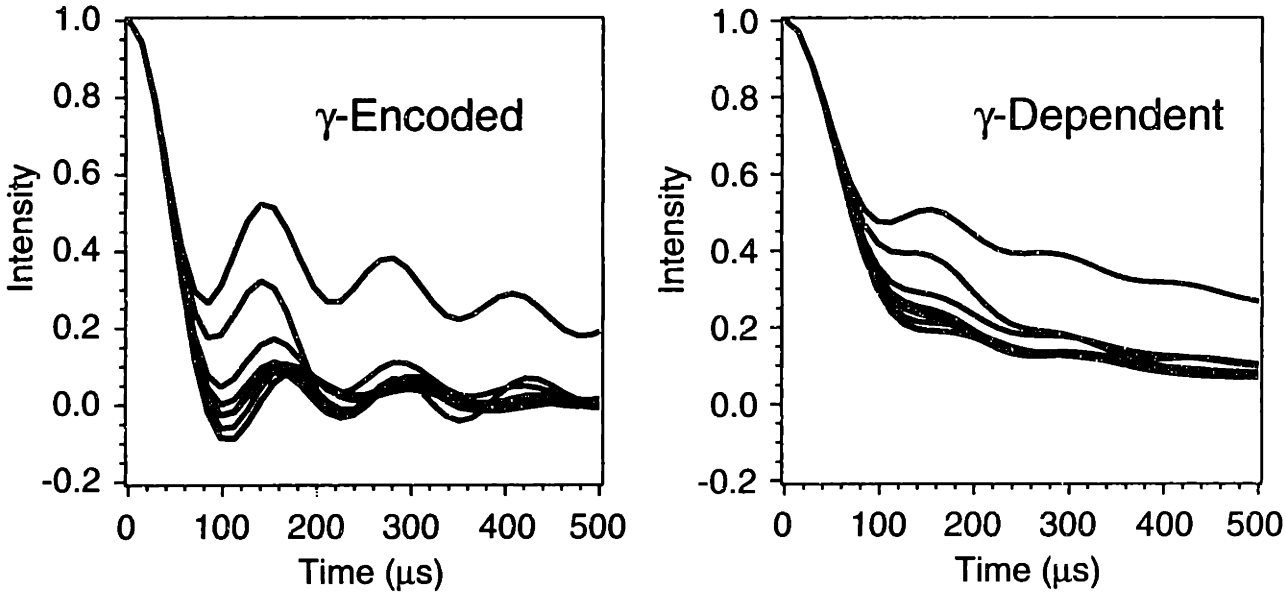

Figure 6-2. Simulated SLF Dephasing for γ-Encoded and -Dependent Sequences

Dephasing under correlated local fields in a simulated four-spin HC-CH system was calculated assuming standard molecular geometry, isotropic C-C polarization transfer, a 0.5 scaling factor for the T-MREV sequence, and a relaxation rate of 2000 s^{-1} on the coherences involving protons. Curves are simulated with χ values from 0 to 180° in steps of 20°. The maximum range of amplitude difference in the γ-encoded case occurs at ~125 μs, where the curves deviate by ~50% of the initial intensity over the range of angles; in the γ-dependent case, the maximum dynamic range is ~30%.

For example, if we assume the uncertainty cutoff of the 0.1 RMSD level, both methods have better than ±5° precision at 180°. However, at 120°, degenerate solutions arise for both methods; the γ-dependent data at 120±15° and 30±25°, the γ-encoded 120±5° and 40±5°. At 60°, the γ-dependent solutions are 60±10°, 105±10°, and 130-145°; for γ-encoded, 60±5° and 105±5°. At 0°, γ-dependent solutions 0±25°, 60±10°, and 105±10° and 140±5°; for γ-encoded, 0±15° and 140±5°. Note that the 5° grid size in the simulation here actually underestimates the improvement observed in the γ-encoded case, and that previous assessments[7,10] may have underestimated the precision of the of γ-dependent techniques near 180° and overestimated the precision near 0°.

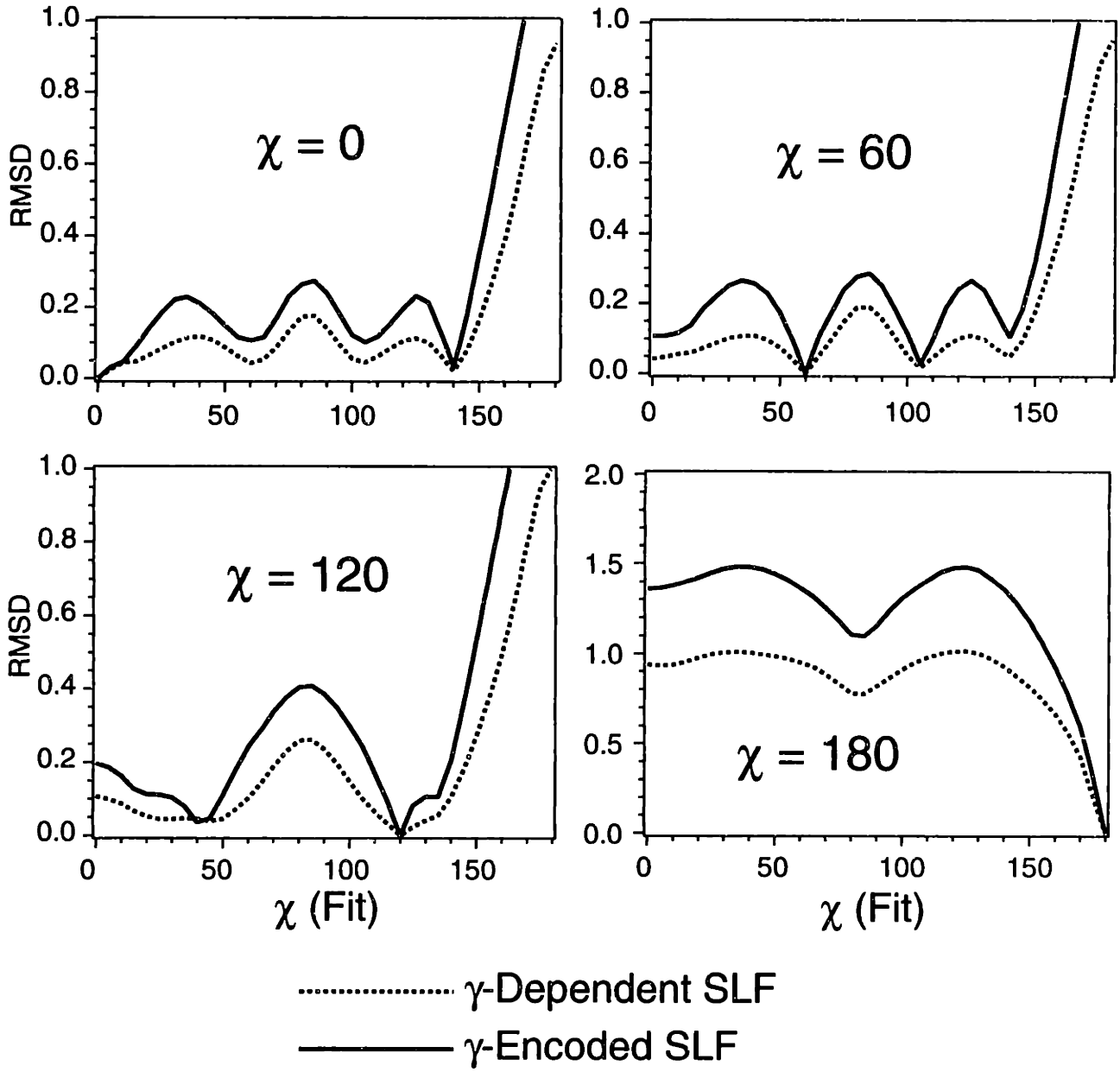

Figure 6-3. Simulated RMSD for γ-Encoded and -Dependent Sequences

Slices from a simulated 2D RMSD contour plot using the same parameters as Figure 6-2. Each plot compares the RMSD between a reference spectrum (χ of 0, 60, 120, and 180° as labeled) with simulations over the range of all χ angles (from 0 to 180 in steps of 5°).

Because of the superior theoretical sensitivity to small changes in torsion angle away from near *trans* geometry, we have chosen the T-MREV sequence in our implementation, to be applied in constant time fashion on top of each chemical shift dimension as required for the given experiment. The remaining concern is whether such a homonuclear decoupling sequence can be applied at high MAS rates required for sufficient spectral resolution and sensitivity in U-^{13}C,^{15}N-labeled samples. In Figure 6-4, the T-MREV dipolar spectra of the Met-C^{α} signal of MLF are shown as a function of the MAS rate. The RF field was constant for all studies, and the T-MREV symmetry number *n* reduced in order to maintain rotor-synchronization. Because the scaled ^{1}H-^{13}C coupling under T-MREV is about 5 kHz, comparable to the slowest MAS rate, a significant cycling sideband arises at the MAS rate. Physically this results from the fact that the T-MREV average Hamiltonian is only strictly valid at multiples of the rotor period, and in the intervening time, deviations from the AHT result may occur, even with perfect pulses. In another study at lower MAS rates, such effects have been simulated explicitly by calculating the entire pulse sequence, with phenomenological relaxation of proton coherences.[49] This may be practical as a final optimization step in the data fitting procedures, but here we focus on interpretation with the analytical model, and would like to achieve MAS fast enough to minimize the effects of cycling sidebands in the dipolar domain.

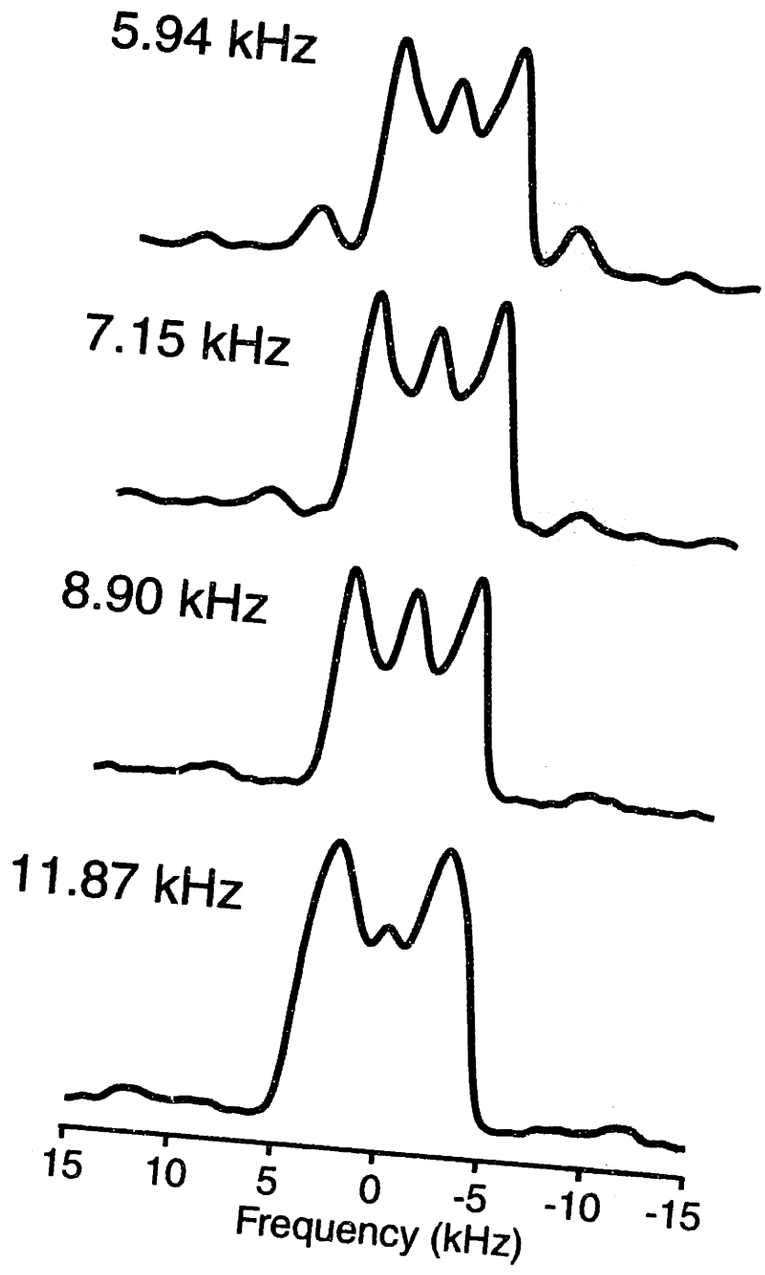

Figure 6-4. T-MREV Dipolar Spectra as Function of MAS Rate.

Met-C^{α} signal dephasing under T-MREV (2.34 μs $\pi/2$ pulse) was observed at the MAS rates indicated, in all cases using the same RF field (~107 kHz). The T-MREV symmetry number (n) was reduced to maintain rotor-synchronization (6 at 5.95 kHz, 5 at 7.15 kHz, 4 at 8.90 kHz, and 3 at 11.87 kHz. The perturbation in the lineshape at 11.87 kHz is due to recoupling of the $m = 2$ spatial component of the dipolar coupling in the dephasing trajectory. Cycling sidebands appear at the MAS rate.

As the MAS rate is increased to 8.9 kHz, the cycling sidebands have substantially decreased amplitude and are well outside the region of interest in the T-MREV lineshape. The lower T-MREV synchronization conditions at higher MAS rates result in slightly poorer homonuclear decoupling, as evidenced in the increased zero-frequency amplitude. This is a minor effect compared to the increased intensity in the dipolar lineshape due to recovery of cycling sideband amplitude, which provides superior fits at high MAS, despite the higher relaxation rate, in all studies performed thus far. In this case, 7.15 kHz is sufficient to achieve reasonable agreement between experiment and simulation, but the ~8.90 kHz is desired when two CH dipole evolution periods are correlated in the full HC-CH 3D SLF experiment. Simulated lineshapes for such a case—a six-spin, H(N)-H-C^{α}-C^{β}-H-H(Cγ) system—are shown in Figure 6-5. Typical coupling and geometry parameters are used. Note that spectral features extend out to approximately ±8 kHz in the frequency domain. Therefore we would like to spin at least this fast for the 3D experiment.

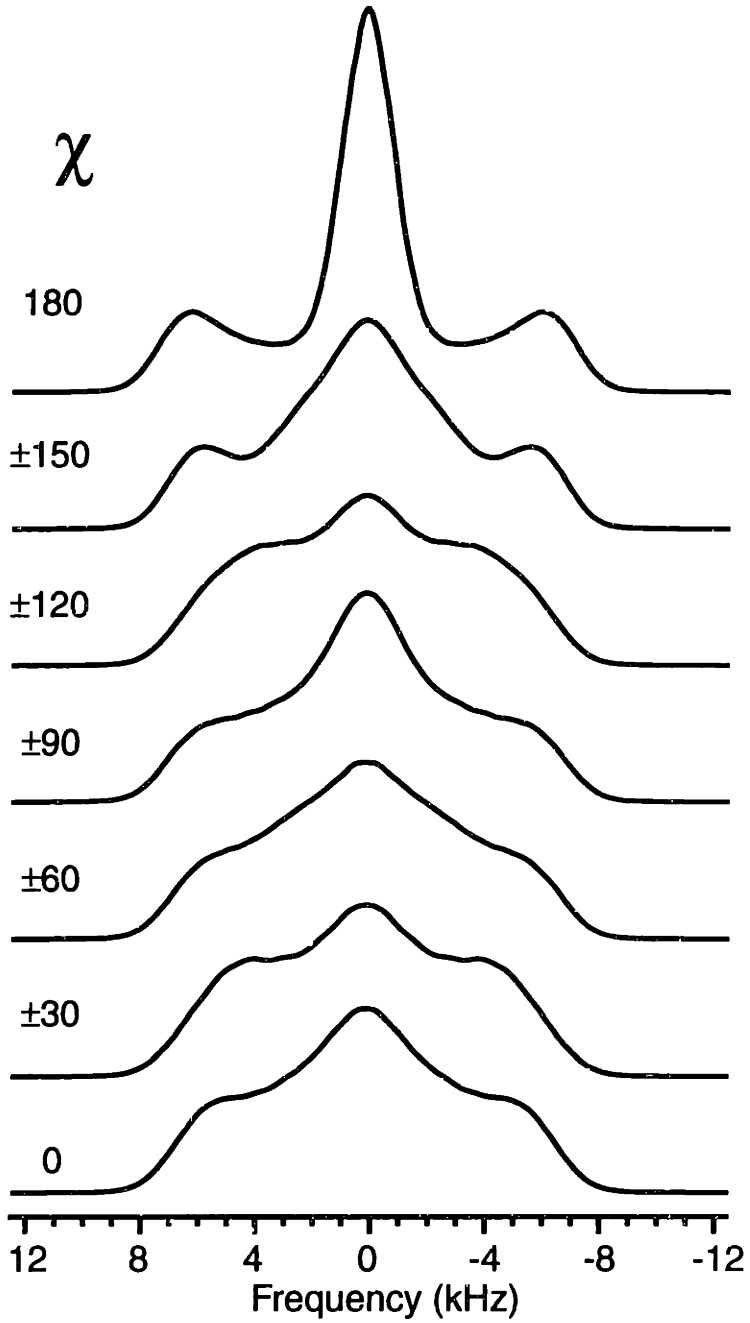

Figure 6-5. Simulated HC-CH Lineshapes (6 spin calculation)

Inclusion of additional protons (H(N) and H(Cγ)) results in a loss of sharp features in the dipolar spectra, as observed experimentally. Although six spins are implicitly included in this calculation, the average Liouvillian must account for only four heteronuclear couplings at a time. Isotropic C-C polarization transfer is assumed. Additional molecular geometry and simulation details are in the text.

Experimental

NMR Spectroscopy

All experiments were performed at 11.7 T (500.06 MHz ^{1}H, 125.7 ^{13}C, 50.6 ^{15}N), using a custom-designed transmission line probe with Varian (Chemagnetics) 4-mm spinner modules. RF fields were typically 120 kHz on ^{1}H during homonuclear mixing, 100 kHz during heteronuclear mixing (CP), 108 kHz during T-MREV (2.34 μs π/2 pulses),[17] and 80-85 kHz TPPM (15° total phase difference, 5.0-5.4 μs switching time)[47] during indirect chemical shift evolution periods and acquisition. Unless indicated otherwise, the MAS rate was 8.9 kHz. CP transfers to and from ^{15}N were performed at 35-45 kHz on ^{15}N, matching the −1 condition to ^{1}H (i.e., 45-55 kHz on ^{1}H) and ±1 condition to ^{13}C, depending on the bandwidth of CP matching condition desired for the ^{13}C-^{15}N transfer step. In all cases ramps of the ^{15}N and/or ^{13}C RF amplitude were used to achieve quasi-adiabatic transfer of polarization, according to the prescriptions of Meier and co-workers.[44-46,50]

The pulse sequences are shown in Figure 6-6. For chemical shift assignment, the T-MREV times were set to zero, and the heteronuclear CP mixing times minimized (2-4 ms) to avoid transfer through space to sidechain ^{13}C signals; for HN-CH SLF experiments, where direct transfers through space from N to $C^{\beta}[i]$ and $C^{\alpha}[i-1]$ were desired, mixing times were increased to ~6 ms. This produces an approximately adiabatic heteronuclear dipolar transfer; however, as the mixing time is increased, separation of the correlated local fields via frequency-labeling with the ^{15}N chemical shift is necessary to distinguish intra- from inter-molecular transfer. For ^{13}C-^{13}C 2D and HCCH 3D experiments, 16 shots were acquired for each increment, with a recycle delay of 2.5 s; 32 time increments (112.32 μs) in the indirect chemical shift dimension (64 points total, with phase cycling according to Figure 6-6 and Ruben and co-workers[51]); and 21 dipolar mixing

time points (28.08 μs increment). For ^{15}N-^{13}C 2D and HNCH 3D, 32 shots were acquired for each increment, with a recycle delay of 2.5 s; 8 time increments (673.92 μs) in the indirect ^{15}N chemical shift dimension; and 21 dipolar mixing time points (sampled every 28.08 μs for ^{13}C-^{1}H and 56.16 μs for ^{15}N-^{1}H periods).

Total measurement time for both 3D experiments in MLF was one day (16 hours for HCCH and 8 hours for HNCH). The 3D HCCH experiments in U-^{13}C,^{15}N-Thr (20% dilute in natural abundance) required 6 hours each (16 shots per increment, 16 t_1 increments, 21 τ increments, 2 s recycle delay). The analogous 2D experiment in ^{15}N-acetyl-valine (NAV), observing natural abundance ^{13}C, required 15 hours, with ten-fold poorer sensitivity.

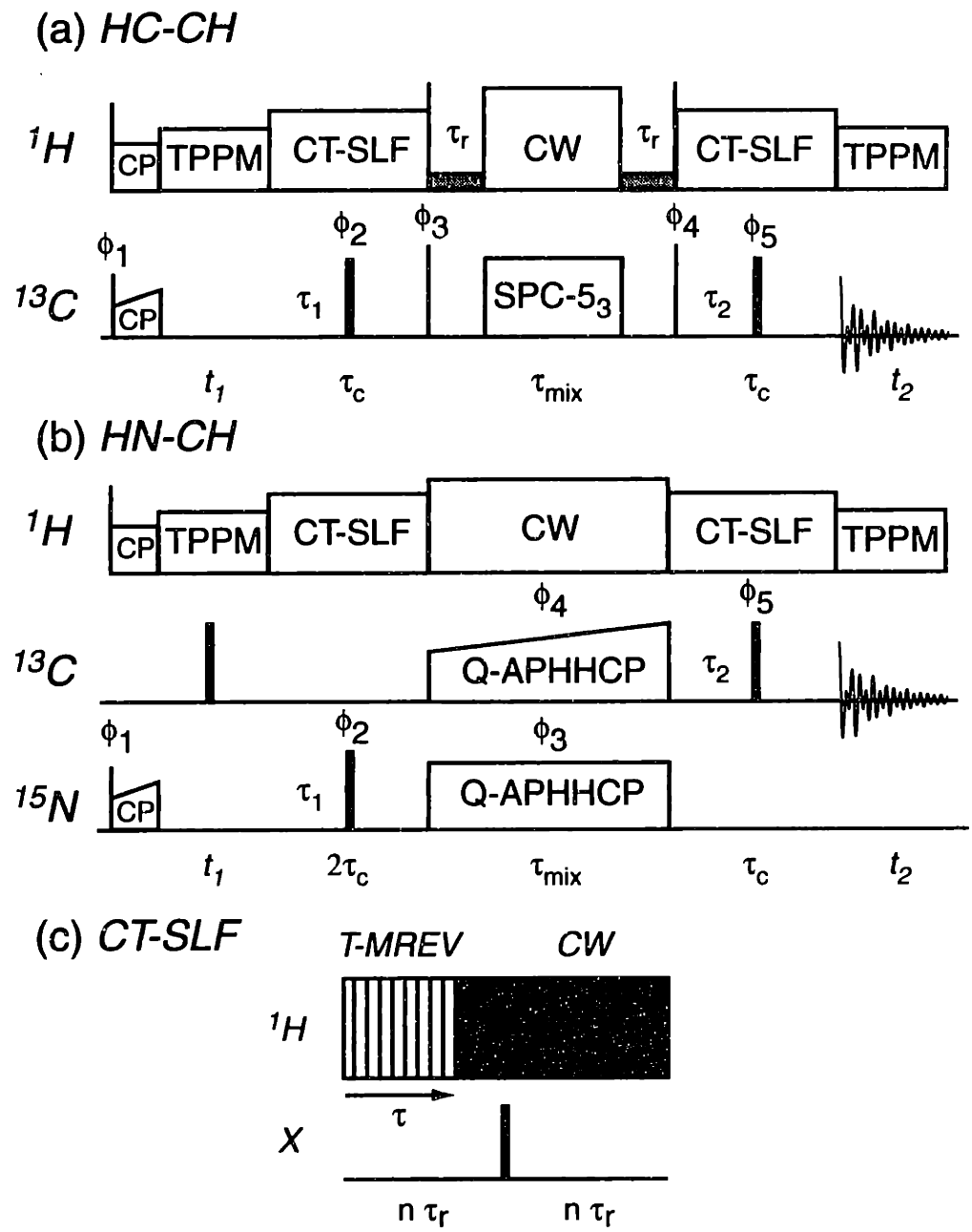

Figure 6-6. 3D HC-CH and HN-CH SLF Pulse Sequences.

Narrow line denote $\pi/2$ pulses, thick lines π pulses. Note the relative ^1H decoupling field amplitudes. Increasing the fields significantly during $\pi/2$ pulses and ^{13}C mixing periods optimally utilizes available ^1H fields. Phase cycling is: (a) $\phi_1 = 1$, $\phi_2 = 1111\ 2222\ 3333\ 4444$, $\phi_3 = 4$, $\phi_4 = 1234$, $\phi_5 = 1234$, $\phi_{rec'r} = 1234\ 3412\ 1234\ 3412$, where X=1, Y=2, etc. (b) $\phi_1 = 13$, $\phi_2 = 11111111\ 22222222\ 33333333\ 44444444$, $\phi_3 = 1$, $\phi_4 = 1$, $\phi_5 = 11223344$, $\phi_{rec'r} = 13311331\ 31133113$. Hypercomplex phase cycling according to Ruben and co-workers[51] is performed by adjusting ϕ_1 in both cases.

The homonuclear mixing schemes were employed with the desired bandwidth of transfer in mind. For broadband ^{13}C-^{13}C mixing, the standard implementation of SPC-5 is used,[22] with synchronization over two rotor periods, requiring ^{13}C RF fields of ~44.5 kHz at 8.9 kHz MAS. However, for the HC-CH experiments, the additional bandwidth for transfer to C' signals is not required. Indeed, superior transfer efficiency can be achieved among aliphatic resonances by using lower amplitude RF fields on ^{13}C, synchronizing the SPC-5 sequence over three rotor periods (SPC-5_3, i.e., ~30 kHz ^{13}C RF at 8.9 kHz MAS).[22] This results in a less favorable ^{13}C-^{13}C dipolar scaling factor (~0.13), but this is permissible because the additional mixing time required is more than compensated for by the improvement in rotating frame relaxation times (by virtue of the increased mismatch of ^{1}H and ^{13}C RF fields, which avoids destructive Hartmann-Hahn contact during the ^{13}C-^{13}C mixing period).[22,30,52,53] With the SPC-5_3 sequence, the optimal mixing time for one-bond transfer in multi-spin systems is increased to ~1.5 ms (compared to ~1 ms with SPC-5). An example, showing the first ^{13}C-^{13}C plane of the 3D HCCH experiment, is presented in Figure 6-7. Due to carrier placement at ~30 ppm (~17.5-18.5 kHz from the C' resonances), and the 30 kHz amplitude of the SPC-5 field, no polarization is transferred to or from the C' signals (although lineshape artifacts arise in the C' region, presumably due to lineshape effects discussed by Böender[54] and/or off resonance rotation errors). Among aliphatic resonances, excellent polarization transfer is achieved, and decoupling interference effects are avoided. A direct comparison of the 1D SPC-5 DQF efficiency under these conditions (not shown), using the two (SPC-5) and three (SPC-5_3) rotor period synchronization conditions (with total mixing times of 8 and 12 τ_r), showed a 25% and 15% greater DQF efficiency in C^{α} and C^{β} resonances, respectively, for SPC-5_3. In the 2D spectra, even greater differences are observed in total sensitivity, because the 1D DQF spectra underestimate polarization transfer.

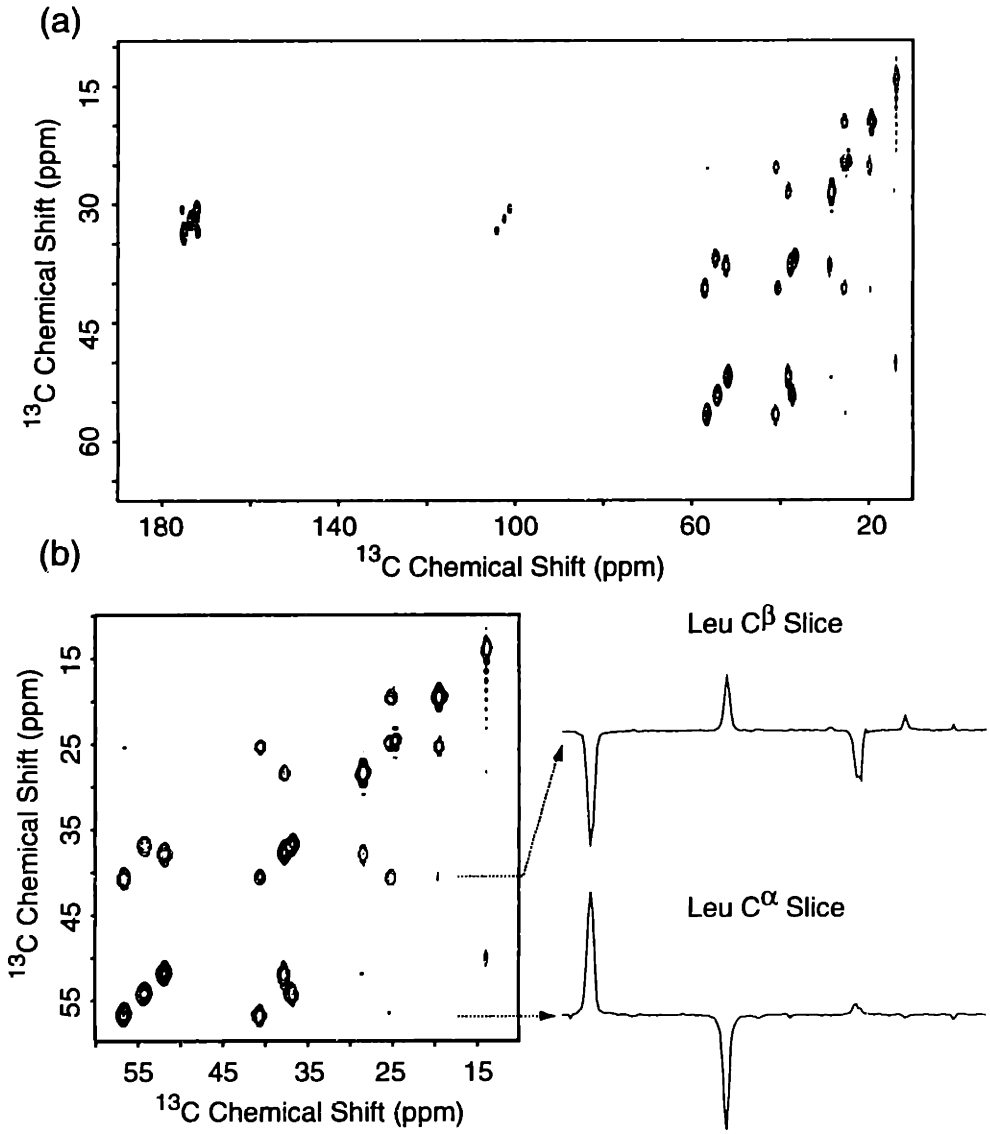

Figure 6-7. 2D ^{13}C-^{13}C Spectrum of MLF with SPC-5$_3$.

By choosing a lower amplitude RF field (timing SPC-5 over three rotor periods), the bandwidth and compensation for CSA in the homonuclear mixing sequence are slightly reduced, but overall efficiency of polarization transfer among aliphatic signals is better than with the standard SPC-5 implementation. (a) Entire ^{13}C bandwidth with frequencies folded in the indirect dimension. No crosspeaks to the C' signals are visible at a contour display level (5%) that shows weak two-bond transfers among aliphatic signals. (b) Expanded plot of aliphatic region, with slices through the Leu C$^{\beta}$ and C$^{\alpha}$ signals. Artifacts at the Met C$^{\delta}$ frequency arise due to the combination of rapid ^{13}C T$_1$ (~100 ms) and narrow linewidth, and can be removed with additional phase cycling.

Numerical Simulations

The heteronuclear Hamiltonian under T-MREV was assumed for each heteronuclear spin pair, and a Liouvillian matrix constructed as follows. First, standard bond angles and lengths were assumed, a set of torsion angles selected, and the coordinates of all nuclei in the peptide fragment calculated. The Euler angles and distances relating each dipole vector to a fixed molecular frame were determined, and these vectors rotated into the laboratory frame for each crystallite. For each period of the T-MREV evolution, a given number (n) of protons were selected, in order of decreasing coupling amplitude in β-sheet, *trans* sidechain geometry. The matrix (2^n x 2^n) was constructed assuming the first n heteronuclear couplings. For example, for three protons the 8 x 8 matrix is:

$$\begin{array}{c} |S_x\rangle \quad |S_y I_\gamma^1\rangle \quad |S_y I_\gamma^2\rangle \quad |S_y I_\gamma^3\rangle \quad |-S_x I_\gamma^1 I_\gamma^2\rangle \quad |-S_x I_\gamma^1 I_\gamma^3\rangle \quad |-S_x I_\gamma^2 I_\gamma^3\rangle \quad |-S_y I_\gamma^1 I_\gamma^2 I_\gamma^3\rangle \\ \begin{pmatrix} -\Gamma_1 & -\omega_1 & -\omega_2 & -\omega_3 & & & & \\ \omega_1 & -\Gamma_2 & & & -\omega_2 & -\omega_3 & & \\ \omega_2 & & -\Gamma_2 & & -\omega_1 & & -\omega_3 & \\ \omega_3 & & & -\Gamma_2 & & -\omega_1 & -\omega_2 & \\ & \omega_2 & \omega_1 & & -\Gamma_3 & & & -\omega_3 \\ & \omega_3 & & \omega_1 & & -\Gamma_3 & & -\omega_2 \\ & & \omega_3 & \omega_2 & & & -\Gamma_3 & -\omega_1 \\ & & & & \omega_3 & \omega_2 & \omega_1 & -\Gamma_4 \end{pmatrix} \end{array} \quad (13)$$

All possible spin topologies for the experiments were included in the same program, permitting direct comparison of 1-6 protons with otherwise identical parameters. All homonuclear I-I couplings are ignored. Separate sets of dipole vectors for each period were calculated based on the position of the relevant low-γ nucleus. Each Liouvillian was diagonalized and applied repeatedly to the initial density operator $\rho(0) = S_x$. Polarization transfer amplitude for each crystallite assumed low-γ coupling topologies consistent with the chosen torsion angles, assuming models discussed by Hohwy[22] for the homonuclear case and isotropic or standard anisotropic, two-spin models for the heteronuclear case, as discussed in more detail where relevant.

Results

HN-CH Experiments

The canonical sample for measurement of ϕ is ^{15}N-acetyl-valine (NAV).[55] Here (Figure 6-8) we performed the 2D analog of the 3D HNCH experiment, which is conceptually similar to the relayed correlation anisotropy (RACO) experiment of Ishii and Terao,[8] but only one (synchronous) dipolar dimension is required because of the improved dynamic range of the γ-encoded T-MREV sequence. In this case, the best fit to the experimental data is $\phi = -142.5^{o}$. Assuming a relationship of

$$\phi = \theta_{C-N-C^{\alpha}-C} = \theta_{H^{N}-N-C^{\alpha}-H^{\alpha}} + 60. \tag{14}$$

However, this relationship is not true according to the crystal structure of NAV,[55] where

$$\phi = \theta_{C-N-C^{\alpha}-C} = -136.5, \tag{15}$$

and

$$\theta_{H^{N}-N-C^{\alpha}-H^{\alpha}} = 153.4. \tag{16}$$

Thus the assumption above would lead to a 10^{o} error in this case. This is a general problem inherent to all torsion angle measurements involving protons if standard relationships between the dihedral angle H-N-C-H and ϕ are assumed.

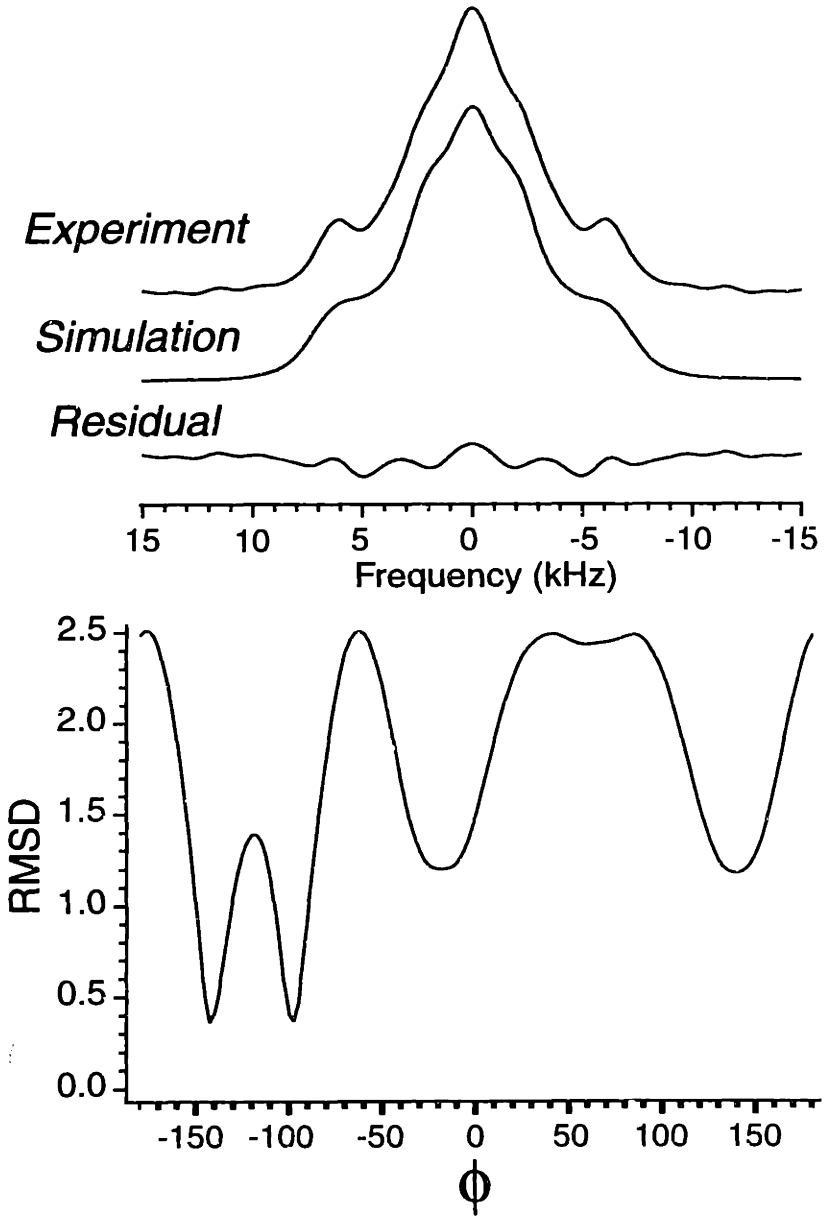

Figure 6-8. HN-CH Result in ^{15}N-Acetyl-Valine.

The 2D analog of the experiment shown in Figure 6-6(b) was used, because no chemical shift resolution in the ^{15}N dimension is required. 21 dipolar dephasing points were acquired, with 1,024 shots averaged. Total measurement time was 15 hours. The experimental data was fit to simulations assuming a T-MREV scaling factor of 0.485, 5000 s^{-1} decay of proton coherences, isotropic polarization transfer, and no distribution of RF field.

Our direct measurement is actually the H-N-C-H dihedral angle, 157.5°. This deviates slightly from the values measured by X-ray. Although the random error of the T-MREV experiment (less than ±1°) here is superior to the X-ray result (±5°), a careful study by Ishii using

relayed-correlation spectroscopy NMR methods, in which complete dipolar evolution of both ^{1}H-^{15}N and ^{1}H-^{13}C dimensions was performed, provided a result of 154±1.4°.[56] This suggests that the present T-MREV result may have a systematic error, for which there are several potential sources: RF inhomogeneity, miscalibration of the T-MREV scaling factor, differential relaxation rates, and the orientation dependence of the ^{15}N-^{13}C polarization transfer. (The aforementioned fit assumed an isotropic, quantitative transfer of polarization via ideal adiabatic transfer in the ^{13}C-dilute spin system; actual transfer efficiency was ~60% with 6 ms mixing.)

Table 6-1. NAV HN-CH Simulation Global Minima.[a]

Relaxation Rate (s^{-1}, ±500)	*T-MREV Scaling* **(±0.005)**	**Polarization Transfer Function**	**Best Fit ϕ (±1°)**	**RMSD**[b]
5000	0.485	isotropic, 100%	-142	0.280
2500	**0.465**	isotropic, 100%	-146	0.466
2500	**0.485**	isotropic, 100%	-145	0.486
2500	**0.505**	isotropic, 100%	-143	0.541
2500	**0.485**	sin 2β, 70%	-146	0.386
5000	**0.485**	sin 2β, 70%	-142	0.240

[a]Parameters in bold are fixed, while other parameters in that row are globally optimized.
[b]Determined by frequency-domain fitting of the spectral range ±10 kHz.

The influence of these factors upon the fitted torsion angle can be assessed by determining the RMSD with various assumptions about the other parameters, and observing the shift in the best fit for ϕ. The results of such an analysis are summarized in Table 6-1. The global minimum in the fit (allowing relaxation, T-MREV scaling, and dihedral angle to vary) overestimates the relaxation rate, relative to the value determined from the 1D ^{15}N and ^{13}C T-MREV control experiments (~2500 s^{-1}, data not shown). This arises from a combination of artifactual features at $\pm\omega_r/2$ and the distribution of T-MREV scaling factors (due to RF inhomogeneity), which may be simulated. If the relaxation rate and scaling factor are fixed at the values determined in the

control experiments, the overall quality of fit is a factor of two worse, but the global minimum in the torsion angle moves toward the RACO and X-ray results (i.e, ϕ = -146 corresponds to H-N-C-H dihedral angle of 154). Also note that anisotropic modeling of the polarization transfer function improves the fits (with other parameters fixed) significantly. Here the mixing time of 6 ms is not sufficient to ensure purely adiabatic behavior.

In the 3D HNCH experiment in MLF (which required half the experiment time of the 2D experiment in NAV), greater dependence upon polarization transfer dynamics is expected, because each ^{15}N has large (~1 kHz) couplings to two directly bonded ^{13}C nuclei, C'[i-1] and C$^{\alpha}$, and two-bond couplings (~200 Hz) to C$^{\beta}$[i] and C$^{\alpha}$[i-1]. The latter pair of nuclei may contribute to the dynamics significantly if the ^{15}N-^{13}C mixing time is relatively long (>5 ms). We approach this problem as follows. First, the heteronuclear transfer is *directed* to the aliphatic ^{13}C resonances by a band-selective CP step. As discussed in Chapter 5, this approach improves transfer efficiency to C$^{\alpha}$ (and C$^{\beta}$) signals; polarization transfer to C' is not desired in the HNCH experiment, due to the lack of directly attached protons by which the C' orientation can be determined (although, of course, analogous CSA experiments could be easily designed to exploit polarization transfer to C' to determine the torsion angle ω). With the C' removed from the dynamics, at relatively short mixing times, the one remaining strong coupling will dominate the evolution, and polarization transfer to C$^{\alpha}$ will proceed according to the two-spin model. However, at longer mixing times, C$^{\beta}$[i] and C$^{\alpha}$[i-1] will receive a portion of the polarization from N[i]. For this reason, 2D analogs (of one dimension of chemical shift and one dipolar dimension) of the HNCH experiment must be applied with caution in multiply-labeled systems. For example, directly observable C$^{\alpha}$[i] magnetization may derive from N[i] or N[i+1], therefore complicating the dipolar domain.

For MLF, in order to ensure that the transfer dynamics are being modeled correctly, or that any estimation does not adversely effect the torsion angle result, isotropic and sin 2β polarization transfer models will be compared for each residue, and the results used to consider appropriate

models for the sidechain polarization transfer model. The orientation dependence of the transfer through weaker (200 Hz) N-C$^{\beta}$ couplings is expected to have a greater role in the spin dynamics.

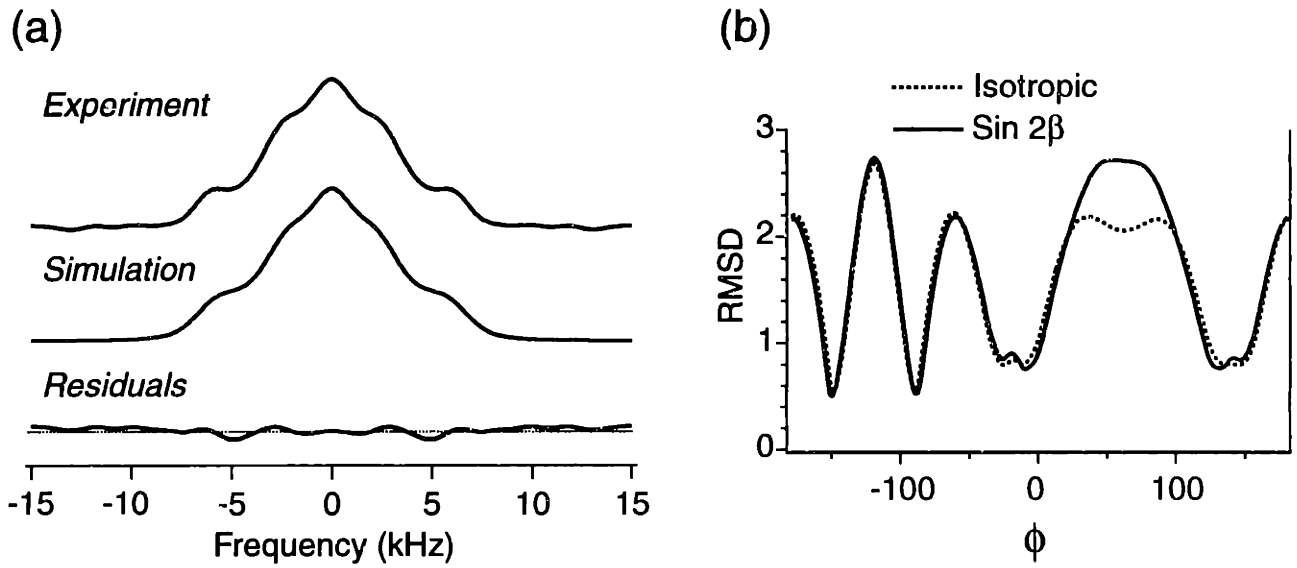

Figure 6-9. Met HN-CH Dipolar T-MREV Spectrum and Best Fit Simulation

Experimental data is extracted from the dipolar dimension of the 3D HNCH SLF experiment. (a) Experimental spectrum and best fit simulation with T-MREV scaling of 0.446, $\Gamma_2 = 4500\ s^{-1}$, ϕ = –151°. (b) RMSD plot comparing polarization transfer models.

The Met and Leu residues give very similar HN-CH dipolar spectra, both fitting degenerate solutions at –150° or –90°. (Again here we assume the relationship $\phi = \theta_{H^N-N-C^\alpha-H^\alpha} + 60$.) In Met (Figure 6-9), the minima are well defined; in Leu (Figure 6-10), additional near-degenerate solutions arise at -12° and 132°. In neither spectrum does the inclusion of anisotropic polarization transfer alter the result, as apparent in the RMSD plots as a function of simulated ϕ value. Only for ϕ values from ~30°-90° (corresponding to *cis* NH-CH geometry) does a large deviation arise. This range of geometry is not typically encountered in the peptide backbone of most native proteins, but may have greater significance in analogous HC-CH experiments (to be discussed below).

Although the large dynamic range of the γ-encoded T-MREV step provides excellent precision in the measurement, two problems remain. First, systematic errors in the fitted angle

may arise from the two regions of the spectra where the quality of the fit is poor: at the zero frequency and at ω_r / 2, in this case 4.45 kHz. The zero-frequency amplitude is poorly reproduced because the distribution of T-MREV scaling factors (due to a distribution of RF fields in the sample volume, in direct analogy with the CMR7 effects discussed in Chapter 10). The simulated relaxation is overestimated to reproduce the broadened outer edge in the experimental data; the incorrectly high relaxation in turn creates additional intensity at the zero frequency. This effect is more prominent in the T-MREV reference spectra, which are peaked at the extrema in the frequency domain, and may lead to inappropriate selection of relaxation parameters. However, as noted in the context of the NAV results, these effects are quite small. The second systematic error in due to the finite MAS rate. Prominent divots appear in the residuals at ω_r / 2 due to cycling sidebands, as discussed above.

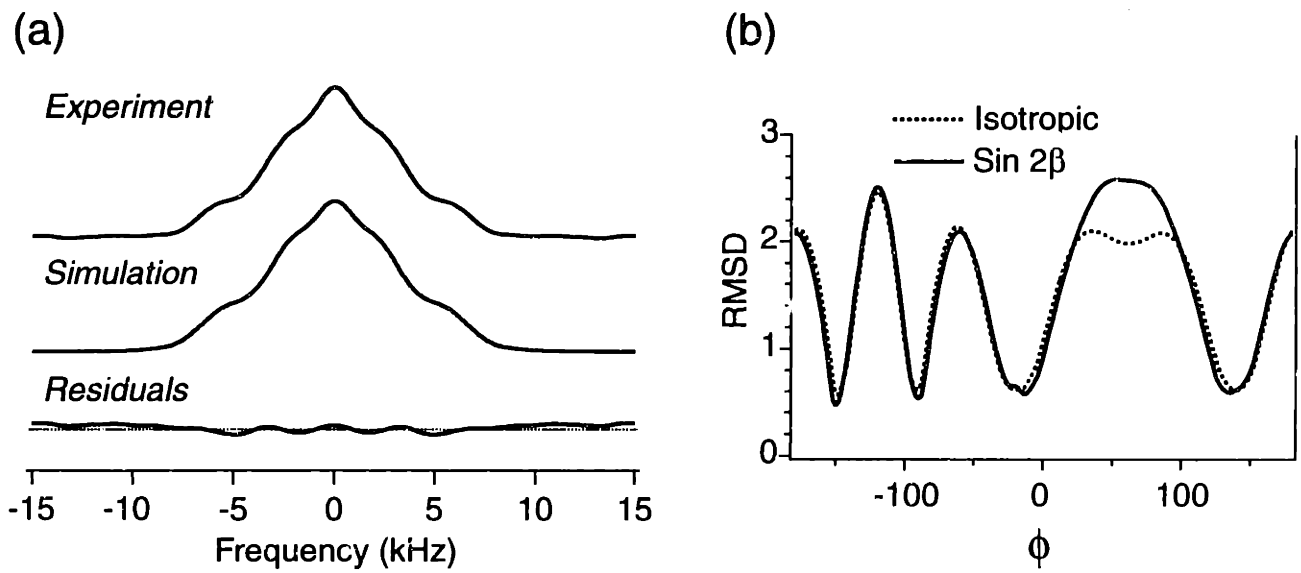

Figure 6-10. Leu HN-CH Dipolar T-MREV Spectrum and Best Fit Simulation

Experimental data is extracted from the dipolar dimension of the 3D HNCH SLF experiment. (a) Experimental spectrum and best fit simulation with T-MREV scaling of 0.446, $\Gamma_2 = 4500\ s^{-1}$, $\phi = -149°$. (b) RMSD plot comparing polarization transfer models.

Overall the systematic errors are less than ±5°. A more careful analysis of these errors will be performed with Monte Carlo simulation methods in the multi-dimensional parameter space.

However, an additional problem exists due to the multiple degenerate solutions in the ϕ space. This is a direct result of the mirror-plane symmetry along the HN-CH plane, as noted in previous studies. In the Phe result (Figure 6-11), this degeneracy is even more pronounced, and six near equivalent solutions are possible. As geometry deviates from canonical β-sheet, these effects are increasingly important. In order to eliminate solutions, it may be acceptable to assume standard low energy regions of Ramachandran space (i.e., negative ϕ values for L-amino acids), or to corroborate the NMR results with supporting crystal structure data. However, this is not always possible. A more direct approach would be to eliminate some of the solutions with additional NMR data.

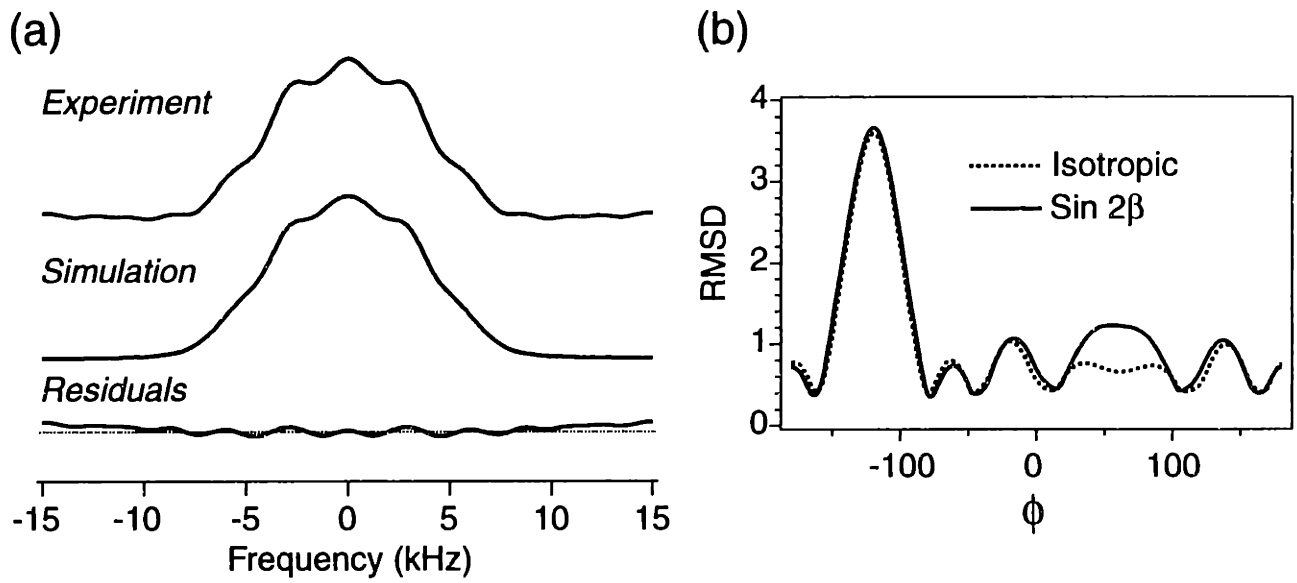

Figure 6-11. Phe HN-CH Dipolar T-MREV Spectrum and Best Fit Simulation.

Experimental data is extracted from the dipolar dimension of the 3D HNCH SLF experiment. (a) Experimental spectrum and best fit simulation with T-MREV scaling of 0.446, $\Gamma_2 = 4500\ s^{-1}$, $\phi = -162°$. (b) RMSD plot comparing polarization transfer models.

We do so by considering the dipolar HN-$C^{\beta}H_2$ dipolar spectra, because the projection angles which will depend on both ϕ and χ_1. Although the CH_2 group is a uniquely difficult case for homonuclear decoupling, it is possible to acquire sufficiently good dipolar lineshapes with T-

MREV at >9 kHz. Previously we have analyzed the T-MREV dephasing in NH_2 groups, and shown that the dipolar lineshapes have extreme sensitivity to the H-N-H angle.[17] Likewise, CH_2 spectra depend strongly on the H-C-H angle, and in principle can be used to determine this parameter with high precision. But our primary focus here is to the use the effective CH_2 director for torsion angle constraints, and this requires relatively fast MAS; otherwise the two strong C-H couplings may produce rapid evolution on a timescale that is fast compared to the T-MREV cycle time. The equivalent frequency domain picture is that cycling sidebands will arise *within* the T-MREV dipolar lineshape, complicating the analysis considerably. Again, we emphasize that such dynamics can be calculated exactly, but such calculations are very computationally demanding and for this reasons may lack generality for extension to total molecular structure determination. To illustrate the effect, we examine the Leu $C^{\beta}H_2$ T-MREV spectra as a function of MAS rate, using constant ^1H RF fields. (This data is from the same MAS-dependent study presented in Figure 6-4.) Note that dramatic changes in the overall lineshapes occur as the spinning rate is increased, corresponding to cycling sideband effects. No combination of molecular geometry, relaxation, and scaling factors was able to provide acceptable fits of the 5.94 and 7.15 kHz data, using the approximate T-MREV model.

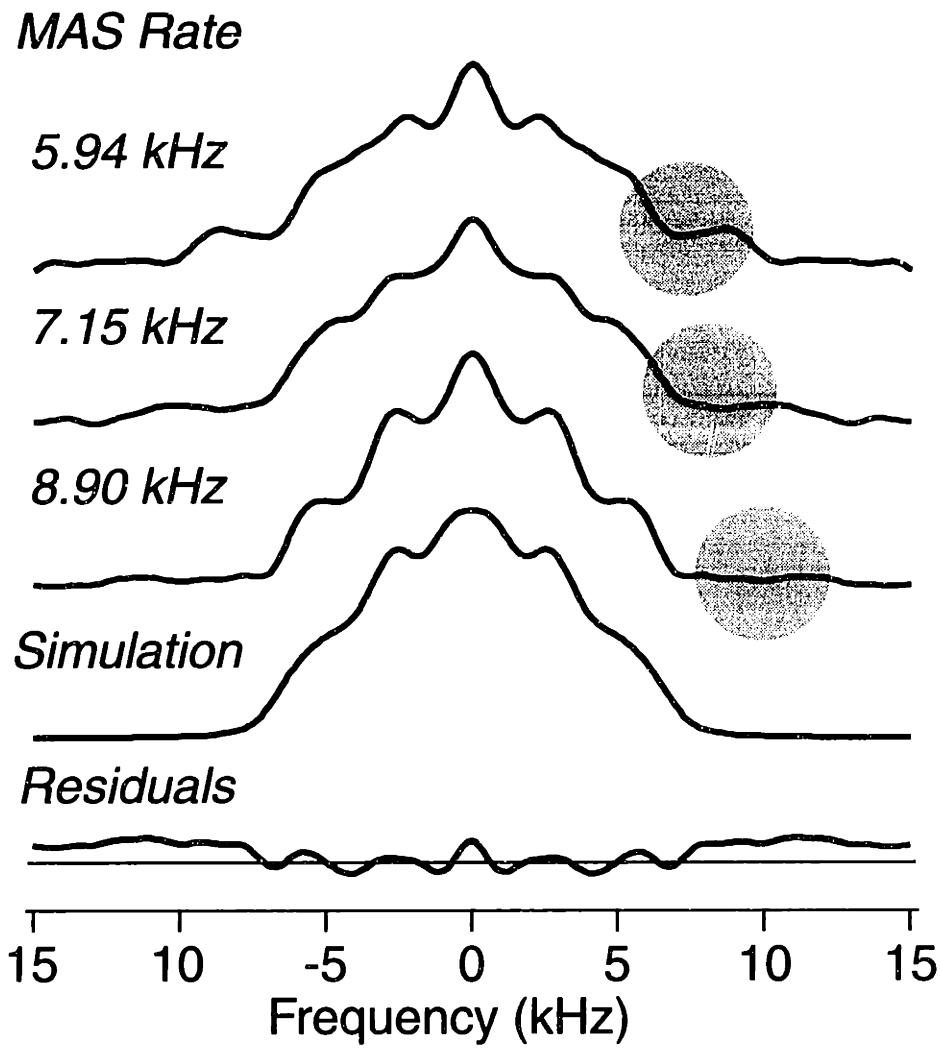

Figure 6-12. Leu $C^{\beta}H_2$ T-MREV Spectra as a Function of MAS Rate.

Experimental parameters (other than MAS rate) are equivalent to the HN-CH experiments throughout, with 108 kHz ^{1}H RF fields matching the appropriate T-MREV symmetry condition. The simulation assumes the geometry of the $C^{\beta}H_2$ with $H(C^{\alpha})$ and $H(C^{\gamma})$ also explicitly considered, with fitted T-MREV scaling of 0.445, 3500 s^{-1} relaxation rate on ^{1}H coherences, χ_1 = -60, and χ_2 = 180.

However, at 8.9 kHz a satisfactory fit is obtained with reasonable parameters. Although the fit does not reproduce all features of the spectrum, the agreement is quite good considering the approximation of residual homonuclear couplings as empirical damping parameters, which are equivalent for all protons. Nevertheless, the shortcomings of the analytical model do not prevent relative orientations from being fit with high precision in some regions of the ϕ/χ space.

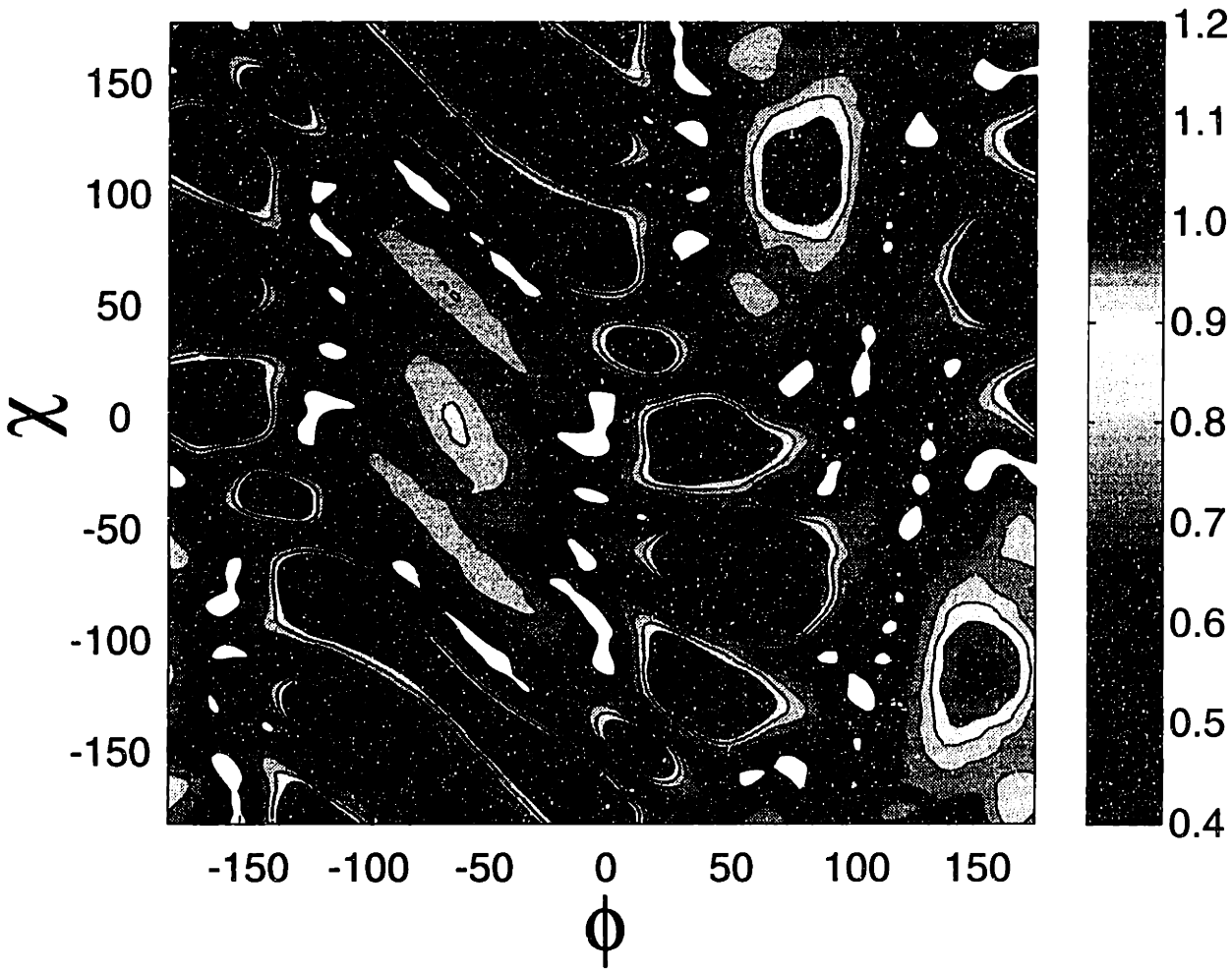

Figure 6-13. 2D RMSD Contour Plot for Leu NH-C$^{\beta}$H$_2$ T-MREV Spectrum.

An isotropic N-C$^{\beta}$ polarization transfer model was assumed in this case. Otherwise simulation parameters are identical to previous figures.

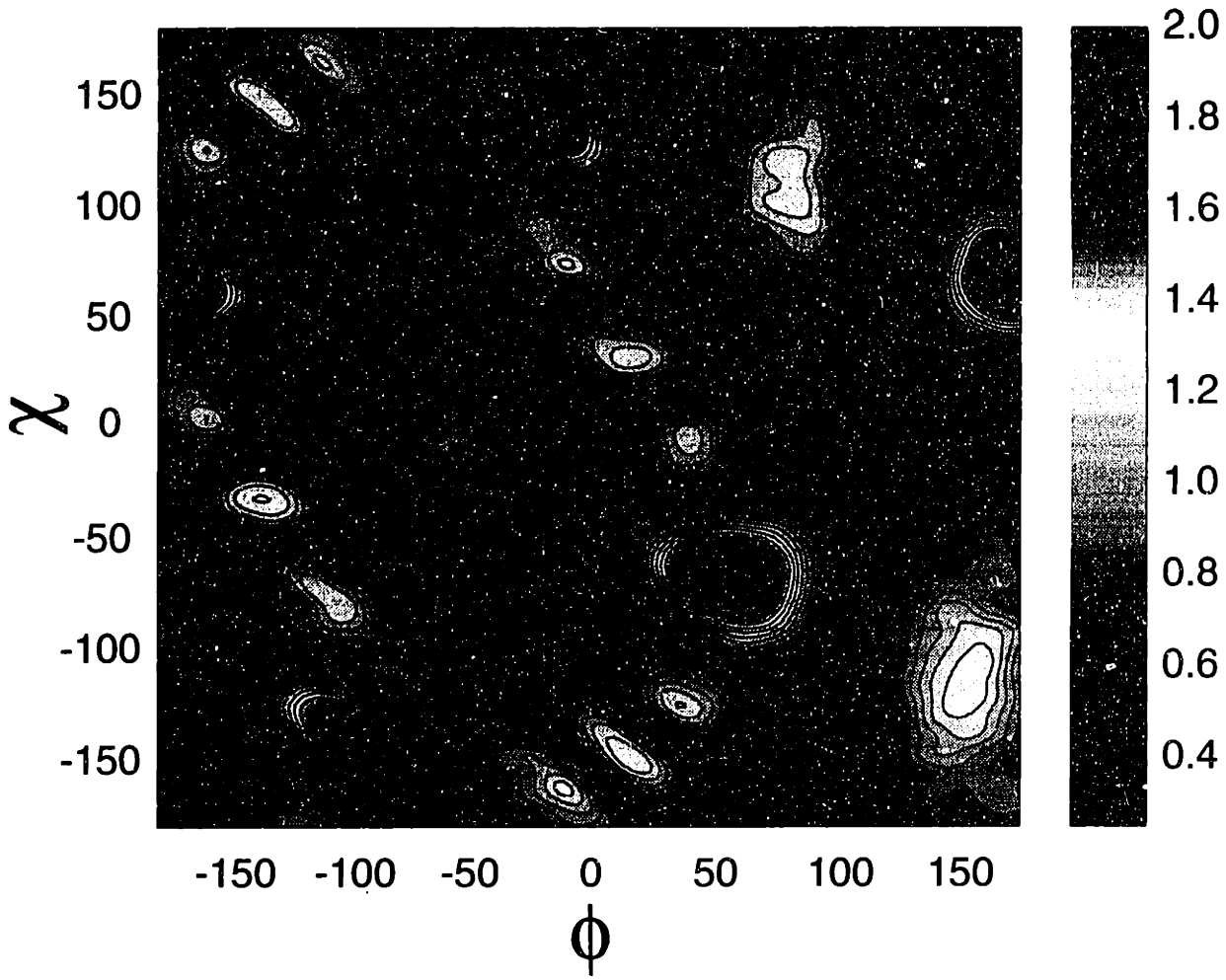

Figure 6-14. 2D RMSD Contour for Met HN-$C^{\beta}H_2$.

Figure 6-13 and Figure 6-14 demonstrate one valuable role of the NH-$C^{\beta}H_2$ data. Rings of solutions, most evident in Figure 6-13, have extremely poor agreement with the experimental data. These rings correspond to geometries in which one of the C^{β}-H vectors is aligned with the N-H vector. These solutions are ruled out with extremely high confidence for Met and Leu, indicating that neither residue possesses such a geometry. In combination with knowledge about χ from the HC^{α}-HC^{β} portion of the 3D HCCH experiment (below), a subset of the ϕ solutions may be discarded. More generally, the probability surfaces would be used as input parameters for a full structure determination protocol, where the relative confidence of the various torsion angle constraints is considered quantitatively. Although the Met and Leu results alone are not

conclusive, the information provided is likely to constrain the total structural parameter space considerably.

An example where the NH-$C^{\beta}H_2$ data provides a positive result is in Phe (Figure 6-15). Here the combination of ϕ and χ result in alignment of one C^{β}-H vector with the N-H vector, as evident in the very steep regions on the RMSD map. Solutions in one of the four minima, which are compatible with other knowledge of the local structure, are in this case likely to constrain both ϕ and χ with high precision.

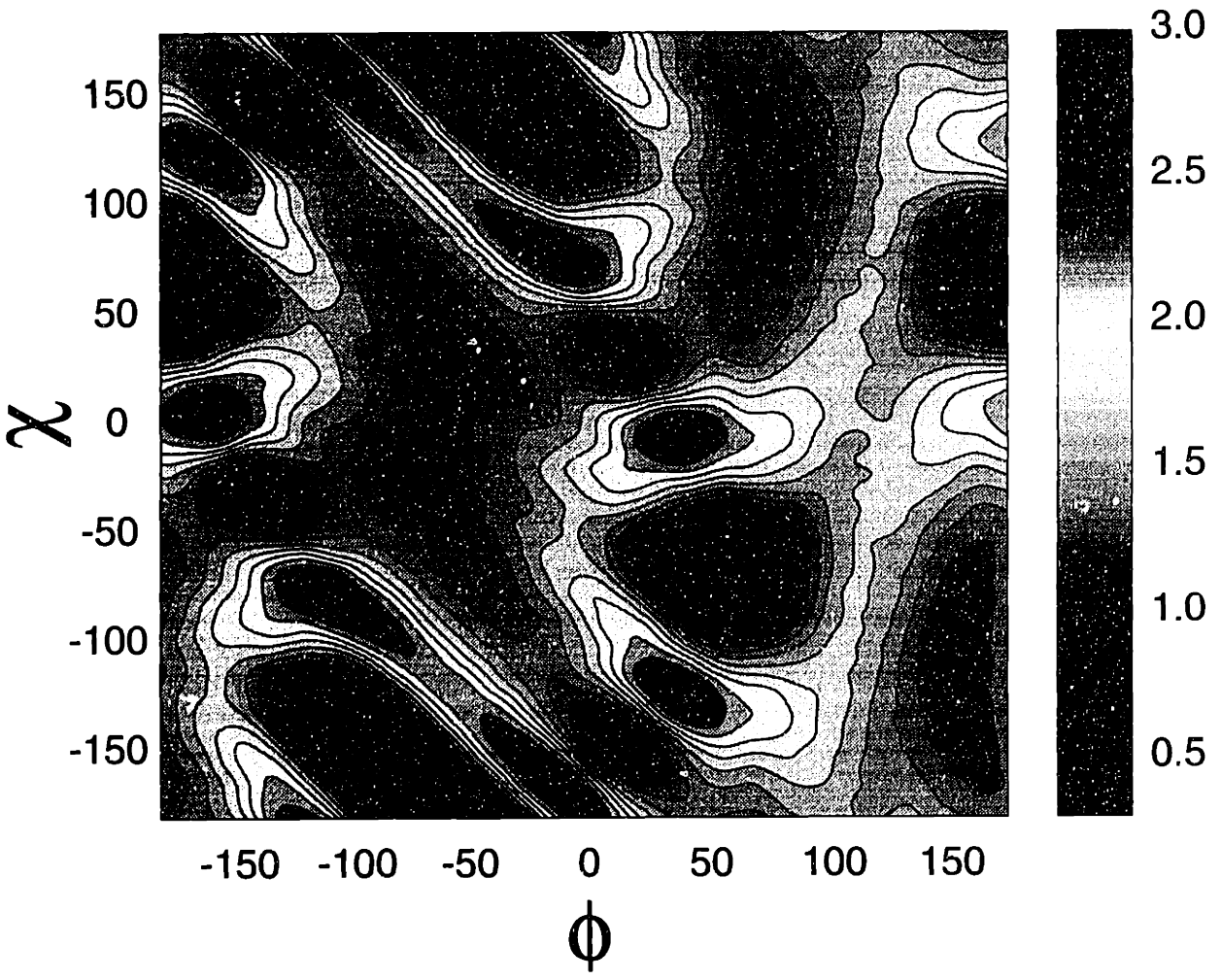

Figure 6-15. 2D RMSD Contour for Phe NH-$C^{\beta}H_2$

In addition, potential systematic errors from the NH-$C^{\alpha}H$, NH-$C^{\beta}H_2$, and $C^{\alpha}H$-$C^{\beta}H$ experiments will cancel, if the source of error is uncorrelated with respect to changes in the angular estimations, as is likely. Although there are several ϕ solutions that are compatible with

Figure 6-15, the knowledge of χ +60 ± 15° (from HCCH experiment below) restricts our attention to one local minimum, as shown in Figure 6-16. The the region near ϕ=-162, χ=60 is a unique solution consistent with all available data (HN-$C^{\alpha}H$, HN-$C^{\beta}H_2$, and HC^{α}-$C^{\beta}H$) that depend upon these torsion angles. More rigorous analysis of this data will require combined simulations of these data with global minimization over all torsion angle parameters.

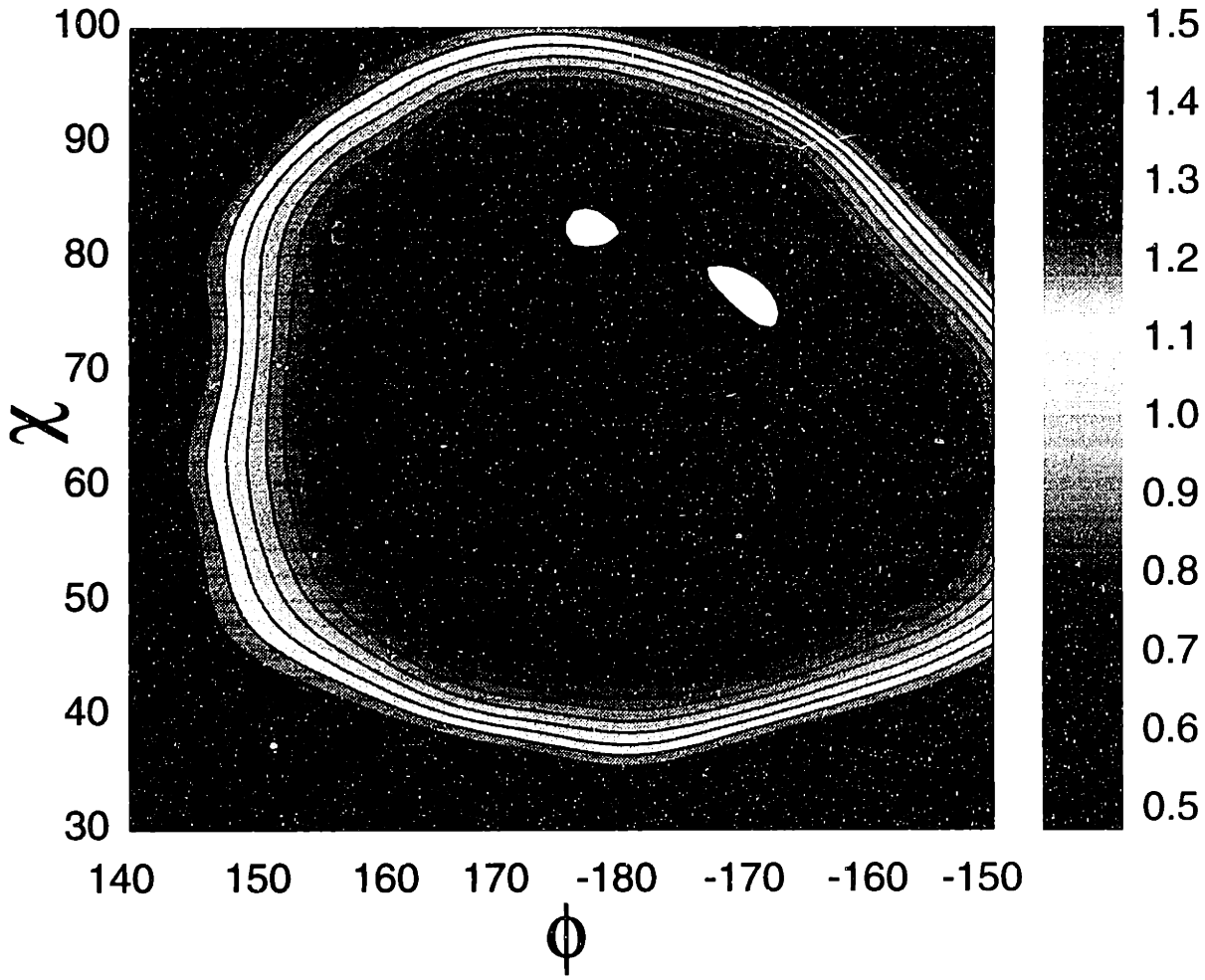

Figure 6-16. Local Minimum on Phe HN-$C^{\beta}H_2$ RMSD Plot.

HC-CH Experiments

The HC-CH experiment builds upon the HN-CH, and presents some additional issues in the data interpretation. Because the C-H couplings are larger than N-H, the limit of spinning much faster than the dominant features in the dipolar spectrum is not rigorously satisfied. High frequency features in the interference spectra may complicate data fitting in the time-domain. In addition, the polarization transfer dynamics among multiple coupled ^{13}C nuclei must be considered explicitly. As with the band selective ^{15}N-^{13}C polarization transfer step, which increases sensitivity and simplifies the polarization transfer dynamics, we employ a similar strategy in the ^{13}C-^{13}C polarization transfer step, by using SPC-5_3 to avoid C' transfer. As demonstrated in Figure 6-17 (as for MLF in Figure 6-7), polarization transfer is limited to the aliphatic signals. Therefore we may safely consider only the C^{α}, C^{β}, and C^{γ} spins for analysis of the dipolar dephasing data projected out of the C^{α}-C^{β} crosspeak. We do so with the three-spin model presented in Ref. 22.

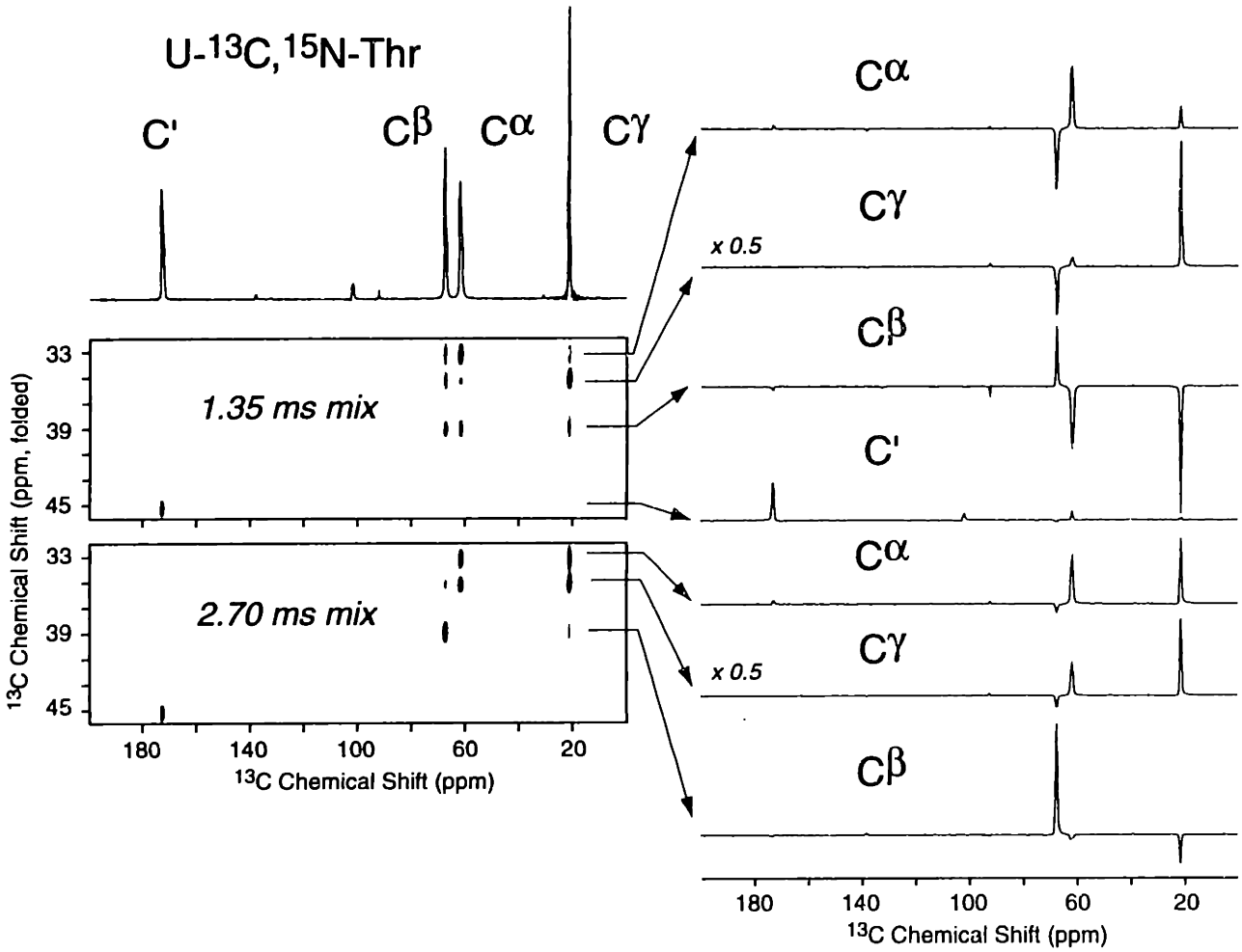

Figure 6-17. 2D ^{13}C-^{13}C SPC-5$_3$ Spectrum of U-^{13}C,^{15}N-Thr

Data is taken from the first ^{13}C-^{13}C slice of the 3D HC-CH experiment. At the short mixing time (1.35 ms, 12 τ_r), transfer is primarily to directly bonded neighbors. At longer mixing time, two-step transfer from C^{α} to C^{γ} (and vice versa) is efficient, and polarization initiating on the C^{β} resonance is not effectively transferred, due to coherent refocusing as discussed by Brüschweiler.[57]

The T-MREV control experiments for U-^{13}C,^{15}N-Thr are presented in Figure 6-18. Four (^1H) spins are required in order to fit the data with high precision. The dominant residual is at the zero-frequency in the C^{α} spectrum, likely due to the assumption we have used to model the NH_3 group as a single proton along the C^{α}-N axis.

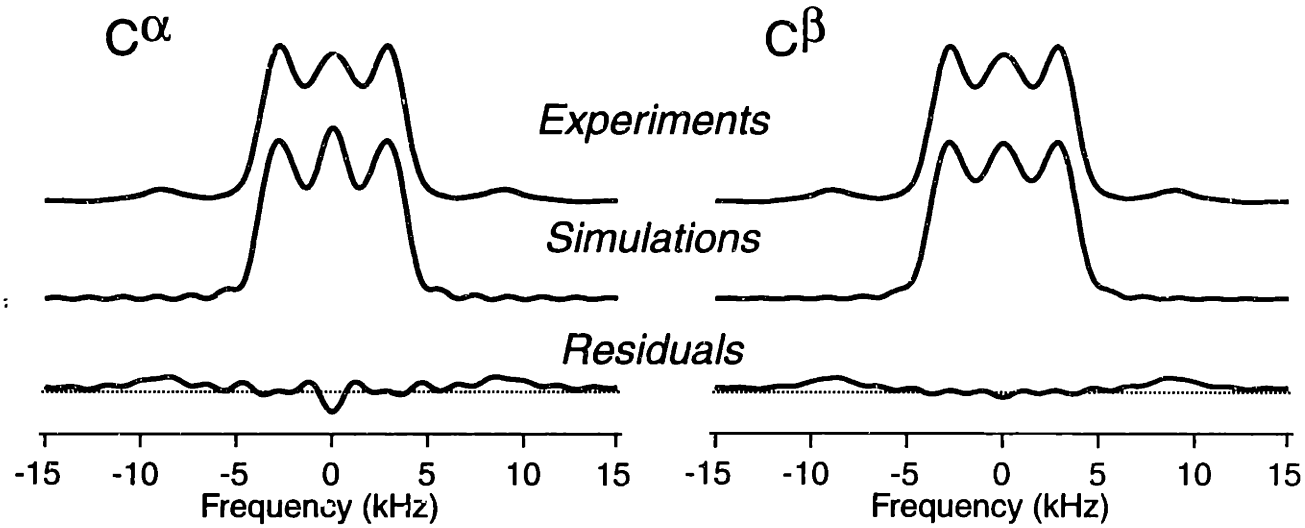

Figure 6-18. ^{13}C T-MREV Spectra of Thr C^{α} and C^{β} (Control Experiments).

C^{α} fit parameters: 0.462 T-MREV scaling, 5500 s^{-1} relaxation, 0.3879 RMSD. C^{β}: 0.460 scaling, 5000 s^{-1} relaxation, 0.2262 RMSD. Fitting was performed in the frequency domain over a range of ±8 kHz, using 4 ^{1}H spins with Thr geometry.[58] The NH_3 group is modeled as a single proton along the C^{α}-N axis.

The dipolar data from the 3D HCCH Thr data set was analyzed with the parameters derived from the control experiment in Figure 6-18, allowing the torsion angle χ to vary in steps of 1°. The results are shown in Figure 6-19. The slight disagreement between the global minima in the C^{α}-C^{β} (±177°) and C^{β}-C^{α} (±175°) may arise from imprecise modeling of distant protons or relaxation during the ^{13}C-^{13}C polarization transfer step. The H-C^{α}-C^{β}-H angle determined from neutron diffraction is 177.8°.[58] The potential systematic errors greatly exceed the random error in this case, and additional simulations will be performed to address these effects.

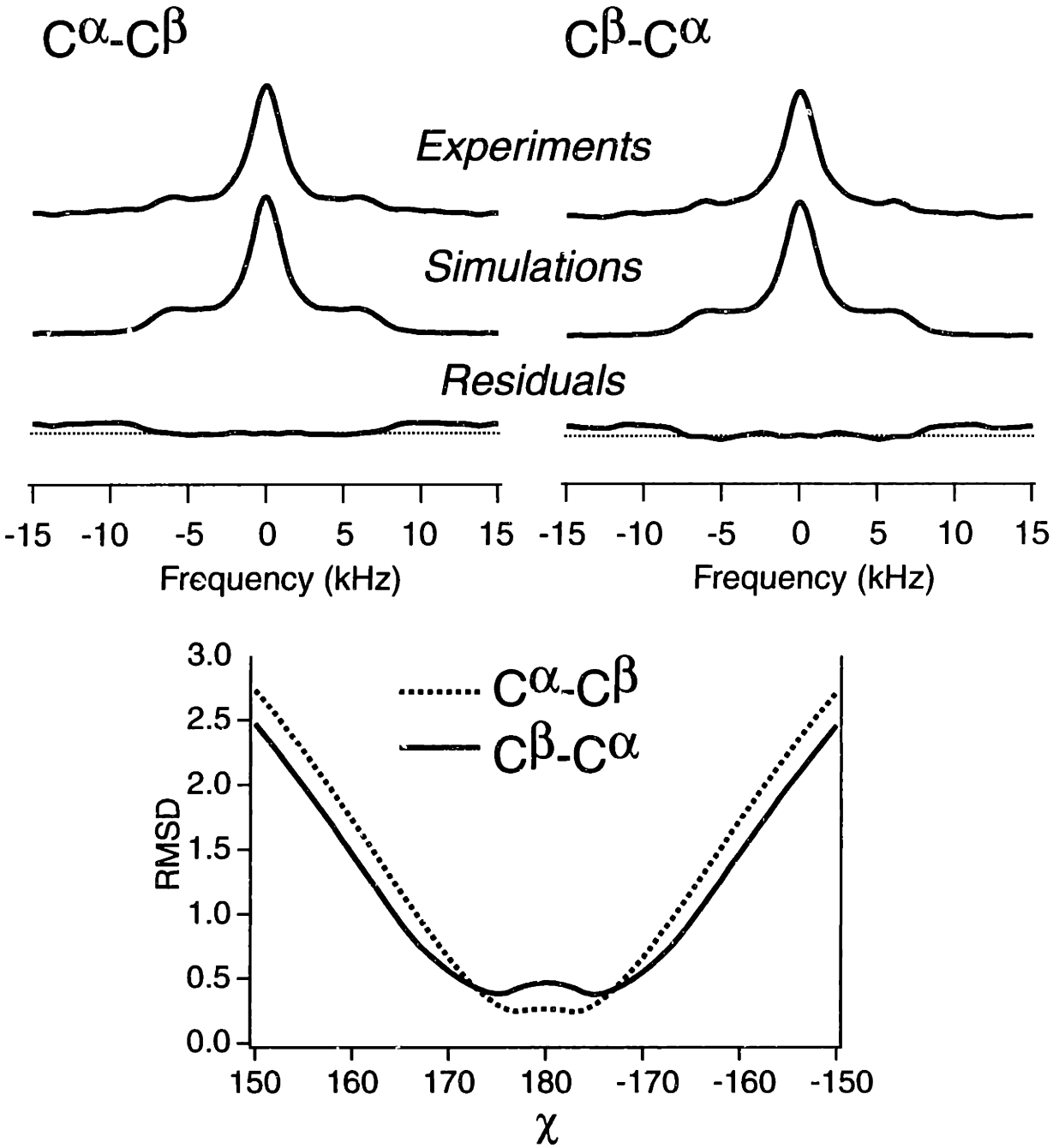

Figure 6-19. Thr HC$^{\alpha}$-C$^{\beta}$H Measurement of χ.

Simulations were performed with the same scaling and relaxation parameters in Figure 6-18, varying χ in steps of 1°.

Analysis of the MLF data proceeds in like manner, with the results shown in Table 6-2. Consistent with earlier results, the C^{α}-H data fits with much higher precision and relaxation rates on the order of 3000-4000 s^{-1}. One unusual aspect of these fits is the 75% scaling of the Met $C^{\beta}H_2$ pattern relative to the other $C^{\beta}H_2$ dipolar signals. The implication of this scaling with respect to motional averaging has not yet been thoroughly investigated. Variable temperature studies may be warranted to analyze the presumed sidechain motion.

Table 6-2. T-MREV Parameters for 1D Dipolar Spectra (MLF)

Signal	T-MREV Scaling	Γ_2	RMSD
Met C^{α}	0.452	3750	0.275
Leu C^{α}	0.458	3750	0.254
Phe C^{α}	0.453	3250	0.254
Met C^{β}	0.332	3500	0.440
Leu C^{β}	0.446	5000	0.488
Phe C^{β}	0.452	4500	0.562

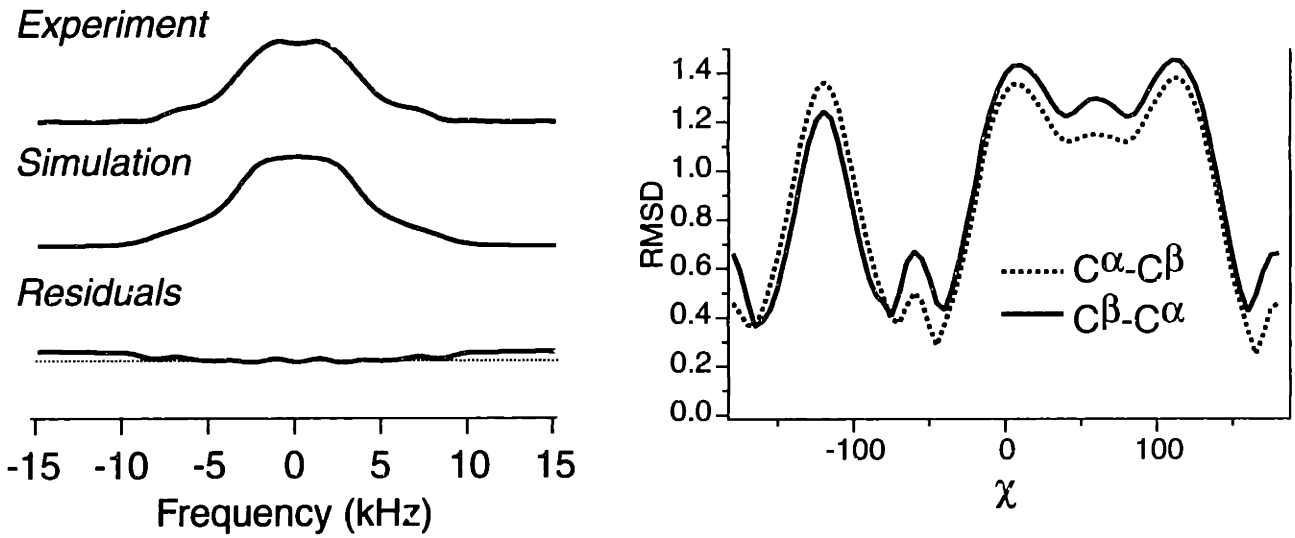

Figure 6-20. Met HC^{α}-$C^{\beta}H_2$ Measurement of χ

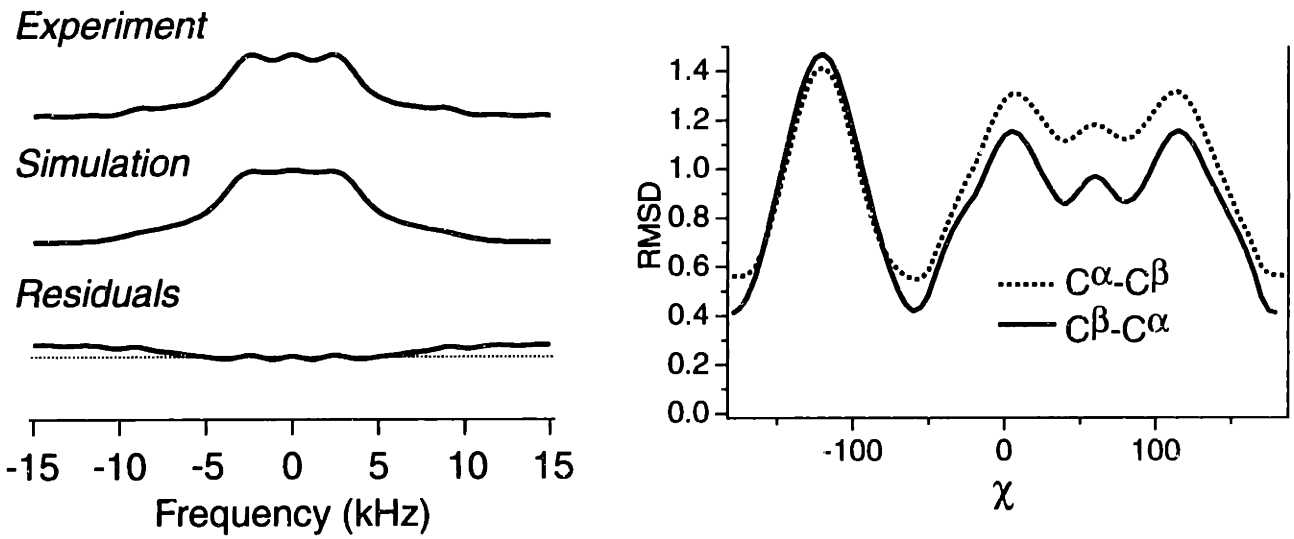

Figure 6-21. Leu HC^{α} -$C^{\beta}H_2$ Measurement of χ

Data shown on the left is the best fit (–60°) for the C^{β}-C^{α} crosspeak.

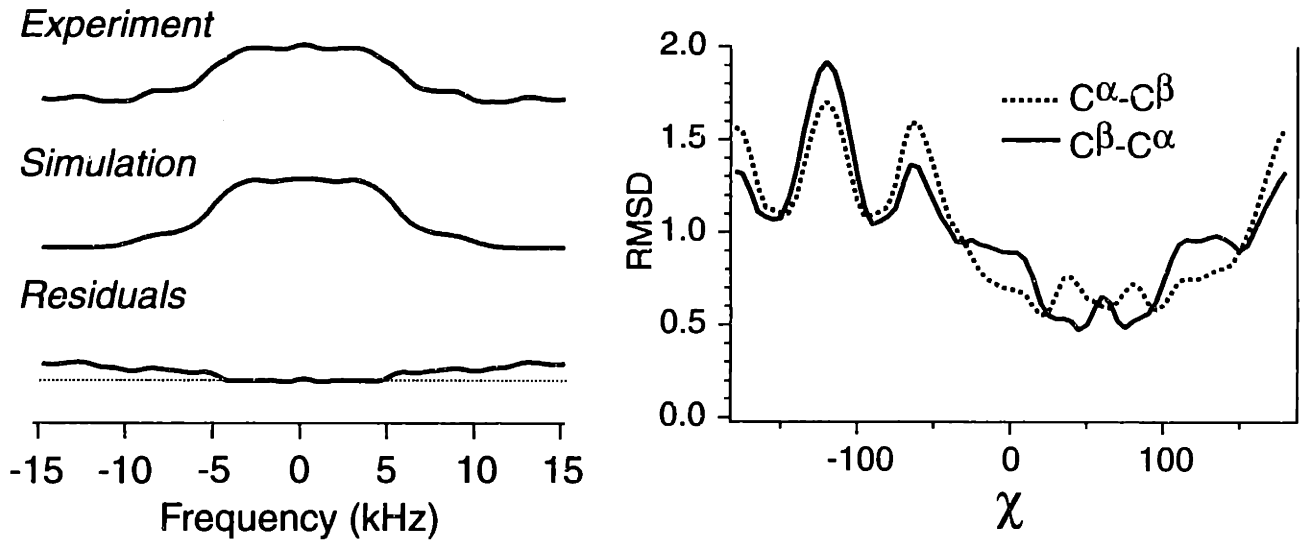

Figure 6-22. Phe HC^{α}-$C^{\beta}H_2$ Measurement of χ.

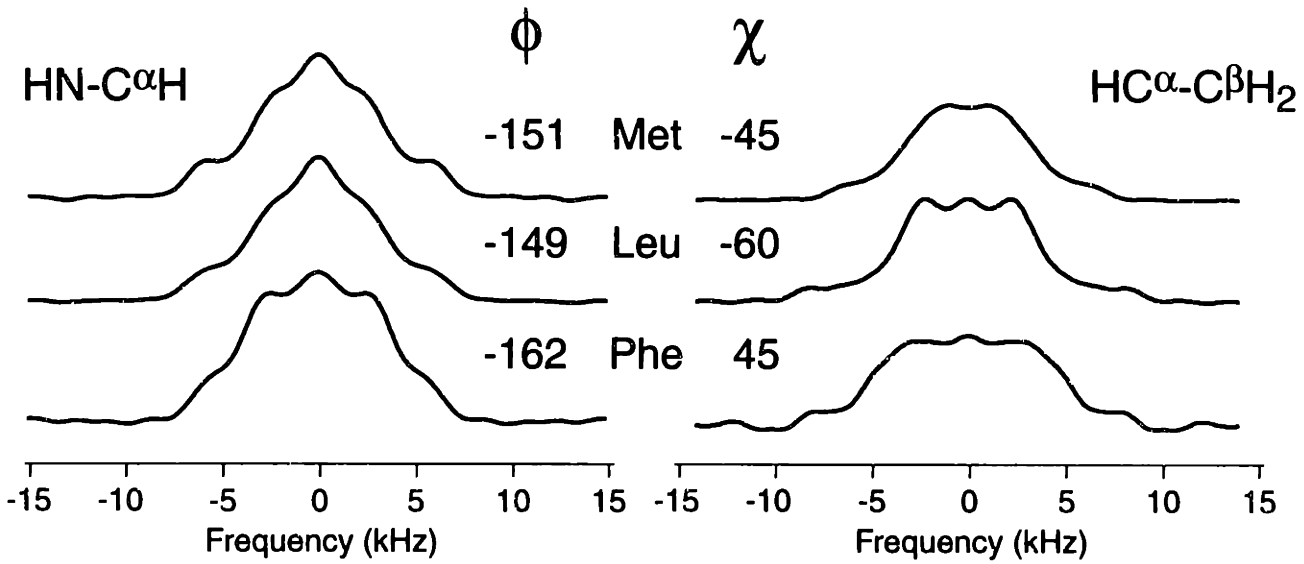

Figure 6-23. Summary of HN-$C^{\alpha}H$ and HC^{α}-$C^{\beta}H_2$ Dipolar Spectra.

Conclusions

Here we have presented several constraints of molecular structure by multi-dimensional torsion angle measurements in solids. At high MAS rates with the 3D versions HCCH, HNCH, and NCCN experiments, numerous redundant constraints are derived from a single data set. This is important for constraining sidechain conformation especially, and for distinguishing *a priori* between degenerate solutions in the α-sheet and β-helix or turn regions of Ramachandran space. We anticipate use of chemical shifts (both isotropic and CSA) to assist in this process further, [59,60] and eliminate unlikely solutions from the SLF-derived parameter space. Once a local minimum has been identified with good confidence, the primary errors remaining are attributable to the small systematic dependence of the fitted torsion angle upon relaxation and dipolar scaling factors. These errors will be characterized further in future studies.

We anticipate that this work can be applied directly to structural problems of interest in U-^{13}C,^{15}N-labeled proteins, because implementation is compatible with conditions of high sensitivity and resolution required to resolve large numbers of resonances in solid state proteins. The four-fold T-MREV sequence requires a ^{1}H RF field which is 12 times the MAS rate; this may be achieved at rates of up to ~18-20 kHz with commercially available, 2.5 mm and 3.2 mm rotor assemblies. In larger proteins, where sensitivity is problematic, the time-efficiency of the experiment may be improved by sampling particular points in the dipolar time domain that have optimal sensitivity to angular resolution.

Acknowledgments

This work was performed in collaboration with Morten Hohwy, Leonard J. Mueller, Christopher P. Jaroniec, and Bernd Reif.

References

(1) Stoll, M. E.; Vega, A. J.; Vaughn, R. W. "Heteronuclear dipolar modulated chemical-shift spectra for geometrical information in polycrystalline solids," *J. Chem. Phys.* **1976**, *65*, 4093-4098.

(2) Rybaczewski, E. F.; Neff, B. L.; Waugh, J. S.; Sherfinksi, J. S. "High resolution C-13 NMR in solids: 13C local fields of CH, CH2, CH3," *J. Chem. Phys.* **1977**, *67*, 1231-1236.

(3) Linder, M.; Höhener, A.; Ernst, R. R. *J. Chem. Phys.* **1980**, *73*, 4959.

(4) Schmidt-Rohr, K. "Torsion angle determination in solid C-13-labeled amino acids and peptides by separated-local-field double-quantum NMR," *J. Am. Chem. Soc.* **1996**, *118*, 7601-7603.

(5) Schmidt-Rohr, K. "A double-quantum solid-state NMR technique for determining torsion angles in polymers," *Macromolecules* **1996**, *29*, 3975-3981.

(6) Dabbagh, G.; Weliky, D. P.; Tycko, R. "Determination of monomer conformations in noncrystalline solid polymers by 2D NMR exchange spectroscopy," *Macromolecules* **1994**, *27*, 6183-6191.

(7) Feng, X.; Lee, Y. K.; Sandström, D.; Edén, M.; Maisel, H.; Sebald, A.; Levitt, M. H. "Direct determination of a molecular torsional angle by solid-state NMR," *Chem. Phys. Lett.* **1996**, *257*, 314-320.

(8) Ishii, Y.; Terao, T.; Kainosho, M. "Relayed anisotropy correlation NMR: Determination of dihedral angles in solids," *Chem. Phys. Letters* **1996**, *256*, 133-140.

(9) Feng, X.; Verdegem, P. J. E.; Lee, Y. K.; Sandström, D.; Edén, M.; Bovee-Geurts, P.; de Grip, W. J.; Lugtenburg, J.; de Groot, H. J. M.; Levitt, M. H. "Direct determination of a molecular torsion angle in the membrane protein rhodopsin by solid-state NMR," *J. Am. Chem. Soc.* **1997**, *119*, 6853-6857.

(10) Hong, M.; Gross, J. D.; Griffin, R. G. "Site-resolved determination of peptide torsion angle phi from the relative orientations of backbone N-H and C-H bonds by solid-state NMR," *J. Phys. Chem. B* **1997**, *101*, 5869-5874.

(11) Hong, M.; Gross, J. D.; Rienstra, C. M.; Griffin, R. G.; Kumashiro, K. K.; Schmidt-Rohr, K. "Coupling amplification in 2D MAS NMR and its application to torsion angle determination in peptides," *J. Magn. Reson.* **1997**, *129*, 85-92.

(12) Feng, X.; Eden, M.; Brinkmann, A.; Luthman, H.; Eriksson, L.; Graslund, A.; Antzutkin, O. N.; Levitt, M. H. "Direct determination of a peptide torsional angle psi by double-quantum solid-state NMR," *J. Am. Chem. Soc.* **1997**, *119*, 12006-12007.

(13) Costa, P. R.; Gross, J. D.; Hong, M.; Griffin, R. G. "Solid-state NMR measurement of psi in peptides: a NCCN 2Q-heteronuclear local field experiment," *Chem. Phys. Lett.* **1997**, *280*, 95.

(14) Reif, B.; Hennig, M.; Griesinger, C. "Direct measurement of angles between bond vectors in high-resolution NMR," *Science* **1997**, *276*, 1230-1233.

(15) Nomura, K.; Takegoshi, K.; Terao, T.; Uchida, K.; Kainosho, M. "Determination of the complete structure of a uniformly labeled molecule by rotational resonance solid-state NMR in the tilted rotating frame," *J. Am. Chem. Soc.* **1999**, *121*, 4064-4065.

(16) Fujiwara, T.; Shimomura, T.; Ohigashi, Y.; Akutsu, H. "Multidimensional solid-state nuclear magnetic resonance for determining the dihedral angle from the correlation of C-13-

H-1-C-13-C-13 dipolar interactions under magic-angle spinning conditions," *J. Chem. Phys.* **1998**, *109*, 2380-2393.

(17) Hohwy, M.; Jaroniec, C. P.; Reif, B.; Rienstra, C. M.; Griffin, R. G. "Local structure and relaxation in solid-state NMR: Accurate measurement of amide N-H bond lengths and H-N-H bond angles," *J. Am. Chem. Soc.* **1999**, submitted.

(18) Eden, M.; Levitt, M. H. "Excitation of carbon-13 triple quantum coherence in magic-angle-spinning NMR," *Chem. Phys. Lett.* **1998**, *293*, 173-179.

(19) Gross, J. D., *Measurements of segmental order parameters and torsional angles in solid state nuclear magnetic resonance*, Ph.D. Thesis, Massachusetts Institute of Technology, **1998**.

(20) Levitt, M. H.; Raleigh, D. P.; Creuzet, F.; Griffin, R. G. "Theory and simulations of homonuclear spin pair systems in rotating solids," *J. Chem. Phys.* **1990**, *92*, 6347-64.

(21) Griffin, R. G. "Dipolar recoupling in MAS spectra of biological solids," *Nat. Struct. Biol.* **1998**, *5*, 508-512.

(22) Hohwy, M.; Rienstra, C. M.; Jaroniec, C. P.; Griffin, R. G. "Fivefold symmetric homonuclear dipolar recoupling in rotating solids: Application to double quantum spectroscopy," *J. Chem. Phys.* **1999**, *110*, 7983-7992.

(23) Andrew, E. R.; Bradbury, A.; Eades, R. G. "Nuclear magnetic resonance spectra from a crystal rotated at high speed," *Nature (London)* **1958**, *182*, 1659.

(24) Andrew, E. R.; Clough, S.; Farnell, L. F.; Gledhill, T. A.; Roberts, I. "Resonant rotational broadening of NMR Spectra," *Phys. Lett.* **1966**, *21*, 505-506.

(25) Raleigh, D. P.; Levitt, M. H.; Griffin, R. G. "Rotational resonance in solid state NMR," *Chem. Phys. Lett.* **1988**, *146*, 71-76.

(26) Mehta, A. K., *High resolution 13C solid-state nuclear magnetic resonance: decoupling and recoupling under high speed magic angle spinning*, Ph.D. Thesis, Yale University, **1998**.

(27) Tounge, B. A., *High field solid state NMR: Assignment strategies and distance measurements using U-13C-labeled samples*, Ph.D. Thesis, Yale University, **1998**.

(28) Zell, M. T.; Padden, B. E.; Grant, D. J. W.; Chapeau, M. C.; Prakash, I.; Munson, E. J. "Two-dimensional high-speed CP/MAS NMR spectroscopy of polymorphs. 1. Uniformly C-13-labeled aspartame," *J. Am. Chem. Soc.* **1999**, *121*, 1372-1378.

(29) Gullion, T.; Vega, S. "A simple magic-angle spinning NMR experiment for the dephasing of rotational echoes of dipolar coupled homonuclear spin pairs," *Chem. Phys. Lett.* **1992**, *194*, 423-428.

(30) Bennett, A. E.; Rienstra, C. M.; Griffiths, J. M.; Zhen, W.; Lansbury, P. T., Jr.; Griffin, R. G. "Homonuclear radio frequency-driven recoupling in rotating solids," *J. Chem. Phys.* **1998**, *108*, 9463-9479.

(31) Lee, Y. K.; Kurur, N. D.; Helmle, M.; Johannessen, O. G.; Nielsen, N. C.; Levitt, M. H. "Efficient dipolar recoupling in the NMR of rotating solids. A sevenfold symmetric radiofrequency pulse sequence," *Chem. Phys. Lett.* **1995**, *242*, 304-309.

(32) Hohwy, M.; Jakobsen, H. J.; Edén, M.; Levitt, M. H.; Nielsen, N. C. "Broadband dipolar recoupling in the nuclear magnetic resonance of rotating solids: A compensated C7 pulse sequence," *J. Chem. Phys.* **1998**, *108*, 2686-94.

(33) Rienstra, C. M.; Hatcher, M. E.; Mueller, L. J.; Sun, B.-Q.; Fesik, S. W.; Herzfeld, J.; Griffin, R. G. "Efficient multispin homonuclear double-quantum recoupling for magic-angle spinning NMR: ^{13}C-^{13}C Correlation spectroscopy of U-^{13}C-erythromycin A," *J. Am. Chem. Soc.* **1998**, *120*, 10602-10612.

(34) Bennett, A. E.; Ok, J. H.; Griffin, R. G.; Vega, S. "Chemical shift correlation spectroscopy in rotating solids: Radio-frequency dipolar recoupling and longitudinal exchange," *J. Chem. Phys.* **1992**, *96*, 8624-8627.

(35) Baldus, M.; Tomaselli, M.; Meier, B. H.; Ernst, R. R. "Broad-band polarization-transfer experiments for rotating solids," *Chem. Phys. Lett.* **1994**, *230*, 329-336.

(36) Gregory, D. M.; Mitchell, D. J.; Stringer, J. A.; Kiihne, S.; Shiels, J. C.; Callahan, J.; Mehta, M. A.; Drobny, G. P. "Windowless dipolar recoupling--The detection of weak dipolar couplings between spin-1/2 nucleic with large chemical-shift anisotropies," *Chem. Phys. Lett.* **1995**, *246*, 654.

(37) Sun, B. Q.; Costa, P. R.; Kocisko, D. A.; Lansbury, P. T., Jr. ; Griffin, R. G. "Internuclear distance measurements in solid state nuclear magnetic resonance: Dipolar recoupling via rotor sychronized spin locking," *J. Chem. Phys.* **1995**, *102*, 702-707.

(38) Baldus, M.; Meier, B. H. "Total correlation spectroscopy in the solid state. The use of scalar couplings to determine the through-bond connectivity," *J. Magn. Reson. A* **1996**, *121*, 65-69.

(39) Peersen, O. B.; Wu, X.; Kustanovich, I.; Smith, S. O. "Variable amplitude cross-polarization MAS NMR," *J. Magn. Reson. A* **1993**, *104*, 334-339.

(40) Wu, X.; Zilm, K. W. "Cross polarization with high-speed magic angle spinning," *J. Magn. Reson. A* **1993**, *104*, 154-165.

(41) Hediger, S.; Meier, B. H.; Ernst, R. R. "Cross-polarization under fast magic-angle sample-spinning using amplitude-modulated spin-lock sequences," *Chem. Phys. Lett.* **1993**, *213*, 627-635.

(42) Peersen, O. B.; Wu, X.; Smith, S. O. "Enhancement of CP-MAS signals by variable amplitude cross polarization. Compensation for inhomogeneous B1 fields," *J. Magn. Reson. A* **1994**, *106*, 127-131.

(43) Hediger, S.; Meier, B. H.; Kurur, N. D.; Bodenhausen, G.; Ernst, R. R. "NMR cross-polarization by adiabatic passage through the Hartmann-Hahn condition (APHH)," *Chem. Phys. Lett.* **1994**, *223*, 283-288.

(44) Hediger, S.; Meier, B. H.; Ernst, R. R. "Adiabatic passage Hartmann-Hahn cross-polarization in NMR under magic-angle sample-spinning," *Chem. Phys. Lett.* **1995**, *240*, 449-456.

(45) Baldus, M.; Geurts, D. G.; Hediger, S.; Meier, B. H. "Efficient N-15-C-13 polarization transfer by adiabatic-passage Hartmann-Hahn cross polarization," *J. Magn. Reson. A* **1996**, *118*, 140-144.

(46) Hediger, S.; Signer, P.; Tomaselli, M.; Ernst, R. R.; Meier, B. H. "A combination of slow and fast RF field modulation for improved cross polarization in solid-state MAS NMR," *J. Magn. Reson.* **1997**, *125*, 291-301.

(47) Bennett, A. E.; Rienstra, C. M.; Auger, M.; Lakshmi, K. V.; Griffin, R. G. "Heteronuclear decoupling in rotating solids," *J. Chem. Phys.* **1995**, *103*, 6951-6958.

(48) Sun, B. Q.; Rienstra, C. M.; Costa, P. R.; Williamson, J. R.; Griffin, R. G. "3D 15N-13C-13C chemical shift correlation spectroscopy in rotating solids," *J. Am. Chem. Soc.* **1997**, *119*, 8540-8546.

(49) Hohwy, M.; Jaroniec, C. P.; Lansing, J.; Rienstra, C. M.; Griffin, R. G. "13C-1H Recoupling in the HCCH torsion angle experiment in solid-state NMR," *Chem. Phys. Lett.* **1999**, in preparation.

(50) Baldus, M. A.; Petkova, A. T.; Herzfeld, J. H.; Griffin, R. G. "Cross polarization in the tilted frame: assignment and spectral simplification in heteronuclear spin systems," *Mol. Phys.* **1998**, *95*, 1197-1207.

(51) States, D. J.; Haberkorn, R. A.; Ruben, D. J. "A two-dimensional nuclear Overhauser experiment with pure absorption phase in four quadrants," *J. Magn. Reson.* **1982**, *48*, 286-292.

(52) Ishii, Y.; Ashida, J.; Terao, T. "13C-1H dipolar recoupling dynamics in 13C multiple-pulse solid-state NMR," *Chem. Phys. Lett.* **1995**, *246*, 439-445.

(53) Bennett, A. E., *Dipolar Decoupling and Recoupling in Solid State Nuclear Magnetic Resonance Spectroscopy*, Ph. D. Thesis, Massachusetts Institute of Technology, **1995**.

(54) Böender, G. J.; Vega, S. "Phase sensitive detection of 2D homonuclear correlation spectra in MAS NMR," *J. Magn. Reson.* **1998**, *133*, 281-285.

(55) Carroll, P. J.; Stewart, P. L.; Opella, S. J. "Structures of two model peptides: N-acetyl-D,L-valine and N-acetyl-L-valyl-L-leucine," *Acta Cryst. C* **1990**, *46*, 243-246.

(56) Ishii, Y.; Hirao, K.; Terao, T.; Terauchi, T.; Oba, M.; Nishiyama, K.; Kainosho, M. "Determination of peptide phi angles in solids by relayed anisotropy correlation NMR," *Solid State Nucl. Magn. Reson.* **1998**, *11*, 169-175.

(57) Bruschweiler, R.; Ernst, R. R. "A cog-wheel model for nuclear-spin propagation in solids," *J. Magn. Reson.* **1997**, *124*, 122-126.

(58) Ramanadham, M.; Sikka, S. K.; Chidambaram, R. "Structure determination of L-threonine by neutron diffraction," *Pramana* **1973**, *1*, 247-259.

(59) Oldfield, E. "Chemical shifts and 3-dimensional protein structures," *J. Biomol. NMR* **1995**, *5*, 217-225.

(60) Heller, J.; Laws, D. D.; Tomaselli, M.; King, D. S.; Wemmer, D. E.; Pines, A.; Havlin, R. H.; Oldfield, E. "Determination of dihedral angles in peptides through experimental and theoretical studies of alpha-carbon chemical shielding tensors," *J. Am. Chem. Soc.* **1997**, *119*, 7827-7831.

Section IV: Tertiary Structure (Distances)

Chapter 7. Quantitative Homonuclear Distance Measurements with CMR7 Double Quantum Recoupling in Rotating Solids

Abstract

The CMR7 recoupling sequence is employed for precise measurement of dipolar couplings between spin pairs under magic-angle spinning conditions. Because the γ-encoded CMR7 dipolar spectrum is peaked at frequency maxima, couplings can be extracted from experimental data with better precision than by previous methods. Information other than the strong coupling—such as experimental artifacts, differential relaxation effects, and natural abundance background—arise near the zero frequency. For strong couplings with minimal relaxation (such as the dicarboxylate anions), these issues are easily addressed and a single exponential relaxation model is sufficient. However, for protonated ^{13}C signals, differential relaxation must be considered explicitly in order to properly fit the data. We use dipolar echo sequences to differentiate relaxation from dipolar dephasing, and the relationship between rotating and laboratory frame relaxation rates is determined by an average Liouvillian analysis. Because the CMR7 sequence depends only minimally on CSA, dephasing trajectories can be described exactly with three parameters: scaled dipolar coupling and effective (interaction frame) transverse and longitudinal relaxation rates. Furthermore, the ratio of the two relaxation rates can be constrained by the Liouvillian model. For relatively strong dipolar couplings (*c.* 500 Hz), the dephasing trajectory alone is sufficient to constrain couplings within ±5 Hz (~2.5±0.01 Å for ^{13}C-^{13}C). For weaker couplings (~100 Hz), the combination of short- and long-time dipolar echo sequences, along with the dephasing data, provides excellent agreement with previous methods (RFDR and R^2T) in the dipeptide glycyl glycine hydrochloride. We find that the dominant errors remaining in the data interpretation are due to the explicit dependence of the dipolar scaling

factor on RF field amplitude. This effect is predicted by average Hamiltonian theory and can be calibrated. Alternatively, in favorable circumstances, the effect can be eliminated by a linear combination of the CMR7 and POST-C7 sequences (POST-CMR7), to cancel the RF-field dependence of the dipolar scaling to second order.

Introduction

The direct measurement of dipolar couplings to determine internuclear distances under conditions of high spectral resolution is one of the most significant goals of magic-angle spinning (MAS) NMR.[1] In addition to the precise study of hydrogen-bonding effects, for example, through strong ^{1}H-^{15}N or ^{1}H-^{13}C couplings,[2] distances between low-γ nuclei (e.g., ^{13}C-^{13}C, ^{13}C-^{15}N) can be used to constrain molecular structure in macroscopically disordered solid materials, including membrane proteins,[3-5] peptide aggregates,[6-8] peptide-protein complexes, [9] amorphous polymers,[10,11] and glasses. Although many applications of NMR distance measurements have been demonstrated, continued development of the methodology is clearly well motivated. Improved control and exact descriptions of the spin dynamics are desirable, in order to account for or eliminate effects other than the dipolar coupling, such as relaxation, RF pulse errors, and chemical shift effects (both isotropic and anisotropic). In addition, improved resolution of dipolar frequencies through MAS methods will be useful for distinguishing time-independent *distributions* of distances from time-*averaged* distances; the ability to distinguish between sample heterogeneity and dynamic processes is one of the unique talents of NMR.

Methodology for both homonuclear and heteronuclear distance determination under MAS has matured rapidly in the last two decades.[1,12,13] The DIPSHIFT[14,15] and REDOR[16,17] experiments were developed to measure strong and weak heteronuclear couplings, respectively. DIPSHIFT has been incorporated into several torsion angle measurement techniques, [18-20] and used for precise measurement of hydrogen bonding in a serine protease active site.[2] REDOR has been applied to successfully to many biological systems,[21-25] in part because of the relative

simplicity of data interpretation. For homonuclear systems, the rotational resonance (R^2) effect was discovered in 1966,[26] and its application to distance determination was investigated starting the late 1980's.[27,28] R^2 has been used to address many problems in membrane proteins,[3-5,29,30] although in heterogeneous systems R^2 can be complicated by chemical shift dispersion effects,[6,31,32] and differential relaxation (i.e, T_2^{ZQ}) must be considered explicitly in order to interpret the data properly. With proper attention to these details, extremely precise measurements of long distances can be obtained.[33,34] However, the R^2 experiment and its analogs are usually limited to spin pairs with relatively large chemical shift differences.

This fact has motivated the development of zero-quantum (ZQ) homonuclear experiments that do not depend as strongly upon chemical shift as R^2. RFDR[35,36] can be considered the first order correction to R^2, in that the rotor-synchronized π pulses broaden the matching conditions, permitting resonances away from R^2 to be recoupled. Because the π pulse echo trains for RFDR (the XY-8 scheme of Gullion and co-workers,[17] and extensions thereof) are simple to implement and well-compensated for many experimental errors, [36] RFDR has found wide applicability to ^{13}C-^{13}C correlation spectroscopy.[35-40] However, for quantitative experiments, both isotropic shift and CSA must be considered explicitly in the data interpretation, because the RFDR dipolar scaling factor depends quite significantly on both of these parameters. A broadband ZQ method (RIL,[41,42]) has been developed to compensate for this dependence, but RIL has not yet been applied for quantitative analysis of spin pair dephasing dynamics, All ZQ methods are difficult to implement for spin pairs with small chemical shift differences.

Recently, several examples of double-quantum (DQ) homonuclear dephasing experiments have been published.[43-47] Within this class of pulse sequences, the DRAWS experiment has been most fully developed for distance measurements,[46,48-50] and implemented in several instances, most notably for determination of peptide backbone structure via $^{13}C'[i]$-$^{13}C'[i+1]$ distances.[7-9] Measurements between neighboring carbonyl resonances, which constrain the torsion angle ϕ, may best be performed with a sequence such as DRAWS, which does not depend on CSA and can be applied to degenerate or near degenerate chemical shifts. (RFDR has

also been applied to carbonyl distance measurements, but data interpretation requires knowledge of the CSA parameters, either by assumption or fitting.[51])

All the advantages of the DRAWS sequence can, in principle, be extended to include the inherent advantages of the γ-encoded dipolar lineshape. However, until now, the severe dependence of γ-encoded methods (including HORROR[52] and C7[47]) has precluded their use for accurate distance measurements. With a carefully optimized CMR7 supercycle,[53] the majority of dependence upon chemical shift, CSA, RF inhomogeneity, and phase transient effects can be avoided. This allows internuclear distances to be determined with extremely high precision, because multiple time-domain oscillations may be observed with CMR7, even for relatively weak couplings. In addition, the control of the dipolar Hamiltonian afforded by CMR7 permits the periodic time-reversal of dipolar evolution (as first demonstrated by Levitt and co-workers[54,55] and developed by Costa[33]). For weaker couplings, this permits the relaxation and coupling parameters to be determined with separate experiments, thereby further increasing precision.

In the continuum of homonuclear recoupling sequences, there appears to be a significant tradeoff between the complexity of RF perturbation and the simplicity of data interpretation. On one extreme, R^2 experiments require minimal RF manipulations but depend on several parameters. By use of π pulses, RFDR reduces the dependence on chemical shifts. And windowless mixing sequences such as DRAWS may provide even greater control over the coherent evolution. Here we extend quantitative DQ homonuclear recoupling to the γ-encoded realm.

Background & Theory

The development of C7[47] and its compensated analogs—including POST-C7,[56] CMR7,[53] and SPC-5[57]—has been described in sufficient detail in previous publications to assume the average Hamiltonian result to first order (numbering the order in agreement with perturbation theory) and treat the coherent evolution in the DQ subspace[58,59]:

$$\tilde{H}^{(1)} = \frac{1}{2}\left(\kappa\omega_D^{(-1)} I_+ S_+ + \kappa^* \omega_D^{(1)} I_- S_-\right) = \left|\kappa\omega_D^{(\pm 1)}\right| I_\gamma^{(14)}, \tag{1}$$

where

$$\omega_D^{(\pm 1)} = \frac{b_{IS}}{2\sqrt{2}} \sin(2\beta) e^{\pm i\gamma}, \tag{2}$$

$$b_{IS} = -\frac{\mu_0}{4\pi} \frac{\gamma_j \gamma_k \hbar}{r_{jk}^3}, \tag{3}$$

and

$$I_\gamma^{14} = \cos(\gamma) I_x^{14} + \sin(\gamma) I_y^{14}. \tag{4}$$

The Euler angles β and γ define the transformation from principal axis system of the dipolar interaction to the rotor-fixed frame, according to the convention of Spiess.[10] The absolute value of the scaling factor κ is nominally 0.232 in this case. We assume here that second-order and third-order effects due to chemical shift offset and RF inhomogeneity are removed. However, we will be concerned with the explicit dependence of the scaling factor κ on the RF power level. For CMR7, this is:

$$\kappa = \frac{147s}{8\sqrt{2}\pi\left(196s^2 - 1\right)}\left[7s\left(i + e^{i\pi/14}\right) - \left(e^{i\pi/7} + e^{i3\pi/7}\right)\sin 2\pi s\right], \tag{5}$$

and for POST-C7,

$$\kappa = \frac{147s}{8\sqrt{2}\pi\left(196s^2-1\right)}\left[7s\left(i+e^{i\pi/14}\right)-e^{i\pi/14}\sin\pi s-e^{i\pi/14}\sin 3\pi s\right] \tag{6}$$

Because these functions are even with respect to s (where $s = {\omega_{1,actual}}/{\omega_{1,ideal}}$), phase inversion supercycles do not effect the scaling factor. Close to the nominal RF field, the scaling factor for CMR7 is

$$|\kappa| = 0.232 - 0.24(s-1) \tag{7}$$

and for POST-C7,

$$|\kappa| = 0.232 + 0.24(s-1) \tag{8}$$

SPC-5 exhibits a functional dependence similar to POST-C7 (although the nominal scaling factor $|\kappa| = 0.203$).

Now if we assume the initial density operator of sum polarization,

$$|\rho(0)\rangle = |I_z + S_z\rangle = 2\left|I_z^{14}\right\rangle, \tag{9}$$

coherent evolution proceeds according to

$$|\rho(t)\rangle = 2\left[\cos\left(\omega_D t\right)\left|I_z^{14}\right\rangle + \sin\left(\omega_D t\right)\left|I_{\gamma-\pi/2}^{14}\right\rangle\right], \tag{10}$$

The pulse sequence phase cycling here will be arranged to observe the $\left|I_z^{(14)}\right\rangle$ component only. The normalized signal over the powder average is:

$$\sigma(t) = \frac{\left\langle I_z^{(14)}\middle|\rho(t)\right\rangle}{\left\langle I_z^{(14)}\middle|\rho(0)\right\rangle} = \frac{1}{\pi}\int_0^{\pi}\cos(\omega_D t)d\beta \tag{11}$$

Analysis over the powder average normally proceeds numerically at this point, with Fourier transformation to produce the frequency domain lineshape. However, we note that this lineshape can also be calculated analytically according to the procedure of Haeberlen[60] as:

$$I(\omega)=\begin{cases}\left|\dfrac{\sin\left[\frac{1}{2}\arcsin\frac{\omega}{\omega_D}\right]}{2\omega_D\cos\left[2\arcsin\frac{\omega}{\omega_D}\right]}\right|+\left|\dfrac{\sin\left[\frac{\pi}{2}-\frac{1}{2}\arcsin\frac{\omega}{\omega_D}\right]}{2\omega_D\cos\left[2\left(\frac{\pi}{2}-\arcsin\frac{\omega}{\omega_D}\right)\right]}\right| & |\omega|<\omega_D \\ 0 & |\omega|>\omega_D\end{cases} \tag{12}$$

This result is valid only for the ideal case, with no relaxation. Including relaxation in the dynamics requires further analysis of the time-domain evolution, according to the Liouvillian,

$$\frac{d}{dt}\left|\rho(t)\right\rangle = L(t)\left|\rho(t)\right\rangle = \begin{pmatrix}-\Gamma_1 & -\omega_D \\ \omega_D & -\Gamma_2\end{pmatrix}. \tag{13}$$

This equation can be solved analytically,[61] and the observable described by

$$S(t)=\frac{1}{2\omega'}\left[\left(\Gamma_\Delta+\omega'\right)e^{-\frac{t}{2}(\Gamma_\Sigma+\omega')}-\left(\Gamma_\Delta-\omega'\right)e^{-\frac{t}{2}(\Gamma_\Sigma-\omega')}\right], \tag{14}$$

where $\Gamma_\Sigma=\Gamma_1+\Gamma_2$, $\Gamma_\Delta=\Gamma_1-\Gamma_2$, and $\omega'=\sqrt{\Gamma_\Delta-4\omega_D^2}$. When the relaxation rates of both coherences ($\left|I_z^{14}\right\rangle$ and $\left|I_{Y-\pi/2}^{14}\right\rangle$) are equal, Eq. 14 reduces to

$$S(t)=e^{-\Gamma_1 t}\cos\omega_D t. \tag{15}$$

Experimental

The pulse sequence of Figure 7-1 was implemented at 198.3 MHz ^{1}H frequency, with a custom-designed spectrometer (D. Ruben) and triple resonance transmission line probe. This probe was designed specifically for purposes of applying high power ^{1}H pulses in conjunction with long ^{13}C mixing. Equipped with a 5 mm spinner module (Chemagnetics), it permits the application >250 kHz ^{1}H decoupling fields and >50 kHz ^{13}C mixing for periods of 30-50 ms. Several aspects of this probe design were optimized for long-pulse, high power performance on ^{13}C. The tuning and matching circuits on each channel are at low voltages, outside the magnet. This permits large, high power capacitors (ITT-Jennings vacuum dielectric) to be used for the ^{13}C tuning. Polyflon capacitors are used for matching on the ^{13}C channel, and tuning and matching on ^{1}H. Purge gas was applied to the tuning box to maintain constant temperature.

Despite these efforts, with the coil volume, RF power, and mixing times used here, some heating is inevitable, and the following additional experimental measures were followed to minimize perturbations at long mixing times. Clearly short-time behavior would not greatly be effected by these issues. First, the pulse sequence was implemented with constant duty cycle; i.e., as the mixing time was incremented, the pulses following acquisition were decremented. The power levels on both the ^{1}H and ^{13}C pulses are equivalent to those used during the mixing period. Second, the probe was tuned in the steady state with pulsing on both ^{1}H and ^{13}C, and all experiments were initiated after a period of at least 5-10 minutes of RF pulsing to ensure return to this steady state. Third, the ^{13}C channel of the probe was capacitively overcoupled,[62] both to reduce the effect of phase transients and to minimize the difference in transmission coefficient upon slight change in fixed capacitance within the circuit. Finally, nutation experiments with both the ^{13}C storage and read-out pulses were compared to ensure that the effective nutation frequency did not change during the mixing period; to perform this test, a sufficiently strong echo signal must be acquired after 30-50 ms mixing. This can be achieved by periodically altering the phase of the DQ Hamiltonian. In 10% [^{15}N,2-^{13}C]-Gly, approximately 50% of the

signal can be recovered after 40 ms, with signal loss dominated by transient errors on the ^{13}C channel (independent of decoupling level, assuming greater than 150 kHz). Typical results indicated a shift in effective ^{13}C field of ~0.5 to 1.0%. By tuning the probe so that heating effects cause a passage *through* tuned resonance, rather than a one-way deviation *from* resonance, the perturbation can be reduced by another 50%, so that effective field on ^{13}C always remains within 0.5% of the nominal value. The mixing period consists of the CMR7 supercycle, as described in detail in Ref. [53].

Data fitting was performed by grid searches of the Γ_1, Γ_2, and ω_D parameter space of Eq. 14, with integration over the Euler angle β. For each simulated curve, two amplitude correction factors were included. The first factor is an overall y-axis scaling of the fitted data, to account for the uncertainty in the first experimental data point; this is restricted to fall within experimental error of unity. The second factor is a correction for natural abundance background, henceforth referred to as NAC ("natural abundance correction"). NAC describes the additional signal, due to molecules that are singly labeled, either due to imperfect isotopic enrichment of the labeled material or the natural abundance background. The signal from the doubly-labeled material is

$$s_1 = d\,l^2, \tag{16}$$

where d is the nominal dilution (mole percentage of labeled material), and l the likelihood of each site being labeled (usually specified by the manufacturer as 0.98-0.99). The signal from enriched material that has only one of the two sites labeled is

$$s_2 = d\,l(1-l), \tag{17}$$

and the signal arising from the natural abundance material is

$$s_3 = p(1-d), \tag{18}$$

where p is the percentage of spin-active nuclei at natural abundance (i.e., 0.011 for ^{13}C). Therefore, to account for isolated spins, the NAC factor must be $\frac{s_2 + s_3}{s_1}$. For example, with 10% ^{13}C dilute samples at 99% nominal enrichment, NAC is 0.111. The signal contribution from isolated spins is assumed to decay at the rate Γ_1. Notice this ignores intermolecular couplings, an approximation which is increasingly poor as the (labeled) spin pair couplings decrease to the limit of the separation between natural abundance spin pairs.

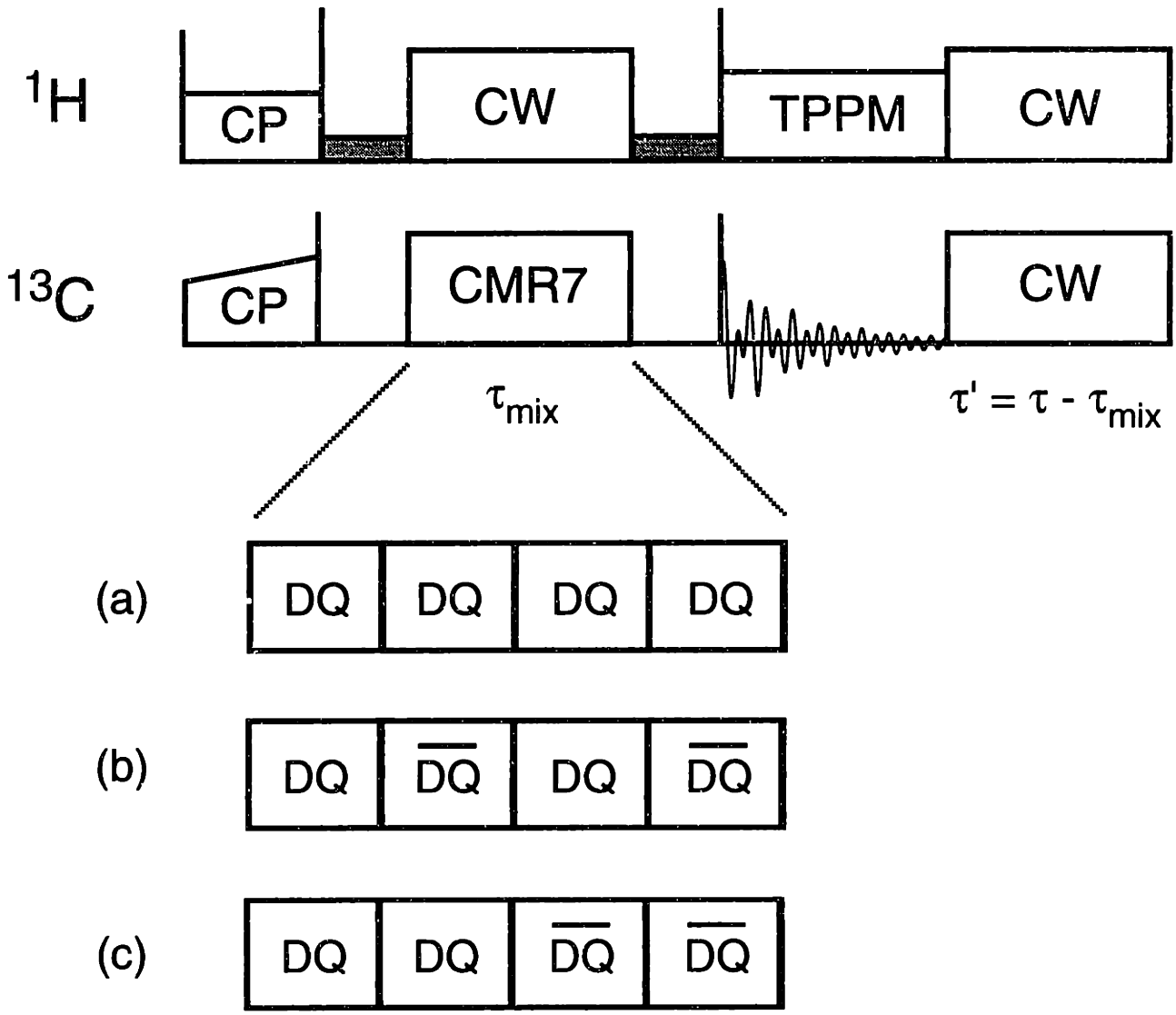

Figure 7-1. CMR7 Pulse Sequence for Homonuclear Dipolar Dephasing.

The general pulse sequence consists of cross polarization, followed by storage of the ^{13}C sum polarization for CMR7 mixing. A rotor period of low power ^{1}H decoupling is inserted before and after the CMR7 periods to dephase residual transverse magnetization. Decoupling power is raised to ~175 kHz during the ^{13}C $\pi/2$ pulses. Standard phase cycling for longitudinal mixing is used: ϕ_1 = 13, ϕ_2 = 2, ϕ_3 = 11223344, $\phi_{receiver}$ = 13243142, where 1=X, 2=Y, 3=-X, 4=-Y. The period τ' is varied in order to maintain a constant RF duty cycle and avoiding probe detuning as the mixing time (τ_{mix}) is incremented. The phase of DQ dipolar Hamiltonian may be periodically inverted by $\pi/2$ phase shifts of the RF phase; (a) the standard mixing sequence, (b) rapid dipolar echoes, (c) longer timescale dipolar echoes. The $\pi/2$ phase shifts are added to the phases of the CMR7 supercycle. [53] Further details are provided in the text.

Results and Discussion

Strong Coupling: Ammonium Hydrogen Oxalate

Figure 7-2 shows the experimental DQ dephasing in ammonium 1,2-^{13}C hydrogen oxalate hemihydrate (9.5% dilute in natural abundance material). The data were fit with the analytical model described above. Assuming $\Gamma_1 \leq \Gamma_2$, the best fit was found with $44s^{-1}$. The monoexponential relaxation indicates that both longitudinal and transverse (DQ) coherences relax at the same rate, resulting from ideal decoupling limit (175 kHz CW in this case). Similar relaxation behavior has been observed in other dicarboxylate salts we have studied (e.g., malonate and succinate), in agreement with Drobny and co-workers, who have fit DRAWS dephasing curves in the corresponding dicarboxylic acids with high precision using monoexponential decay models. We note here that the empirically determined NAC is 0.132, in good agreement with the theoretical value (0.117) assuming 99% enrichment of the labeled material.

The coupling extracted from the experimental fit is 451.2 Hz. Assuming the theoretical scaling factor, this corresponds to a 1.944 kHz coupling, or 1.575 Å ^{13}C-^{13}C distance. The C-C distance measured by x-ray crystallography is 1.549 Å.[63] The longer effective bond length in the NMR result may be due to vibrational averaging effects,[64] or the RF-dependence of the dipolar scaling factor. Here the RF fields we set according to the measured ^{13}C π pulse lengths; we did not conduct a careful study of the scaling factor as a function of RF field. Therefore the absolute value of the coupling may have a small systematic error (~±2-3%), either due to differences between the effective field during CMR7 and the measured π pulse, or the fact that the single coupling simulation fits the weighted average of the scaled couplings. Because of RF inhomogeneity over the sample volume (approximately ±3-4% at half-height, with a pronounced asymmetry giving rise to larger amplitude at the low field edge, common to most solenoid coil geometries) will cause a distribution of scaling factors, the depth of the oscillation may not be

precisely described by the single coupling model. This effect is evident in the first several oscillations, where the amplitude of the simulated curve exceeds the experimental curve. Greater precision in the fitting procedure may be derived by explicitly accounting for the distribution of scaling factors. However, even if we assume a relatively large systematic error of ±3% due to the uncertainties in field distribution, the error in the distance is ±0.015 Å; that is, the NMR determined distance is at least 0.5% greater than the *X*-ray determined distance, and perhaps as much as 3%.

The remaining systematic errors in the residuals are: (1) two slight deviations from steady state at the 32nd and 64th experimental data points (~9 and 18 ms), due to brief interruptions of the data acquisition prior to the these points; and (2) disagreement at long time, possibly due to intermolecular couplings. Clearly for the strong couplings these considerations are of minimal importance, and the systematic errors from RF field misset and distribution far exceed the random error derived from the assumption of the analytical model and/or other contributions. More careful calibration of RF fields, measurement of dephasing curves at several field strengths, and/or work with a restricted volume sample would help to resolve this issue.

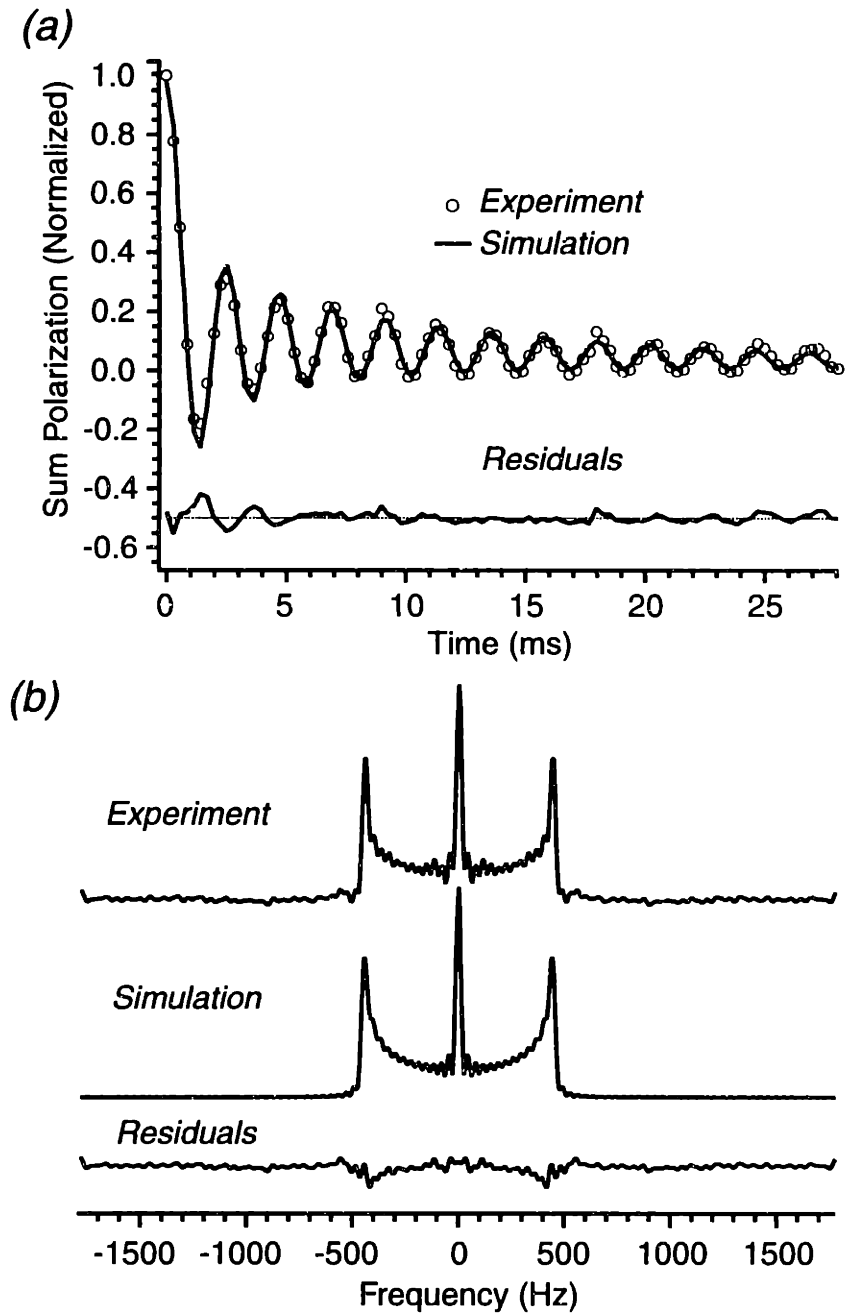

Figure 7-2. Experimental CMR7 Dipolar Dephasing and Lineshape in Ammonium Hydrogen 1,2-^{13}C-Oxalate Hemihydrate.

Sum polarization dephasing with CMR7 mixing is demonstrated in the strong coupling case. (a) Time domain dephasing data. Experimental data points (101 total) were acquired at 280.56 μs intervals (4 τ_r at 7.129 kHz MAS rate), with 50 kHz ^{13}C RF field, 175 kHz CW ^{1}H decoupling. (b) Frequency domain plot of same data, using real FT with 512 points. Fitting parameters were 451.2 Hz scaled dipolar coupling, 0.132 natural abundance correction factor, 44 s^{-1} relaxation rate (equal on all coherences).

Dipolar Echoes with CMR7

The use of echoes to differentiate inhomogeneous from homogeneous signal decay has a rich history in NMR.[65] Recent applications have attempted to address the issues of multi-body reversibility in strongly coupled ^{1}H networks[66] and the spin-space relaxation anisotropy in homonuclear spin pairs.[33,54,55] Here we are concerned with the latter type of experiment. Our approach is conceptually based on that of Levitt and co-workers,[54,55] and Costa,[33] who have demonstrated control of ZQ and/or DQ dipolar evolution by inserting periods of chemical shift interruption in R^2 experiments. In the CMR7 experiment, rather than inserting periods of chemical shift evolution, the sign of the dipolar evolution is reversed simply by shifting the RF phase by $\pi/2$. This permits essentially complete control over the dipolar evolution, and the timescale of phase shifts can be altered to vary the amount of DQ coherence created before time-reversal. Likewise, non-orthogonal phase shifts can be used to create composite dipolar rotations, as demonstrated by Costa and co-workers in the R^2 case.[33]

A straightforward example (ammonium hydrogen oxalate) is shown in Figure 7-3. As with the dephasing data, the fitted rates Γ_1 and Γ_2 are equal. (Fits are not shown here.) This is evident in the fact that all echoes (markers in the figure) are quite similar in amplitude, independent of the timescale of dipolar phase reversal. This is a special case. Normally, as in the examples in following sections, the relaxation rate Γ_2 will be significantly greater than Γ_1, due to the fact that ^{1}H couplings have greater influence on the DQ state. Therefore greater signal decay will occur as the timescale of refocusing is increased.

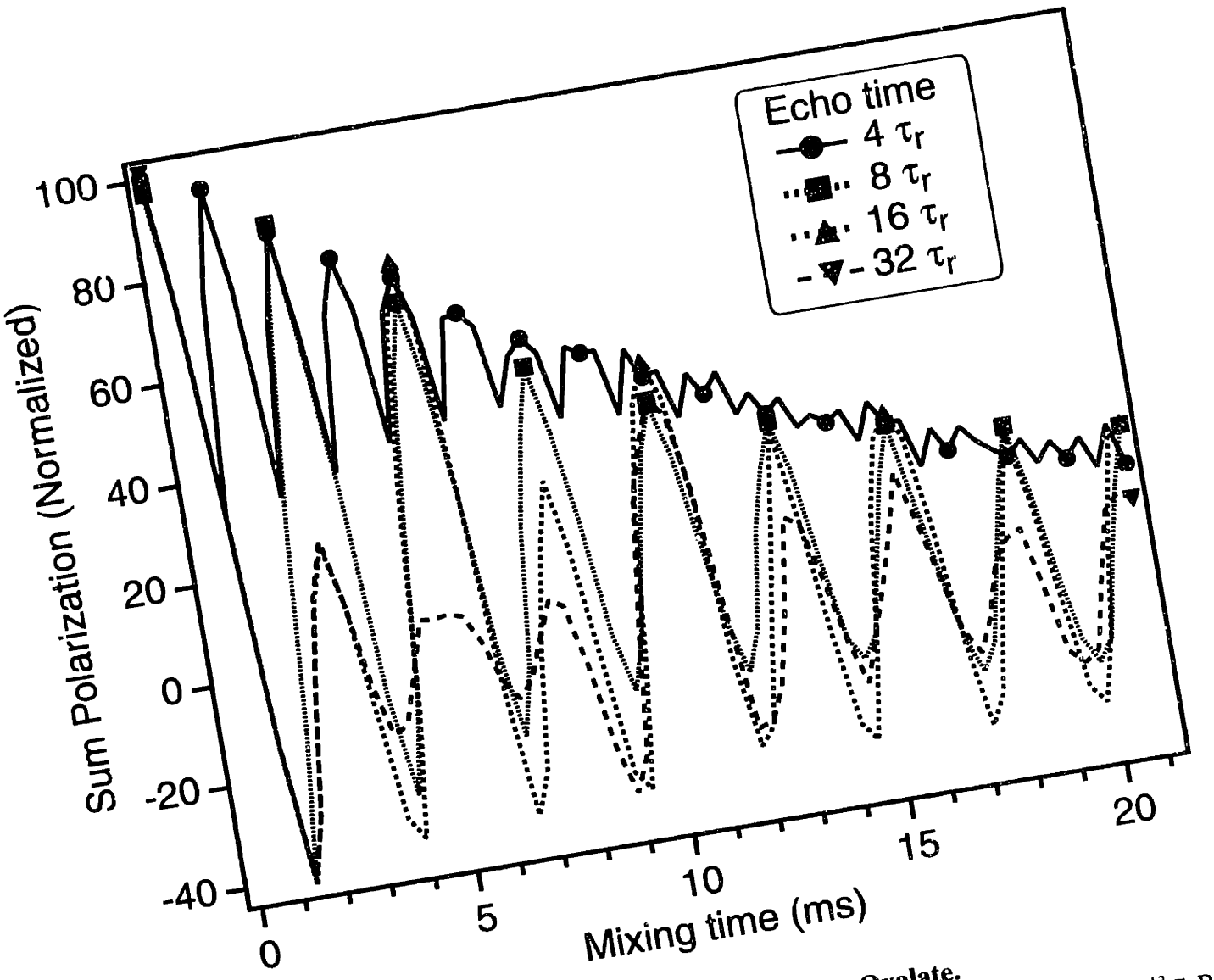

Figure 7-3. CMR7 Dipolar Echoes in Ammonium Hydrogen Oxalate.

The phase of the DQ dipolar Hamiltonian is periodically inverted by shifting the ^{13}C RF phase by $\pi/2$. Local maxima (peak of each echo) are marked with circles, squares and triangles as indicated.

A few observations deserve mention here. First, the DQ "filtration" experiment is simply the admixture of the sum polarization decay curve with the "long-time" limit dipolar echo, where the time-reversal period is always half the total mixing time. Second, the $\pi/2$ phase shift is *added to* the CMR7 supercycle phase shifts. Therefore a potential limitation of these sequences is that the supercycle compensation is compromised by destructive interference with the time-reversal phase shifts. We find that the relaxation rates determined in the echo sequences therefore depend

more strongly of RF errors than the relaxation rates extracted directly from the dipolar dephasing data. In all cases, the decay is more rapid in the echo sequences (once the correction is made for the expected relative decay, based on the average Liouvillian model). Although in a limited number of examples independent optimization of the CMR7 supercycle for each type of time-reversal experiment yielded improved agreement between the rates extracted from time-reversal and dephasing experiments, this approach is time-consuming and inelegant, and the results will depend upon chemical shift offset, CSA, propagation of rotation error, etc. In addition, the multiple echo behavior may depend upon weak couplings to the natural abundance background; the contribution to dephasing due to these numerous, weak couplings can be described with a second moment expansion over the populations,[36] but this evolution is not reversible. Because both the RF error and multi-body effects would lead to an overestimate of the relaxation, for non-trivial cases, we use the echo decay rates as an upper bound on the relaxation parameters.

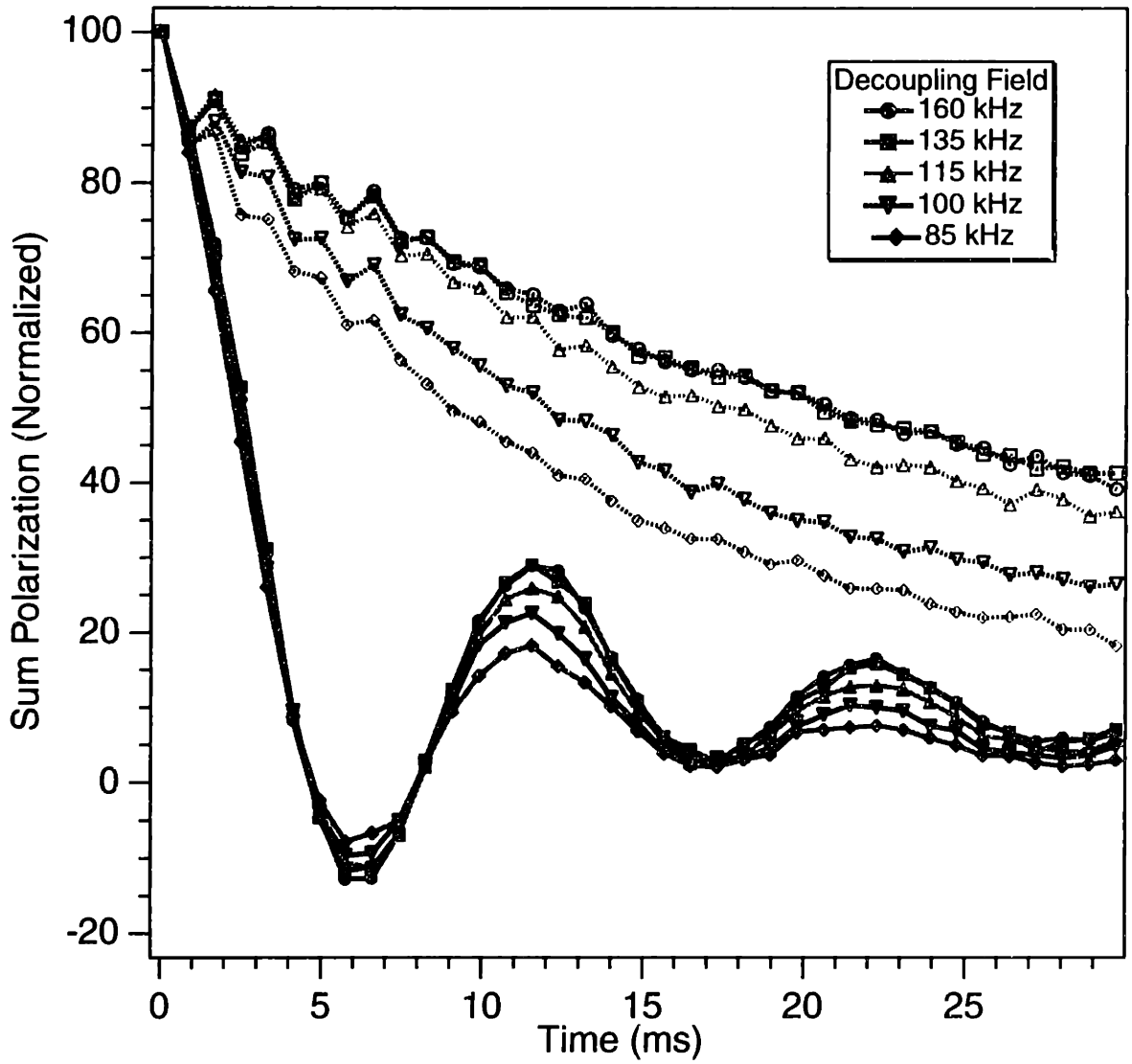

Figure 7-4. CMR7 Dephasing in 1,3-^{13}C,^{15}N-Alanine as a Function of ^{1}H Decoupling Field. The CMR7 dephasing ("S") curves are the solid lines with filled markers; the reference curves (most rapid echo refocusing, "S_0") are the dotted lines with open markers. In this case, each CMR7 cycle (4 rotor periods) was followed with 1 rotor period of free evolution. MAS rate is 5.1 kHz and nominal ^{13}C RF field 35.7 kHz.

Differential Relaxation

In order to explore the relaxation dynamics in greater detail, a complete CMR7 study was performed with 1,3-^{13}C,^{15}N-alanine (10% dilution) as a function of ^{1}H decoupling field. A subset of the data is shown in Figure 7-4. In this case, multiple time-domain oscillations are observed, and fits of the coupling are therefore trivial, but the quality of fit bears some elaboration. As the decoupling field is decreased, damping of the time domain oscillations is immediately evident, although the best fit frequency is not significantly perturbed (1 Hz deviation over the entire range of decoupling fields). The best fit parameters for simulations of the data are presented in Table 7-1. Here we have assumed $2\Gamma_1 \leq \Gamma_2 \leq 3\Gamma_1$.

Table 7-1. 1,3-^{13}C,^{15}N-Alanine CMR7 Fits as Function of ^{1}H Decoupling Level.

Decoupling Field (kHz)	Scaled Dipolar Coupling (Hz)	Γ_1 (s^{-1})	Γ_2 (s^{-1})	NAC[a]	RMSD
160	119.5	30	90	0.185	0.0101
135	119.5	35	90	0.205	0.0107
115	119.5	40	110	0.185	0.0077
100	120.5	55	135	0.170	0.0073
85	120.5	65	180	0.145	0.0091

[a]Natural abundance correction; a signal monoexponential with decay rate Γ_1 and intensity NAC is added to the simulated dephasing curve to account for signal arising from isolated spins.

Relaxation more than doubles over the range of decoupling fields studied here, but the precision with which the coupling can be fit is not significantly impaired by the more rapid relaxation, assuming the differential relaxation model is employed. Fits assuming monoexponential decay give qualitatively similar results, but with significantly greater RMSD

deviation, poorer fits of the long-time behavior well, and unphysically large NAC factors. With the ~120 Hz scaled couplings observed here, these effects are not limiting; for weaker couplings the disagreement between single and differential relaxation rate models will be increasingly important.

Table 7-2. 1,3-^{13}C,^{15}N-Alanine CMR7 Fits Assuming Single Exponential Decay.

Decoupling Field (kHz)	Scaled Dipolar Coupling (Hz)	$\Gamma_1 = \Gamma_2$ (s^{-1})	NAC[a]	RMSD
160	118.0	40	0.275	0.0185
135	118.5	40	0.275	0.0172
115	118.0	50	0.280	0.0146
100	119.5	60	0.270	0.0129
85	119.5	80	0.280	0.0146

Precision of the grid search is ±0.5 Hz in the coupling, ±5 s^{-1} in the relaxation rate.

The exact dipolar scaling in this series of experiments shows a significant systematic error (120 Hz / 0.232 = 517 Hz, corresponding to a 2.45 Å distance, substantially shorter than the value of 2.514 Å determined neutron diffraction[67]). This resulted from the empirical optimization of ^{13}C RF field to maximize the depth of the first sum polarization oscillation at a fixed mixing time (e.g., 32 rotor periods of CMR7 mixing). This procedure is inappropriate, because it yields a scaling factor that is matched to the arbitrary choice of fixed mixing time. (At the time these experiments were performed, the strong dependence of the dipolar scaling factor on RF field was not fully appreciated.) Despite this relatively large misset, the quality of the data and agreement with simulation (an example in shown in Figure 7-5) are excellent, providing further evidence that the CMR7 supercycle compensates extremely well for deviations from ideal RF power. This study merits presentation because of what it reveals about the relaxation dynamics. With an effective relaxation model in place, the variability in the scaling factor can be addressed more carefully in the following section.

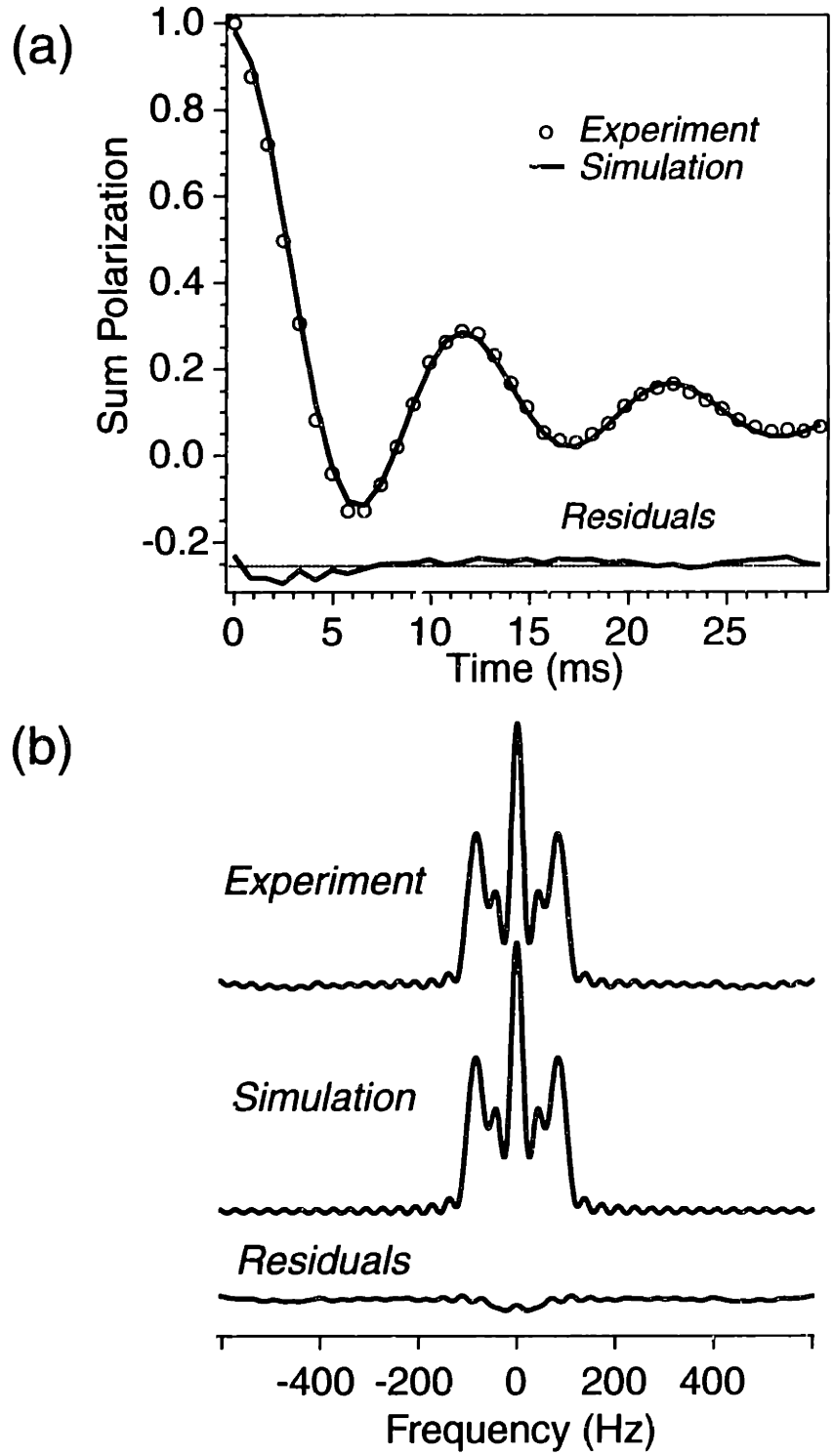

Figure 7-5. CMR7 Dephasing (Experimental Data with Simulation) in 1,3-^{13}C,^{15}N-Ala. Data from the 160 kHz ^{1}H decoupling condition of Figure 7-4 are compared with the best fit simulation, according to the parameters in Table 7-1.

Compensation for Variable Dipolar Scaling with POST-CMR7

For scaled couplings greater than ~100 Hz, the largest source of experimental error in these experiments arises from the variable dipolar scaling. The exact dependence of dipolar scaling on the RF field (from Eqs. 5 and 6) is shown in Figure 7-6. It is clear that CMR7 and POST-C7 have equal but opposite dependencies on RF field, in the regime close to the nominal value (s = 1). This can be understood by considering that CMR7 elements (C and C') are equivalent to C7 and a π-pulse permutation thereof; permutation of a π pulse does not change the sign of DQ spin terms. In contrast, POST-C7 is a $\pi/2$-permuted version of C7; $\pi/2$ permutation inverts the DQ error term. Therefore, a linear combination of CMR7 and POST-C7 would be expected to remove the dependence on RF field. Experimentally, this can be achieved by interleaving the mixing periods of CMR7 and POST-C7, using a minimal cycle of each (in this case, 4 rotor periods).

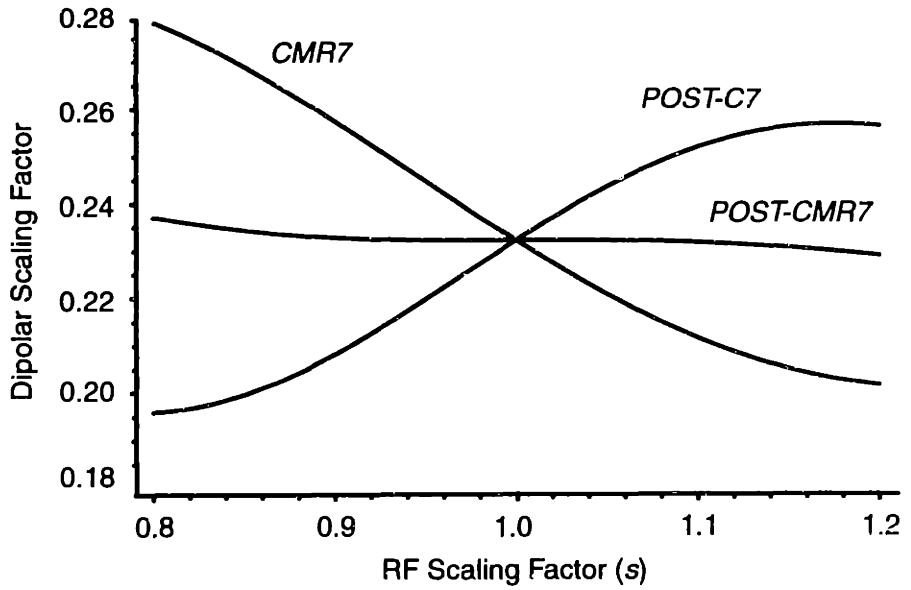

Figure 7-6. Theoretical Dependence of Dipolar Scaling Factors on RF Field.

The experimental data shown in Figure 7-7 illustrates the sensitivity of the scaling factor to RF field strength. For CMR7, the first minimum in the curve shifts with RF field (resulting in the aforementioned behavior with respect to empirical optimization of the field), and the long-time behavior indicates further separation of the curves based on RF misset. Nevertheless, the absolute depth of the curves is not dramatically altered (though larger amplitude oscillations are observed at lower RF field, because the spread of couplings over the inhomogeneous sampling volume is reduced, due to the pedestal in the scaling factor v. RF profile at approx. $s = 0.8$.) In contrast, the POST-C7 data exhibits a strong dependence, in terms of oscillation depth and overall goodness of fit with the theoretical π We attribute this to the strong dependence of POST-C7 on finite risetime effects at th , in particular symmetric phase transients. Although the probe was overcoupled for these experiments (thereby minimizing the *magnitude* of transient effects), no empirical optimization of probe tuning was performed specifically for the POST-C7 experiment (although supercycling of the POST-C7 sequence was optimized, according to MLEV procedures).[68] Changing the RF field amplitude by another ±4% resulted in qualitatively similar curves for CMR7 (with the now obvious shift in effective coupling constant), but under these conditions POST-C7 did not provide useful dephasing data. The linear combination of CMR7 and POST-C7, here dubbed POST-CMR7, as expected has compensation properties that are roughly the average of its parent sequences. The long-time behavior is sub-par, in comparison to CMR7, but the effect of compensating for the RF misset is apparent in the first oscillation (in particular, the maximum at ~10 ms, which is essentially identical for all three curves).

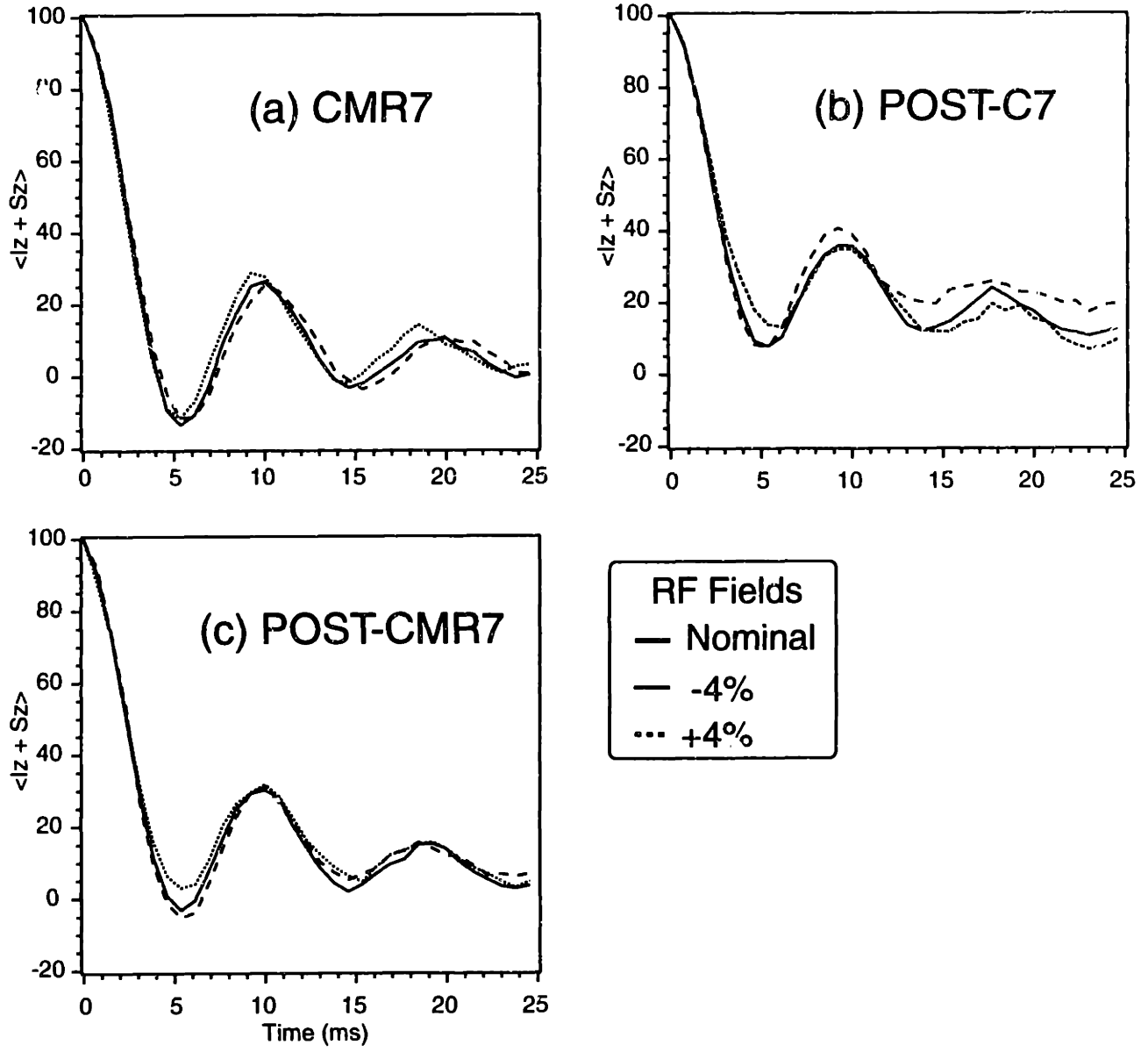

Figure 7-7. CMR7, POST-C7, and POST-CMR7 Data for 1,3-^{13}C,^{15}N-Alanine

Beyond this qualitative assessment, we have performed fits of all the dephasing data in Figure 7-7 (and additional dephasing curves not shown at intermediate power levels). The results are presented in Table 7-3. The quality of fits for POST-C7 are clearly poorer, requiring extremely high NAC values to account for the portions of the sample volume where the RF is outside of the range of POST-C7 compensation. In addition, the relaxation rates for the POST-C7 fits are a very strong function of the ^{13}C RF field, whereas with CMR7 these values are

essentially constant. In order to assess the errors in coupling in the context of a multi-parameter model, Monte Carlo error estimation was performed according to established methods.[69,70] The results of this fitting procedure are shown in Figure 7-8 (with the y-axis corrected by the theoretical scaling factor). The downward slope of the CMR7 data is in excellent agreement with theory, and the upward trend in the POST-C7 data also follows the theory, though with greater scatter. The POST-CMR7 result is an essentially constant coupling, with average value of 470 Hz. This corresponds to a 2.53 Å ^{13}C-^{13}C distance, slightly longer than the neutron diffraction value of 2.514 Å.

Table 7-3. CMR7, POST-C7, and POST-CMR7 Simulation Results.

(a) CMR7

^{13}C Field (kHz)	Scaled Dipolar Coupling (Hz)	Γ_1 (s^{-1})	Γ_2 (s^{-1})	NAC	RMSD
33.6	111.5	45	90	0.205	0.0122
34.4	110.0	45	90	0.190	0.0151
35.2	107.5	45	90	0.170	0.0159
35.8	105.0	45	90	0.180	0.0140
36.6	103.0	50	100	0.180	0.0134

(b) POST-C7

^{13}C Field (kHz)	Scaled Dipolar Coupling (Hz)	Γ_1 (s^{-1})	Γ_2 (s^{-1})	NAC	RMSD
33.6	110.0	55	110	0.660	0.0124
34.4	114.0	40	80	0.580	0.0101
35.2	113.5	40	80	0.530	0.0048
35.8	112.0	35	100	0.370	0.0066
36.6	117.0	25	75	0.510	0.0168

(c) POST-CMR7

^{13}C Field (kHz)	Scaled Dipolar Coupling (Hz)	Γ_1 (s^{-1})	Γ_2 (s^{-1})	NAC	RMSD
33.6	109.5	50	100	0.410	0.0122
34.4	110.0	50	100	0.360	0.0116
35.2	109.0	50	100	0.320	0.0135
35.8	108.0	50	100	0.250	0.0102
36.6	109.5	40	95	0.280	0.0075

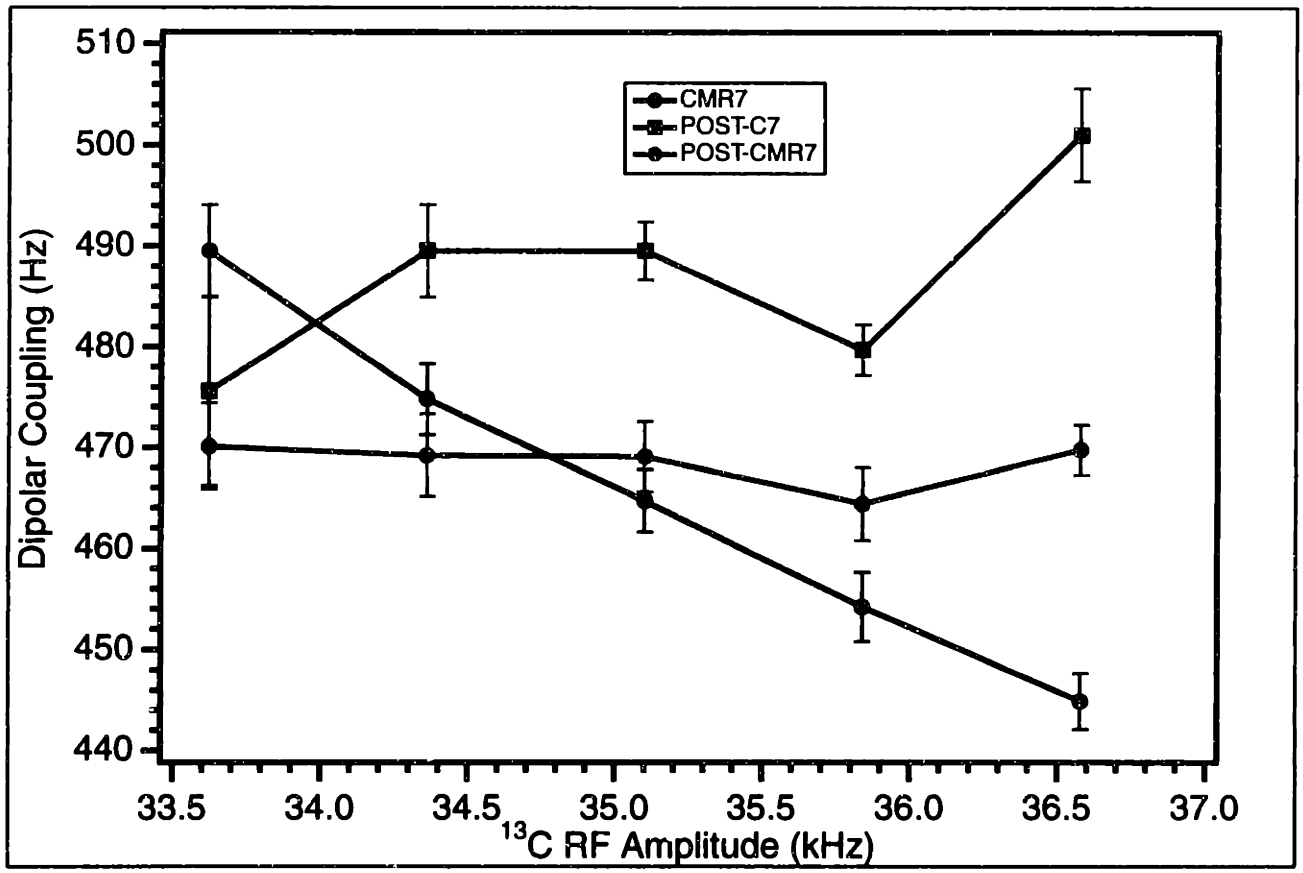

Figure 7-8. Plot of Fitted Couplings as Function of RF Field

Although the POST-CMR7 experiment worked in this instance, the data fitting procedures and the appearance of the POST-C7 curves are inelegant, and the effort required for empirical experimental optimization of the sequence was substantial. The RF rotation errors associated with the POST element may restrict its use for longer mixing times, which are required for the measurement of weaker couplings. Nevertheless, the demonstration of the dipolar scaling effect compensation highlights the importance of RF field calibration in the precise measurement of couplings. Similar effects are inherent to all windowless mixing sequences, such as DRAWS and MELODRAMA, and awareness of these effects is important, especially for extremely high precision work. Development of a sequence with higher order compensation without rotation error dependence may be the best long-term solution. For the time being, we use the CMR7 sequence for the measurement of weak couplings, and carefully calibrate the RF field level in

subsequent experiments. Because the scaling error is linear in the *coupling* (not the distance), this systematic error is less of a concern for long distance measurements (i.e., >4 Å ^{13}C-^{13}C).

Measurement of Weak Dipolar Couplings

Measurement of weaker dipolar couplings (b_{IS} <100 Hz) with high precision can be achieved by using longer mixing times, in order to observe an oscillation in the CMR7 dephasing trajectory. Even when the scaled coupling is comparable to the relaxation rates, a prominent time-domain oscillation is observed due to the γ-encoded lineshape. For example, in Figure 7-9, data for glycyl glycine hydrochloride (GlyGly) is shown. Despite the 3% dilution in natural abundance material, an oscillation below zero is observed, and recovery of the curve to >10% of the initial intensity. We expect to observe a slightly dipolar coupling than in the neutron structure (80 Hz, from the [1-^{13}C]-[4-^{13}C] distance of 4.56 Å),[71] due to intermolecular coupling effects. In slightly more concentrated samples, Bennett *et al.*[36] and Costa *et al.*[34] observed effective couplings of 95 Hz. (Bennett and co-workers corrected for intermolecular couplings by a second-moment analysis, resulting in an effective coupling of 85 Hz.) However, CMR7 recouples all spin pairs, regardless of chemical shift difference, whereas the RFDR and R^2T experiments primarily recouple the C'-C^α pairs. The near degenerate C'-C' and C^α-C^α shift pairs experience essentially little dephasing under RFDR and R^2T, but are recoupled by CMR7 with scaling equal to the C'-C^α pairs. This results in approximately a threefold increase in the intermolecular effect at the same dilution, and accounts for the slightly larger effective coupling of 108 Hz observed with CMR7.

Future work will include a more thorough comparison of the quality of fit using short and long mixing time data, and a direct comparison of γ-encoded and γ-dependent methods in the weak coupling limit.

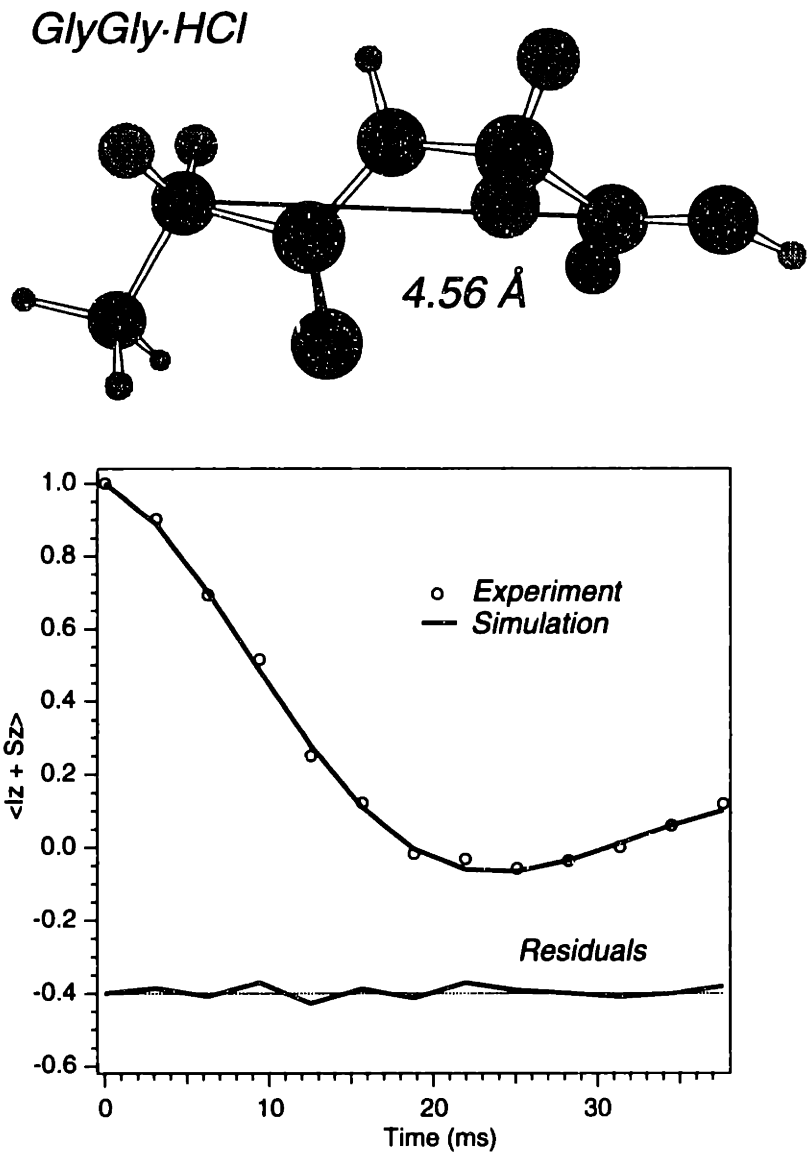

Figure 7-9. Glycyl Glycine Hydrochloride Structure and CMR7 Dephasing Data

Best fit parameters are a scaled coupling of 25 Hz. Relaxation rates are $\Gamma_1 = 20\ s^{-1}$, $\Gamma_2 = 50\ s^{-1}$. The reference curve (S_0) fits an average relaxation rate of 24 s^{-1}. The scaled coupling corresponds to $b_{IS} = 108$ Hz.

Heterogeneous Systems

In order to test the ability of CMR7 to measure multiple couplings at degenerate chemical shifts, a heterogeneous dicarboxylate sample was prepared. [1,4-^{13}C]Succinic acid was diluted (4.5%) in natural abundance material, and dissolved in aqueous ammonium hydroxide (one molar equivalent of NH_4OH). However, over the course of several weeks, as the solution slowly evaporated, it is likely that NH_3 gas was lost, and therefore a mixture of succinic acid (SA), [72] ammonium hydrogen succinate (AHS),[73,74] and diammonium succinate (DAS)[75] was expected. The CMR7 dephasing curves were acquired, and each resolved peak in the spectrum fit to two couplings, as shown in Figure 7-10. The fits assume identical relaxation and NAC parameters, but fit the ratio of peak amplitudes and two independent couplings. All three peaks in the frequency domain show pronounced weak couplings, which a single coupling model does not reproduce; these features would be obscured by the zero-frequency component in γ-dependent dipolar lineshapes with the same couplings and relaxation rates. However, the γ-encoded lineshape permits both the intensities and couplings to be fit with high precision. The couplings correspond to crystal structure values, with a few percent difference in scaling factor.

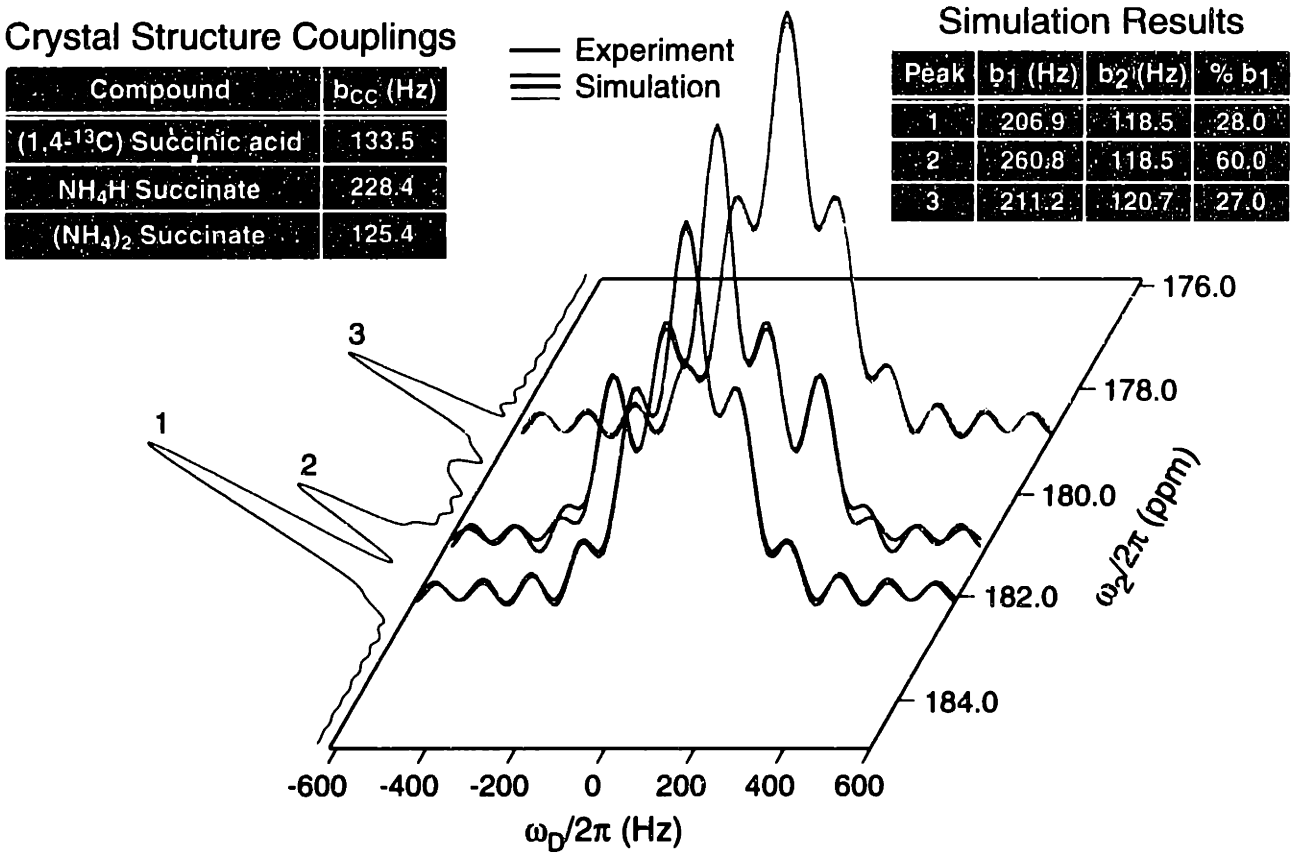

Figure 7-10. CMR7 in Heterogeneous [1,4-^{13}C]Succinate Sample.

Determination of ^{13}C-^{13}C distances in a heterogeneous system likely containing different crystal forms of succinic acid species (the sample was prepared by evaporating an aqueous solution having 1:1 ammonia/succinic acid mole ratio). Dipolar dephasing curves for each resonance were simulated using two dipole couplings.

Conclusions

We have measured several internuclear ^{13}C-^{13}C distances, ranging from 1.5 to 4.6 Å, using the CMR7 homonuclear DQ mixing sequence. Precision of the fits to a differential relaxation model is excellent, due to the γ-encoded dipolar lineshape and the effective long-time behavior under the CMR7 supercycle. The random errors in the measurements correspond to uncertainty in the distances of <0.05 Å, although some systematic errors must be considered for proper interpretation of the dephasing trajectories. The dominant systematic errors are due to intermolecular couplings and the RF-dependence of the CMR7 scaling factor. The former effect is well known from previous studies, and the latter can be accounted for by calibration of RF power levels and/or measurements of known couplings.

Studies here have been performed at low frequency (200 MHz ^{1}H) with high decoupling fields (>150 kHz) in most cases. However, in at least one instance, the reduction of ^{1}H decoupling to ~85 kHz does not substantially compromise the quality of fit, assuming the differential relaxation model is used. In addition, we have recently extended CMR7 studies to 360 MHz ^{1}H frequency, and although the relaxation rates increase, the quality of data is sufficient to fit couplings on the order of 100 Hz with random error of <5 Hz. In most experiments here, we have used ^{13}C fields of 35 kHz; at this power level at 200 MHz ^{1}H frequency, the effects of chemical shifts are quite small. Likewise, at 360 MHz with ~40-50 kHz fields, chemical shift effects are small compared to insufficient decoupling (using ~125 kHz ^{1}H decoupling). The primary shortcoming of the technique at this point is the requirement for high ^{1}H decoupling fields, although the high precision and accuracy of the method may motivate the use of smaller coils to achieve RF fields appropriate for such experiments at higher frequencies.

The focus of this Chapter has been the measurement of couplings between spin pairs. However, another application of the quantitative description of CMR7 dipolar evolution is the accurate description of dipolar evolution in spin clusters. Because the CMR7 effective Hamiltonian does not depend on chemical shift offset or RF inhomogeneity (other than the exact

scaling factor), clusters of spins can be simulated with high confidence using the AHT model.[33,57] If necessary, numerical Liouvillian models for spin clusters can be implemented as well. Specifically, many torsion angle techniques rely upon a dipolar Hamiltonian to create DQ coherence and/or transfer polarization between spins, in order to measure effects that depend upon the relative orientation of dipole vectors on the two spins. Analysis of the total effective Hamiltonian for the spin cluster is necessary in order to model the dynamics properly. Generally some form of the polarization transfer model is assumed; for spin diffusion or chemical shift-dependent recoupling sequences (e.g., RFDR), such models may be problematic. However, the high quality of CMR7 (and for short mixing times, POST-C7 and SPC-5) dephasing trajectories provides assurance that the multi-spin simulated powder average is a faithful representation of the crystallites represented in separated local field trajectories. This issue was explored in greater detail in Chapter 6.

Acknowledgments

These studies were performed in collaboration with Mary E. Hatcher, Leonard J. Mueller, Morten Hohwy, and Christopher P. Jaroniec.

References

(1) Griffin, R. G. "Dipolar recoupling in MAS spectra of biological solids," *Nat. Struct. Biol.* **1998**, *5*, 508-512.

(2) Mueller, L. J.; Rienstra, C. M.; Griffin, R. G.; Ash, E L.; Bachovchin, W. W. "High precision NH bond distance measurements in a serine protease active site by solid-state NMR," *Science* **1999**, submitted.

(3) McDermott, A. E.; Creuzet, F.; Griffin, R. G.; Zawakzke, L. E.; Ye, Q. Z.; Walsh, C. T. "Rotational resonance determination of the structure of an enzyme-inhibitor complex: phosphorylation of an (amino alkyl) phosphonate inhibitor of D-alanyl-D-alanine ligase by ATP," *Biochem.* **1990**, *29*, 5767.

(4) Creuzet, F.; McDermott, A. E.; Gebhard, R.; van der Hoef, K.; Spijker-Assink, M. B.; Herzfeld, J.; Lugtenburg, J.; Levitt, M. H.; Griffin, R. G. "Determination of membrane protein structure by rotational resonance NMR: bacteriorhodopsin," *Science* **1991**, *251*, 783-786.

(5) Thompson, L. K.; McDermott, A. E.; Raap, J.; van der Wielen, C. M.; Lugtenberg, J.; Herzfeld, J.; Griffin, R. G. "Rotational resonance NMR study of the active site structure in bacteriorhodopsin: Conformation of the schiff base linkage," *Biochemistry* **1992**, *31*, 7931-7938.

(6) Lansbury, P. T., Jr.; Costa, P. R.; Griffiths, J. M.; Simon, E. J.; Auger, M.; Halverson, K. J.; Kocisko, D. A.; Hendsch, Z. S.; Ashburn, T. T.; Spencer, R. G. S.; Tidor, B.; Griffin, R. G. "Stuctural model for the β amyloid fibril: Interstrand alignment of an antiparallel β sheet comprising a C-terminal peptide," *Nat. Struct. Biol.* **1995**, *2*, 990-998.

(7) Gregory, D. M.; Benzinger, T. L. S.; Burkoth, T. S.; Miller-Auer, H.; Lynn, D. G.; Meredith, S. C.; Botto, R. E. "Dipolar recoupling NMR of biomolecular self-assemblies: determining inter- and intrastrand distances in fibrilized Alzheimer's beta-amyloid peptide," *Solid State Nucl. Magn. Reson.* **1998**, *13*, 149-166.

(8) Benzinger, T. L. S.; Gregory, D. M.; [illegible] T. S.; Miller-Auer, H.; Lynn, D. G.; Botto, R. E.; Meredith, S. C. "Propagating structure of Alzheimer's .beta.-Amyloid(10-35) is parallel .beta.-sheet with residues in exact register," *Proc. Natl. Acad. Sci. USA* **1998**, *95*, 13407-13412.

(9) Long, J. R.; Dindot, J. L.; Zebrowski, H.; Kiihne, S.; Clark, R. H.; Campbell, A. A.; Stayton, P. S.; Drobny, G. P. "A peptide that inhibits hydroxyapatite growth is in an extended conformation on the crystal surface," *Proc. Nat. Acad. Sci. USA* **1998**, *95*, 12083-12087.

(10) Spiess, H. W. "Dynamic NMR Spectroscopy," In *NMR Basic Principles and Progress*; P. Diehl; E. Fluck and E. Kosfeld, Ed.; Springer: Berlin, **1978**; Vol. 15; 58-214.

(11) Schmidt-Rohr, K.; Spiess, H. W. *Multidimensional Solid-State NMR and Polymers*; Academic Press: London, **1994**, pp 478.

(12) Griffiths, J. M.; Griffin, R. G. "Nuclear-magnetic-resonance methods for measuring dipolar couplings in rotating solids," *Anal. Chim. Acta* **1993**, *283*, 1081-1101.

(13) Bennett, A. E.; Griffin, R. G.; Vega, S. "Recoupling of Homo- and Heteronuclear Dipolar Interactions in Rotating Solids," In *Solid State NMR IV: Methods and Applications of Solid-State NMR*; B. Blumich, Ed.; Springer-Verlag: Berlin, **1994**; Vol. 33; 1-77.

(14) Munowitz, M. G.; Griffin, R. G.; Bodenhausen, G.; Huang, T. H. "Two-dimensional rotational spin-echo nuclear magnetic resonance in solids: correlation of chemical shift and dipolar interactions," *J. Am. Chem. Soc.* **1981**, *103*, 2529-2533.

(15) Munowitz, M. G.; Griffin, R. G. "Two-dimensional nuclear magnetic resonance in rotating solids: an analysis of line shapes in chemical shift-dipolar spectra," *J. Chem. Phys.* **1982**, *76*, 2848-2858.

(16) Gullion, T.; Schaefer, J. "Rotational-Echo Double-Resonance NMR," *J. Magn. Reson.* **1989**, *81*, 196-200.

(17) Gullion, T.; Baker, D. B.; Conradi, M. S. "New, compensated Carr-Purcell sequences," *J. Magn. Reson.* **1990**, *89*, 479-484.

(18) Hong, M.; Gross, J. D.; Griffin, R. G. "Site-resolved determination of peptide torsion angle phi from the relative orientations of backbone N-H and C-H bonds by solid-state NMR," *J. Phys. Chem. B* **1997**, *101*, 5869-5874.

(19) Hong, M.; Gross, J. D.; Rienstra, C. M.; Griffin, R. G.; Kumashiro, K. K.; Schmidt-Rohr, K. "Coupling amplification in 2D MAS NMR and its application to torsion angle determination in peptides," *J. Magn. Reson.* **1997**, *129*, 85-92.

(20) Hong, M.; Gross, J. D.; Hu, W.; Griffin, R. G. "Determination of the peptide torsion angle phi by 15N chemical shift and 13Calpha-1Halpha dipolar tensor correlation in solid-state MAS NMR," *J. Magn. Reson.* **1998**, *135*, 169-177.

(21) Christensen, A. M.; Schaefer, J. "Solid-state NMR determination of intramolecular and intermolecular P-31-C-13 distances for shikimate 3-phosphate and [1-C-13]glyphosate bound to enolpyruvylshikimate-3-phosphate synthase," *Biochem.* **1993**, *32*, 2868-2873.

(22) Naito, A.; Nishimura, K.; Tuzi, S.; Saito, H. "Inter- and intra-molecular contributions of neighboring dipolar pairs to the precise determination of interatomic distances in a simple [13C,15N]-peptide by 13C, 15N-REDOR spectroscopy," *Chem. Phys. Letters* **1994**, *229*, 506-511.

(23) Anderson, R. C.; Gullion, T.; Joers, J. M.; Shapiro, M.; Villhauer, E. B.; Weber, H. P. "Conformation of [1-C-13,N-15]acetyl-L-carnitine: REDOR NMR spectroscopy," *J. Am. Chem. Soc.* **1995**, *117*, 10546-10550.

(24) McDowell, L. M.; Klug, C. A.; Beusen, D. D.; Schaefer, J. "Ligand geometry of the ternary complex of 5-enolpyruvylshikimate-3-phosphate synthase from rotational-echo double-resonance NMR," *Biochem.* **1996**, *35*, 5395-5403.

(25) McDowell, L. M.; Schaefer, J. "High-resolution NMR of biological solids," *Curr. Opin. Struct. Biol.* **1996**, *6*, 624-629.

(26) Andrew, E. R.; Clough, S.; Farnell, L. F.; Gledhill, T. A.; Roberts, I. "Resonant rotational broadening of NMR Spectra," *Phys. Lett.* **1966**, *21*, 505-506.

(27) Raleigh, D. P.; Levitt, M. H.; Griffin, R. G. "Rotational resonance in solid state NMR," *Chem. Phys. Lett.* **1988**, *146*, 71-76.

(28) Levitt, M. H.; Raleigh, D. P.; Creuzet, F.; Griffin, R. G. "Theory and simulations of homonuclear spin pair systems in rotating solids," *J. Chem. Phys.* **1990**, *92*, 6347-64.

(29) Lakshmi, K. V.; Auger, M.; Raap, J.; Lugtenburg, J.; Griffin, R. G.; Herzfeld, J. "Internuclear distance measurement in a reaction intermediate: Solid-State 13-C NMR rotational resonance determination of the Schiff base configuration in the M photointermediate of bacteriorhodopsin.," *J. Am. Chem. Soc.* **1993**, *115*, 8515-8516.

(30) McDermott, A. E.; Creuzet, F.; Gebhard, R.; VanderHoef, K.; Levitt, M. H.; Herzfeld, J.; Lugtenburg, J.; Griffin, R. G. "Determination of internuclear distances and the orientation of functional groups by solid-state NMR - rotational resonance study of the conformation of the retinal in bacteriorhodopsin," *Biochem.* **1994**, *33*, 6129-6136.

(31) Griffiths, J. M.; Ashburn, T. T.; Auger, M.; Costa, P. R.; Griffin, R. G.; Lansbury, P. T., Jr. "Rotational resonance solid-state NMR elucidates a structural model of pancreatic amyloid," *J. Am. Chem. Soc.* **1995**, *117*, 3539-46.

(32) Spencer, R. G. S.; Halverson, K. J.; Auger, M.; McDermott, A. E.; Griffin, R. G. "An unusual peptide conformation may precipitate formation in Alzheimer's disease: application of solid state NMR to the determination of protein secondary structure," *Biochem.* **1991**, *30*, 10382.

(33) Costa, P. R., *Spins, peptides, and Alzheimer's disease: Solid-state nuclear magnetic resonance investigations of amyloid peptide conformation*, Ph.D. Thesis, Massachusetts Institute of Technology, **1996**.

(34) Costa, P. R.; Sun, B. Q.; Griffin, R. G. "Rotational resonance tickling: Accurate internuclear distance measurements in solids," *J. Am. Chem. Soc.* **1997**, *119*, 10821-10830.

(35) Bennett, A. E.; Ok, J. H.; Griffin, R. G.; Vega, S. "Chemical shift correlation spectroscopy in rotating solids: Radio-frequency dipolar recoupling and longitudinal exchange," *J. Chem. Phys.* **1992**, *96*, 8624-8627.

(36) Bennett, A. E.; Rienstra, C. M.; Griffiths, J. M.; Zhen, W.; Lansbury, P. T., Jr.; Griffin, R. G. "Homonuclear radio frequency-driven recoupling in rotating solids," *J. Chem. Phys.* **1998**, *108*, 9463-9479.

(37) Griffiths, J. M.; Lakshmi, K. V.; Bennett, A. E.; Raap, J.; Vanderwielen, C. M.; Lugtenburg, J.; Herzfeld, J.; Griffin, R. G. "Dipolar correlation NMR spectroscopy of a membrane protein," *J. Am. Chem. Soc.* **1994**, *116*, 10178-10181.

(38) Böender, G. J.; Raap, J.; Prytulla, S.; Oschkinat, H.; de Groot, H. J. M. "MAS NMR structure refinement of uniformly C-13 encriched chlorophyll-A water aggregates with 2D dipolar correlation spectroscopy," *Chem. Phys. Lett.* **1995**, *237*, 502-508.

(39) Egorova Zachernyuk, T. A.; van Rossum, B.; Boender, G. J.; Franken, E.; Ashurst, J.; Raap, J.; Gast, P.; Hoff, A. J.; Oschkinat, H.; deGroot, H. J. M. "Characterization of pheophytin ground states in Rhodobacter sphaeroides R26 photosynthetic reaction centers from multispin pheophytin enrichment and 2-D C-13 MAS NMR dipolar correlation spectroscopy," *Biochem.* **1997**, *36*, 7513-7519.

(40) McDermott, A. E.; Polenova, T.; Coker, G.; Montelione, G.; Zilm, K. W. "NMR resonance assignments of uniformly (13C,15N)-labeled proteins in the solid state," **1999**, manuscript in preparation.

(41) Baldus, M.; Tomaselli, M.; Meier, B. H.; Ernst, R. R. "Broad-band polarization-transfer experiments for rotating solids," *Chem. Phys. Lett.* **1994**, *230*, 329-336.

(42) Baldus, M.; Meier, B. H. "Broadband polarization transfer under magic-angle spinning: application to total through-space-correlation NMR spectroscopy," *J. Magn. Reson.* **1997**, *128*, 172-193.

(43) Tycko, R.; Dabbagh, G. "Measurement of nuclear magnetic dipole-dipole couplings in magic-angle spinning NMR," *Chem. Phys. Lett.* **1990**, *173*, 461-465.

(44) Tycko, R.; Smith, S. O. "Symmetry principles in the design of pulse sequences for structural measurements in magic-angle spinning nuclear magnetic resonance," *J. Chem. Phys.* **1993**, *98*, 932-943.

(45) Sun, B. Q.; Costa, P. R.; Kocisko, D. A.; Lansbury, P. T., Jr. ; Griffin, R. G. "Internuclear distance measurements in solid state nuclear magnetic resonance: Dipolar recoupling via rotor sychronized spin locking," *J. Chem. Phys.* **1995**, *102*, 702-707.

(46) Gregory, D. M.; Mitchell, D. J.; Stringer, J. A.; Kiihne, S.; Shiels, J. C.; Callahan, J.; Mehta, M. A.; Drobny, G. P. "Windowless dipolar recoupling--The detection of weak dipolar couplings between spin-1/2 nucleic with large chemical-shift anisotropies," *Chem. Phys. Lett.* **1995**, *246*, 654.

(47) Lee, Y. K.; Kurur, N. D.; Helmle, M.; Johannessen, O. G.; Nielsen, N. C.; Levitt, M. H. "Efficient dipolar recoupling in the NMR of rotating solids. A sevenfold symmetric radiofrequency pulse sequence," *Chem. Phys. Lett.* **1995**, *242*, 304-309.

(48) Mehta, M. A.; Gregory, D. M.; Kiihne, S.; Mitchell, D. J.; Hatcher, M. E.; Shiels, J. C.; Drobny, G. P. "Distance measurements in nucleic acids using windowless dipoalr recoupling solid state NMR," *Solid State Nucl. Magn. Reson.* **1996**, *7*, 211-288.

(49) Gregory, D. M.; Mehta, M. A.; Shiels, J. C.; Drobny, G. P. "Determination of local structure in solid nucleic acids using double quantum nuclear magnetic resonance spectroscopy," *J. Chem. Phys.* **1997**, *107*, 28-42.

(50) Kiihne, S.; Mehta, M. A.; Stringer, J. A.; Gregory, D. M.; Shiels, J. C.; Drobny, G. P. "Distance measurements by dipolar recoupling two-dimensional solid-state NMR," *J. Phys. Chem. A* **1998**, *102*, 2274-2282.

(51) Bennett, A. E.; Weliky, D. P.; Tycko, R. "Quantitative conformational measurements in solid state NMR by constant-time homonuclear dipolar recoupling," *J. Am. Chem. Soc.* **1998**, *120*, 4897-4898.

(52) Nielsen, N. C.; Bildsøe, H.; Jakobsen, H. J.; Levitt, M. H. "Double-quantum homonuclear rotary resonance: Efficient dipolar recovery in magic-angle spinning nuclear magnetic resonance," *J. Chem. Phys.* **1994**, *101*, 1805-1812.

(53) Rienstra, C. M.; Hatcher, M. E.; Mueller, L. J.; Sun, B.-Q.; Fesik, S. W.; Herzfeld, J.; Griffin, R. G. "Efficient multispin homonuclear double-quantum recoupling for magic-angle spinning NMR: ^{13}C-^{13}C Correlation spectroscopy of U-^{13}C-erythromycin A," *J. Am. Chem. Soc.* **1998**, *120*, 10602-10612.

(54) Karlsson, T.; Levitt, M. H. "Longitudinal rotational resonance echoes in solid state nuclear magnetic resonace: Investigation of zero quantum spin dynamics," *J. Chem. Phys.* **1998**, *109*, 5493-5507.

(55) Karlsson, T.; Helmle, M.; Kurur, N. D.; Levitt, M. H. "Rotational resonance echoes in the nuclear magnetic resonance of spinning solids," *Chem. Phys. Letters* **1995**, *247*, 534-540.

(56) Hohwy, M.; Jakobsen, H. J.; Edén, M.; Levitt, M. H.; Nielsen, N. C. "Broadband dipolar recoupling in the nuclear magnetic resonance of rotating solids: A compensated C7 pulse sequence," *J. Chem. Phys.* **1998**, *108*, 2686-94.

(57) Hohwy, M.; Rienstra, C. M.; Jaroniec, C. P.; Griffin, R. G. "Fivefold symmetric homonuclear dipolar recoupling in rotating solids: Application to double quantum spectroscopy," *J. Chem. Phys.* **1999**, *110*, 7983-7992.

(58) Vega, S. "Fictitious spin 1/2 operator formalism for multiple quantum NMR," *J. Chem. Phys.* **1978**, *68*, 5518-27.

(59) Wokaun, A.; Ernst, R. R. "Selective excitation and detection in multilevel spin systems: Application to single transition operators," *J. Chem. Phys.* **1977**, *67*, 1752.

(60) Haeberlen, U. *High Resolution NMR in Solids: Selective Averaging*; Academic Press: New York, **1976**.

(61) Hohwy, M.; Jaroniec, C. P.; Reif, B.; Rienstra, C. M.; Griffin, R. G. "Local structure and relaxation in solid-state NMR: Accurate measurement of amide N-H bond lengths and H-N-H bond angles," *J. Am. Chem. Soc.* **1999**, submitted.

(62) Chingas, G. C. "Overcoupling NMR probes to improve transient response," *J. Magn. Reson.* **1983**, *54*, 153-157.

(63) Küppers, H. "The crystal structure of ammonium hydrogen oxalate hemihydrate," *Acta Cryst. B* **1973**, *29*, 318-327.

(64) Ishii, Y.; Terao, T.; Hayashi, S. "Theory and simulation of vibrational effects on structural measurements by solid-state nuclear magnetic resonance," *J. Chem. Phys.* **1997**, *107*, 2760-2774.

(65) Hahn, E. L. "Spin Echoes," *Phys. Rev.* **1950**, *80*, 580.

(66) Tomaselli, M.; Hediger, S.; Suter, D.; Ernst, R. R. "Nuclear magnetic resonance polarization and coherence echoes in static and rotating solids," *J. Chem. Phys.* **1996**, *105*, 10672-10681.

(67) Lehmann, M. S.; Koetzle, T. F.; Hamilton, W. C. "Precision neutron diffraction structure determination of protein and nucleic acid components. I. Crystal and molecular structure of the amino acid L-alanine," *J. Am. Chem. Soc.* **1972**, *94*, 2657-60.

(68) Levitt, M. H.; Freeman, R.; Frenkiel, T. "Broadband heteronuclear decoupling," *J. Magn. Reson.* **1982**, *47*, 328-330.

(69) Bevington, P. R.; Robinson, D. K. *Data reduction and error analysis for the physical sciences;* 2nd ed.; McGraw-Hill: Boston, **1992**, pp 328.

(70) Mueller, L. J., *Chemical Exchange in Nuclear Magnetic Resonance*, Ph.D. Thesis, California Institute of Technology, **1997**.

(71) Koetzle, T. F.; Hamilton, W. C.; Parthasarathy, R. *Acta Cryst. B* **1972**, *29*, 509.

(72) Leviel, J.-L.; Auvert, G. "Hydrogen bond studies. A neutron diffraction study of the structures of succinic acid at 300 and 77 K," *Acta Cryst. B* **1981**, *37*, 2185-2189.

(73) Haussühl, S.; Schreuer, J. "Crystal structure, elastic properties and phase transition of triclinic ammonium hydrogen succinate, NH4HC4H4O4," *Z. Krist.* **1993**, *206*, 255-265.

(74) Hirano, A.; Kubozono, Y.; Maeda, H.; Ishida, H.; Kashino, S. "Structure of ammonium hydrogen succinate above and below the phase transition around 170 K," *Acta Cryst. B* **1996**, *52*, 323-327.

(75) Kutzke, H.; Wiehl, L.; Klapper, H. "Crystal structure of diammonium succinate (NH4)2C4H4O4," *Z. Krist.* **1994**, *209*, 256-259.